

Spectroscopic Investigation of a Repetitively-Pulsed Nanosecond Discharge

by

Benjamin T. Yee

A dissertation submitted in partial fulfillment
of the requirements for the degree of
Doctor of Philosophy
(Nuclear Engineering and Radiological Sciences)
in the University of Michigan
2013

Doctoral Committee:

Associate Professor John E. Foster, Chair
Edward V. Barnat, Sandia National Laboratories
Isaiah M. Blankson, National Aeronautics and Space Administration
Professor August Evrard
Professor Mark Kushner

©Benjamin T. Yee

2013

Acknowledgments

TABLE OF CONTENTS

Dedication	ii
Acknowledgments	iii
List of Figures	vii
List of Tables	xi
List of Appendices	xii
List of Abbreviations	xiii
 Chapter	
1 Introduction	1
1.1 Overview	1
1.1.1 Motivation	1
1.1.2 History	4
1.1.3 Questions	7
1.1.4 Approach	8
1.2 Literature Review	9
1.2.1 Early History of Pulsed Discharges	9
1.2.2 The Streamer Model	11
1.2.3 Diffuse Streamers	12
1.2.4 Repetitively-Pulsed Nanosecond Discharges	14
1.3 Summary	16
2 Theory	19
2.1 Ionized Gas	19
2.2 Plasma Criteria	23
2.2.1 Debye Length	23
2.2.2 Debye Sphere	24
2.2.3 Plasma Oscillations	24
2.3 Discharge Initiation	26
2.3.1 Townsend Mechanism	26
2.3.2 Streamer Mechanism	27
2.3.3 Homogeneity Condition	28
2.4 Atomic Spectroscopy & Notation	31

2.4.1	Spectral Lineshapes	34
2.4.2	Absorption	38
3	Experiment	40
3.1	Discharge Apparatus	40
3.2	Field Calculations	45
3.3	Operating Procedures	47
3.4	Electrical Characteristics	48
3.5	Energy Coupling	51
4	Metastable Measurements	53
4.1	Setup	55
4.2	Noise Suppression & Absorption Analysis	59
4.3	Results	62
4.3.1	Temperatures	63
4.3.2	Line-integrated Densities	66
4.3.3	Metastable Destruction	69
4.4	Summary	73
5	Modeling	75
5.1	Model Development	76
5.1.1	Continuity Equation	77
5.1.2	Distribution Effects	80
5.1.3	Energy Equation	87
5.1.4	Model Solutions	89
5.2	Perturbation Study	91
5.3	Plasma Dynamics	94
5.4	Summary	102
6	Population Kinetics	104
6.1	Emission Measurements	104
6.2	Wave Velocities	106
6.3	Electron Temperatures	107
6.3.1	Boltzmann Plots	108
6.3.2	Coronal Model	112
6.4	Emission Comparisons	118
6.4.1	Excitation Duration	118
6.4.2	Radiation Trapping	120
6.5	Summary	124
7	Conclusions	126
7.1	Overview of Results	127
7.2	Future Work	134
7.3	Final Remarks	135
Appendices	136

Bibliography	201
---------------------	------------

LIST OF FIGURES

Figure

1.1	A simplified depiction of the avalanche breakdown process in a gas.	2
1.2	A sketch of J.J. Thomson's early experiments on pulsed plasmas in long vacuum tubes [1].	10
2.1	Comparison of the Maxwell-Boltzmann energy distribution and the Druyvesteyn distribution for the same average energy (illustrated by the dotted line).	21
2.2	Illustration of the various regimes of plasma in terms of electron temperature and density with the RPND regime highlighted, adapted from [2].	25
2.3	An illustration of the development of a single streamer. (a) A seed electron is accelerated by the applied electric field. (b) The initial electron develops into an avalanche which leaves a large region of positive space charge, slowing further advance. (c) The streamer propagates toward the cathode via photoionization and the anode via nonlocal electrons and photoionization. Adapted from [3] and [4].	28
2.4	Numerical calculations of the avalanche length and avalanche radius for in helium at a pressure of 4.0 Torr as a function of the slope of the electric field, dE/dt	30
2.5	Minimum preionization densities required at a variety of pressures and breakdown delays. The dotted line indicates the background ionization level as a result of cosmic radiation.	31
2.6	A partial Grotrian diagram of neutral helium, from [5].	35
2.7	A comparison of the three primary spectral lineshapes, each with the same full width.	37
3.1	Two illustrations of the RPND apparatus. The upper version is an annotated sketch of the device, and the bottom version simplifies the geometry into its three electrical components.	41
3.2	Simplified diagram of the gas flow path and pumping system.	43
3.3	Photograph of the discharge apparatus.	44
3.4	Sketch of the unassembled back-current shunt, and a photograph of it assembled around the transmission line.	45
3.5	Heatmap and vector plot of the electric field in the RPND discharge apparatus.	46
3.6	Typical voltage waveform of the RPND. Arrows indicate reflections back to the power supply. The dotted line delineates the time at which the power supply begins to exhibit double pulsing.	48

3.7	High resolution views of the voltage and current waveforms for the first incident and reflected pulse, at each of the operating pressures.	50
3.8	Plot of the energy coupled into the discharge with the first pulse as a function of pressure.	52
4.1	Optical beam path of the laser in the absorption spectroscopy experiment. DFB - Distributed feedback laser diode; FI - Faraday isolator; ND - neutral density filter; S - shutter; PD - photodiode; AP - aperture.	56
4.2	Measurement of the transmitted laser light at the nominal transition wavelength at 4.0 Torr of helium.	58
4.3	Heatmaps of the transmitted laser signal for the 4.0 Torr condition at various stages of post-processing.	60
4.4	Comparison of the measured transmission profile (open symbols) and the computer-generated matches for at several different times for the 4.0 Torr operating condition.	62
4.5	Plot of the gas temperatures at each of the operating pressures and each axial location as a function of time.	64
4.6	Plot of the average gas temperature as a function of deposited energy.	65
4.7	Plots of the line-integrated metastable densities at each of the operating pressures and each axial location as a function of time.	67
4.8	Zoomed in view of the increases in metastable density as a result of pulse reflections.	68
4.9	Measurements of the long-duration metastable density trends. Exponential fits are indicated by the dotted lines.	70
4.10	Peak line-integrated metastable densities as a function of pressure.	71
4.11	Comparison of the decay rates for various processes at 0.3 Torr as a function of metastable density.	72
5.1	Schematic description of the PIC simulation process, adapted from [6].	82
5.2	Contour plots of the EEDFs determined from PIC simulations, and the corresponding Maxwell-Boltzmann distributions for a range of electric fields.	85
5.3	Simulations showing the effects of perturbations to the initial conditions on the metastable dynamics.	92
5.4	Ionization rates coefficients corresponding to the perturbed electric field simulations.	94
5.5	Comparison of measured metastable values (open circles) to simulations (solid lines) for a range of pulse-widths.	95
5.6	The emissions of the 4^1P^o - 2^1S transition in the RPND, overlaid on top of the voltage pulse.	96
5.7	The electric fields necessary to generate the same metastable density at 4.0 Torr as a function of the pulse-width.	96
5.8	Ionization and metastable rate coefficients as functions of electron temperature.	97

5.9	Comparison of the measured metastable densities (open circles) to the global model simulations. The shaded region illustrates the measured voltage pulse. The parentheses following the 8.0 Torr labels indicate the axial location of the measurement: U - upstream, M - midstream, and D - downstream.	98
5.10	Global model predictions of the electron temperatures at the simulated conditions, overlaid on the corresponding electric field.	100
5.11	Global model predictions of the electrons densities at the simulated conditions overlaid on the reduced electric field.	101
6.1	Temperatures estimated using Boltzmann plots of the measured emissions (dashed, red lines) and simulated emissions (dotted, blue lines) compared to the simulated temperatures (solid, black line).	110
6.2	Boltzmann plot examples for the RPND. Open symbols represent the measured values and the solid lines are the corresponding best fits.	111
6.3	The emission ratios of $4^3S-2^3P^o$ over $4^1D-2^1P^o$ and $3^3S-2^3P^o$ over $3^1S-2^1P^o$, as functions of the electron temperature.	113
6.4	Estimates of the electron temperatures based on the ratio of the $4^3S-2^3P^o$ and $4^1D-2^1P^o$ transitions. The estimates were generated for the simulated emissions (dotted, blue lines) and measured emissions (dashed, red lines), and are compared to the actual temperature results from the global model simulation (solid, black lines).	114
6.5	Estimates of the electron temperatures based on the ratio of the $3^3S-2^3P^o$ to $3^1S-2^1P^o$, transitions. The estimates were generated for the simulated emissions (dotted, blue lines) and measured emissions (dashed, red lines), and are compared to the actual temperature results from the global model simulation (solid, black lines).	116
6.6	Comparison of the measured and simulated emissions from the $3^1D-2^1P^o$ transition at pressures of 1.0, 4.0, and 8.0 Torr.	119
6.7	Comparison of the measured and simulated $3^1P^o-2^1S$ and $3^3P^o-2^3S$ emissions normalized to the most intense condition at 1.0, 4.0, and 8.0 Torr.	122
A.1	Vacuum chamber used in RPND experiments at the NASA GRC along with an intensified CCD used for fast imaging.	138
A.2	The electrodes used in the RPND at NASA GRC. The electrodes are made of copper with a ceramic sheath made of Mykroy.	139
A.3	The evolution of the density (—) and the collision frequency (··) in a RPND over a period of 30 minutes. These quantities reach their respective maximum and minimum after approximately five minutes, however these are not equilibrium values. The RPND continues to change over long durations.	144
A.4	A Fortrat diagram for the (0, 0) transition of $c^3\Pi_u - b^3\Pi_g$. The P branch is identified by an open circle (\circ), the Q branch is identified by an open diamond (\diamond) and the R branch is identified by an open square (\square). Each branch features a number of sub-branches which can distinguished with an imaging system of sufficient resolution.	150

A.5	A plot of the rotational lines generated by the Budó's expression for a varying degree of spin-coupling. All branches and their respective sub-branches are shown. The intensities were calculated by assuming a Boltzmann distribution and were normalized by the appropriate Honl-London factors.	151
A.6	Each spectrum was processed using a computer program, described by this flowchart. The only required inputs are the spectrometer settings, the CCD image and the wavelength calibrations. Each measured spectrum is compared to a number of simulated spectra in order to determine the appropriate match.	152
A.7	A plot of a measured spectrum, the simulated match and the difference between the two. The measured spectrum is illustrated with solid circles while the simulation is represented by the solid black line and the differences are shown with a dashed red line. The peak of the simulated spectrum is shifted toward higher wavelengths when compared to the measured spectrum.	154
A.8	Rotational temperature trends for three operating conditions: ± 4.3 (solid black), ± 6.1 (dashed red) and ± 7.3 kV (dotted blue). The first two cases exhibit significant variations near the end of the measurement period as a result of low signal-noise ratios. Only ± 7.3 kV case shows any clear trends over the duration of the measurement.	155
D.1	Singlet emissions at 0.3 Torr.	185
D.2	Triple emissions at 0.3 Torr.	186
D.3	Singlet emissions at 0.5 Torr.	187
D.4	Triple emissions at 0.5 Torr.	188
D.5	Singlet emissions at 1.0 Torr.	189
D.6	Triple emissions at 1.0 Torr.	190
D.7	Singlet emissions at 2.0 Torr.	191
D.8	Triple emissions at 2.0 Torr.	192
D.9	Singlet emissions at 3.0 Torr.	193
D.10	Triple emissions at 3.0 Torr.	194
D.11	Singlet emissions at 4.0 Torr.	195
D.12	Triple emissions at 4.0 Torr.	196
D.13	Singlet emissions at 8.0 Torr.	197
D.14	Triple emissions at 8.0 Torr.	198
D.15	Singlet emissions at 16.0 Torr.	199
D.16	Triple emissions at 16.0 Torr.	200

LIST OF TABLES

Table

4.1	Listing of the extrapolated, pre-pulse line-integrated metastable densities, and decay coefficients as a function of pressure.	73
5.1	Nominal simulation parameters for the 4.0 Torr operating condition.	91
5.2	Summary of the peak values for several plasma parameters from the global model simulations.	100
6.1	Table of the observed optical transitions and their transition rates.	105
6.2	Wave velocities in the RPND.	107
6.3	The effective lifetimes of the 3^1P - 1^1S transition resulting from radiation trapping.	123

LIST OF APPENDICES

Appendix

A Measurements in an Air RPND	136
B Laser-Absorption Analysis Code	158
C Global Model Code	170
D Additional Emission Measurements	184

LIST OF ABBREVIATIONS

- RPND** repetitively-pulsed nanosecond discharge
DBD dielectric-barrier discharge
APP atmospheric-pressure plasma
EEDF electron energy distribution function
FIW fast ionization wave
LAS laser-absorption spectroscopy
LCIF laser collision-induced fluorescence
MHD magnetohydrodynamic
FWHM full-width half maximum
FID fast ionization dynistor
CCD charge-coupled device
PTFE polytetrafluoroethylene
PIC particle-in-cell
NASA National Aeronautics and Space Administration
GRC Glenn Research Center
mmW millimeter-wave
EMI electromagnetic interference
PMT photomultiplier tube
GUI graphical user interface
PLTE partial local thermodynamic equilibrium
CFL Courant-Friedrich-Lowy

CHAPTER 1

Introduction

1.1 Overview

1.1.1 Motivation

Plasmas, commonly called the fourth state of matter, are a gas where a significant fraction of the neutral atoms or molecules have been split into pairs of electrons and positive ions. Initially, a curiosity of the laboratory, they have become a critical part of every day life. The electrically charged nature of plasmas makes them a practical means by which to convert electrical energy into electromagnetic, chemical, kinetic, or even nuclear energy. From an applications perspective, they are indispensable in lighting, semiconductor manufacturing, plastic processing, and space propulsion. On a more broad scale, virtually all observable light in the universe is the result of a plasma in some form or another [7].

Some exceptions aside, only three things are required to create a plasma: a gas, an energy source, and a means of transferring the energy to the gas. In man-made applications, the energy source is typically electricity, and the simplest transfer mechanism is via two electrodes placed on either side of the gas. The application of a potential difference to these electrodes produces an electric field as seen in figure 1.1. The field accelerates a single seed electron in the gas (often created by background cosmic radiation) until it collides with a neutral particle. The electron, having acquired a sufficient amount of energy, liberates a second electron loose from the particle, leaving behind a relatively heavy and immobile

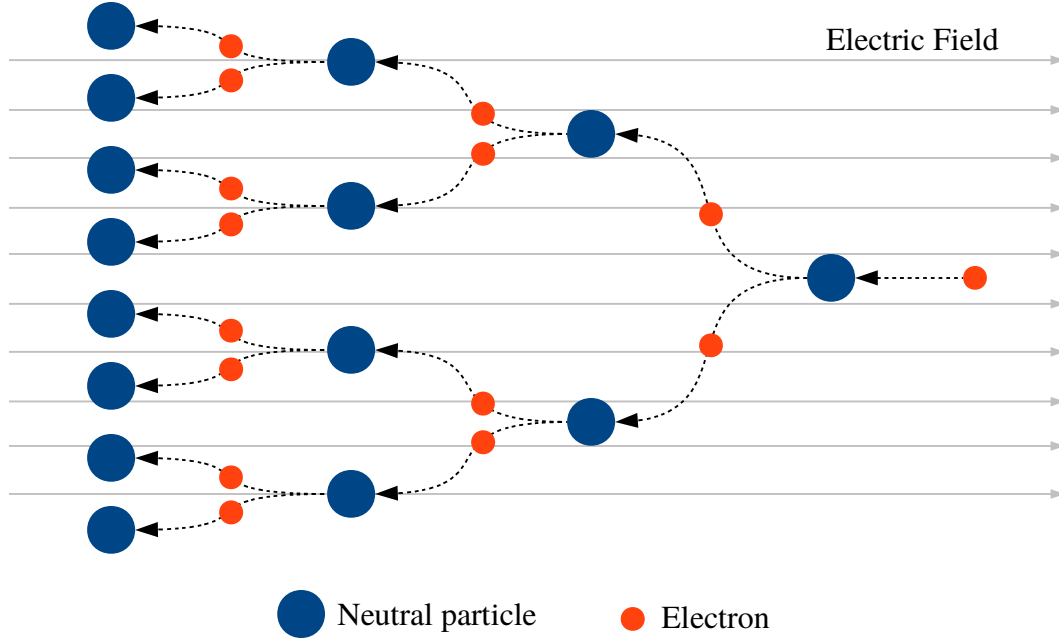


Figure 1.1: A simplified depiction of the avalanche breakdown process in a gas.

ion. Subsequently, both the first and second electron are now accelerated by the electric field. Again, they collide with two more neutral atoms, creating two new electrons. As long as the electric field persists, the number of electron and ion pairs increases exponentially. This process is generally referred to as an avalanche.

Eventually, the production of ions and electrons in the gap balances out with the rate at which they leave the system, whether by collection at the electrodes or some other process. The resulting ionized gas may be referred to as a plasma if it meets certain criteria. Simply put, there must be a high enough density and number of charged particles for their electromagnetic interaction to dominate over random collisions with neutral gas particles.

Despite this relatively simple recipe, the physical characteristics can vary greatly depending on what gas is used, what pressure it is at, what voltage is used, whether the electricity is applied constantly or varied over time, what kind of electrodes are used, etc. As a result, man-made plasmas are generally produced under very specific conditions. For example, a plasma etcher used in semiconductor manufacturing may need to operate oper-

ate at pressures that are one-thousandth of atmospheric pressure with ultra-pure (99.999%) gases [8].

Plasmas like those which occur in plasma etchers, feature ions and neutral gas particles with temperatures that are below 1,000 K, or roughly 1,340° F. Though this temperature is relatively high compared to room temperature, it is well below the temperature of the electrons which may be in excess of 20,000 K. Plasmas which exhibit this disparity in temperatures are often called nonequilibrium or “low-temperature” plasmas.

Conversely, there exists another class of plasmas where the electrons, ions, and neutral particles are all at the same temperature. These are called thermal plasmas. Generally speaking, the closer the gas pressure is to atmosphere, the more thermal a plasma is owing to the rapid increase in the frequency of collisions between neutral and charged particles [9]. Additionally, the temperatures in a thermal plasma can be quite high and, in many cases, can easily melt all metals assuming that the total energy content of the plasma is high enough. For example, the arc of an arc welder is a thermal plasma. Similar high temperature plasmas, have a number of other applications which include a variety of high-intensity lamps, metal cutting, and surface coating.

There are, however, a number of applications which would benefit from operation at higher pressures, but with low-temperature ions and neutrals so as to avoid heat damage. This has spurred a substantial amount of research on nonequilibrium atmospheric-pressure plasmas (APPs) in recent years [10]. Ideally, such a plasma could be generated at or near atmospheric pressure with hot electrons, but minimal heating of surrounding gas. Though this field of research is still relatively young, it has produced a variety of new plasmas and capabilities. One of the more ubiquitous examples is use of plasmas to process the surface of plastics so that ink can adhere. Separately, nonequilibrium APPs are the technology which drives plasma televisions [11].

As mentioned, these applications promise to be the first of many for such plasmas. More recently, there have been innovative proposals to use these plasmas in water purification

[12], wound sterilization [13], improved combustion engines [14], nanoparticle production [15], and more. However, each situation has its own challenges when it comes to the design and development of a plasma source, particularly at these elevated pressures. Particularly problematic is the tendency of APPs to develop instabilities which can cause them to rapidly transition to thermal plasmas in a matter of nanoseconds.

There exist a few ways of getting around these instabilities. One example is the dielectric-barrier discharge which passively regulates the amount of power which can be deposited into the plasma [16]. Another example includes split-ring resonators which use natural feedback mechanisms to damp out potential instabilities [17]. The technique considered here, referred to as the repetitively-pulsed nanosecond discharge, or RPND, uses high voltage pulses which are so short that the instability does not have time to develop [18]. The RPND is a nonequilibrium plasma which can operate at pressures ranging from approximately 10^{-3} –1 atmospheres [19]. At atmospheric pressure the RPND can produce a uniform plasma in volumes on the order of 10 mL [20]. As the pressure is reduced, the plasma volume can reach the order of liters [21].

The importance of large-area, uniform, high-pressure plasmas such as the RPND was highlighted in the National Academies' most recent decadal survey of plasma science [7]. However, there is still much that is not known about such plasmas. From the same survey, it is said that “the full promise of APPs will be known only if they can be understood and managed based on fundamental scientific principles at two extremes—the nanoscopic kinetic level, where selective chemistry occurs, and the global stability level.” It is this challenge, specifically the investigation of the nanoscopic kinetic level, which drives the research presented here.

1.1.2 History

Historically, the study of low-temperature APPs has been almost indistinguishable from the study of plasmas as a whole. However, this was not necessarily a matter of reasoned choice.

Plasma generation at atmospheric-pressure obviates the need for an effective vacuum pump. Additionally, prior to the creation of large battery banks, early sources of electrical energy had relatively small capacities. This precluded the generation of thermal atmospheric plasmas which required large amounts of energy.

Indeed, the requirements for a low-temperature APP are sufficiently rudimentary that the first man-made one (and likely the first man-made plasma), was probably a spark generated by rubbing fur against amber. This is commonly attributed to Thales of Milêus from around 600 B.C. Following Thales, electrical sparks came to intrigue many scientists including Gottfried Liebniz, Benjamin Franklin, and Charles Wheatstone. By the mid-1800s, Plücker, Geißler, and Hittorf began some of the first work on low-pressure plasmas though it was Crookes who would later identify plasma as a separate state of matter. Later, J.J. Thomson's discovery of the electron and discretized charge in 1897 marked the beginning of modern plasma research.

By this time, the necessary tools and techniques existed to create steady plasmas in pure, rarified gases. The behaviors of which were dominated by the motion and interaction of the charged electrons and ions. Critically, the effects of the neutral particles were negligible, thus isolating the electrical properties of the plasma. These carefully controlled systems were ideal for basic studies of plasma behavior and were used to great effect by individuals such as Lewi Tonks and Irving Langmuir [22]. In fact, many modern concepts in plasma physics can be traced back to their work.

In contrast, the pulsed APPs, characteristic of the earliest man-made plasmas [23], were easy to create, but notoriously difficult to work with. It could take them only a few nanoseconds to form, and less than a millisecond to decay away. For many years, there were simply no instruments capable of taking measurements this quickly. Furthermore, the neutral particles which were of no consequence in the low-pressure plasmas, could not be ignored. The neutral particles were present in such quantities that they could confound or obscure otherwise simple measurements.

As a consequence, there is still a great deal that is not known about pulsed APPs, particularly lightning, streamers, and a type of plasma which Thomson referred to as a “luminous front.” By the 1970s, this latter plasma had come to be called the fast ionization wave, or FIW [19]. It was generated by a single voltage pulse lasting around 100 nanoseconds and peaking at 10s or 100s of kilovolts. For the right pressure and gas, the FIW could fill volumes of nearly 40 L with a relatively uniform plasma, but with little heating of the gas.

These properties were attractive for a number of uses, but the FIW faced a number of implementation-related challenges. The switches used to trigger the FIW could only operate up to 100 times each second [24]. Unfortunately, the lifetime of a plasma at elevated pressures is relatively short, and the plasma generated by the FIW would decay away quickly after each pulse. This meant that the FIW-generated plasma had a relatively low duty cycle; the ratio of the time the plasma spends on to the time it spends off. This was disadvantageous for plasma-processing applications where low duty cycles are equivalent to long processing times. The low duty cycle also necessitated so-called preionization of the gas with UV lamps or a secondary plasma generator, adding to the cost and complexity of the system [3]. Finally, the pulse generators used for FIWs were not considered reliable enough for long operational lifetimes.

Recent advances in solid-state switching technology has largely solved these issues. At present, switches exist which can reliably operate 100,000 times a second; sufficiently fast that the plasma duty cycle approaches 100% [25]. This has the additional benefit of obviating the need for a preionization stage, as a sufficient number of electrons persist between pulses. The discharge produced by the use of these new switches is what we refer to as the RPND.

1.1.3 Questions

The large pedigree of pulsed plasma research belies the fact that they are still not well-understood. This remains especially true for RPNDs which present significant experimental challenges. A major component of this has to do with the time scales associated with the RPND. The formation of a RPND often requires no more than a few nanoseconds. Very sensitive equipment is required in order to measure changes which occur during this period. Unfortunately, such equipment is particularly susceptible to the broadband electronic noise generated by both real and displacement currents of the fast pulses. There is a plethora of other problems that can be traced back to topic of timing. For example, the length and insulators of detector cables can introduce substantial delays, and must be considered in order to synchronize different measurements.

Consequently, the majority of RPND studies focus on measurements after the discharge has occurred, when changes happen at a much slower rate. A great deal of information is available for this period of time, including chemical compositions, atomic densities, electron densities, gas temperatures, and more. While undoubtedly important, these measurements provide limited insight on what is happening *while* the plasma is forming. It is natural, then, to ask, what are the RPND plasma properties during formation?

Additionally, most studies have used a limited range of gases: oxygen, nitrogen, air, hydrogen, or some mixture thereof. The choice of these gases is deliberate and reflects specific applications in combustion and aerospace. However, the use of rare gases (such as helium) and rare gas mixtures has become popular because they provide for a wider range of stable operating conditions. Notably, it has been found that the unique internal electronic structure of rare gases can produce very different discharges. Given this, there is the question of how rare gas RPNDs compare to more conventional ones.

Finally, the persistence of the plasma between pulses makes the development of a RPND very different from a FIW.

Finally, though the RPND and FIW are qualitatively similar, there are some fundamental

differences between the two. These largely stem from the persistence of the plasma between pulses. It is this plasma which guarantees uniform breakdown in the case of RPND, while the FIW is largely dependent on very high energy electrons. At the same time, if the plasma is too dense at the beginning of the voltage pulse, it can limit the final density of the electrons and excited atoms. Because plasma-induced chemistry is a product of these particles, this pre-pulse plasma plays a decisive role in the number of reactions a RPND can produce. Therefore, one must ask how the properties of a RPND compare to those of a FIW and how they vary with the operating conditions.

1.1.4 Approach

The dissertation presented here represents efforts to either answer or provide a foundation to answer these questions. In order to develop the appropriate context for this work, the next section will be a comprehensive review of the RPND literature. It begins with the first reported pulsed APPs and concludes with contemporary studies.

The following two chapters set the basis for the experimental and numerical studies. Chapter 2 presents the theory necessary to understand RPNDs including streamer discharges, atomic spectroscopy, and collision processes. Subsequently, Chapter 3 describes the design of the helium RPND discharge apparatus used for the experimental studies and as the basis for the simulations. Also included in this chapter are several measurements of the basic discharge properties.

Chapters 4 through 5 provide more detailed measurements and analysis of the RPND dynamics. In Chapter 4, the measurements of the helium metastables in a RPND are presented and analyzed as a function of pressure and axial location in the discharge apparatus. Chapter 6 presents and analyzes similar measurements of the spontaneous plasma emissions. Finally, Chapter 5 discusses the development of a global model for a helium plasma and its use with the experimental data to infer the plasma properties of the RPND. The dissertation concludes with a summary of the results and suggestions for further avenues of

research.

1.2 Literature Review

RPNDs are only a recent invention which resulted from advances in fast-switching semiconductors. However, the physics of their formation is related to a much more broad category of plasmas which includes lightning, streamers, and even some transient phenomena in DC glows [26]. These plasmas are unique in that their spatial structure develops at speeds much faster than can be accounted for by the conventional Townsend mechanism. Loeb refers to this phenomena as “ionizing waves of potential gradient.”¹.

1.2.1 Early History of Pulsed Discharges

In 1835 (as reported by Thomson [1]), Charles Wheatstone attempted to measure what he thought to be the speed of electricity in a six-foot long discharge tube of unspecified pressure [27]. It is now known that he was actually measuring the speed with which a plasma formed between the two electrodes. He accomplished this by the use of a rotating mirror which allowed him to see images of two sections of the tube, slightly displaced. The displacement between the images was proportional to the speed with which the plasma traveled between them. Wheatstone estimated this speed to be at least 8×10^7 cm/s.

Interestingly, von Zahn later noted that this was *not* the speed of the emitting particles [28]. The visible light did cross the gap at an appreciable speed, but there was no detectable Doppler shift in the light emitted parallel to the propagation. As a result, it was concluded the light-emitting particles could not be traveling at the same speed as the light.

Later, Thomson revisited this work with an improved apparatus [1]. This included a tube that was now 15 m in length and five mm in diameter, as seen in figure 1.2. Also

¹It should be noted that the phrase wave does not indicate any kind of periodic motion or spatial arrangement. Simply put, it describes a boundary which separates ionized and unionized gas which travels from one electrode to another.

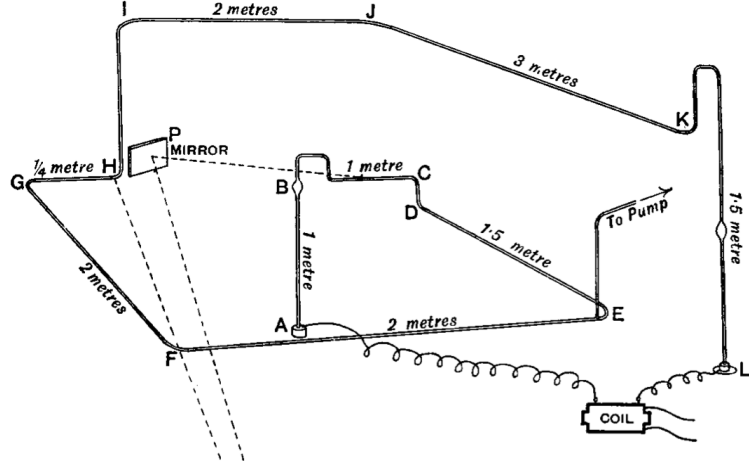


Figure 1.2: A sketch of J.J. Thomson’s early experiments on pulsed plasmas in long vacuum tubes [1].

using the rotating mirror apparatus, Thomson was able to greatly improve on the estimates of Wheatstone. He estimated that the so-called “luminous front” had a speed that was more than 1.5×10^{10} cm/s, or in excess of half of the speed of light. Furthermore, Thomson determined that the luminous front always appeared to travel from the positively pulsed electrode (anode) to the ground electrode (cathode).

The study of these luminous fronts was revisited by several researchers in the wake of Thomson [29–31], but their attempts to duplicate the measured speeds were met with varied success. In 1930, Beams confirmed definitively those of Thomson. He also found that the front always initiated at the electrode with the highest, absolute potential, relative to ground. Beams hypothesized that the rapid motion of the front was a result of a self-propagating region of high space charge, quote:

In the neighborhood of the electrode . . . the field is very high and intense ionization should take place. This ionization due to the large difference in mobilities of positive ions, negative ions and electrons respectively should result in the establishment of a space charge. This space charge, once formed near the high potential electrode . . . must move down the tube regardless of the polarity of the applied potential because of the changes it produces in the field near its edges.

At about the same time, Schonland and Collens reported on their observations of lightning [32]. Though the general structure and length scale of lightning is substantially different from the luminous fronts observed by Beams and Thomson, the two phenomena would later prove to be very similar. In their work Schonland and Collens noted that lightning would usually occur in a two-step process. Based on the images they obtained, they suggested that the leader was generated by a relatively small “dart” with a mean vertical velocity of 7.2×10^8 cm/s. The dart moved in a random manner, changing directions at random intervals, but always moving toward the ground.

The second step began when this dart reached the ground. Once there, a bright return stroke would occur along the same path that the leader had traced out. In contrast to the leader stroke, the return stroke had a velocity of 5×10^9 cm/s. Schonland and Collens hesitantly attributed the leader stroke to an extended electron avalanche, and the return stroke to thermal ionization along the conductive path generated by the dart. However, calculations by Cravath and Loeb showed that the speeds of the proposed avalanche was inconsistent with the fields at the head of a lightning stroke [33]. Instead, they suggested that the dart was actually a moving region of space charge which locally accelerated electrons to ionizing energies. This was similar to the mechanism earlier proposed by Beams.

1.2.2 The Streamer Model

It was long known that sparks in air were similar to lightning. Advances in technology during the 1930’s led to experiments which reinforced this similarity. In response to the measurements of Schonland and Collens; Snoddy, Beams, and Dietrich studied the breakdown of gas in a long tube with both positive and negative applied potentials [34]. Using an oscilloscope, they observed both the leader and a return stroke in both cases. However, the propagation of the plasma wave toward the cathode required a source electrons ahead of the wave. The authors proposed that photoionization might provide these necessary electrons.

Around the same time, Flegler and Raether had come to a similar conclusion regarding

the importance of photoionization. This led them to develop a more thorough theoretical model for these waves [35] which came to be known as the streamer theory. This was followed by a similar treatment by Loeb and Meek [36–38]. The streamer theory divided the initial plasma formation into two steps. In the first step, an electron avalanche is initiated between two electrodes. The avalanche travels toward the anode and leaves behind a region of positive space charge. In the second step, the return stroke begins at the anode and travels along the conductive path generated by the initial avalanche toward the cathode.

The streamer model proved relatively successful in describing the development of sparks and lightning. Theoretical estimates of the speed matched the velocity measurements that were acquired with photographs and oscillographs. Additionally, the theory was able to account for the branching manner in which lightning was formed as well as the constriction in space.

Following the initial work of Flegler, Raether, Loeb, and Meek, a number of researchers began to explore the boundary between the Townsend mechanism and the streamer mechanism. Most notable was Fisher and Bederson’s work in 1951 [39], which was later extended to nitrogen [40] and argon [41]. These studies suggested that the streamer theory was incomplete. Furthermore, the reliance of the streamer theory on photoionization would later prove very contentious [42]. Finally, there was a whole class of discharges that it did not readily explain.

1.2.3 Diffuse Streamers

As noted by Chalmers [43], Rogowski and Buss [44, 45] observed a fast, diffuse, glow discharge immediately prior to the filaments of a streamer discharge. Allibone and Meek, noted similar diffuse discharges in air based on oscillographs and photographs [46–48]. However, the Boys apparatus [49] which was employed in these studies (an ancestor to the modern streak camera) was unable to capture the evolution of the diffuse glow, given its large spatial extent.

This was first noted by Allibone who attempted to use Lichtenberg figures² to definitively capture this diffuse glow [50]. Later, Saxe and Meek used the recently invented photomultiplier tube to record the evolution of the light emissions in the brief, diffuse glow [51] as a function of space. Both studies agreed in the existence of the diffuse glow, despite some disagreement on the nature of its geometry and propagation.

By 1968 (according to Kunhardt and Byszewski [4]), Stankevich and Kalinin had provided the most firm evidence yet of a diffuse discharge in a dense gas [52]. This was later confirmed by experiments with a pulsed nanosecond discharge by Mesyats, Bychkov, and Kremnev [53]. In their analysis, they concluded that photoionization could not play a role in such short-lived discharges. The formation of their discharge only required several nanoseconds, much shorter than the lifetimes of the excited states responsible for photon emission. They suggested that the streamer model required some extension.

In addition to the diffuse discharge, Stankevich and Kalinin also noted the detection of x-rays with each pulse. This suggested the presence of high-energy electrons impinging on the surface of the electrodes, despite the high collisionality of the dense gas. Not only that, but the electron energies could even exceed what would be expected from the vacuum electric fields [54]. The eventual conclusion was that the electric field associated with the space charge at the head of the streamer produced very energetic electrons which deposited their energy far from the streamer tip [4,55], allowing the streamer to spread out beyond the diffusive region of the electrons.

It was based on the studies of the fast electrons in these discharges that Mesyats, Bychov, and Kremnev proposed the use of a fast electron beam for pumping high-pressure gas lasers. Similar work was conducted simultaneously by Fenstermacher et al. [56]. Palmer [57], and Levatter and Lin [3] determined that there was a threshold amount of preionization required to ensure homogeneity of the discharge. Hunter [58], and Koval'chuk and Mesyats [59] later proposed that such discharges be used for fast-closing switches. Gas lasers and fast

²Such figures directly exposed photographic emulsions to the electrical discharge. The developed image was a time-integrated representation of the discharge.

switches would drive much of the later research on fast, pulsed discharges.

Eventually these discharges came to be referred to as fast ionization waves (FIWs). A large body of Russian literature developed around their study, though much of it has remained untranslated. In 1994, Vasilyak produced an extensive review of these studies [19]. The data include wave velocities for a variety of gases and pressures. Other parameters such as attenuation coefficients for the waves, high energy electron currents, electric field measurements, and a circuit model of the FIW are also included.

1.2.4 Repetitively-Pulsed Nanosecond Discharges

The type of discharge originally studied by Babich, Loika, and Tarasova came to be known as the fast ionization wave (FIW). In the years following its discovery, a substantial effort was made to document the properties of the FIW over a wide range of conditions. In these studies, the wave velocity, current, and attenuation were the most frequently measured quantities. Much of this work is summarized in a review by Vasilyak [19]. Also reviewed are Slavin and Sopin's work which was the first to attempt a computation of the electron energy distribution function EEDF in FIWs [60].

The experimental measurements and computational work reported by Vasilyak were expanded on by a series of studies conducted at the Moscow Institute of Physics. These are reviewed by Starikovskaia et al. [24] and included measurements of the electron density, electric field, and energy coupling for FIWs in air, nitrogen, and hydrogen. The computational work by Starikoskaia and Starikovskii [61] still represents the most detailed study of the EEDF in nitrogen FIWs.

However, Starikovskaia et al. noted that the usefulness of FIWs were limited, in part, by their repetition rates. The power supplies for FIWs were capacitor banks, charged in parallel, and discharged in series (also referred to Marx banks). Unfortunately, the spark gaps used to trigger these capacitor banks would not operate above a few hundred Hz. This changed in the late 1990's with the development and commercialization of fast, solid-state

switches. Specifically, with the fast ionization dynistor it was possible to achieve repetition rates of 100 kHz [25].

This led to a new class of repetitively-pulsed discharges, or the RPND. These discharges operated at sufficiently high rates such that the electrons and ions would persist in significant quantities between pulses. This meant that the plasma duty cycle was increased by a significant amount. These improved qualities of the RPND over the FIW inspired a number of novel, application-driven studies. This included:

- Plasma-assisted combustion [18, 62, 63]
- Magnetohydrodynamic energy bypass engines [18, 64, 65]
- Plasma actuators [66, 67]
- High-pressure xenon lamps [68]
- Plasma medicine [13, 69]
- Water treatment [70]

Though not specific to the RPND, Becker et al. [10] provide an extensive discussion of the potential uses for non-equilibrium air plasmas.

As a result, contemporary researchers have produced a wealth of literature on the operation of RPNDs. More recently, there have been detailed measurements of the gas temperatures [62, 71–77], chemical composition [73–75], electric fields [78–80], and energy coupling [62, 81]. Notably, these studies have been generally restricted to molecular gases; air, nitrogen, and occasionally, hydrogen.

The first such study was the work of Laroussi and Lu who examined a RPND excited in a stream of helium flowing from a tube into air [82, 83]. The resulting plasma had the appearance of a jet, emitted from the open end of the tube. Using fast photography they observed that the jet was actually a series of plasma “bullets” formed with each pulse. Measurements of the bullet velocities showed that their speed greatly exceed what would be expected purely from electrons drifting under the applied electric field. They described the bullet as a classic cathode-directed streamer propagated by photoionization.

The plasma bullets of Laroussi and Lu spawned a great deal of interest in RPND helium plasma jets³ For example, Walsh et al. studied the atomic oxygen production for helium-oxygen mixtures with the use of emission spectroscopy and a global plasma chemistry model [84]. Urabe et al. employed a variety of laser diagnostics to measure the radial density profiles of helium metastable atoms and molecular nitrogen ions in a similar jet. This work was supported by a number of two-dimensional plasma simulations such as those by Naidis [85] and Breden, Miki, and Raja [86].

Simultaneously, there has been a decline in the study of FIWs, and relatively little on large-volume RPNDs. One of the most recent FIW studies was produced by Takashima et al. [87]. In it, the authors reported on FIWs in helium and nitrogen which were studied using capacitive probes and voltage-current characteristics. The results were compared to extensive two-dimensional fluid simulations and an analytic, one-dimensional drift model. In most cases, the measurements and simulations showed good agreement.

1.3 Summary

Contemporary RPND studies have mostly focused on measurements in the afterglow plasma or of time-integrated quantities. This has limited the understanding of how RPNDs develop as only so much can be inferred from these measurements. Particular issues, such as the electron energetics in the wave front are not firmly known. Relatedly, the relative importance of photoionization and nonlocal electrons is still under debate. Even measurements of common plasma parameters such as electron densities and temperatures are in short supply. Each of these issues is important in the development of a thorough theoretical understanding of RPNDs, as well as the validation of simulations, and optimization for real world applications.

³A distinction should be made between plasma jets, excited by sinusoidal power supplies, similar to the well-known dielectric-barrier discharge [16], and those produced by nanosecond pulses. Differences between the two were reported by Walsh, Shi, and Kong [20].

Relatedly, the study of RPNDs has generally been limited to molecular gases such as air, nitrogen, oxygen, or combustion-related mixtures. Consequently, little information has been published on rare gas RPNDs, in spite of the fact that their unique physics makes them ideal for certain uses. For example, rare gas discharges exhibit very little gas heating, making them desirable for the treatment of highly sensitive materials. Additionally, the radiative emissions of rare gases have a range of uses from commercial lighting to gas lasers. Finally, the large degree of Penning ionization resulting from rare gases may make them useful in RPND gas mixtures as a means of optimizing discharge properties.

In order to address these issues, this work will use a combination of experiments and modeling to examine the plasma dynamics of a helium RPND on time scales ranging from 5 ns to 100 μ s and at pressures from 0.3 to 16.0 Torr. The nanosecond time scale results will be one of a very few datasets available on the evolution of the RPND during its formation. This will provide new insight on the dominant physical processes in the wave front. To complement this, the microsecond time scale measurements will reveal the dominant loss mechanisms in between pulses as well as the time-averaged characteristics of the RPND. Lastly, the parameterization with pressure will offer the chance to examine how the physics of the discharge is altered by the collisionality.

Experimentally, the RPND will be studied by its current and voltage characteristics, optical emissions, and with laser absorption spectroscopy. The current and voltage characteristics will be used to determine the energy absorbed by the plasma with each pulse. The optical emissions will provide information about the excited state dynamics and the wave velocity. Finally, the laser absorption spectroscopy will be used to resolve the short time scale dynamics and as a benchmark for the numerical modeling. The modeling will focus on the development of a detailed global model of a helium discharge. This model will be informed by additional particle-in-cell simulations, and solutions of the Boltzmann equation. Using the metastable measurements as a baseline, the global model will be used to predict the electric field, electron temperature, electron density, excited state densities, and

emissions of the RPND.

CHAPTER 2

Theory

In order to properly understand the RPND—the experimental measurements, and the models, it is necessary to develop a theoretical underpinning. The RPND is an ionized gas, and, dependent on its characteristics, a plasma. Therefore, we begin with a review of the statistical description of an ionized gas, equilibrium solutions, and several approximations. Subsequently, the discharge initiation process is considered from the perspective of a single avalanche. The Townsend model is briefly reviewed, followed by a more detailed explanation of the streamer model. This naturally leads to the development of a homogeneous discharge condition based on the preionization density—the basis for the RPND. Following this, a qualitative introduction to atomic structure is provided in order to introduce spectroscopic concepts such as energy levels, transitions, lineshapes, and absorption cross sections.

2.1 Ionized Gas

An ionized gas is a volume of gas in which some fraction of the neutral atoms and/or molecules have been separated into electron and ion pairs. For a sufficiently large number of particles and collision rate, the behavior of each species in the ionized gas can be described by a continuous distribution function.

This function is an expression of the likelihood of finding a particle within a specific range of velocities in a specific volume, as a function of time. This function is denoted as

$f_\alpha(\vec{r}, \vec{v}, t)$, where the subscript α denotes the species, f is the distribution function, \vec{r} is the position, \vec{v} is the velocity, and t is the time.

The behavior of f_α can be shown [88] to be governed by the Boltzmann equation,

$$\frac{\partial f_\alpha}{\partial t} + \vec{v} \cdot \nabla f_\alpha + \frac{q_\alpha}{m_\alpha} (\vec{E} + \vec{v} \times \vec{B}) \cdot \nabla_v f_\alpha = \left(\frac{\partial f_\alpha}{\partial t} \right)_{\text{coll}}. \quad (2.1)$$

Here, m is the particle mass, q is its charge, \vec{E} is the electric field, \vec{B} is the magnetic field, and $(\partial f_\alpha / \partial t)_{\text{coll}}$ is a term which represents changes to the distribution function as a result of collisions. Coupled with Maxwell's equations, equation 2.1 provides a complete description of the behavior of the fields and particles in a plasma.

For a species in equilibrium in the absence of external forces and $(\partial f_\alpha / \partial t)_{\text{coll}} = 0$, it can be shown [89] that the distribution of energies is

$$f_\alpha(\epsilon) = C \epsilon^{1/2} \exp\left(-\frac{\epsilon}{k_B T_\alpha}\right) \quad (2.2)$$

where C is a normalizing constant, ϵ is the energy, k_B is Boltzmann's constant, and T_α is the temperature of the species. This is referred to as the Maxwell-Boltzmann distribution. It should be emphasized that this solution only applies when the classical species can be considered to be in equilibrium. Gradients and electromagnetic fields can both significantly alter the distribution function of a species. This can be of particular importance in the calculation or reaction rates, or the measurement of temperatures.

Additionally, the Boltzmann equation may be solved for electrons in equilibrium constant electric field, provided that a constant current density, and only elastic collisions. This is generally valid if the electric field strength is sufficiently small such that the mean energy of the electrons does not become comparable to the threshold energies for inelastic collisions. This result was originally presented by Druyvesteyn and Penning [89] and has come

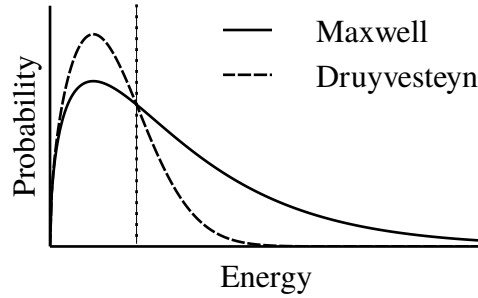


Figure 2.1: Comparison of the Maxwell-Boltzmann energy distribution and the Druyvesteyn distribution for the same average energy (illustrated by the dotted line).

to be known as the Druyvesteyn distribution. It is defined as,

$$f_\alpha(\varepsilon) = C \varepsilon^{1/2} \exp\left(-\frac{\varepsilon^2}{\langle \varepsilon \rangle^2}\right) \quad (2.3)$$

where $\langle \varepsilon \rangle$ is some mean energy, determined by the gas properties. This solution tends to suppress the probability of higher and lower-energy electrons in favor of more intermediate values. Figure 2.1 compares the probability distributions from equations 2.2 and 2.3 for the same temperature T_α . The dotted line illustrates the average energy for the two distributions, which is not the same as the most probable energy.

Additional solutions of equation 2.1 in anything but these simple cases can be very challenging (c.f. Chapter 18 of [90]). Even computational approaches can be stymied by the seven-dimension phase space and high dynamic range. In most situations, the Boltzmann equation is reduced to more tenable expressions by integrating over velocity-space (leaving f as a function of space and time). The first so-called moment is the conservation equation or continuity equation [90],

$$\frac{\partial n_\alpha}{\partial t} + \nabla \cdot (n_\alpha \vec{u}_\alpha) = G_\alpha - L_\alpha. \quad (2.4)$$

In this case, there is now a mean velocity \vec{u} , as well as gain (G) and loss (L) terms which

replace the collision operator. The gain and loss terms are generally expressed as the product of the densities of the interacting species, and a rate coefficient. For an electron-impact interaction where the target is relatively stationary, the rate coefficient is

$$K = \int_0^\infty f_e(\varepsilon) \sigma(\varepsilon) \sqrt{\frac{2\varepsilon}{m_e}} d\varepsilon, \quad (2.5)$$

where σ is the energy-dependent cross section.

The definition of the mean velocity, \vec{u} can be obtained by multiplying equation 2.1 by v and integrating over velocity-space, to obtain the second moment [90],

$$m_\alpha n_\alpha \left[\frac{\partial \vec{u}_\alpha}{\partial t} + (\vec{u}_\alpha \cdot \nabla) \vec{u}_\alpha \right] = q_\alpha n_\alpha (\vec{E} + \vec{u}_\alpha \times \vec{B}) - \nabla \cdot \vec{\Pi} + \vec{f}_{\text{coll}}. \quad (2.6)$$

This expresses the conservation of momentum by the plasma. It provides a means by which to solve for the mean velocity of the system, however it also introduces two additional terms. \vec{f}_{coll} deals with the forces transferred to α via collisions. This is often approximated as the Krook collision operator, which is only dependent on known quantities: m , n , \vec{u} , G , L , and the momentum transfer frequency, ν_m , for the species α and all species it interacts with. The second term, $\vec{\Pi}$, is the pressure tensor and can only be defined by the third moment of the Boltzmann equation. In fact, each additional moment introduces a new term requiring a higher order moment, *ad infinitum*. In most situations, this chain of equations is terminated after the first two or three moments by the use of an additional assumption such as an equation of state. One common example of an equation of state is the isothermal relation, $p = nk_B T$, which can be used to remove the pressure tensor.

For the purposes of this paper, one more moment will suffice. Assuming that the pressure is isotropic, one can multiply equation 2.1 by $mv^2/2$, and integrate over velocity-space to find the energy conservation equation,

$$\frac{\partial}{\partial t} \left(\frac{3}{2} p_\alpha \right) + \nabla \cdot \frac{3}{2} (p_\alpha \vec{u}_\alpha) + p_\alpha \nabla \cdot \vec{u}_\alpha + \nabla \cdot \vec{q}_\alpha = \frac{\partial}{\partial t} \left(\frac{3}{2} p_\alpha \right) \Big|_{\text{coll}}. \quad (2.7)$$

In this case, p represents the isotropic pressure, and \vec{q} is the heat flow. The first term on the LHS represents the total energy contained by the species, the second term is the energy flux in and out of the volume, and the third term accounts for changes due to compression or expansion. The RHS is the collision operator which describes energy added or removed from the system as a result of collisions.

Equations 2.4 and 2.7 are particularly important for this study. As will be detailed in Chapter 5, the two can be used to create a global model of the plasma. Such a model assumes spatial homogeneity of the plasma in order to reduce the associated computational costs. This allows the model to address large numbers of species over long periods of time as will be required in the case of the RPND.

2.2 Plasma Criteria

Though the Boltzmann equation describes both an ionized gas and a plasma, the two are distinct as a plasma is necessarily an ionized gas, but not vice versa. A plasma is unique in that its dynamics are governed by long range electromagnetic forces, unlike gases in which short-range collisions dominate. As a result, plasmas frequently exhibit large scale structure and organization. Examples of these structures are ubiquitous in astronomy where phenomena such as the aurora borealis, coronal mass ejections, and even interstellar media are all plasmas [91]. There are three criteria which form a more exact definition of what constitutes a plasma.

2.2.1 Debye Length

If an electrical perturbation is introduced into an ionized gas, the charged particles will tend to rearrange themselves to shield it out. A plasma is an ionized gas which is large enough for this shielding effect to occur. The characteristic length scale for this shielding effect to take place is referred to as the Debye length, denoted λ_D . It can be shown to be equal to

$\sqrt{\epsilon_0 T_e / (en_0)}$, where ϵ_0 is the vacuum permittivity, T_e is the electron temperature, and n_0 is the plasma density. If the characteristic length scale of the ionized gas is L , then $\lambda_D < L$ for it to be considered a plasma.

2.2.2 Debye Sphere

However, the above condition by itself is not sufficient for shielding to occur. It is possible that an ionized gas may have a relatively small Debye length, but also lack enough charged particles for shielding to occur. More simply put, it would be impossible for a single electron to shield out even the smallest of perturbations. For that reason, the number of particles in a Debye sphere must be greater than unity in a plasma, or $n_0(4\pi\lambda_D^3/3) \gg 1$.¹

2.2.3 Plasma Oscillations

Finally, a plasma may exhibit Debye shielding, but lack the collective behavior of a plasma. This can occur when the collision frequency with neutral particles is too high. In this case, the behavior of the ionized gas would be determined more by the random collisions. Therefore, the characteristic response frequency of a plasma, commonly called the plasma frequency, must be greater than the neutral collision frequency, or $\omega_p > \nu$. The plasma frequency can be shown to be $\omega_p = \sqrt{e^2 n_0 / (\epsilon_0 m_e)}$.

There are many natural and man-made plasmas of varying size and quality. Figure 2.2 shows several categories of plasma, plotted as a function of their electron density and temperature. As can be seen in this example, the electron densities span seven decades, and the densities cover in excess of 20. This broad range of conditions presents a particularly challenging problem for both simulations and experimental measurements. Also highlighted in the figure is the range spanned by the RPND.

¹This condition is also implied in the derivation of the Debye length.

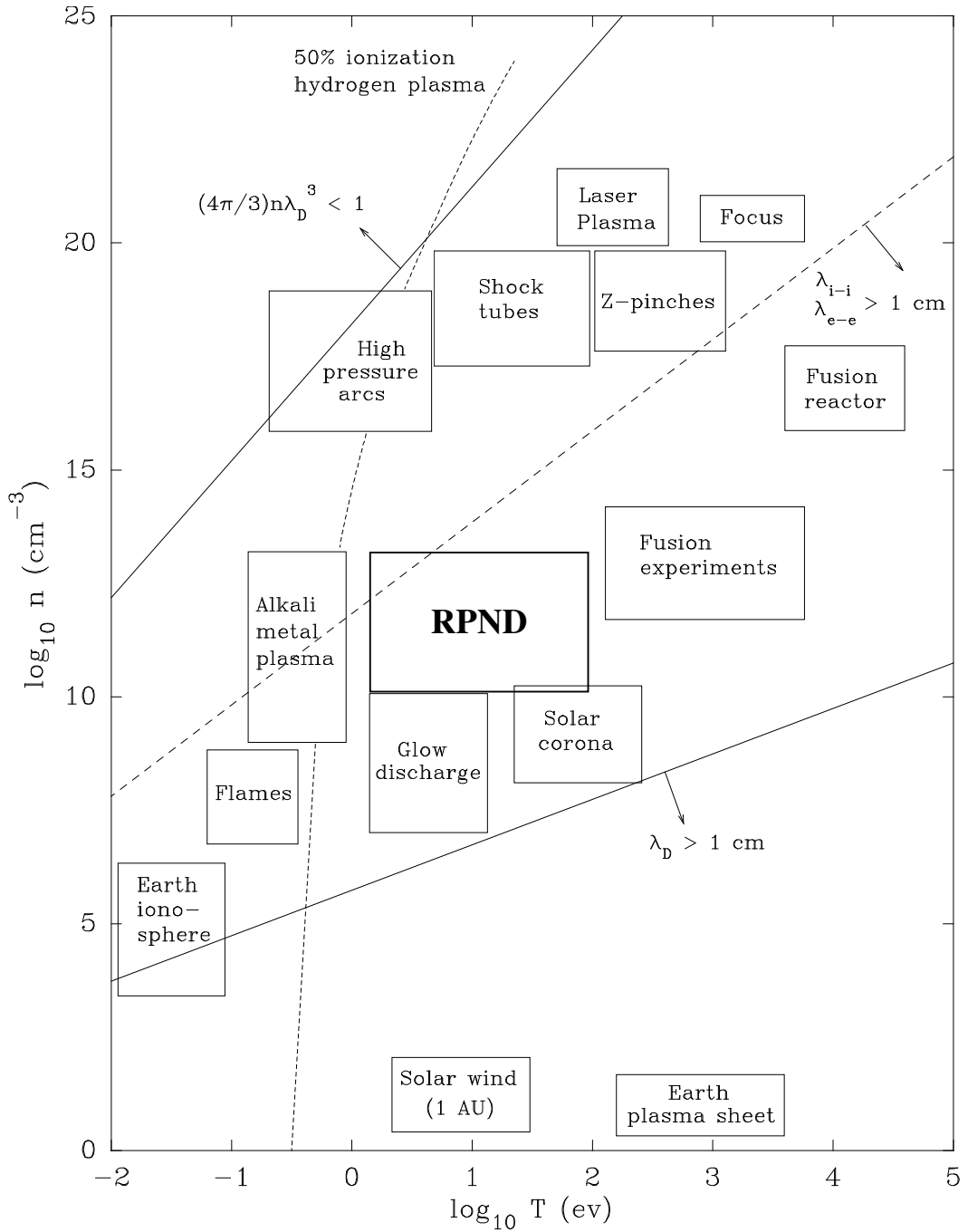


Figure 2.2: Illustration of the various regimes of plasma in terms of electron temperature and density with the RPND regime highlighted, adapted from [2].

2.3 Discharge Initiation

The Boltzmann equation is a continuous, statistical description of a plasma. By comparison, the initial breakdown of a plasma is a highly discontinuous process marked by its stochasticity. The initiation of a discharge is typically the result of electron avalanches which occur randomly throughout a volume of gas [89]. Often, the seed electrons for a plasma are the products of ionizing cosmic rays. At sea level this results in a few electrons per cubic-centimeter. As a result, it is necessary to consider the initiation of a discharge separately from a pre-existing plasma.

2.3.1 Townsend Mechanism

Classically, plasmas are created by two different mechanisms, the applicability of which depends on primarily on the strength of the electric field relative to the neutral gas density, a value called the reduced electric field [92]. At lower reduced fields, the Townsend mechanism is responsible for the formation of a plasma. Consider two electrodes separated by a gap filled with some gas. An electron starting near the cathode will drift toward the anode. For a large enough electric field, the electron will gain sufficient kinetic energy to ionize a neutral atom, producing a second electron. The two electrons are now accelerated by the field, instigating further ionization of the background gas. The population of electrons quickly grows, thus the process is referred to as an electron avalanche. Eventually, the avalanche electrons are collected at the anode.

In their wake are ions which slowly drift toward the cathode. As the ions impact the surface of the cathode, they occasionally cause a secondary electron to be emitted. This secondary electron initiates a new avalanche and helps to sustain the discharge. A steady state electric discharge occurs when the current of the ion collection at the cathode matches the current of the electron collection at the anode. The time scale of the Townsend discharge is usually determined by the positive ions, as their large mass results in slow drift velocities.

For an electric field of 50 V/cm at 200 mTorr, the drift velocity of a helium ion in helium is about 7×10^4 cm/s [93]. For a gap of 10 cm, this gives a drift time on the order of 10–4 s.

The Townsend mechanism is characterized by two parameters: α and γ , the first and second Townsend coefficients. α is the number of ionization events that occur per unit length, often expressed as a function of the reduced field [89]. The second Townsend coefficient is the probability that an ion impinging on the cathode produces a secondary electron. The values for γ can vary widely and depends on the type of ion, its energy, the cathode material, contamination of the surface, and many other factors. That said, typical values are around 0.01-0.1 [90].

2.3.2 Streamer Mechanism

In contrast, the streamer discharge which occurs for larger values of the reduced field does not depend on secondary emission. Additionally, streamer discharges can develop in time periods as short as 1 ns, much less than the time required for Townsend breakdown. In order to describe the streamer mechanism, again consider an electron between two electrodes, as seen in (a) of figure 2.3. As with the Townsend discharge, this electron initiates an avalanche which moves toward the anode. As the electrons travel toward the anode, they randomly collide and diffuse, leaving behind a cone of ions, as seen in part (b). However, the higher reduced field drastically increases α . This causes the space charge of the avalanche to create an electric field comparable to the one that is applied, slowing the propagation of the avalanche.

At this point the avalanche can be considered a streamer as it begins to increase its extent by several additional processes. The large internal fields of the avalanche can accelerate individual electrons and “inject” them in the direction of the anode [4]. In addition, as the excited atoms in the wake of the avalanche begin to radiate, they can cause photoionization throughout the volume. Photoelectrons generated close enough to the negative head, or positive tail of the streamer will initiate secondary avalanches which eventually connect

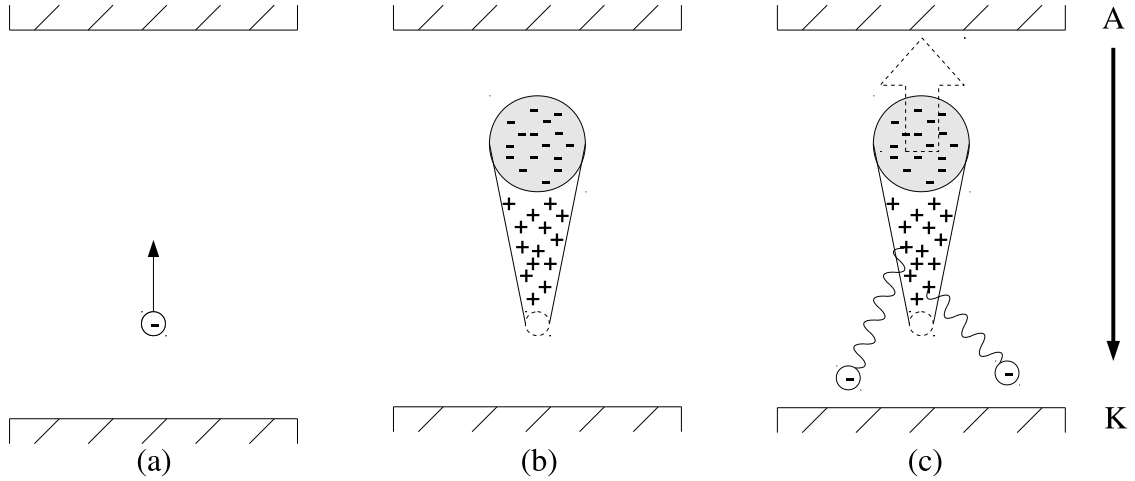


Figure 2.3: An illustration of the development of a single streamer. (a) A seed electron is accelerated by the applied electric field. (b) The initial electron develops into an avalanche which leaves a large region of positive space charge, slowing further advance. (c) The streamer propagates toward the cathode via photoionization and the anode via nonlocal electrons and photoionization. Adapted from [3] and [4].

to the primary one. While photoelectrons may cause some additional broadening of the streamer, the injection of electrons toward the anode is aligned with the direction of the internal field of the avalanche. As a result, the ionization caused by these electrons do not appreciably increase the radius of the streamer.

2.3.3 Homogeneity Condition

However, these processes are not critical in the formation of a large-volume discharge by an RPND. This description of a streamer only considers an avalanche generated by a single electron. In reality, many can form simultaneously assuming that there is more than one seed electron in the volume. With moderate preionization of the volume, the strong fields of the individual avalanches can begin to overlap². This smoothes out the field gradients which would otherwise radially constrict the streamers. Instead, ionization progresses homogeneously throughout the volume.

In order to determine the necessary preionization density, we refer to the work done by

²If the preionization of the volume is too large, it can effectively short out the electric field.

Levatter and Lin on gas laser discharges [3]. First, the electron drift velocity in an applied field can be expressed as the product of the field and the electron mobility μ . The electron mobility multiplied by the electric field is the steady-state drift velocity for an electron in that field and represents the balance between the frictional force of the neutral gas collisions and the electric field. Consequently, the mean velocity of electrons drifting in a time-varying field $E(t)$ can be expressed as

$$u(t) = \mu(E)E(t). \quad (2.8)$$

The length of the avalanche can be written as a time-integrated function of the electron drift velocity,

$$\xi = \int_{t_0}^t u(t)dt. \quad (2.9)$$

Here, t_0 is the time at which $E(t)$ becomes high enough that the first Townsend coefficient, α , exceeds 0. Because no electron multiplication occurs while $\alpha < 0$, this effectively represents the beginning of the avalanche.

The electric field in the head of the avalanche depends on its radius, which is dependent on the diffusion of the electrons as they cross the gap. This is governed by the free diffusion coefficient, D . For a fixed diffusion constant, the final avalanche radius would simply be $R = \sqrt{2D\Delta t}$, where Δt is the time after breakdown. As the diffusion coefficient typically varies with the applied electric field, the final avalanche radius will be assumed to be equal to $R = \sqrt{2\bar{D}\Delta t}$, where \bar{D} is the time-averaged diffusion coefficient.

Levatter and Lin assume that the avalanche slows when the peak field of the avalanche is equal to the applied field. Assuming that the electrons diffuse equally in all directions, the electric field of the avalanche head can be expressed as

$$E_a(r) = \frac{eN_e}{4\pi\epsilon_0 R^2} F(r/R), \quad \text{where} \quad (2.10)$$

$$F(r/R) = \frac{1}{R^2} \left[\operatorname{erf}(r/R) - \frac{2}{\pi^{1/2}} (r/R) \exp(-r^2/R^2) \right], \quad (2.11)$$

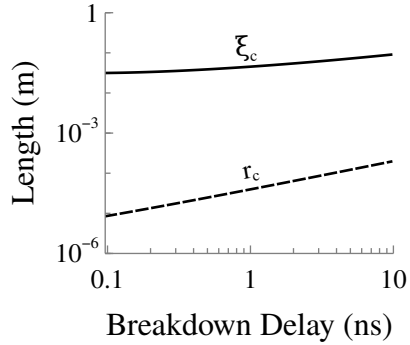


Figure 2.4: Numerical calculations of the avalanche length and avalanche radius for in helium at a pressure of 4.0 Torr as a function of the slope of the electric field, dE/dt .

where r is the radius with respect to the center of the avalanche, N_e is the number of electrons in the avalanche, erf is the error function. F is a dimensionless function which has a peak value of 0.428. Provided α as a function of reduced field, the number of electrons in the avalanche is equal to

$$N_e = \int_0^{\xi} \alpha(\xi') d\xi'. \quad (2.12)$$

Here, Levatter and Lin make a number of assumptions in order to develop an analytic and dimensionless solution for $E_{a,\max}(t) = E(t)$. However, it is possible to numerically integrate equations 2.9 and 2.12 to determine the time required for the avalanche to slow. This should provide a more accurate, but less general result. Assuming a linearly increasing electric field, figure 2.4 shows the results of such calculations for an avalanche in 4.0 Torr of helium, as a function of various breakdown delays. The breakdown delay is defined as the time it takes for $\alpha > 0$. The mobilities, diffusion coefficients, and Townsend coefficients were interpolated from solutions of the Boltzmann equation provided by the BOLSIG+ code with Phelps' cross sections [94]. For this range of breakdown delays, the avalanche was able to develop up to nearly 10 cm in length before it slowed. The times required for the avalanche to slow ranged from around 23 ns for the shortest breakdown delay, and 389 ns for the longest.

From this, a criteria for homogeneous breakdown of the gas can be developed. In order

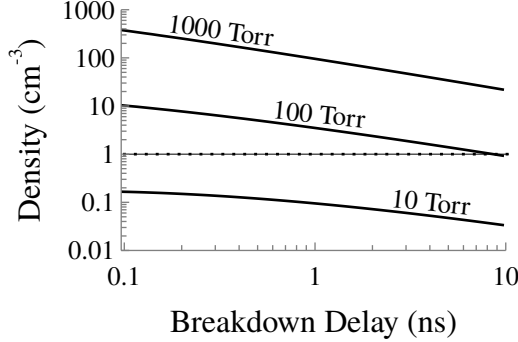


Figure 2.5: Minimum preionization densities required at a variety of pressures and breakdown delays. The dotted line indicates the background ionization level as a result of cosmic radiation.

for the field gradients to be smoothed out, the individual avalanche heads should roughly overlap by the time they have slowed. Assuming that all seed electrons in the volume initiate avalanches, this can be approximated as $n_{e,c} > r_c^{-3}$, where $n_{e,c}$ is the critical electron density, and r_c is the avalanche radius when it has slowed. As seen in figure 2.5, the required preionization density depends on both the breakdown delay and the operating pressure. Generally, the preionization density increases with pressure and decreases with breakdown delay. The dotted line in the figure indicates the anticipated background electron density from cosmic radiation. This suggests that, for the breakdown delays in question, the discharge will almost always be homogeneous at pressures below 100 Torr. While the plot suggests that large values of dE/dt might guarantee homogeneous breakdown at near-atmospheric pressure, the increasing likelihood of ionization instabilities [95] will preclude homogeneous discharge development.

2.4 Atomic Spectroscopy & Notation

As described, much of the experimental work presented will concern the use of spectroscopic techniques. Careful measurements of the light emitted from excited atomic states can yield electron densities and temperatures, excited state densities and temperatures, elec-

tric fields, and magnetic fields [96]. The topic of spectroscopy is extensive and it is neither necessary nor desirable to cover it in full. Instead we will only consider what is necessary to understand the emissions from a singly-excited, multi-electron atom.

An atom is composed of a small, positively charged nucleus, orbited by negatively charged electrons. The actual position of any single electron is probabilistic and described by a wavefunction—solutions of the Schrödinger equation for the atom in question. Each wavefunction is associated with a number of eigenvalues which quantize aspects of the state of bound electrons. In simple atoms, four such quantum numbers are of interest [97],

- $n = 1, 2, \dots$: the principal quantum number,
- $l = 0, 1, \dots, n - 1$: the orbital angular momentum number,
- $m_l = -l, \dots, l$: the projection of l , and
- $m_s = \pm 1/2$: the projection of the spin quantum number.

The quantum numbers are hierarchical such that each n , or shell, possesses a series of subshells, l , while each subshell possesses a number of individual orbital, m_l , and each orbital possess one of two spins. As a result of the Pauli exclusion principle, the wavefunction of each electron around an atom is described by a *unique* set of quantum numbers. This means, that any particular subshell can only contain $2(2l + 1)$ electrons. The subshells are often referred to using the nomenclature $0, 1, 2, 3, \dots = s, p, d, f, \dots$

As a result of their separation from the nucleus, the electrons in an atom possess some degree of potential energy. As the n and l of an electron increase, so does its potential energy. In the absence of electric and magnetic fields, m_l and s do not affect the potential energy of an electron. As an example, an electron in the $1s$ ($n = 1$ and $l = 0$) subshell has the lowest possible potential energy.

Absent from external influences, the individual states are populated with electrons so as to minimize the total potential energy of the system. This natural arrangement is referred to as the ground state configuration. Often, but not always, the subshells are filled sequentially and in order from lowest to highest l [97]. Provided some input energy in the form of a

collision or a photon, one or more of the electrons surrounding the atom may transition to another state, increasing the potential energy of the system. In low-temperature plasmas it usually one of the electrons from the outermost or partially filled subshell to be excited.

The potential energies of the electron configurations for multi-electron atoms are determined by the collective effects of all the surrounding electrons.

It is the collective effects of all electrons surrounding an atom which determine its potential energy. This results in a single set of total angular momenta which can be used to describe the atom. In lighter atoms [97], the contributions of the individual electrons are combined assuming a condition called L-S coupling. Under this assumption, the total angular momentum of the atom can written as $\vec{L} = \sum \vec{l}_i$, where i is each electron in a partially filled subshell (filled subshells sum to zero). Likewise, the total spin can be written as $\vec{S} = \sum \vec{s}_i$. These can be combined to form the total angular momentum of the atom, $\vec{J} = \vec{L} + \vec{S}$. Finally, the each atom is said to have an even or odd parity, defined as $(-1)^{\sum l_i}$, where -1 is odd, and 1 is even.

These quantities can be used to write a “term symbol” for the atom, of the form $^{2S+1}L_J^p$, where p is ‘o’ if the parity is odd, and omitted if it’s even. The term symbol can be augmented by prepending additional terms which address the subshells in which electrons can be found. This is typically written as nL^N , where N is the number of electrons in a given subshell (omitted if $N = 1$). For example, $1s2s^3S_1$, describes the triplet helium metastable state. In this case, there is a single electron in the $1s$ subshell and a second atom in the $2s$ subshell. The configuration has a total orbital angular momentum of 0 (denoted by the ‘S’), an even parity (denoted by the absence of a superscript ‘o’), a total spin of 1 (the superscript 3 is equal to $2S + 1$), and a total angular moment of 1.

Excited atomic states usually have finite lifetimes. Normally, electrons will undergo transitions to lower the potential energy of the system. This can also occur spontaneously, through the emission of a photon, or through a superelastic collision with another particle. In the case of spontaneous transitions, only certain states can transition to others, as defined

by a series of selection rules [97]:

- $\Delta S = 0$
- $\Delta L = \pm 1$ or 0
- $\Delta J = \pm 1$ or 0
- $L = 0$ cannot transition to $L = 0$
- $j = 0$ cannot transition to $J = 0$

These rules are determined from a lower order approximation, and thus are not strict. As a result, forbidden transitions can occur, however these generally take place at much lower rates.

Figure 2.6 is a Grotrian diagram of the energy levels in neutral helium and the allowed transitions. In this case, the atomic states are separated into the singlet ($S = 0$) and triplet ($S = 1$) manifolds. The singlet manifold is composed of excited states where the electron spins are anti-parallel, and the triplet manifold represents excited states where the electron spins are parallel. As indicated by the first selection rule, transitions between these two manifolds is forbidden, thus each is something of a self-contained system [98].

Also observable in the diagram are two “metastable” states. These are the 2s states at the bottom of the singlet and triplet manifolds. An electron in either state cannot spontaneously transition to a lower energy state. As a result, an electron in either state can be extremely long-lived. In addition, they are also the lowest-lying excited states of helium. For these reasons, helium plasmas tend to have high densities of metastable atoms. This makes them a good candidate for spectroscopic study as will be seen in Chapter 4.

2.4.1 Spectral Lineshapes

Electrons which transition to lower energy states emit photons which can be detected. Conversely, if an atom is exposed to a photon with an energy matching a transition, the atom may absorb the photon. Both processes are useful in determining the prevalence and dynamics of the excited states. This, in turn, can be used to infer various plasma properties.

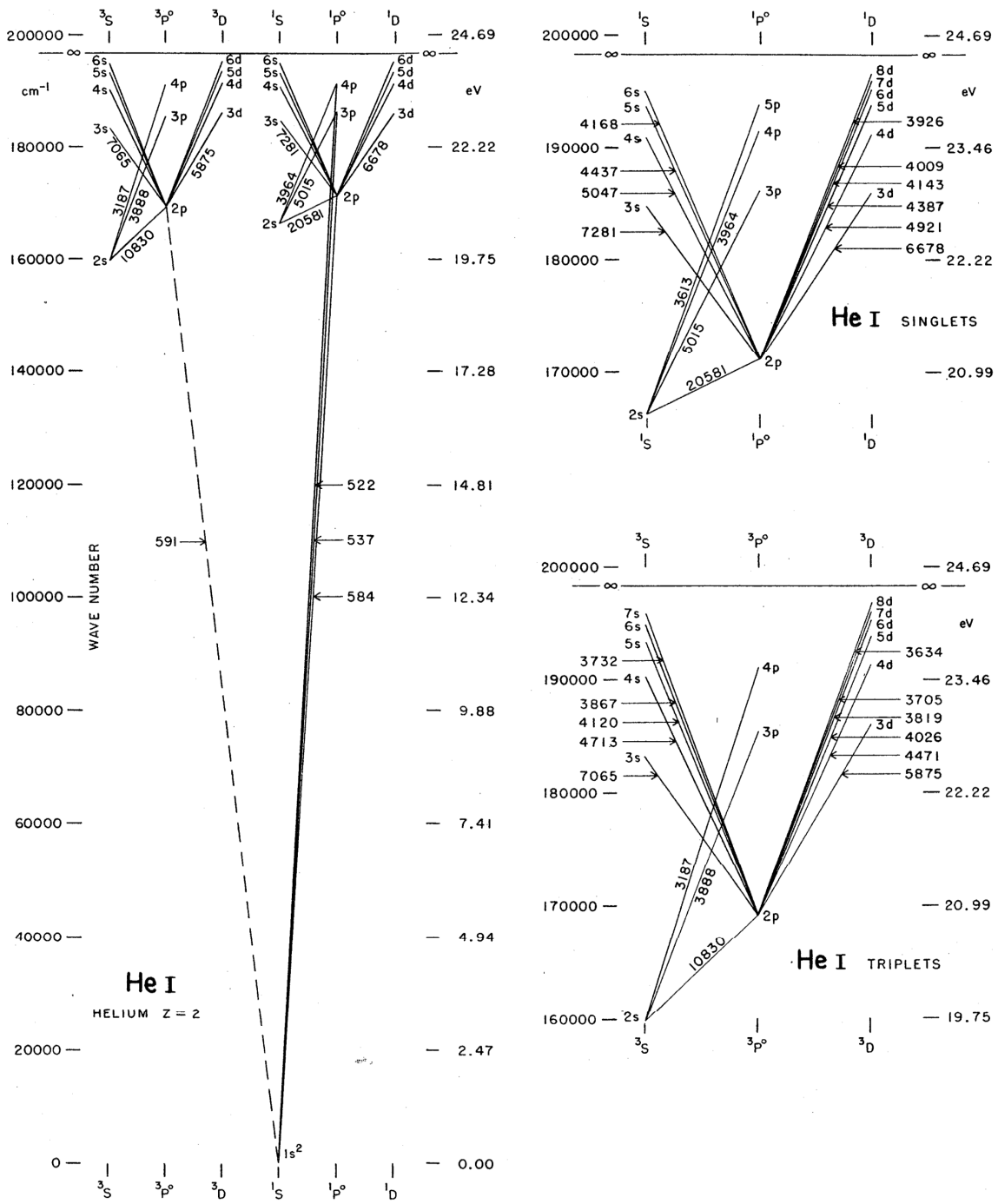


Figure 2.6: A partial Grotrian diagram of neutral helium, from [5].

Conservation of energy requires that the energy of the absorbed or emitted photon match the energy difference between the two states. However, the finite lifetime of excited atomic states implies, via the time-energy formulation of the uncertainty principle, some uncertainty in the actual energy difference between the states. As a result, the emitted photon will possess an energy selected from a distribution of energies.

This distribution is referred to as the spectral lineshape. The narrowest permissible lineshape, or natural lineshape, of an atomic transition can be shown [99] to be a Lorentzian of the form,

$$g(\omega) = -\frac{1}{4\pi^2} \frac{A\lambda^3}{\Delta\omega_a} \frac{1}{1 + [2(\omega - \omega_a)/\Delta\omega_a]^2}, \quad (2.13)$$

where ω is the photon frequency, A is the Einstein coefficient for the transition, λ is the wavelength of the transition, ω_a is central frequency of the transition, and $\Delta\omega_a$ the full-width half maximum (FWHM) of the transition. In the ideal case, where the atoms motionless and unaffected by external perturbations, $\Delta\omega_a = A$ [99]. This is known as the natural linewidth.

Other processes can act to broaden or alter the spectral lineshape [100]. For example, inter-atomic collisions can reduce the lifetimes of excited states. This results in additional broadening of the line, though it retains its Lorentzian nature. As the frequency of inter-atomic collisions increases linearly with pressure, this phenomena is referred to as pressure broadening. It can be included in equation 2.13 by using $\Delta\omega_a = A + BP$, where B is a measured or calculated broadening coefficient, and P is the pressure [99].

Atomic motion can also play a role in the spectral lineshape. If an atom is moving toward or away an observer as it emits a photon, the emitted photon will be blue or red shifted. Likewise, if the atom is moving toward or away an incident photon, the energy of that photon will be shifted [99]. If this effect is averaged over the random motion of atoms in a gas, the result is an additional broadening of the lineshape, called Doppler broadening. Unlike pressure broadening, Doppler broadening introduces a Gaussian component to the

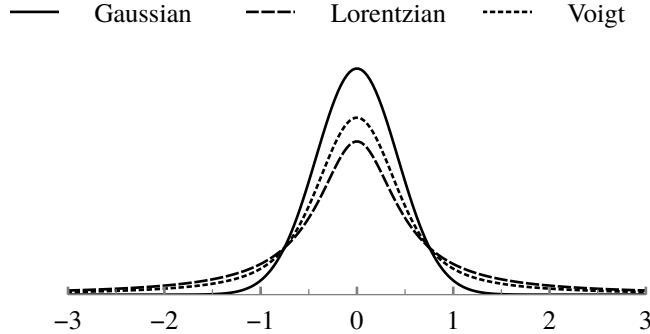


Figure 2.7: A comparison of the three primary spectral lineshapes, each with the same full width.

lineshape such that,

$$g(\omega) = \sqrt{\frac{2 \ln 2}{\pi^3} \frac{\Delta\omega_a}{\Delta\omega_d}} \int_{-\infty}^{\infty} \frac{1}{[(\omega - \omega_a) - \omega']^2 + 4\Delta\omega_a^2} \times \exp \left[4 \ln 2 \left(\frac{\omega'}{\Delta\omega_d} \right)^2 \right] d\omega'. \quad (2.14)$$

Here, $\Delta\omega_d = \omega_a \sqrt{\frac{8k_B T_g \ln 2}{Mc^2}}$, is the width of the Doppler broadening, where T_g is the gas temperature, M is the particle mass, and c is the speed of light. This form of the spectral lineshape is known as the Voigt profile, and it must be numerically integrated. In the case that $\Delta\omega_d \gg \Delta\omega_a$, equation 2.14 can be simplified to a standard Gaussian distribution,

$$g(\omega) = \sqrt{\frac{4 \log 2}{\pi \Delta\omega_d^2}} \exp \left[-(4 \log 2) \left(\frac{\omega - \omega_a}{\Delta\omega_d} \right)^2 \right]. \quad (2.15)$$

The effect of the various broadening mechanisms is most apparent in the wings of the lineshape, far from the peak. Figure 2.7 illustrates the three major lineshapes with equivalent full widths. The Voigt profile is composed of equally broad Lorentzian and Gaussian distributions. As can be seen, the wings of the Gaussian distribution fall off very quickly. In comparison, the Lorentzian component is observable well out to the edges of the figure.

The spectral lineshape can be altered by a number of other processes. Electric fields can

influence the emissions via the Stark effect, while magnetic fields can split up degenerate states via the Zeeman effect. The fields of electrons and nearby molecules can also alter the lineshape of a transition. While not used in this study, such effects can be used as effective diagnostic tools in the measurement of field strengths, and charged particle densities in plasmas.

2.4.2 Absorption

As has been mentioned, a photon which closely matches the energy between two states can be absorbed by an atom. This property forms the basis for absorption spectroscopy where light with a known spectrum is used to illuminate a sample. The spectrum of the light that passes through the sample is measured and used to infer properties of the sample. In contrast to the emission processes occur spontaneously with a characteristic lifetime, often 10s of nanoseconds or more, absorption is almost instantaneous. This makes absorption-based spectroscopic methods desirable for fast phenomena, such as the RPND [101].

The cross section for a single atom to interact with a photon can be shown [99] to be,

$$\sigma(\omega) = A \frac{\lambda^2}{8\pi} \frac{g_1}{g_2} g(\omega). \quad (2.16)$$

where g_1 and g_2 are the number of degenerate configuration for the lower state and upper state respectively. $g(\omega)$ is the appropriate spectral lineshape, determined from the operating conditions.

It is important to recognize that absorption spectroscopy can also perturb the system it is measuring. Suppose two consecutive photons were incident on the atom. If the first was absorbed, the likelihood that the second photon would be absorbed is zero. The cross section for absorption has not changed, there are simply no atoms available for the second photon to interact with. Therefore, if a photon field is incident on a volume of atoms susceptible to absorption, the degree to which the field is absorbed will depend on its intensity. The more

intense the photon field is, the more it reduces the number of atoms available to interact with.

Eventually, this effect is balanced by a process called stimulated emission. In this process, an atom is already in an excited state with one or more lower states. If an photon is incident on the atom and matches the energy difference between its current state and a lower one, the photon may induce a transition to the lower state. This results in the emission of a second photon with the same energy and phase as the first. The cross section for stimulated emission is identical to that for photon absorption.

This feedback process where the absorption and emission processes balance with each other is known as saturation. The saturation of a volume of gas is a continuous process, and depends on the atomic states in question and areal density of the incident photons, or intensity. From a practical standpoint, absorption measurements require that the interrogating photon field remain below a threshold value. This saturation intensity can be shown [99] to be,

$$I_s = \frac{2\sqrt{2}h\nu_0A}{\lambda^2}, \quad (2.17)$$

where h is Planck's constant, and ν_0 is the nominal frequency of the transition [99].

In this report, absorption and spontaneous emission diagnostics provide the experimental basis on which the RPND analyzed. Both are direct measures of the excited states that exist within a RPND. However, neither provides any direct measurement of the quantity or energies of the electrons. In the RPND, as with all plasmas, the electrons play a fundamental role in how the discharge behaves and develops. At the most basic level, it is the electrons which are accelerated by the electric field and collide with the gas atoms to produce the aforementioned excited states. Consequently, it should be possible for a sufficiently detailed model to use measurements of the excited states in order to infer the properties of the electrons, as will be seen in Chapter 5.

CHAPTER 3

Experiment

3.1 Discharge Apparatus

The RPND apparatus used in the forthcoming experiments was similar in design to the coaxial geometry used by Vasilyak and others used in FIW studies [19]. As depicted in figure 3.1, it is essentially a cylindrical inner conductor, surrounded by a dielectric, covered by an outer conductor. An electrode, connected to the transmission line, and the RPND serve as the inner conductor. The dielectric took the form of a glass tube and an air gap. Finally, the outer conductor consisted of a series electrically connected metal shells which served as the current return path. Following from right to left, the inner conductor was composed of a vacuum window, a nipple, a double-sided flange tapped for an NPT connection, and the discharge tube containing the RPND. Unless otherwise noted, all vacuum components featured DN35 CF flanges with copper gaskets.

The tube was composed of borosilicate glass with metal vacuum flanges on both ends. The flanges of the tube also acted as the electrodes for the generation of the RPND. The glass tube had an inner diameter of 3.3 cm, an outer diameter of 4.0 cm, and a length of 22.9 cm. The overall length of the tube including the flanges was 30 cm. In the figure shown here, the right electrode served as the anode, and the left electrode was the cathode.

The dielectric surrounding the inner conductor was composed of several components. The vacuum window, nipple, double-sided flange, and anode were separated from the outer

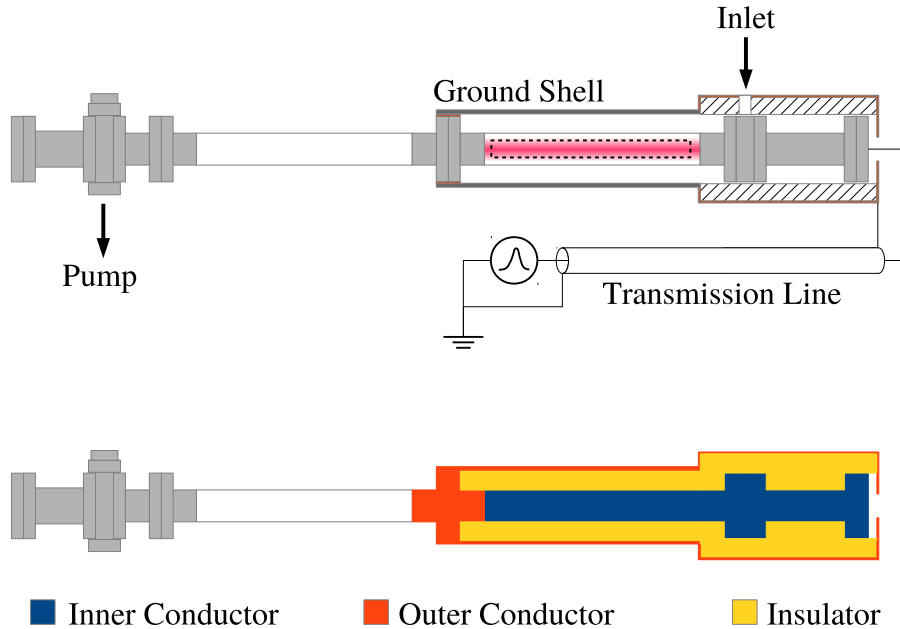


Figure 3.1: Two illustrations of the RPND apparatus. The upper version is an annotated sketch of the device, and the bottom version simplifies the geometry into its three electrical components.

conductor by an air gap and a polytetrafluoroethylene (PTFE) tube, 20 cm in length with an inner diameter of about 7.5 cm, and an outer diameter of 10 cm. The RPND portion of the inner conductor was separated from the outer conductor by the glass tube and an air gap of about 2.54 cm.

The left side of the discharge tube, or cathode, connected to the outer conductor and served as part of the current return path. Directly attached to the cathode was an aluminum tube, held in place by an acetyl resin shaft collar and a copper shim. Radial optical access to the discharge was provided by two slots milled into the ground shell. The slots were positioned on opposite sides of the shell and were 3.8 by 25.4 cm in length. The tube itself was 30 cm in length.

The end of the aluminum tube nearest the anode was affixed to a copper sheet which was oriented perpendicular with respect to the tube's axis of rotation. The sheet was 10 cm square, and was attached to the tube with conductive copper tape. A 5 cm diameter

hole was cut into the copper sheet to allow the discharge tube to pass through it. The sheet was secured to the edge of the PTFE tube by nylon screws. Surrounding the PTFE tube was a second shell, made of rolled copper sheet. This was electrically connected to the aluminum tube by a braided copper strap. The right end of the PTFE tube was covered by a second copper sheet, 10 cm square. Again, the sheet was secured to the PTFE tube by nylon screws and in electrical contact with the copper shell. In the center of the copper sheet was a HN bulkhead adapter for connection to the transmission line. The inner conductor of the bulkhead adapter was connected by a straight run of 5 cm of silicone-coated wire to the vacuum window flange. The outer conductor of the bulkhead adapter provided the ground connection for the discharge apparatus.¹

The voltage pulse was generated by a FID power supply, supplied by ANVS, Inc. (model PT510NM). The amplitude of each pulse was fixed at 6.4 kV with a repetition rate of 1.0 kHz. Each pulse had a fixed width of 25 ns, required approximately 4 ns to rise from 10% of its peak to 90% of its peak, and was roughly Gaussian in shape. A SRS DG645 delay generator was used to trigger the power supply output for all experiments and provided a reference time base for all measurements.

Preliminary experiments revealed multiple reflections between the power supply and the anode. A long run of RG 213 coaxial cable was used to temporally separate the reflections. This made it possible to study the effects of individual pulses. Based on the length of the cable (about 13.7 m), the delay was predicted to be 69.2 ns. As the reflection would have to cross the length of the transmission line twice before it reached the anode again, the total separation time between the initial pulse and each subsequent reflection was predicted to be 138.4 ns. This calculated delay was found to closely match the measured time period between the incident and reflected pulse.

A simplified version of the gas flow system can be seen in figure 3.2. The gas supply

¹Measurements confirmed that the entirety of the outer conductor had a low DC impedance to ground. However, it is likely that at frequencies relevant to the RPND, the impedance is not negligible. As a result, the outer conductor likely floats to a finite voltage during operation.

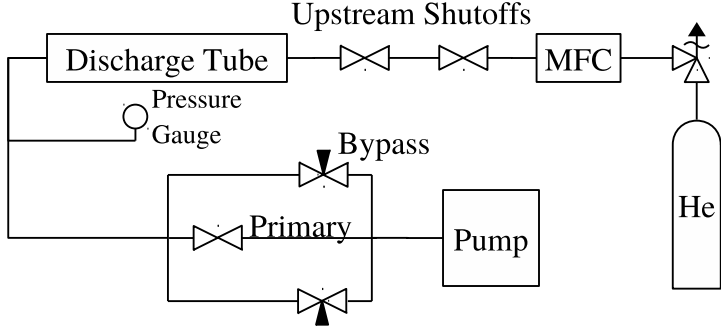


Figure 3.2: Simplified diagram of the gas flow path and pumping system.

was provided by a bottle of ultra-high purity helium. Following the regulator, the helium passed through a digital flow controller which was set at 25.0 sccm for all experiments. The helium then entered a gas distribution manifold, followed by a shutoff valve, a short run of 1/4" stainless steel tubing, another shutoff valve, about 2 m of 1/4" polyethylene tubing, and then the discharge tube via the double-sided flange.

The gas exited the discharge tube via an identical tube, on the side opposite the inlet, see figure 3.1. This second tube was intended to electrically isolate the discharge portion of the apparatus so that only a single conductive path to ground existed. The pressure was monitored downstream of the second tube with two capacitance manometers (one with a full scale range of 10 Torr, the other with a range of 100 Torr). The gas exhaust of the second tube was connected to an oil-seal roughing pump via three independent paths. The primary pump path had the highest gas conductance and was controlled by a bellows valve. However, this path was typically closed in favor of two needle valve bypasses. The needle valves were used to control the pumping speed and obtain the desired operating pressure. Immediately upstream of the roughing pump was a zeolite trap in order to limit oil backstreaming.

The base pressure of the system was measured to be approximately 15 mTorr. The leak rate was measured several times by evacuating the apparatus and then sealing it from the pump by all three pump paths. The leak rate was found to be 2.0×10^{-3} sccm. Given a constant flow rate of 25.0 sccm, the fractional impurity can be conservatively estimated to be 80 ppm.

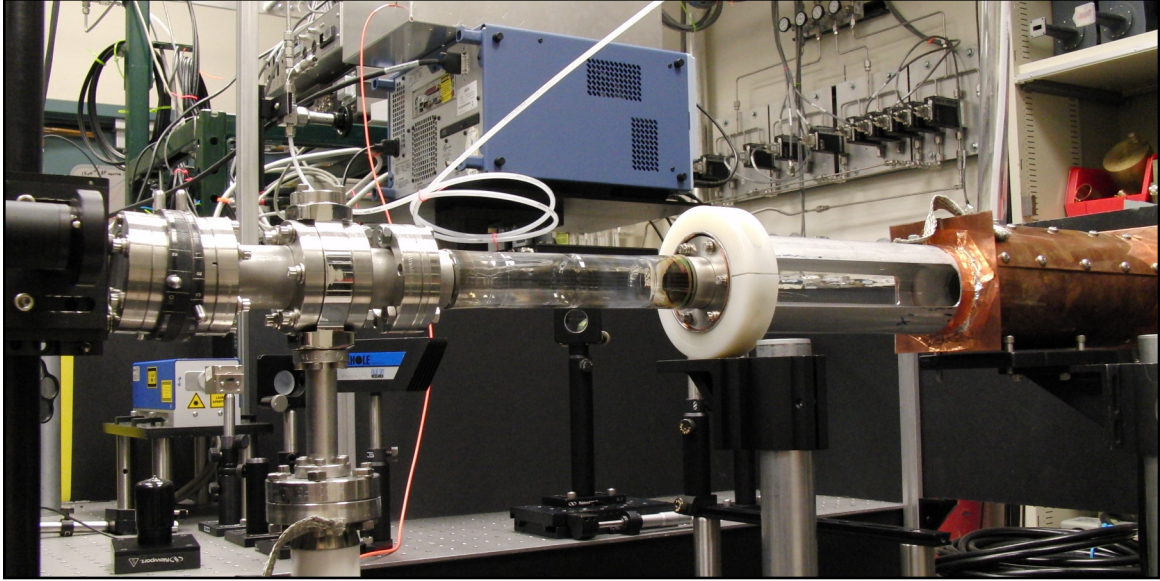


Figure 3.3: Photograph of the discharge apparatus.

The assembled discharge apparatus can be seen in figure 3.3. The RPND apparatus was supported two 1.5 in mounting posts with angle brackets. The mounting posts attached to a 122 cm by 76 cm optical breadboard, supported by urethane shock absorbers, and a rigid frame. The roughing pump was attached to the apparatus with flanged bellows in order to reduce mechanical vibrations.

All electrical measurements were made with a LeCroy 6100A WaveRunner oscilloscope which had a bandwidth of 1.0 GHz. Electrical connections to the oscilloscope were made with RG 50/U coaxial cable and standard BNC connectors. All connections were terminated at $50\ \Omega$ unless otherwise noted. The voltage of the pulses was monitored from a 1 : 1000 divider built into the power supply. The current was measured from a current shunt which crossed a small electrical break in the outer conductor of the transmission line. The shunt was built into the transmission line as close as possible to the power supply, about 3 cm from the output connector.

The current shunt was composed of nine, low inductance, 1.0Ω resistors connected in parallel. As illustrated in figure 3.4 the resistors were soldered to two strips of copper foil. This assembly was then wrapped around the electrical break in the transmission line, bridg-

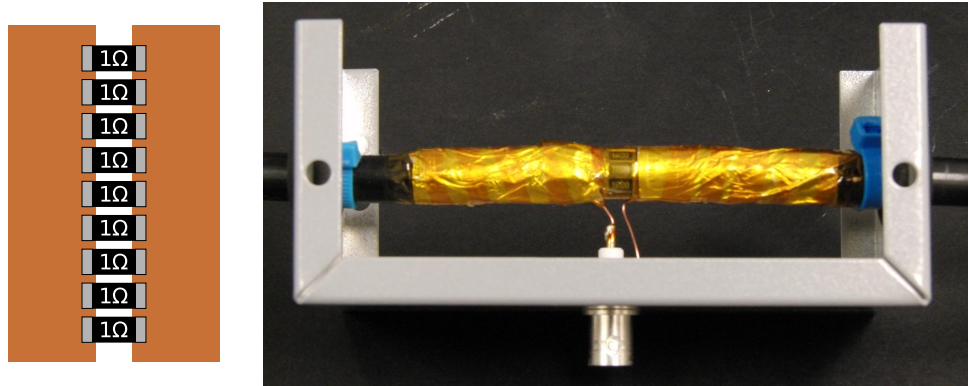


Figure 3.4: Sketch of the unassembled back-current shunt, and a photograph of it assembled around the transmission line.

ing it. Two short lengths of No. 18 copper wire were soldered to each side of the shunt assembly. These were then attached to a BNC bulkhead connector, fitted to a metal project box. The voltage across the resistors was used to measure the current traveling through the outer conductor of the transmission line. The copper foil was then secured to the outer conductor with several wraps of aluminum foil, followed by a layer of polyimide tape.

Data were retrieved from the oscilloscope with a desktop computer via the GPIB interface. Instrument control, data acquisition, and data storage were all managed by a LabView program. Analog input and output was handled with the auxiliary input and output ports of a SRS SR850 DSP lock-in amplifier.

3.2 Field Calculations

The electric field characteristics of the discharge apparatus were analyzed using Ansoft Maxwell 9, a two-dimensional, electrostatic solver. At the top of figure 3.5 is a logarithmic heatmap of the electric field magnitudes within the device. Overlaid are the electric field vectors in magenta. Below this is a plot of the electric field on a linear scale, across the central axis of the apparatus and along the outer edge, adjacent to the glass tube. It is apparent that the field strength is the strongest at the triple point which occurs near the glass-metal seal. Also noticeable is the fast fall off of the electric field with distance from the anode.

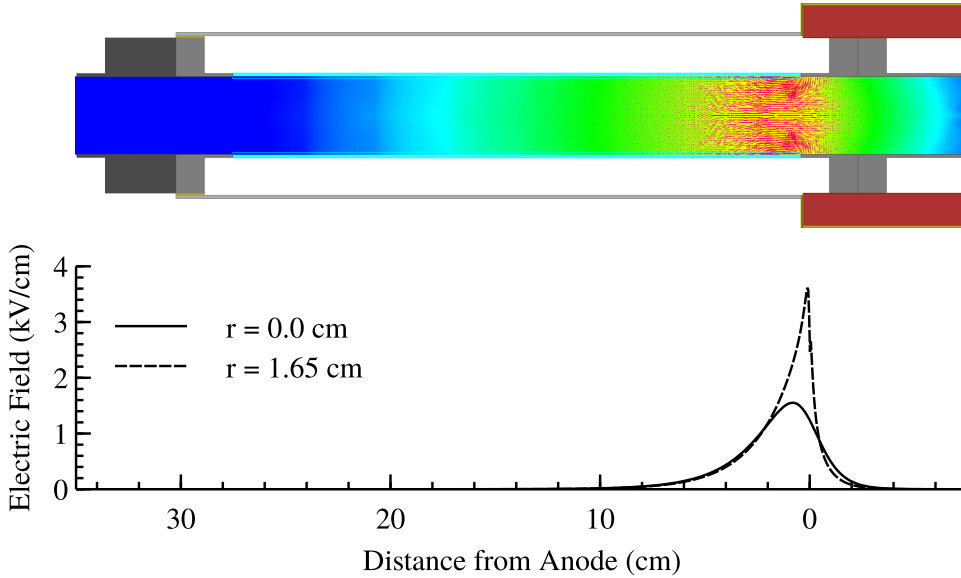


Figure 3.5: Heatmap and vector plot of the electric field in the RPND discharge apparatus.

The presence of the external ground shield produces an electric field contour vastly different from that of two parallel plates. This is also reflected in the electric field vectors. Specifically, the many locations possess fields with strong radial components, especially those near the anode.

These static fields are only valid in the absence of free charge within the system. However, these characteristics suggest that the discharge formation will be somewhat different than the one-dimensional description of a streamer in Chapter 2. First, assume that the electrons are distributed uniformly throughout the discharge tube, prior to the pulse. As a pulse is applied, ionization would preferentially take place near the anode. As the electrons would be drawn toward the anode, and leave behind some amount of positive space charge. However, as the positive space charge builds up, it would begin to act as a virtual anode, increasing the electric field further from the physical anode. The virtual anode would then begin to draw its own electron current, predominantly from around the edges, near the wall. In this manner, the discharge would propagate away from the anode, leaving a quasineutral ionized gas in the center of the discharge tube and a positive space charge region along the wall.

3.3 Operating Procedures

One of two operating procedures for the RPND was used depending on how recently the discharge had last been turned on. If the discharge was inactive for over one hour, then a full startup procedure was used. Otherwise, an abbreviated process was used.

In the case that the discharge had not been operated for over an hour, the roughing pump was turned on and the primary pump path valve was opened as was the first shutoff valve upstream of the discharge chamber, seen in figure 3.2. The system was then allowed to pump down to its base pressure. Afterward the second upstream shutoff valve was opened and the system was again allowed to reach base pressure. At this point the helium flow was turned on and set to 25.0 sccm. The primary pump path was then closed and the needle valve bypasses were used to adjust the system pressure to 3.0 Torr.

Next, the delay generator was turned on and the output for triggering the power supply was activated. Then, the FID power supply was turned on. This would produce an easily visible discharge within the discharge tube. The system was allowed to operate at this condition for one hour in order to remove potential contamination on the walls and electrodes. At the end of this period, the voltage waveform was checked to ensure that it was consistent with previous experiments. Once this was confirmed, the pressure was adjusted to the desired operating condition.

The discharge was shutdown by first shutting off the power supply, followed by the delay generator. Then, the helium flow was shut off, and the primary pump path was opened. The system was allowed to come to base pressure before the two upstream shutoff valves were closed, after which the primary pump path was closed. The roughing pump was then shut off.

In the cases that the discharge had been operated within the last hour, it was possible to use an abbreviated startup procedure. This process was fundamentally the same as the previous one, however once the pump-related procedures were complete the discharge only required five minutes to reach a steady state. This was verified with multiple measurements

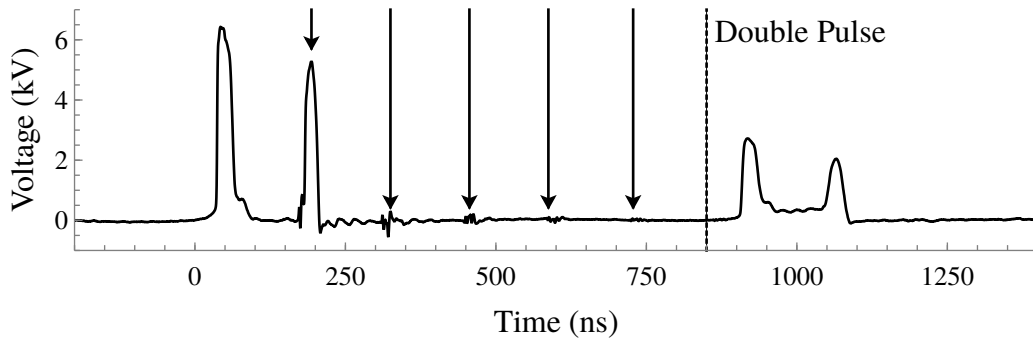


Figure 3.6: Typical voltage waveform of the RPND. Arrows indicate reflections back to the power supply. The dotted line delineates the time at which the power supply begins to exhibit double pulsing.

of the current and voltage characteristics as well as the discharge emissions. At times prior to this five minute equilibration period, the reflected pulse energy was noticeably higher, and the delay between the trigger pulse and the output pulse was variable.

It seems likely that the increased reflected pulse energy during the equilibration period is due to poor matching between the output impedance of the power supply and the plasma load [62]. When the pulse train is initiated, the first series of pulses perceive an almost open load. During this time, the plasma density tends to increase more with each pulse than is lost between pulses. This increase in plasma density, reduces its impedance and improves energy coupling to the plasma. At the same time, the increasing plasma density results in an increasing shielding effect of the applied voltage. Eventually, these effects balance out and the density increased caused by each pulse equals the density decrease which occurs between pulses. At this point the energy coupled into the plasma with each pulsed remains essentially fixed.

3.4 Electrical Characteristics

The typical voltage waveform, as seen in figure 3.6, exhibited a number of features. It begins with an incident pulse at $t = 0.0$. 138 ns later, it is followed by the pulse that has

been reflected from the anode. The reflected pulse is somewhat smaller, proportional to the energy deposited in the discharge. Additional reflections are visible at integer multiples of 138 ns. These subsequent reflections are much smaller than the initial one, suggesting that much of the remaining pulse energy was dissipated after the first reflection reached the anode. Curiously, a second pulse appears at 800 ns. This is believed to be a peculiarity of the power supply. For the most part, analysis of the RPND will focus on the times which precede 280 ns (the incident pulse and first reflected pulse).

The properties of the RPND were examined at: 0.3, 0.5, 1.0, 2.0, 3.0, 4.0, 8.0, and 16.0 Torr. The appearance of the discharge varied with the pressure in a continuous fashion, however it was apparent that there were three regimes of operation. At the low pressures, 0.3 and 0.5, it was difficult to initiate the discharge. Often, it would be necessary to increase the pressure to initiate the discharge, and then reduce the pressure to the desired conditions. The discharge appeared dim and relatively constricted about the central axis of the discharge tube, with a radial extent of approximately 1 cm. Accompanying these pressures was a large degree of electronic noise. This manifested primarily in the current waveforms, as seen in figure 3.7, as well as a number of equipment malfunctions.

As the pressure was increased (from 1.0-4.0 Torr), the electrical noise was observed to subside. The current waveforms showed significant reductions in the ringing that was particularly prominent at lower pressures. In addition, the visual extent of the discharge increased substantially, to the point where it could be considered volume-filling. The discharge also increased its axial extent as well, eventually reaching well past its intended limit at the cathode. This occurred despite attempts to isolate the downstream pump sections from the discharge.

Such behavior is similar to that observed in plasma bullets [83] where the discharge is able to continue far past the cathode. This suggests that development of the RPND along the discharge tube led by a large region of positive space charge, as suggested in the discussion of the field characteristics. The ions that produce this positive space charge are eventually

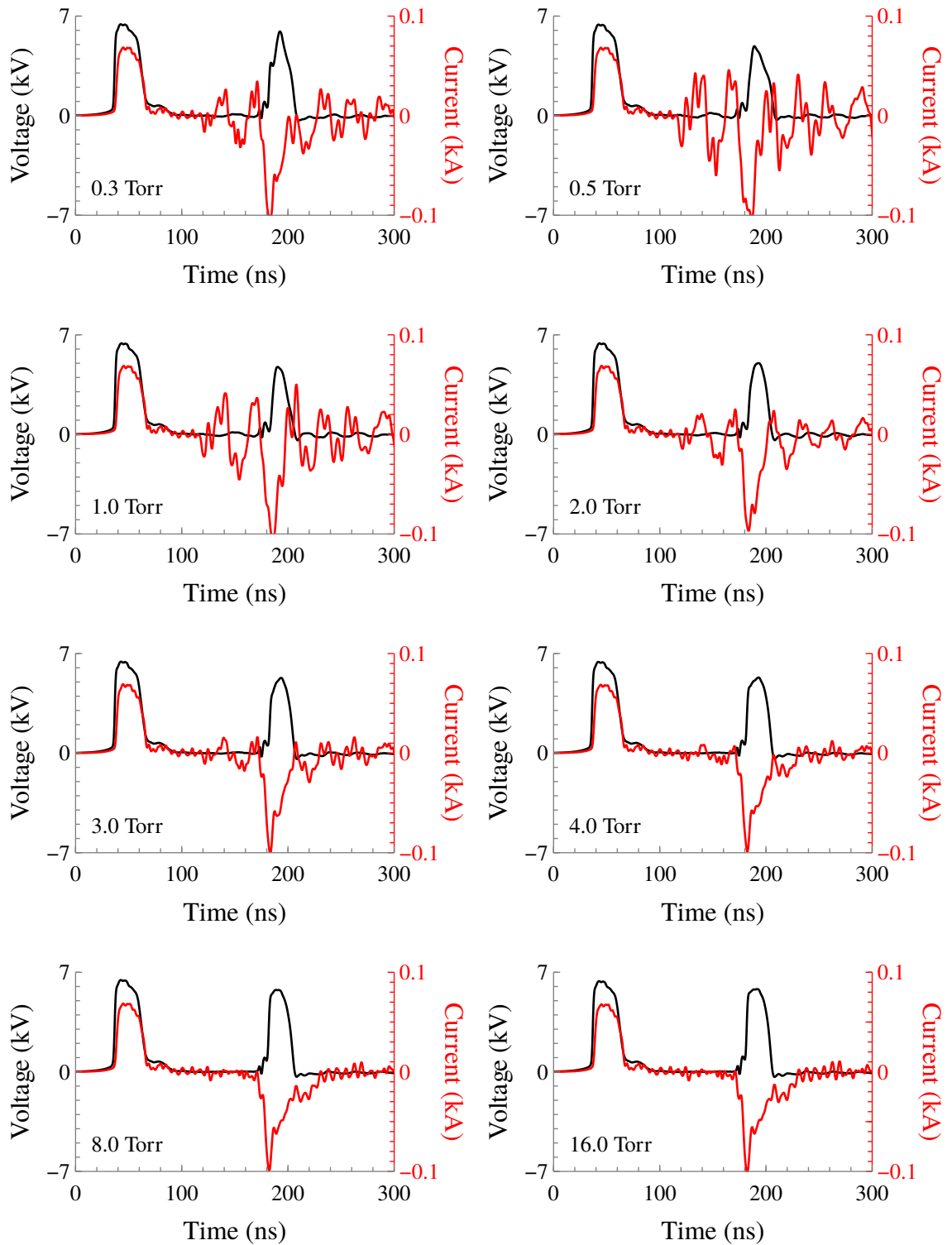


Figure 3.7: High resolution views of the voltage and current waveforms for the first incident and reflected pulse, at each of the operating pressures.

collected at the cathode or neutralized at the walls, however their low mobility (as noted in Chapter 2) prevents this from happening on time scales relevant to the RPND formation.

At higher operating pressure (8.0 and 16.0 Torr), the discharge receded back toward the cathode. This was accompanied by a decrease in the apparent brightness of the discharge to levels similar to that of the low pressure conditions. In contrast, the discharge appeared to remain volume-filling. While discharge initiation was difficult at the higher pressures, it was not accompanied by the electrical noise observed at lower pressures.

3.5 Energy Coupling

The product of the voltage and current waveforms, as seen in figure 3.7, gives the power deposited in the discharge as a function of time. Subsequently, the power integrated over time gives the total energy deposited in the discharge. However, this approach is somewhat complicated by several features of the RPND. As previously mentioned, the pulses produced by the power supply are not completely absorbed by the discharge. Therefore, the integration must be carried out over both the incident and the reflected pulse. Additionally, there is the concern that the oscillations in the current measurements could introduce fluctuations in the calculated energy deposition. However, the small voltage signal limits the error introduced by these fluctuations to less than 1%.

Figure 3.8 gives the total energy deposited for the first pulse at each of the operating conditions. The energy coupled to the discharge peaks at an energy of 5.5 mJ (out of a total incident energy of 8.8 mJ) at a pressure of 1.0 Torr, after which it slowly decreases. This peak in the coupled energy is coincident with the peak brightness of the discharge. Together, these suggest that the density of excited states will be optimized at intermediate pressures.

Though there appear to be no direct comparisons available in the literature, several papers report on energy coupling for similar systems. Macheret, Schneider, and Murray studied a parallel plate RPND in air, at 1-10 Torr and reported a total energy deposition of

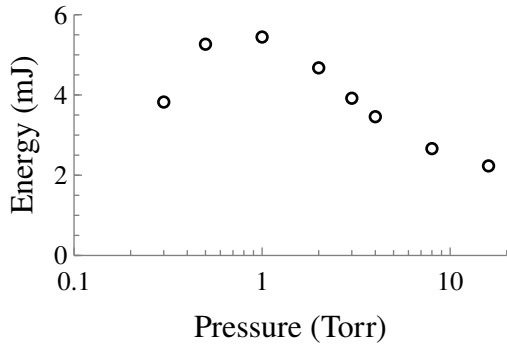


Figure 3.8: Plot of the energy coupled into the discharge with the first pulse as a function of pressure.

0.30-0.36 mJ, increasing with pressure [81]. Nishihara et al. recorded values of 1-2 mJ in a nitrogen RPND [72]. Pancheshnyi et al., in the study of an air-propane mixture at 750 Torr, found that each pulse deposited about 1.9 mJ of energy. Overall, the measured values for the deposited energy appear to be in comparable with those previously measured.

From an applications standpoint, the potential existence of a condition which optimizes the production of excited states is an interesting one. This behavior is also compelling from a physical standpoint as it suggests a phase change in the competition of two or more processes. Though this kind of competition is reminiscent of Paschen's law, the duration of the pulse is too short for appreciable ion drift to occur (an estimated maximum of 3 mm), therefore secondary electron emission is not important. These observations provide further impetus for a close examination of the RPND properties, particularly the excited state dynamics.

CHAPTER 4

Metastable Measurements

As was noted in Chapter 1, measurements of the RPND have been mostly limited to the afterglow plasma or time-integrated quantites. Electric field measurements, either with capacitive probes or nonlinear wave-mixing, thus far provide the only insight on the development of the RPND [79, 80, 87]. Though the electric field can be used to estimate electron densities and reaction rates in the plasma, this requires a number of additional assumptions regarding electron locality, and equilibrium with the applied field.

As a result, there is a lack of reliable information on particle properties of the RPND during its development. That said, such information is necessary to confirm the present understanding of how these discharges develop, how they may be optimized for specific applications, and how to improve existing numerical simulations. Therefore, a clear need exists for direct measurements of the RPND particle properties.

Unfortunately, this presents a significant challenge for most traditional plasma diagnostics. In most situations, the obvious choice would be the Langmuir probe given its simplicity and ease of implementation. However, the fast variations in the plasma potential, slow response of the ions, and high collisionality all preclude this approach [90]. Furthermore, any physical probe could potentially act as a large perturbation to the very system it is measuring.

The logical alternative to physical probes is the use of optical diagnostics, however these have their own associated difficulties. Electrons cannot be studied by their light emissions because, with the exception of bremsstrahlung and cyclotron radiation, they do not emit.

This leaves the light emitted from excited atoms. Atomic emission spectroscopy can be used to measure many different plasma quantities, from electron density, to local electric field strength [96]. Unfortunately, spontaneous emission can be a slow process compared to the development of the RPND. For example, the fastest neutral helium transition in visible wavelengths (3^3D_3 - 2^3P_2) has a decay rate of 14 ns [102].

This suggests that instead of waiting for spontaneous emission to occur, it may be better to use some form of active spectroscopy. Though the added complexity of a well-characterized light source is undesirable, it allows for several interesting opportunities. For example, a sufficiently intense laser can be used to directly interact with the electrons through Thomson scattering. It has a high spatial and temporal resolution and is able to measure the electron density and temperature simultaneously [103]. However, the RPND may have densities well below the interaction limit of $5 \times 10^{12} \text{ cm}^{-3}$ [75].

If it is not possible to directly interact with the electrons, the next alternative is interact with the atomic population. Probing of the ground state is difficult given its large separation from any excited state. Furthermore, the high densities of the neutral states would completely absorb all incident radiation, even over short pathlengths (leaving nothing to measure). Instead it makes more sense to probe an excited atomic state. The lowest lying one is the triplet metastable (2^3S), which resides at 19.82 eV above ground [102]. This relatively large energy gap assures that no such states will be naturally present at room temperature. The triplet metastable (and all higher-energy states in helium) will be populated almost exclusively by energetic electrons. Therefore, the triplet metastable density is a useful indicator of the electron energetics in the RPND as it develops. With a sufficiently complex model, it may even be used to infer properties of the electron population.

Perhaps the most straightforward means by which to measure the triplet metastable density is with absorption spectroscopy. This approach has a long history in the study of gas discharges, going back at least six decades [104]. At its most basic, the technique involves illuminating a plasma with light matching a transition between the metastable, and some

upper level. The amount of transmitted light is then measured with a detector on the opposite side of the plasma. The amount of transmitted light is proportional to the metastable density, integrated along the path of the light. As the temporal bandwidth of this technique is only limited by the time required for the light to traverse the plasma, it presents a promising approach for particle measurements during the development of the RPND.

4.1 Setup

Traditionally, the light used in absorption spectroscopy has been supplied by discharge tubes of same gas as the system under study. Though straightforward, this approach is limited by the luminosity of the discharge tube, and the fact that the emitted radiation is isotropic. More recently, Millard et al. noted that diode lasers provide a greatly improved light source for absorption experiments [105]. The laser light is easily directed and collimated for spatial selectivity, and has more than sufficient intensity [105]. Therefore, it was decided to use a diode laser in the measurement of the triplet metastable level.

As with the study by Millard et al., the decision was made to study the transition from the triplet metastable to the $2^3P_{0,1,2}^o$ state (a transition wavelength of approximately 1083 nm). This was done for several reasons. For one, the closest helium transition is over 7 nm away, making it relatively isolated. In addition, the different levels or values of J are all within the tuning range of a single diode. As each level has a different degeneracy, g , the strength of absorption varies depending on the selected level. Thus, the absorption strength can be increased for low densities, or decreased at high densities, improving the dynamic range of the diagnostic.

The laser used was a distributed feedback laser diode, produced by Toptica, model LD-1083-0070-DFB-1. The specified linewidth of the laser was 3 MHz, well below the natural linewidth of the transition at 10.2 MHz. This can be exploited to directly measure the gas temperature of the system, as will be seen in the next section. The diode was rated for a total

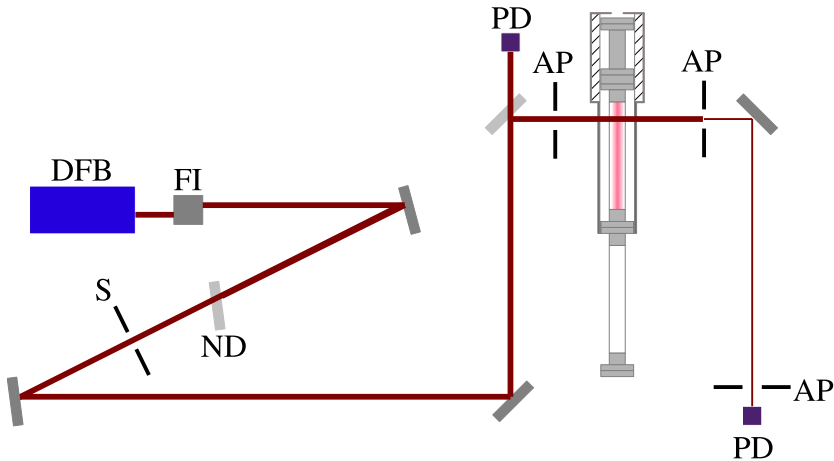


Figure 4.1: Optical beam path of the laser in the absorption spectroscopy experiment. DFB - Distributed feedback laser diode; FI - Faraday isolator; ND - neutral density filter; S - shutter; PD - photodiode; AP - aperture.

output power of 70 mW, with a beam size of 1 mm by 3 mm and vertical polarization. The diode was housed in a Toptica DL DFB housing which incorporated the collimating optics. A Toptica DCC 110 was used to provide current control for the diode laser, and a Toptica DTC 110 was used to control the thermoelectric cooler for the diode.

The layout in figure 4.1 reflects the optical beam path used in the absorption experiment. The laser light is produced by the distributed feedback laser diode (DFB). It then enters an Electro-Optics Technology, Inc. Faraday isolator (FI) which prevents back-reflections from entering the diode. Without the isolator in place, such back-reflections can cause mode-hopping, resulting in unreliable tuning. The laser intensity is then reduced by a neutral density filter (ND). After which, the laser passes through a Vincent Associates electronic shutter (S). Then, the beam is split by a Thorlabs BSF10-C beam sampler at a 45° angle. This reduced the laser intensity below the saturation intensity (0.45 mW/cm^2) of the transition. The beam was collimated with two apertures (AP) on both sides of the discharge apparatus. The beam exiting the apparatus was then sent through a final aperture to filter nearly-colinear plasma emissions before it was coupled into an optical fiber by a Thorlabs F240SMA-780 collimation package.

Behind the beam sampler was a Thorlabs DET300 germanium photodiode. The signal from this photodiode was terminated at $1\text{ M}\Omega$ and used to monitor the beam. The opposite end of the optical fiber was affixed to a Thorlabs DET410 InGaAs photodiode. The photodiode signal was amplified by a Femto HVA-200M-40-B voltage amplifier before being sent to the oscilloscope. The time resolution of the metastable measurements was determined by the InGaAs photodiode which had a specified rise time of 5 ns.

In order to measure the absorption of the laser, it was first necessary to tune the laser to the correct wavelength. This matter was complicated by the lack of a wavemeter with sufficient precision and accuracy. As a result, a signal generator was used to sweep the laser current so as to cover a frequency range of 40 GHz while the plasma was operating. The temperature of the diode was then slowly adjusted until absorption peaks corresponding to the $2^3S_1 - 2^3P_{0,1,2}^0$ transition were observed in the output of the InGaAs photodiode. This allowed the laser current to be tuned to coincide with the desired transition and provided a rough conversion between changes in the diode current and changes in the laser wavelength. A more accurate measurement of this relation was made with a CVI Melles Griot ET-25.4-10.00-30, solid dielectric etalon. It was found that a temperature of 36° C and a current of 63 mA produced resulted in an output wavelength of approximately 1082.9 nm and the conversion between diode current and wavelength was 0.6067 mA/GHz.

As described in Chapter 3, data acquisition was handled by a LabView program, connected to the oscilloscope by a GPIB cable. The auxiliary outputs of the SRS SR850 lock-in amplifier were used to adjust the diode laser current (via the DCC 110 module), and to trigger the electronic shutter. One of the auxiliary inputs of the lock-in amplifier was used to read out the pressure from the pressure controller.

Data were acquired for a range of pressures from 0.3-16.0 Torr, and at three axial locations: 5.08, 12.7, and 20.32 cm, relative to the glass-metal seal of the anode. In reference to their location relative to the gas inlet these will be referred to as the ‘upstream’, ‘midstream’, and ‘downstream’ locations, respectively. For each combination of location and pressure,

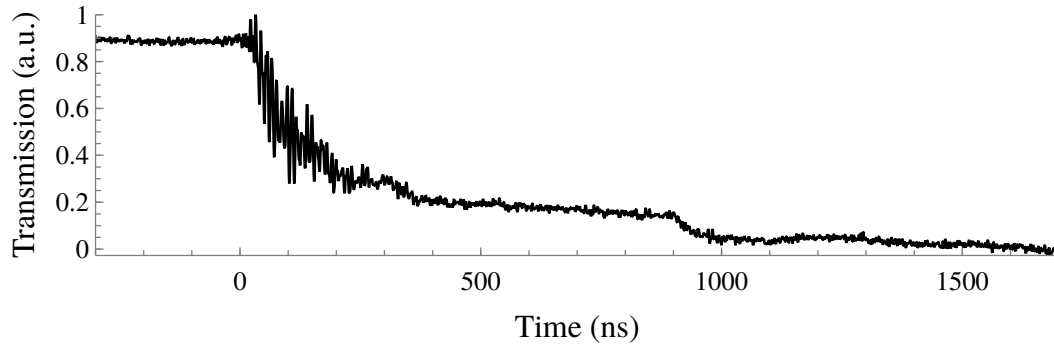


Figure 4.2: Measurement of the transmitted laser light at the nominal transition wavelength at 4.0 Torr of helium.

absorption spectra were measured over ± 3.85 GHz relative to the nominal transition frequency of the 2^3S_1 - $2^3P_0^o$ transition at intervals of 154 MHz. The absorption spectra were measured for time domains of -300 - 1700 ns relative to the voltage pulse. Additional measurements were made at the midstream position of the metastable densities from -88 - 700 μ s in order to investigate the loss mechanisms of the metastables.

The broadband electronic noise emitted by the fast pulses was a persistent issue and presented one the greatest challenges in the acquisition of accurate measurements. In order to reduce the noise present in the detector signal, the InGaAs photodiode was removed from the immediate area surrounding the discharge by the use of an optical fiber. The optical fiber was routed through a small opening in a grounded metal box where both the photodiode and the voltage amplifier resided. In addition, the DC power supply of the voltage amplifier was connected to an outlet on a Tripp-lite Isobar intended to provide isolation for the power input. The photodiode was connected directly to the input terminal of the amplifier minimizing the length between the two. Likewise, the amplifier was connected to a BNC bulkhead adapter by a 10 cm length of RG 50/U. The final connection to the oscilloscope was made by an additional 10 cm length of RG 50/U, running from the BNC bulkhead connection.

Figure 4.2 shows the transmission signal measured at the nominal transition wavelength while the plasma was active in 4.0 Torr of helium. The signal is an average of 200 indepen-

dent pulses. Further sampling had no appreciable effect on the waveform. As can be seen, despite the efforts to limit the electrical interference, there is still a substantial amount of noise present in the transmission signal. This is most noticeable in the large ringing which occurs for the first 200 ns after the voltage pulse. Without any kind of compensation for this noise it would be impossible to obtain reliable measurements of the transmission signal.

4.2 Noise Suppression & Absorption Analysis

The noise produced by the RPND was relatively consistent between pulses as well as over the duration of each experiment. As a result, it was possible to correct for the electrical noise and emissions from other transitions by measuring the signal from the photodiode in the absence of the laser and subtracting this from the signal with the laser. The acquisition process proceeded as follows:

1. Set desired laser wavelength.
2. Wait 5 s for laser output to settle.
3. Acquire 200 waveforms from photodiode.
4. Close shutter.
5. Acquire 200 waveforms from photodiode.
6. Repeat

The effect of this subtraction can be seen in figure 4.3 where the top heatmap shows the initial set of acquisitions with the laser on, and the middle heatmap shows the transmitted signal with the noise subtracted.

As the wavelength of the laser diode changed, so did the output power. This led to the gradient-like appearance of the top two plots in figure 4.3. In order to correct for this a measurement was made of the unattenuated laser power as a function of diode wavelength. This was done by deactivating the plasma and repeating the above acquisition procedure. The intensity of each point in the transmission spectra was then divided by the unattenuated laser power, producing the properly normalized transmission spectra.

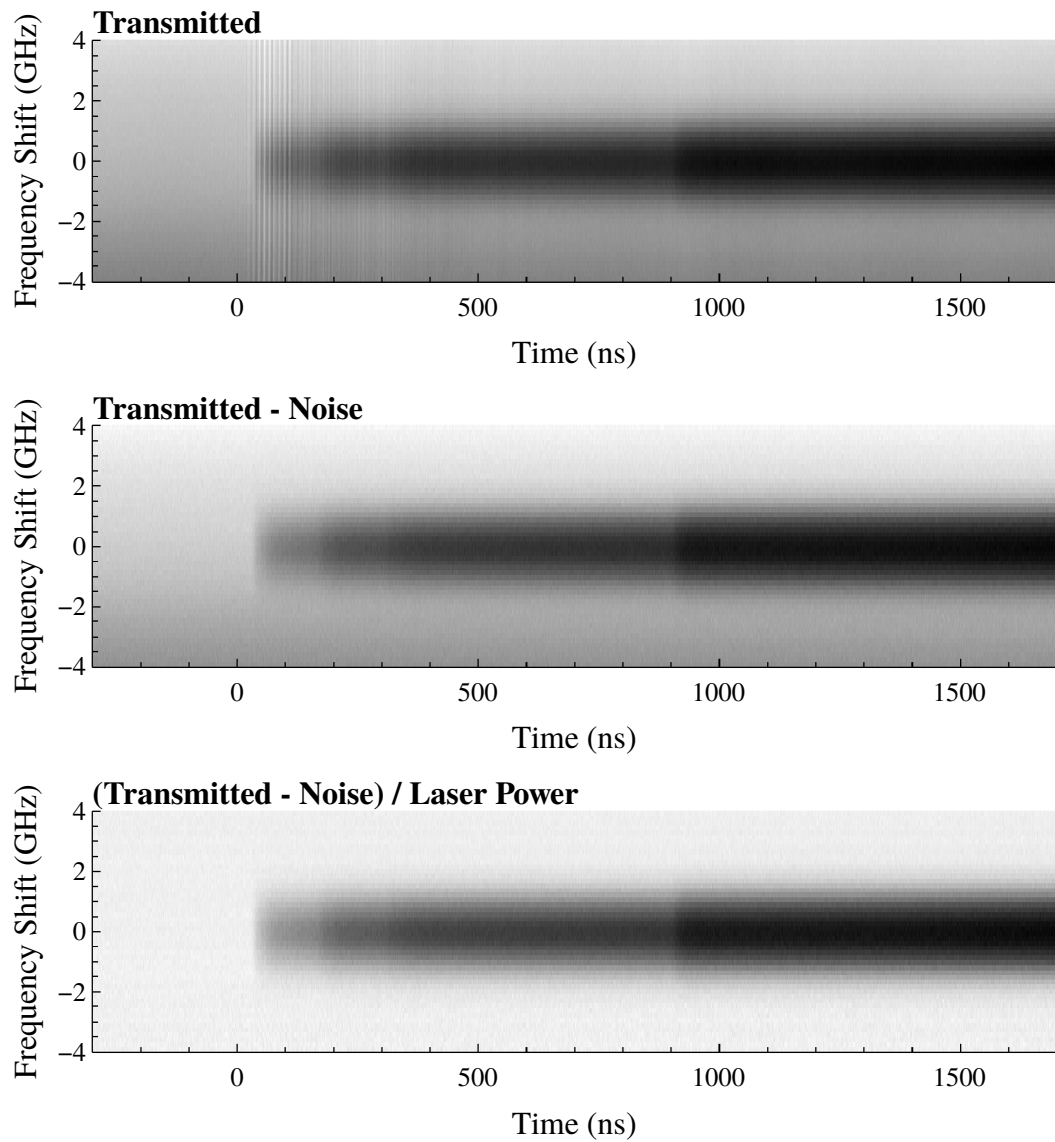


Figure 4.3: Heatmaps of the transmitted laser signal for the 4.0 Torr condition at various stages of post-processing.

These spectra were then analyzed using a transmission model based on the absorption cross sections described in Chapter 2. In a one-dimensional system, the change in intensity of an incident photon field (below the saturation limit), can be expressed as

$$\frac{dI(x, \omega)}{dx} = -\sigma(\omega)N(x)I(x, \omega) \quad (4.1)$$

where I is the intensity of the photon field as a function of distance x , ω is the frequency of the photons, N is the density of the interacting species, and σ is the interaction cross section. This equation has the simple solution,

$$T(\omega) = \frac{I(x, \omega)}{I_0(\omega)} = \exp \left[-\sigma(\omega) \int_0^x N(x') dx' \right], \quad (4.2)$$

where T is the transmitted intensity fraction, and I_0 is the initial intensity of the photon field. The absorption can be trivially obtained from the relation $A(\omega) = 1 - T(\omega)$.

For the purpose of analyzing the absorption spectra, a quantity called the line-integrated density will be defined. This is simply, $\langle N \rangle = \int_0^x N(x') dx'$. While equation 2.16 can be used to determine the absorption cross section it requires that a lineshape be specified. In general, it is preferable to select either a purely Gaussian or purely Lorentzian lineshape. This reduces the computational cost of spectral calculations in comparison to the use of the Voigt profile (equation 2.14). Whether the Voigt profile is necessitated or not can be determined by a comparison of the relative widths of the different broadening mechanisms. For a temperature of 300 K and a pressure of 8.0 Torr, it is found that $\Delta\omega_d = 1.7$ GHz and $\Delta\omega_a = 0.21$ GHz. Because neither broadening mechanism appears dominant, the choice was made to analyze the data with a Voigt profile, despite the added computational cost.

Equations 4.2, 2.16, and 2.14 can be combined to form a model equation for the absorption spectrum. It can be seen that only two unknowns exist: the gas temperature, T_g , and the line-integrated density, $\langle N \rangle$. The model equation was matched to the measured spectrum at each time point using the Levenburg-Marquardt algorithm [106], as implemented by the

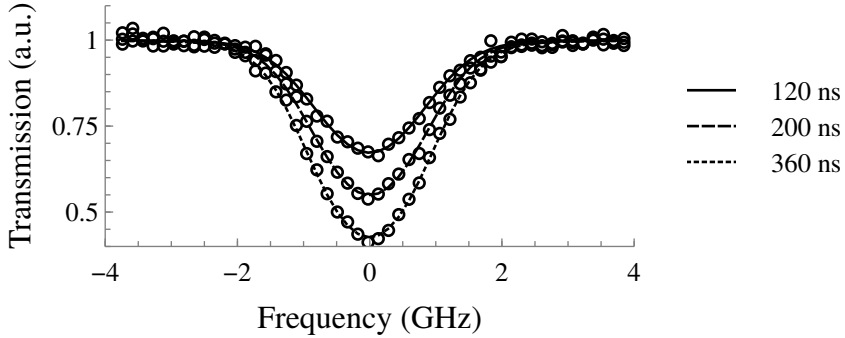


Figure 4.4: Comparison of the measured transmission profile (open symbols) and the computer-generated matches for at several different times for the 4.0 Torr operating condition.

SciPy library [107]. During the matching process, small variations in the center frequency of the laser diode were observed. This was assumed to be the result of long-term variations in the diode temperature that were not adequately compensated for by the temperature control system. The magnitude of these drifts were on the order of ± 60 MHz between experiments. This fluctuation in center frequency was measured for each experiment and used to correct the wavelengths in the post-processing. A full report and code listing for the laser analysis software is presented in Appendix B.

4.3 Results

The matching algorithm proved robust enough to automatically match the transmission spectrum at each time step with no user intervention. Figure 4.4 shows three examples of the measured transmission spectra along with the computer-generated matches. The measured data cleanly coalesce to complete transmission far from the peak. In addition, the spectra show no evidence of the noise caused by the discharge. This suggests that the compensation described in the previous section was adequate for these conditions. Across all cases, the total variation in the baseline transmission signal was approximately 0.02. This set a minimum line-integrated detection limit of approximately $3.0 \times 10^{14} \text{ m}^{-2}$, though the actual

value varied with respect to the pressure and temperature.

4.3.1 Temperatures

The temperatures calculated for the metastables from the laser-absorption spectroscopy diagnostic are shown in figure 4.5. Prior to the pulse, the temperature estimates are subject to large variations. This is a result of the low metastable densities which precede the pulse. Without a substantial metastable population, the matching algorithm had difficulty discriminating between a combination of low temperatures and low densities (a small, narrow absorption spectrum) versus high temperatures and high densities (a very broad absorption spectrum).

Though it is not possible to provide an exact value of the errors in the calculated temperatures, the algorithm does provide an estimate of the standard deviation in its results. In all cases, the estimated standard deviation was less than 10 K by the end of the measurement period. Given this value, there appear to be no meaningful trends throughout the measurement period, and between the measurement locations.

In order to more clearly compare the temperatures at the different operating conditions, the results for each location were combined and averaged over the final 200 ns. This was then plotted with respect to the energy deposition calculations from Chapter 3, divided by the gas density. If the discharge was appreciably heating the helium, the temperature would be expected to increase with respect to the density-normalized energy deposition. As seen in figure 4.6 this does not appear to be the case. Indeed, most of the operating conditions show little to no statistical difference between each other and room temperature. The only exception to this is the 16.0 Torr operating condition with a mean temperature of 255 K. As no effort was made to cool the discharge tube, this appears to be an erroneous result. A comparison of the calculated spectra and the original absorption spectra revealed no obvious errors. However, as will be seen later, the metastables were the least dense at 16.0 Torr. This, along with the large variation of the temperatures between time points suggest that the

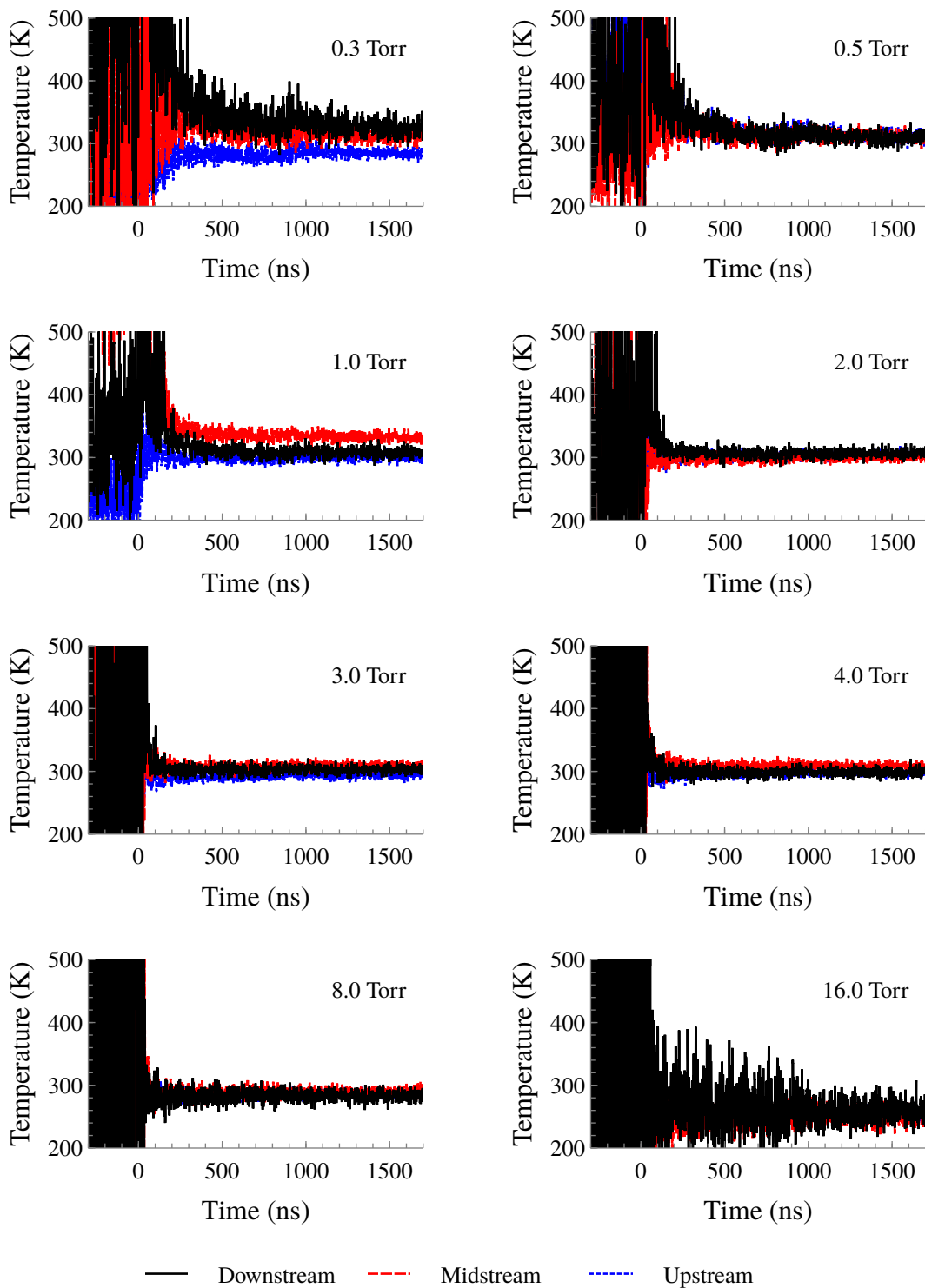


Figure 4.5: Plot of the gas temperatures at each of the operating pressures and each axial location as a function of time.

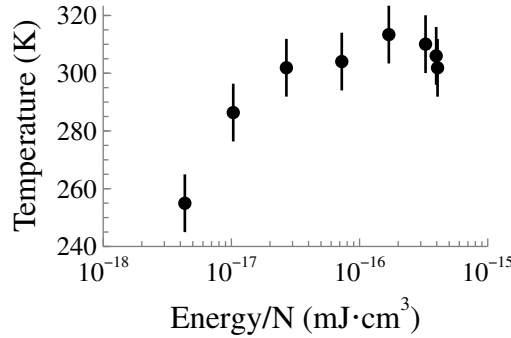


Figure 4.6: Plot of the average gas temperature as a function of deposited energy.

standard deviation in the calculations is higher than estimated.

Only a limited number of similar direct temperature measurements exist within the literature. The work of Walsh et al. [84] provides the most direct comparison. In their study, they measured the heating in a planar discharge with helium and a small admixture of oxygen as the working gas. The system was held at atmospheric pressure and had a gas flow rate of 5 slm. Instead of absorption spectroscopy, the rotational spectra of the oxygen was used to determine the temperature. Temperatures ranged from 300-340 K, depending on the average power dissipated in the plasma. Walsh et al. suggested that the observed temperature increase was a result of Joule heating, that is, heating of the gas as a result of electrons colliding with neutral particles. As this process scales with temperature, it would not be expected to be present in the trends from figure 4.6. The presence of a measurable fraction of a molecular gas (oxygen) allows for several other heating mechanisms to occur. Dissociation of the oxygen can impart translational energy to the daughter particles, heating the gas. Additionally, excited the energy contained in rotational and (to a lesser extent) vibrational states can be converted to translational energy in collisions [108].

Other experiments have demonstrated minimal gas heating for RPNDs. Plasma bullets, like those of Laroussi and Lu [82, 83], tend to be associated with minimal heating. However, others have observed measurable heating with temperatures ranging from 400-1000 K [75, 76, 109, 110] (see appendix A for detailed study in air at NASA Glenn Research Cen-

ter). A comparison of the experimental conditions shows that heating was only observed in molecular gases, though there were cases in which no heating was observed [111], likely a result of the low repetition rate and energy deposition. These similarities emphasize the importance of the additional heating pathways linked to molecular gases.

For comparison recent simulations and rate calculations [87, 112] have provided estimates of the electron temperature in the range of 10-20 eV. As a result, all of the discharges mentioned are very much nonthermal in nature. That said, the negligible heating in the helium RPND studied here may provide a significant advantage in some applications, as even the moderate temperature increases in molecular discharges can threaten material integrity. For example, most commercial polymers are only rated to 300° C, making them susceptible to damage without careful thermal management.

4.3.2 Line-integrated Densities

As described in the analysis section, the laser-absorption spectroscopy also yielded the line-integrated metastable densities. Figure 4.7 shows the metastables dynamics for each operating pressure and at each location. Similar to the temperature measurements, there is a substantial uncertainty during the pre-pulse period for pressures greater than 1.0 Torr. However, for 1.0 Torr and below, there are detectable populations of triplet metastables, around $7 \times 10^{14} \text{ m}^{-2}$. These excited atoms are the remnants of the previous pulses which have not been destroyed or left the system. Despite the efforts made to limit the noise in the signals, there is a significant number of erroneous data points in the downstream measurements for pressures below 3.0 Torr. It is not clear why this measurement location was particularly susceptible to plasma-related noise. In all cases, the photodiode remained in the grounded enclosure and only optical components were moved.

In each case, the metastable population exhibits two short bursts at 140 and 280 ns. This is shown in more detail in figure 4.8. The timing of these bursts correlate with the arrival of pulse reflections. This suggests that even after the plasma has formed, additional

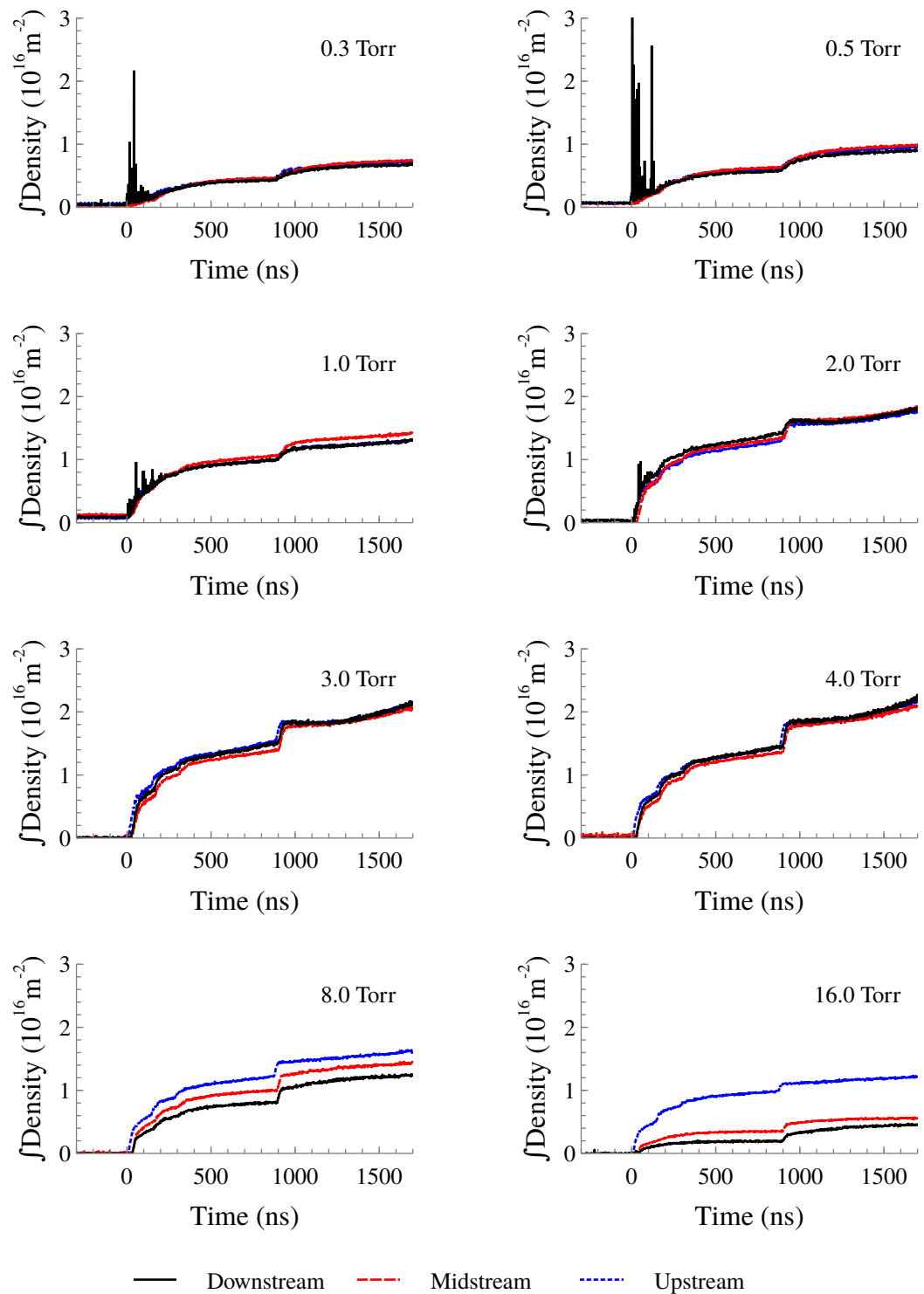


Figure 4.7: Plots of the line-integrated metastable densities at each of the operating pressures and each axial location as a function of time.

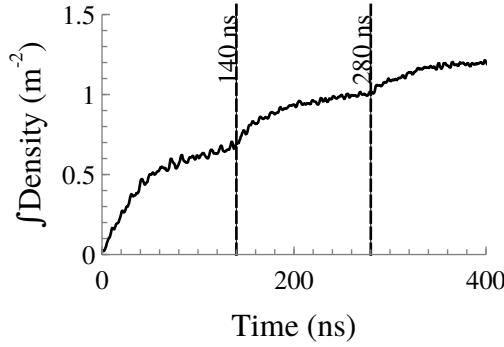


Figure 4.8: Zoomed in view of the increases in metastable density as a result of pulse reflections.

pulses are still able to deposit a significant amount of energy in the plasma. This appears to contradict the predictions made by the one-dimensional drift models of Adamovich et al. [67] and Nikandrov et al. [68] which stated that little energy is coupled into the plasma after breakdown occurs. In addition to the smaller bursts in density, another can be noted at about 900 ns which corresponds to the double-pulsing observed in the current-voltage characteristics of Chapter 3.

By 200 ns after the pulse, the estimated standard deviation in all cases is approximately $2 \times 10^{14} \text{ m}^{-2}$. Based on this, it can be concluded that the metastable populations had no significant axial dependence below 8.0 Torr. However, both 8.0 and 16.0 Torr conditions showed notable differences in the metastable population as a function of distance from the anode. As might be expected, the upstream location (closest to the anode) has a high metastable population than the other two. At 16.0 Torr, the line-integrated density at the upstream location was over twice that of either location.

This behavior is reminiscent of that observed by Vasilyak et al. [19] in FIW devices. It was noted that the electric field of the wave would attenuate with distance. In order to interpret this, they considered the wave to consist of two components: a moving ionization front with a finite width, and the plasma left in its wake. They state that the plasma, with its finite conductivity, will have some voltage drop across it, and as it grows, this drop increases.

As a results the voltage drop across the ionization front can never be greater than the overall potential applied to the system and is constantly diminishing as it moves away from the energized electrode. If true, this behavior would be associated with a reduction in the rate of metastable generation in the front, thus explaining the high pressure data in figure 4.7.

In order to compare the metastable measurements to other results, it's necessary to know the density as opposed to the line-integrated value. In this case, it shall be assumed that the metastable atoms are distributed uniformly along the beam path through the plasma. This suggests that the metastable densities in the RPND lie in the range of $0\text{--}1 \times 10^{12} \text{ cm}^{-3}$. This is significantly less than the measurements of Stevfelt, Pouvesle, and Bouchoule [113], however their system involved an atmospheric-pressure discharge and energy deposition of up to 0.2 J (compared to a maximum of 5.5 mJ in this experiment). Urabe et al. [114] measured metastable densities of up to $4 \times 10^{11} \text{ cm}^{-3}$ with laser-absorption spectroscopy in a helium jet at atmospheric pressure. Nersisyan, Morrow, and Graham made measurements suggesting a metastable density of about $1.5 \times 10^{10} \text{ cm}^{-3}$ in a DBD [115]. Though the discharge was not pulsed, Millard et al. measured densities from 5×10^9 - $1.2 \times 10^{11} \text{ cm}^{-3}$ in helium glow at 2.0 and 5.0 Torr [105]. While none of these experiments are a direct comparison, they do suggest that the results obtained above are within reason.

4.3.3 Metastable Destruction

In addition to the fast metastable dynamics, measurements were made of the long-term trends of the metastable populations. Afterglow measurements such as these are less subject to the noise and bandwidth limitations of the short timescale measurements. This makes it possible to obtain relatively clean and precise values for the metastable densities. However, without the applied electric field, the nonequilibrium dynamics of the system rapidly disappear. Therefore, while these measurements provide some insight on the initial conditions, they cannot describe the dynamics of the RPND alone.

That said, a large body of work has been conducted on helium afterglow discharges,

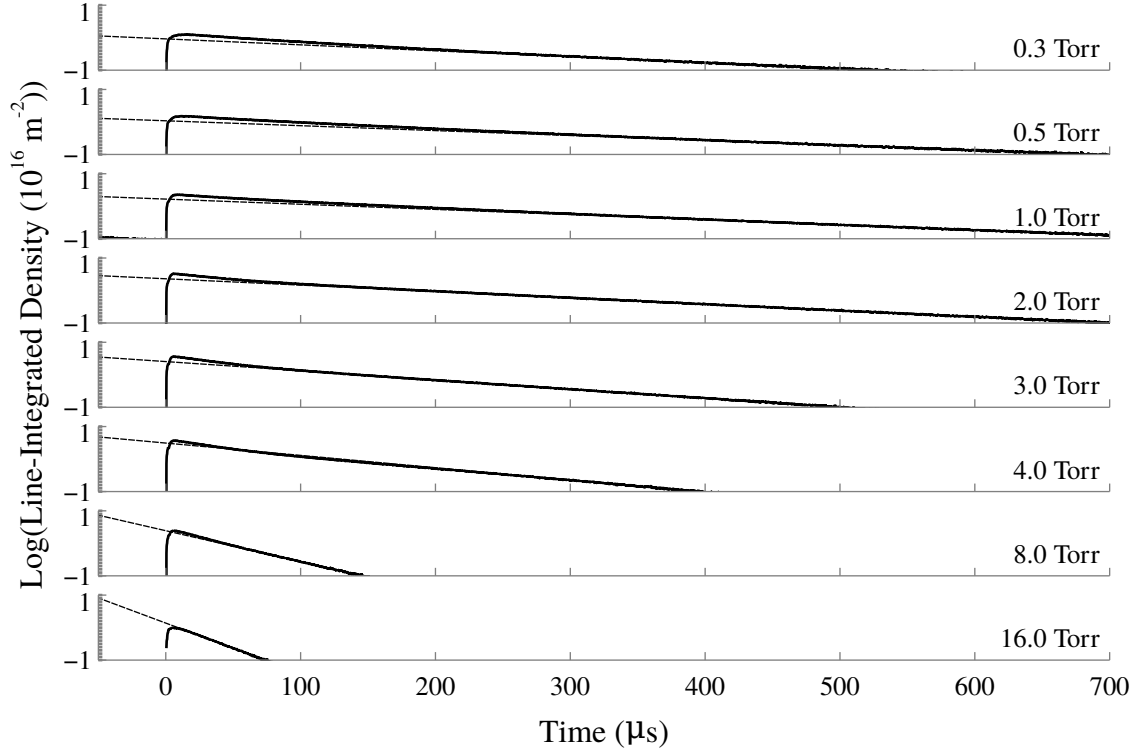


Figure 4.9: Measurements of the long-duration metastable density trends. Exponential fits are indicated by the dotted lines.

which makes this regime attractive as a point of comparison. Furthermore, these measurements include the peak metastable populations for each operating pressure (which are missing from figure 4.7). The peak metastable densities and the lifetime of the metastable populations are of interest as they can produce charged particles through Penning ionization of each other or impurities [115]. This extends the ionization period in rare gas RPNDs well past the voltage pulse itself. Also, as seen in figure 2.6, all excited states in the triplet manifold will eventually decay to the triplet metastable level. Thus, a substantial portion of the energy deposited in the plasma is contained in this one level.

Figure 4.9 contains logarithmic plots of the metastable populations for each operating condition, all measured at the midstream location. In addition, an exponential function was fit to the tail of each trend, represented by the dotted line. On these time scales, the destruction of metastables in the RPND apparatus can be described by four different mechanisms:

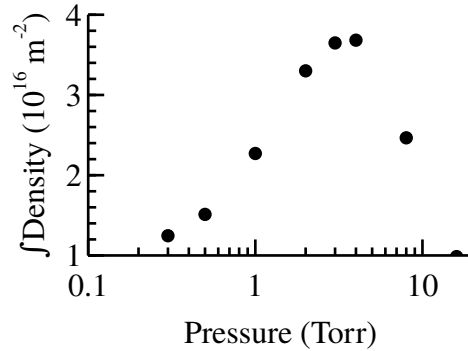


Figure 4.10: Peak line-integrated metastable densities as a function of pressure.

diffusion, Penning ionization of impurities, Penning ionization between metastables, and three-body collisions resulting in helium dimer formation. All processes with the exception of the Penning ionization between metastables have an exponential dependence, thus any deviation from an exponential decay is likely a result of Penning ionization [116].

As can be seen, a number of the decay curves deviate from a strictly exponential decline. This deviation appears to be more substantial at the lower pressures. For example, the decay at 16.0 Torr appears strictly exponential. Initially, this deviation was believed to be the result of Penning ionization between metastables. The rate at which this takes place is proportional to the square of the metastable density. Therefore, if this is the process responsible for these deviations, it should be most severe for the highest metastable densities. However, per figure 4.10, this is not the case. If Penning ionization between metastables were the dominant loss mechanism, it would be reduced at the lower pressure conditions, contrary to what was observed.

Ultimately, the behavior of the metastable populations in the afterglow can be best understood by a comparison of the depopulation rates for each process. Figure 4.11 illustrates the aforementioned decay processes at 0.3 Torr, for a variety of metastable densities. The rate constants for these processes were obtained from the study by Deloche et al. [116] and the work of Pouvesle et al. [113] (specifically for the rate of Penning ionization of nitrogen impurities). The gas impurities were assumed to be nitrogen, and the mole fraction was

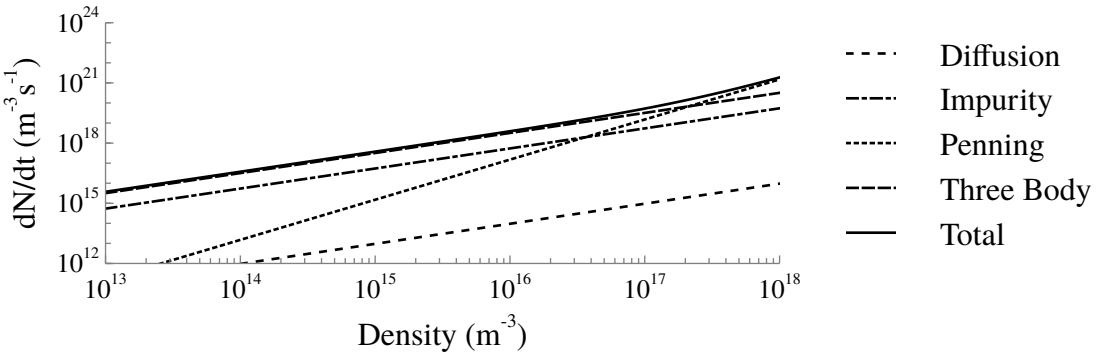


Figure 4.11: Comparison of the decay rates for various processes at 0.3 Torr as a function of metastable density.

assumed to be 80 ppm, as was estimated in Chapter 3.

As can be seen, the dominant loss mechanism above metastable densities of $2 \times 10^{17} \text{ m}^{-3}$ was Penning ionization between two metastable atoms. Below this density, the three-body process responsible for dimer formation was dominant. However, the three-body process scales with the square of the neutral gas pressure. As a result, as the pressure is increased this mechanism quickly overtakes all the others. Therefore, the exponential dependence of the decay at higher pressures is not representative of any change in the importance of Penning ionization between metastables, but rather the increasing importance of three-body collisions. This severely restricts the longevity of the metastable states at higher pressures, and reduces their ability to prolong the charged particle population.

From figures 4.11 and 4.9, it can be seen that, aside from the deviations at lower pressures, the decay curves are well-matched by the exponential functions. As a result, it is possible to use the fitting functions to estimate the pre-pulse metastable densities as a function of pressure. These estimates are consistent with the short-scale measurements from figure 4.7. The estimated values of the pre-pulse metastable densities are compiled in table 4.1, along with the decay constants. These results show reasonable agreement with the earlier pre-pulse metastable densities, and are within a factor of two or less. This supports the previous measurements, and provides some confidence that the other extrapolations are

Table 4.1: Listing of the extrapolated, pre-pulse line-integrated metastable densities, and decay coefficients as a function of pressure.

Pressure (Torr)	Integral Density (m^{-2})	Decay Constant (s^{-1})
0.3	1.34×10^{14}	4.23×10^3
0.5	3.36×10^{14}	3.47×10^3
1.0	4.29×10^{14}	3.65×10^3
2.0	2.60×10^{14}	4.48×10^3
3.0	3.94×10^{13}	6.47×10^3
4.0	5.04×10^{12}	8.73×10^3
8.0	7.08×10^6	2.20×10^4
16.0	4.74×10^0	3.56×10^4

also accurate representations of the pre-pulse metastable densities.

The decay constants are about an order of magnitude larger than those recorded by Phelps and Molnar [104] at similar pressures. This almost certainly reflects the presence of the impurities in the system. Figure 4.11 shows that impurities are a moderate contributor to the decay of the metastable atoms even at low pressures. Similar measurements and calculations by Deloche et al. [116] confirm the lower decay constants of Phelps and Molnar. In addition, their results showed a relatively consistent proportionality between the electron density and metastable density (on the order of one for every ten). Therefore, these density values may be read as a rough approximation of the electron densities within the RPND.

4.4 Summary

A laser diode-based absorption spectroscopy experiment was set up to observe the development of the RPND on short (0-1700 ns) and long (0-700 μs) time scales. The measurements on the short time scale provide some of the only detailed measurements of the RPND during its development. The design of the system and post-processing software carefully accounted for plasma-related noise, background emissions, and laser drift. The absorption spectra model showed excellent agreement with the measured spectra and the matching algorithm produced consistent and reliable results almost all cases.

Temperature measurements from the Doppler broadening of the absorption spectra showed no appreciable gas heating at any operating pressure. These results contrast with some measurements made in molecular RPNDs where a variety of additional mechanisms are available to transfer kinetic energy from electrons to heavier species.

The line-integrated density results indicate that the plasma is axially uniform across the tube at lower pressures. The 8.0 and 16.0 Torr conditions show significant attenuation in the metastable densities as a function of distance from the anode. This may present a geometric limit to the use of similar RPNDs in material processing. The dominant metastable loss mechanism at low pressures and short time periods is Penning ionization between metastables. However, losses are eventually dominated by three-body dimer formation for all cases. Peak metastable generation is optimized at 4.0 Torr. However, the peak pre-pulse metastable densities, and possibly the electron densities, are optimized at 1.0 Torr. Interestingly, this corresponds with the maximum measured energy deposition from Chapter 3.

These measurements provide an important foundation upon which to develop a more encompassing perspective of how the RPND develops. Specifically, the generation of the metastable atoms is related to a number of other plasma parameters, including: electron density, electron temperature, EEDF, and electric field. Provided a sufficiently detailed model, it should be possible to capture these relationships, and use the measured metastable densities to infer the evolution of these quantities as well as other excited states in the system.

CHAPTER 5

Modeling

Though the metastable density measurements appear to be one of only a few diagnostics conducted during the development of the RPND, they only provide a limited view of the energy transport in the discharge. Quantities, such as the ions, electrons, additional excited states, and fields all evolve in time along with the metastable population. However, the gas phase excitation and emission processes are closely related and provided a sufficiently detailed model, it should be possible to infer some or all of these parameters during the development of the RPND. The ideal model would solve equation 2.1, the Boltzmann equation for each species, over the entire geometry, for all velocities, for as long as required to reach equilibrium.

Unfortunately, these requirements are somewhat problematic. Solutions of the Boltzmann equation for a single species are difficult [90], notwithstanding for the dozens of species which may be present in the RPND. In order to resolve the behavior of the plasma, any spatial discretization of the geometry must be on the scale of the Debye length or smaller. A conservative estimate of the Debye length for the RPND is about $20 \mu\text{m}$. A cube of this dimension has a total volume of $8 \times 10^{-15} \text{ m}^3$, thus requiring a total of approximately 3.2×10^{10} cells for the RPND in question. Assuming that each dimension of velocity space is discretized into 100 components, a total of 0.26 exabytes would be required to describe a single species in the RPND at each timestep.

5.1 Model Development

Therefore, some approximations of the Boltzmann equation were required in order to obtain a computationally tractable problem. As discussed in Chapter 2, the most common approach, and the one applied here, is the use of *moments* of the Boltzmann equation. The moments represent an average over the velocity-space of the Boltzmann equation, resulting in macroscopic properties and relations, such as the continuity equation. They are often used to develop various fluid approximations for plasmas [91] (e.g. the two fluid model and the magnetohydrodynamic equations). Fluid models have been tremendously successful in the description of everything from plasma display panels [117] to interstellar plasmas [118].

The use of moments of the Boltzmann equation does introduce some additional problems. Reaction rates, such as those which describe ionization and excitation, are sensitive to changes in the distribution of particle velocities. However, the distribution velocity of particles is determined from the solution of the Boltzmann equation. As a result, a distribution function either be generated by an approximate solution of the Boltzmann equation [119] or assumed from a equilibrium solution of Boltzmann equation, such as the Maxwell-Boltzmann and Druyvesteyn distributions from Chapter 2. The choice of which approach to use is not easy as the EEDF is rarely known *a priori*. Consequently, this topic is considered more thoroughly in section 5.1.2.

Despite the simplification in velocity-space, the resulting fluid models can still be computationally demanding for large geometries. This has motivated the development of models which reduce the geometric complexity of the system in order to address a larger number of species and transitions [90]. In the extreme case, the geometric dependence of the solutions can be completely eliminated by assuming some sort of spatial distribution.

Several FIW studies were found to have successfully applied these “global models” to their systems [109, 112]. By the elimination of the geometric discretization, they were able to consider a large number of species and reaction pathways. In this work, a global model was used to simulate the RPND. The final model tracked a total of 32 different excited

states of helium from 50 ns prior to the pulse to 140 ns after the pulse (just prior to the first reflection). Between these possible states a total of 535 different reaction processes were incorporated including electron-related reactions, radiative processes, and inter-atomic interactions.

In order to compare the metastable measurements to the global model predictions, it was necessary to convert the line-integrated densities from Chapter 4 to volumetric densities, along the path of the laser. It has been noted that a similar FIW [19] and the same RPND [120] exhibited radial variations in emission intensity, electron density, and metastable density. Unfortunately, the cause of these variations is not clearly understood. It has been suggested that high-energy electrons from the walls may be responsible [121]. However, lacking any empirical, theoretical, or numerical results with which describe the evolution of the radial profile during the discharge, the metastable distribution was simply assumed to be uniform. This assumption likely affects the inferred plasma parameters, however more accurate results are possible provided time-resolved measurements of the radial metastable density or an improved understanding of the RPND.

5.1.1 Continuity Equation

Equation 2.4, the continuity equation, forms the basis for tracking the populations of the excited states in the plasma. Eliminating the spatial gradients reduces this to,

$$\frac{dn_\alpha}{dt} = G_\alpha - L_\alpha, \quad (5.1)$$

where α identifies the particle species, G is the gain term, and L is the loss term. The gain and loss terms represent all possible reactions which can alter the population of α . The model presented incorporates helium states up to $n = 4$, helium ions, and electrons. It should also be noted that the experimental measurements suggested the presence of air impurities up to 80 ppm, and helium dimers are also likely present in the experimental

discharge [113]. However, they were neglected in the case of this model. As observed in Chapter 4, the total e-folding time for the metastable decay was approximately $25 \mu\text{s}$. This indicates that the processes associated with the dimers and impurities are irrelevant on the sub-microsecond time scale.

There were several possible processes that were considered for inclusion in the model:

- electron impact ionization,
- electron impact (de)excitation,
- atomic impact (de)excitation,
- atomic excitation transfer,
- dielectronic recombination,
- three-body recombination,
- radiative decay, and
- diffusion.

As with the impurities and dimer formation, diffusion occurs on a much longer time scale, and was subsequently neglected. Three-body recombination in the volume of the discharge is not important at the estimated temperatures and densities [90], therefore this too was neglected. In general, dielectronic recombination is a rare process [122], however it was incorporated in early versions of the model and was subsequently retained. The importance of ground state excitation or ionization is generally small as the kinetic energy of an atom cannot be easily transferred to the orbital electron [90].

While inter-atomic collisions of excited states can result in a redistribution of excited states or ionization, these processes are not significant in the RPND as the reaction rates are proportional to the product of two (relatively small) excited state densities. The most dominant excited-excited interaction is associative ionization by metastable states [116]. Based on the rates reported in by Deloche et al. and the measured metastable densities, associative ionization could be expected to change the metastable density by less than 0.1% over the course of the 140 ns simulation period.

The remaining processes were found to be the most important for the RPND. This included electron-impact ionization and excitation which dominated the short time-scale dynamics. In addition, excitation transfer between atoms was found to occur at rates relevant

to the simulation period [90]. Likewise, radiative decay occurred fast enough relative to the simulation period to necessitate inclusion [102].

For these processes, equation 5.1 was rewritten as,

$$\frac{dN_i}{dt} = n_e \left[\sum_{j \neq i} N_j K_{j,i}^e(T_e) - N_i \sum_{j \neq i} K_{i,j}^e(T_e) \right] + \left[\sum_{j > i} N_j K_{j,i}^o - N_i \sum_{j < i} K_{i,j}^o \right] + N_g \left[\sum_{j \neq i} N_j K_{j,i}^a - N_i \sum_{j \neq i} K_{i,j}^a \right]. \quad (5.2)$$

Here, the subscripts of i and j represent different states of helium, N is the state density, K is a rate coefficient, T_e is the electron temperature, and N_g is the neutral helium density. The first subscript of the rate coefficients represents the initial excited state while the second coefficient represents the final excited state. Therefore, K_{ij} is a rate coefficient for a process that transfers an atom from state i to state j .

The equation is split into three sets of processes, represented by the superscripts of the rate coefficients: e - electron impact processes, o - radiative decay, and a - atomic excitation transfer. Therefore, the first bracketed term on the right hand side contains all the rate coefficients for electron impact excitation and de-excitation (including ionization). The second bracketed term contains the rate coefficients for optical transitions in and out of the excited state. The final bracketed term contains the gains and losses as a result of excitation transfer caused by collisions with the ground state.

The rate coefficients in equation 5.2 are compiled from a number of different sources. The optical transition rates and the energies of each level were obtained from the NIST Atomic Spectra Database [102]. The excitation transfer rate coefficients came from the studies of Catherinot and Dubreuil [123, 124]. Coefficients were only available for the transitions with $\Delta n = 0$ and $n = 3, 4$. No constants were found for other excitation transfer reactions. The dielectronic recombination rates were adapted from the work of Nahar [122].

The semi-empirical relations derived by Ralchenko et al. [125] were used to calculate the

electron (de)excitation and ionization cross sections for levels through $n = 4$. At the time of this writing, these are the most accurate set of cross sections available for neutral helium with a quoted accuracy of 10-30% for $\Delta S = 0$, and $> 30\%$ for $\Delta S \neq 0$. Only reactions resulting in an energetically uphill reaction were tabulated. The inverse or superelastic cross sections were calculated using the principle of detailed balance [100],

$$\sigma_{ji}(\varepsilon) = \frac{\varepsilon}{\varepsilon - \Delta\varepsilon_{ij}} \frac{g_j^2}{g_i} \sigma_{ij}, \quad (5.3)$$

where $\Delta\varepsilon$ is the threshold energy of the ij reaction and g is the statistical degeneracy of the corresponding state. These cross sections can be used to calculate the rate coefficients for each reaction using equation 2.5. However, this equation requires an appropriate EEDF and leads back to the topic of which one is appropriate for the RPND.

5.1.2 Distribution Effects

Per the discussion of the Boltzmann equation in Chapter 2, there are two analytic equilibrium solutions: the Maxwell-Boltzmann distribution, and the Druyvesteyn distribution. However, research by Starikovskaia and Starikovskii [61] has shown that the EEDF in a nitrogen FIW can deviate from both. This is not surprising given the non-equilibrium nature of the FIW discharge. Since the RPND shares many of its properties, there was the possibility that the equilibrium solutions would not apply to the RPND either.

In order to better understand the energy distributions in a RPND, a numerical study of the EEDF in a helium RPND was conducted. First, a particle-in-cell (PIC) code was used to simulate the effect of a voltage pulse on electrons in a quasi zero-dimensional geometry. This generated an evolution of the EEDF in a helium plasma as a function of time. Then, the mean energy for the EEDF was calculated for a series of time steps. These values were then used to generate equivalent Maxwell-Boltzmann distributions and approximate solutions of the Boltzmann equation.

A PIC simulation does not attempt to solve the Boltzmann equation directly. Instead, the code simulates the behavior of many plasma particles in an experimental geometry using the basic laws of motion and electromagnetism [6]. A discrete EEDF can then be calculated from the particle population (or subset thereof). As the number of simulated particles increases the discrete EEDF will approach the continuous EEDF which would result from a solution of the Boltzmann equation. The relative small number of approximations used in PIC simulations allow them to fully capture the collisionless plasma dynamics [126] while the accuracy of the collisional processes is dependent on the of Monte Carlo techniques.

Generally, PIC simulations do not use a one-to-one correspondence between computer particles and physical particles—most plasmas involve more particles than can be reasonably simulated. Instead, they treat a population of macro-particles, each of which possesses some statistical weight [6]. This allows the macro-particle to represent a group of physical particles. The macro-particles each possess velocities and positions which are continuous within the limits of floating point representation. However, the electromagnetic fields are spatially discretized. This necessitates a mapping of the particle-related fields to the discretized coordinates, and the force of the fields from the discretized coordinates to the particles.

Each PIC simulation begins with a definition of the system geometry and the external fields. Some specified number of macro-particles with a known distribution of velocities are then placed within this geometry. After these steps have been completed, the physics loop, illustrated in figure 5.1, begins. The equations in the loop reflect a one-dimensional system, thus each macro particle possesses only one spatial component, x . However, the simulation supposes the existence of a magnetic field which induces motion perpendicular to the simulation domain. Thus, each macro-particle must possess a velocity vector, \vec{v} , with three components. While all the necessary bookkeeping is done to track the velocity vector of the particle in all three dimensions, the particle’s position is only calculated in one.

The loop generally begins with an initial field calculation based on the external fields combined with that of the particles. This is followed by a particle “push” where the Lorentz

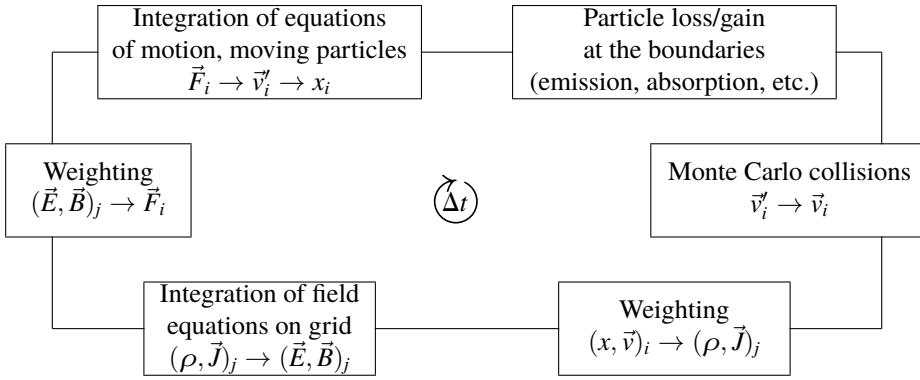


Figure 5.1: Schematic description of the PIC simulation process, adapted from [6].

equation, $\vec{F} = q(\vec{E} + \vec{v} \times \vec{B})$, is used to calculate a new position for a given time step, Δt . Afterward, particles which have moved out of the boundaries of the system are removed from the simulation. Next, collisions (including ionization and excitation) are modeled using Monte Carlo methods [6]. Finally, the fields of the macro-particles are mapped to the spatial grid, the total fields are recalculated, and the next time step begins.

The XDPD1 code, developed by Verboncoeur et al. [127], was used for the PIC simulations. The code was originally designed to simulate a one-dimensional discharge between two parallel electrodes. However, collection at these electrodes complicated the study of the EEDF and did not correspond well to the zero-dimensional nature of the global model. Charged particle collection near the boundaries induced spatial variations in the EEDF. Additionally, the high mobility of electrons often meant that they were preferentially collected on short time scales. This led to the formation of large regions of positive space charge which shielded the plasma from the applied electric field.

In order to address these issues, the code was modified to use periodic boundary conditions. Such conditions resulted in a quasi zero-dimensional simulation, equivalent to a plasma of infinite extent. This eliminated the issue of spatial variations in the EEDF and was more consistent with the assumptions that led to the development of the global model.

Previous measurements of the electric field in a similar FIW found that the electric field

values varied from 0-350 Td [87]. Based on these results, it was decided to examine the distribution characteristics over the range of 10-600 Td. In each case, the electric field was applied from the start of the simulation. Though the actual field in the RPND has a finite rise and fall, the use of an impulse field exacerbated non-equilibrium characteristics of the EEDF. Therefore, the results of these PIC simulations would overestimate deviations from equilibrium solutions of the Boltzmann equation.

Helium gas was used as the background gas and was kept at a pressure of 2.0 Torr for all simulations. An initial plasma was assumed to exist within the volume with a density of $1.0 \times 10^8 \text{ cm}^{-3}$. The plasma was considered quasineutral (equal numbers of ions and electrons), and was modeled with one computational particle for every 10^6 physical particles. Electrons were initialized with a thermal energy of 2.0 eV, and the helium ions were given an initial energy of 0.025 eV (equal to room temperature).

XPDPI's internal set of cross sections were used. These included: elastic scattering, atomic excitation, and charge exchange. The cross sections had a semi-empirical form which increased linearly with energy to a peak value. After the peak they declined as the logarithm of the energy, divided by the energy [127]. The spatial domain of the code was 10 cm, discretized at 1 μm intervals. The time domain of the simulation was 10 ns. This period was long enough to observe fast EEDF dynamics associated with the impulse electric field. A time step of $4 \times 10^{-13} \text{ s}$ was used to satisfy the Courant-Friedrich-Lowy (CFL) stability condition. This condition requires that particles not traverse more than one grid cell during each time step. Failure to meet this condition leads to numerical instabilities in the simulation.

BOLSIG+ was used to obtain the approximate solutions of the Boltzmann equation [119]. BOLSIG+ is a publicly available computer code which uses the two-term expansion of the Boltzmann equation to solve for the equilibrium EEDF in a given electric field. The basis for this approach is the realization that, within a uniform electric field, the distribution function can be expressed as a series of spherical harmonics. For a sufficiently small

electric field and diffusion gradient [128], the expansion can be truncated after the first two terms. This expansion begins to fail at larger fields [129] and, for the cross sections used below, BOLSIG+ failed to converge for field values greater than 1000 Td.

The solver was initialized with the cross sections for helium generated by Alves and Ferreira [130]. The temporal growth model for electrons was used, and the electron-electron collisions were neglected as a result of the low ionization fraction in the RPND (about 10^{-5}). The EEDF was calculated for a range of mean energies from 2-50 eV at intervals of 0.25 eV. EEDFs for intermediate mean energies were calculated by interpolation of EEDFs for the two closest mean energies. This process was somewhat complicated by the adaptive energy mesh used by BOLSIG+ necessitating the use of a triangle-based cubic interpolation method [107].

These same energies were used to determine equivalent Maxwell-Boltzmann distributions for comparison. The EEDFs generated by the PIC simulations, approximate Boltzmann solutions, and Maxwell-Boltzmann distributions can be seen in figure 5.2, as a series of contour plots on a logarithmic scale. The jaggedness of the PIC simulations results from the finite number of particles in the system and the low probability of high energy electrons. This problem is ameliorated at higher electric fields where the probability of high-energy electrons increases. It is also helped by the ionization processes which begin to occur after the first few nanoseconds.

At 10 Td, the EEDFs are relatively unchanged over the duration of the simulation. The subtle slopes of the contours suggest a small increase in the overall temperature and energy of the system as a function of time. This is more noticeable at 30 Td, where the contours have a more distinct slope. The spacing between the slopes is relatively constant for each case—equivalent to a Maxwell-Boltzmann distribution. However, there is some deviation at low energies in the case of the BOLSIG+ solutions.

At 60 and 100 Td, the PIC results begin to exhibit contour spacings which are consistent at low energies, but begin to grow at higher energies. This is evidence of a growing pop-

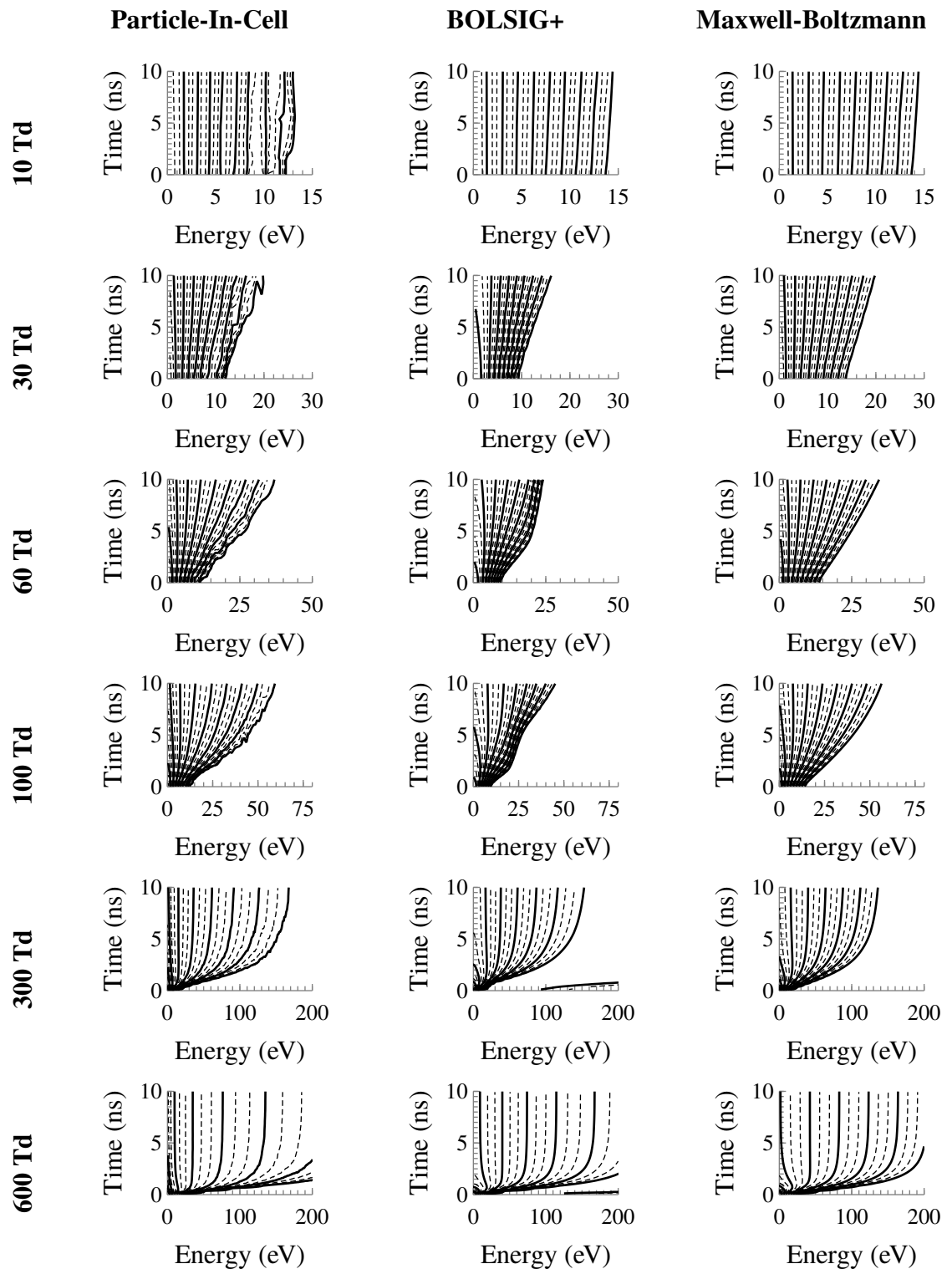


Figure 5.2: Contour plots of the EEDFs determined from PIC simulations, and the corresponding Maxwell-Boltzmann distributions for a range of electric fields.

ulation of high-energy electrons, in excess of what is predicted by a Maxwell-Boltzmann distribution. Interestingly, the BOLSIG+ solutions exhibit unique contour shapes which are inconsistent with the other cases. Additionally, the spacing of the contours is less consistent, with a dearth of high energy electrons.

By 300 and 600 Td this situation is reversed, as the Maxwell-Boltzmann distributions exhibit a smaller population of high energy electrons when compared to the PIC simulations. Examination of the individual distributions shows that the PIC EEDFs have a larger population of low energy (less than 20 eV) and high energy (greater than 100 eV) electrons. This can be explained by the general shape of the cross sections. The only reactions available to electrons in the PIC simulations are elastic scattering, excitation (19.6 eV threshold), and ionization (24.6 eV threshold). As the inelastic processes turn on at energies in excess of the 20 eV, the electron population undergoes depletion. Likewise, the electron population begins to rebound at higher energies as the cross sections fall off.

In the previous work by Starikovskaia and Starikovskii [61], it was shown that strong electric fields in a nitrogen FIW (600 Td) could produce an EEDF with an elevated number of high-energy electrons relative to the two-term approximation. However, it was also noted that the two-term approximations showed reasonable agreement at weaker field strengths. This is similar to results presented here for helium, there was no similar comparison to the Maxwell-Boltzmann distribution. Notably, the Maxwell-Boltzmann and the PIC simulations showed better agreement at electric fields of 100 Td and below. Conversely, the BOLSIG+ and PIC results are more consistent at the higher fields values, particularly for energies greater than 100 eV.

Of the three methods used to generate the EEDFs, only the PIC simulations are strictly valid in the strong field limit. This suggests that the PIC EEDFs are the most representative of the EEDFs found in the RPND. While time-dependence of the PIC results prevents their direct inclusion in the rate coefficient calculations, they can be used to judge the relative merits of the BOLSIG+ solutions compared to the Maxwell-Boltzmann distributions.

While the two-term expansion shows greater agreement in the high-energy tail, the Maxwell-Boltzmann distribution was used in the global model. This assumption was made as the improved agreement from the BOLSIG+ solutions only became apparent at fields values of 300 Td or greater—near the upper limit of the expected fields in the RPND. In contrast, the Maxwell-Boltzmann distributions proved to provide better agreement at the lower electric fields and mean electron energies.

5.1.3 Energy Equation

With an EEDF, the rate coefficients in equation 5.2 can be calculated. However, as was seen in figure 5.2, the distribution function changes over time. Previously, the PIC simulations were used to determine the time evolution of the mean electron energy, but an alternate approach was required for the global model.

Recall, from Chapter 2, the energy equation,

$$\frac{\partial}{\partial t} \left(\frac{3}{2} p_\alpha \right) + \nabla \cdot \frac{3}{2} (p_\alpha \vec{u}_\alpha) + p_\alpha \nabla \cdot \vec{u}_\alpha + \nabla \cdot \vec{q}_\alpha = \frac{\partial}{\partial t} \left(\frac{3}{2} p_\alpha \right) \Big|_{\text{coll}}. \quad (5.4)$$

Given the assumptions underlying the global model, it can be modified to calculate the evolution of the electron temperatures in the RPND. First, per the assumption of a homogeneous system, the spatial derivatives can be neglected,

$$\frac{d}{dt} \left(\frac{3}{2} p_e \right) = \frac{d}{dt} \left(\frac{3}{2} p_e \right) \Big|_{\text{coll}}. \quad (5.5)$$

Subsequently, the ideal gas law can be used to relate the pressure of the electrons to their energy density,

$$\frac{d}{dt} \left(\frac{3}{2} n_e k_B T_e \right) = \frac{d}{dt} \left(\frac{3}{2} n_e k_B T_e \right) \Big|_{\text{coll}}. \quad (5.6)$$

The term on the RHS is the collision operator which expresses energy gained or lost by

electrons¹ in particle collisions.

Several different types of energy transfer were considered by the global model. The first was the heating caused by the electric field. This was followed by electron energy losses as a result of elastic scattering by the atoms. Finally, inelastic collisions with all helium states through $n = 4$ were considered. Together, these phenomena replace the term on the RHS of equation 5.6 with,

$$\frac{e^2 n_e E(t)^2}{m_e k_m(T_e) N_g} - n_e k_m(T_e) N_g \left(\frac{3m_e}{M} \right) \frac{3}{2} k_B(T_e - T_g) - n_e \sum_i \sum_{j \neq i} K_{ij}^e N_i \Delta \varepsilon_{ij}, \quad (5.7)$$

where $E(t)$ is the time-varying electric field, k_m is the electron momentum transfer frequency from Pack et al. [131], and $\Delta \varepsilon_{ij}$ is the energy lost or gained by the electron in atomic (de)excitation reactions. The first term includes the DC conductivity [90] of the plasma, and accounts for the heating of the electrons by the electric field. The second term is the elastic cooling of the electrons by the neutral atoms, where the gas temperature. The third term is the energy gained or lost by the electrons in atomic (de)excitation reactions. The equations 5.7, 5.6 and 5.2 form the primary components of the global model. Together they can be used to solve for the evolution of the electron temperatures, electron densities, excited state densities, and plasma emissions as functions of time.

¹In some plasmas, it is desirable to also treat gas heating with a similar equation as it can have an appreciable impact on certain rate constants. However, as noted in Chapter 4, the gas temperature of the RPND in question remains at room temperature.

5.1.4 Model Solutions

For the purposes of computation, equation 5.2 can be rewritten for each atomic state, i , resulting in a set of linear, first order differential equations,

$$\begin{aligned}
 \frac{d}{dt} \begin{pmatrix} N_1 \\ N_2 \\ \vdots \\ N_M \end{pmatrix} &= n_e \begin{pmatrix} -\sum_{j \neq 1} K_{1,j}^e & K_{2,1}^e & \dots & K_{M,1}^e \\ K_{1,2}^e & -\sum_{j \neq 2} K_{2,j}^e & \dots & K_{M,2}^e \\ \vdots & \vdots & \ddots & \vdots \\ K_{1,M}^e & K_{2,M}^e & \dots & -\sum_{j \neq M} K_{M,j}^e \end{pmatrix} \cdot \begin{pmatrix} N_1 \\ N_2 \\ \vdots \\ N_M \end{pmatrix} \\
 &+ \begin{pmatrix} 0 & K_{2,1}^o & \dots & K_{M,1}^o \\ 0 & -\sum_{j < 2} K_{2,j}^e & \dots & K_{M,2}^o \\ \vdots & \vdots & \ddots & \vdots \\ 0 & 0 & \dots & -\sum_{j < M} K_{M,j}^e \end{pmatrix} \cdot \begin{pmatrix} N_1 \\ N_2 \\ \vdots \\ N_M \end{pmatrix} \\
 &+ N_g \begin{pmatrix} -\sum_{j \neq 1} K_{1,j}^a & K_{2,1}^a & \dots & K_{M,1}^a \\ K_{1,2}^a & -\sum_{j \neq 2} K_{2,j}^a & \dots & K_{M,2}^a \\ \vdots & \vdots & \ddots & \vdots \\ K_{1,M}^a & K_{2,M}^a & \dots & -\sum_{j \neq M} K_{M,j}^a \end{pmatrix} \cdot \begin{pmatrix} N_1 \\ N_2 \\ \vdots \\ N_M \end{pmatrix},
 \end{aligned} \tag{5.8}$$

where M is the total number of atomic states and $\varepsilon_i < \varepsilon_{i+1}$. An additional equation can be added to separately account for electrons as and electron-specific processes, however the global model used here assumed quasineutrality by enforcing the relation $N_{\text{ion}} = n_e$. Changes in the density of each atomic state were calculated by numerical integration of these equations. A fourth order Runge-Kutta integration scheme with a time step of 5 fs was used to solve the equations. Solutions with a time step of 2.5 fs produced results with less than a 0.1% difference from the 5 fs case. The full code listing and a description of its methods is presented in Appendix C.

The initial metastable densities came from the LAS measurements while the initial elec-

tron densities were determined from LCIF measurements made by Weatherford [121]. Electron density measurements were only available for 1.0, 4.0, and 8.0 Torr; therefore, the global model analyses only consider these conditions. Sensitivity to changes in the initial electron density will be addressed in the following section.

It was necessary to assume a pre-pulse electron temperatures as no such measurements were available. The 1 ms period between pulses is sufficiently long such that the electrons lose much of their energy. Therefore the initial electron temperature was expected to be significantly less than the 1-5 eV which is characteristic of low temperature plasmas. As a starting point, an initial temperature of 0.2 eV was assumed. Subsequent simulations varied this value between 0.1 eV and 1.0 eV, but the resulting metastable densities changed by less than 1%. Following this observation, all simulations used 0.2 eV as the initial electron temperature.

The relatively long period of time between pulses was assumed to be sufficient for the excited states (excluding ions and metastables) to reach equilibrium with the electron population. Therefore, the initial densities of excited states were calculated from their values in equilibrium with the measured electron densities at a temperature of 0.2 eV. The gas temperatures for all of the global model simulations were fixed at 300 K.

Even though the waveform of the applied potential is known, the actual time-evolution of the electric field at the metastable measurement points is not well known. This is a result of the distinctly nonlinear impedance of the RPND plasma. Takashima et al. performed measurements of the electric field in a FIW using a capacitive probe and found it to be significantly different from the vacuum field. Separately, Ito et al. [79] and Müller et al. [80], measured the electric fields in a RPND with a 1.2 mm gap between parallel electrodes using a wave-mixing approach. They too found a large difference between the vacuum field and the actual field.

In all three cases, the evolution of the electric field could be best described by a Gaussian-like pulse, followed by a small, persistent electric field. This persistent field was on the order

Table 5.1: Nominal simulation parameters for the 4.0 Torr operating condition.

Pressure (Torr)	Initial Electron Density (m^{-3})	Pulse width (ns)	Peak Electric Field (Td)
4.0	5.36×10^{13}	40	207

of 20-25% of the peak field value, and would remain for at least several tens of nanoseconds. The total duration and magnitude of the persistent field varied between studies, though some, such as Anikin et al. [132], did not find evidence of it. Given the uncertainty associated with the nature of this persistent field, the global model simulations only considered a single Gaussian pulse. The time domain of the simulations covered 190 ns with the peak of the pulse centered at 40 ns.

5.2 Perturbation Study

It was difficult to predict the sensitivity of the metastable density predictions produced by the global model to variations in the input parameters. Given the lack of knowledge regarding the electric field, the sensitivity of the results to changes in it were of particular interest. Therefore, three simulations were run for four different input parameters: peak electric field, pressure, pulse-width, and initial electron density. One simulation used a nominal value, while the other two varied this value by $\pm 10\%$. Each parameter was varied independently in order to isolate its effects.

The nominal values for the simulation were determined by a preliminary fit of the global model results to the measured metastable densities at 4.0 Torr. The fit was accomplished by iterative changes to the electric field and the pulse-width until the metastable density trend and magnitude matched the measured results. The resulting nominal values are recorded in table 5.1.

Figure 5.3 illustrates the metastable trends for each of the varied parameters. The dotted line indicates the case where the nominal value has been increased by 10%, and the

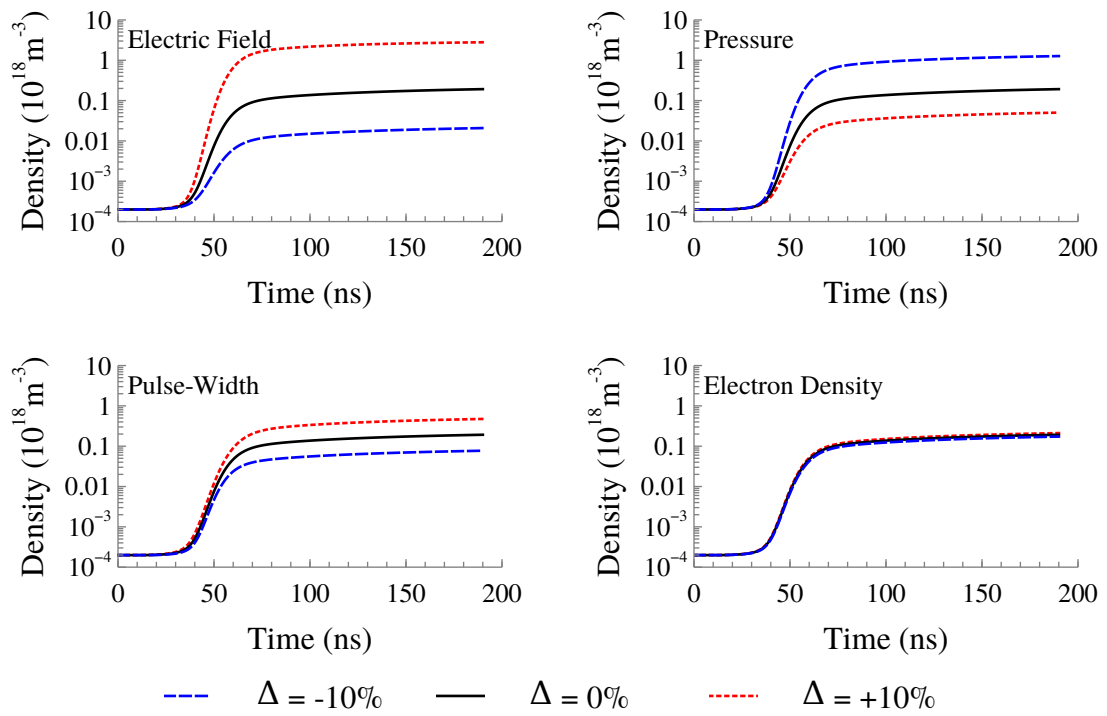


Figure 5.3: Simulations showing the effects of perturbations to the initial conditions on the metastable dynamics.

dashed line is used where the nominal value has been decreased by 10%. The metastable trends suggest that the initial electron density has a relatively small impact on the metastable dynamics. Closer examination reveals that the final metastable densities change by approximately $\pm 10\%$, almost one-to-one with the initial electron density. In contrast, changes to the pulse-width produce much more significant changes in the metastable densities. As the pulse-width is increased, the metastable densities increase. As the electric field was fixed for these simulations, this change can be attributed to the increase in energy deposited in the electron population.

The two most influential factors in the determination of the metastable densities were the neutral gas pressure and the electric field. The perturbations to these quantities resulted in largest changes in the final metastable densities. As can be seen in figure 5.3, increases in pressure corresponded to a decrease in metastable densities. Changes to the neutral gas pressure tend to affect the system via several different mechanisms. As seen in equation 5.7, increases to the gas pressure tend to decrease the energy deposited in the electrons, and increases losses due to elastic scattering. This reduces the energy that can be deposited in excited states. However, the reduced electron energy density competes with the increased number of ground state atoms available for excitation. The perturbation results indicate that the reduced energy deposition in the electrons is more significant than the increased availability of neutral atoms.

The large influence of the electric field can be traced back to changes in the ionization rate for each condition. As seen in figure 5.4, the magnitude of the ionization rate coefficient corresponds to the magnitude of the electric field. While the changes are somewhat modest, as seen in Chapter 2, ionization processes exponentially with time. This means that small changes to the rate coefficient manifest as large differences in the final electron density. Since the rate of metastable generation is proportional to the electron density, large changes to the electron density equate to large changes in the metastable density.

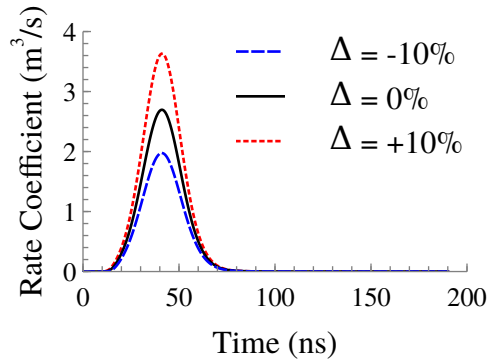


Figure 5.4: Ionization rates coefficients corresponding to the perturbed electric field simulations.

5.3 Plasma Dynamics

The plasma dynamics for the 1.0, 4.0, and 8.0 Torr conditions were obtained by matching the simulated metastable densities to the measured metastable densities. This was accomplished by iterative adjustments to the pulse-width and the peak electric field. As mentioned earlier, despite the fact that the input voltage pulse shape and amplitude are known, the plasma acts as a nonlinear circuit component which can either broaden or shorten the pulse.

The matching process was complicated by the fact that multiple combinations of the peak field and pulse-width could produce the same final metastable density. Therefore, it was necessary to establish a method by which a unique combination of the two values could be determined. Fortunately, each combination was found to have slightly different shape in the metastable density trends.

This effect can be seen in figure 5.5 where 10 separate simulations were run with different combinations of peak electric fields and pulse-widths. Each simulation produced the same final metastable density, however the shorter pulse-widths (and higher electric fields) corresponded to increasingly sharper increases in the metastable density during the applied pulse. Despite this, the behavior of the metastable density after the pulse is largely the same, regardless of the applied electric field.

It is immediately apparent from figure 5.5 that the shorter pulse-widths do not pro-

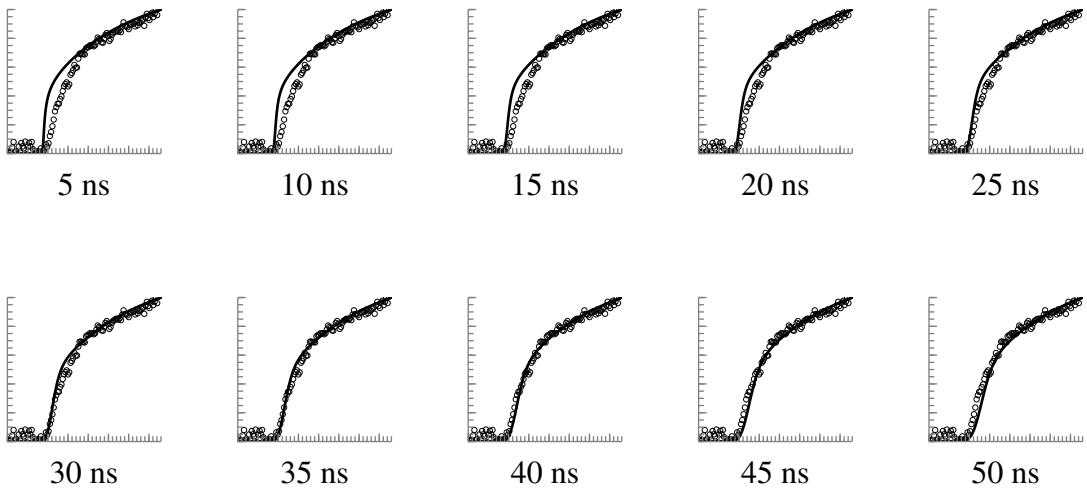


Figure 5.5: Comparison of measured metastable values (open circles) to simulations (solid lines) for a range of pulse-widths.

vide the best fit to the observed data. This conclusion includes the results for the 25 ns pulsedwidth, a result which was somewhat unexpected as the width of the applied voltage pulse was no longer than 25 ns. As previously mentioned, the photodiode used in the laser-absorption measurements had a response time of 5 ns, well below the observed rise time of the metastables.

The best fit to the measured results was obtained for a simulation with a pulse-width of 40 ns. Though this value provided the best fit to the data, there was no obvious physical mechanism associated with it. The long duration suggested that additional or extended excitation may occur within the RPND. A survey was made of the neutral emissions spectra in search of the origin of this extended excitation. The specifics of these measurements will be discussed in more detail in Chapter 6. The emissions for each transition were expected to follow the same basic trend: an initial rise correlating with the voltage pulse, followed by a monotonic decay. However, several transitions exhibited trends that differed from this. The evolution of the 4^1P^o - 2^1S transition at 396 nm was a good example of this deviation and is reproduced in figure 5.6. Here the emissions for each operating condition have been overlaid

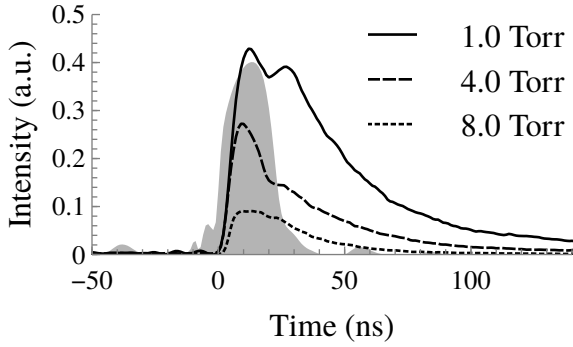


Figure 5.6: The emissions of the 4^1P^o - 2^1S transition in the RPND, overlaid on top of the voltage pulse.

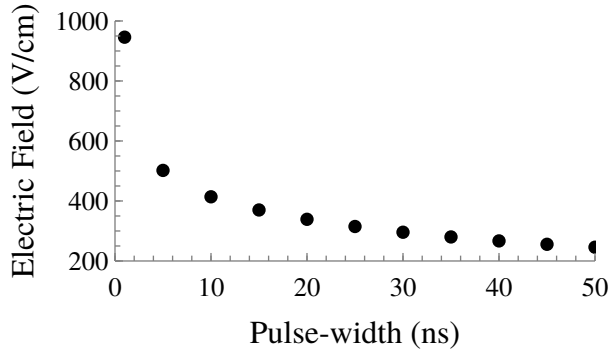


Figure 5.7: The electric fields necessary to generate the same metastable density at 4.0 Torr as a function of the pulse-width.

on the applied voltage pulse for comparison. The voltage pulse clearly coincides with an initial increase in the number of helium atoms occupying the 4^1P^o state. 15 ns later, another increase is visible, particularly at 1.0 and 4.0 Torr. This second transient is similar to the return strokes observed in streamer research [34, 36, 133]. The observation of return strokes in similar studies [19, 75, 134] suggests that this is a reasonable explanation for the double-peaked emissions. If the forward and return strokes possess durations equal to the applied voltage (25 ns), separated by 15 ns, then the excitation period would be approximately 40 ns. This is consistent with the pulse-width required to match the observed data. As a result, a pulse-width of 40 ns was used in all subsequent simulations.

Figure 5.7 is a scatter plot of the peak electric fields necessary to obtain the same final

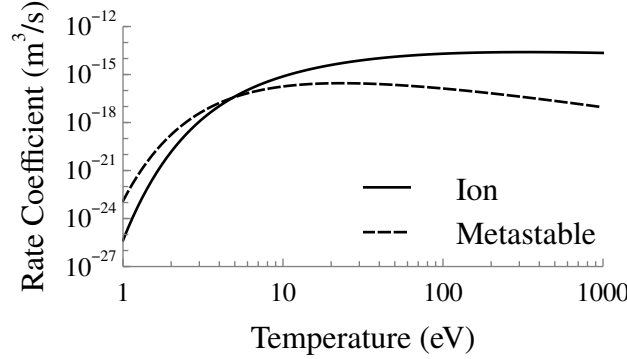


Figure 5.8: Ionization and metastable rate coefficients as functions of electron temperature.

metastable density as a function of the pulse-width. Initially, as the pulse-width is decreased from 50 ns, only small increases of the electric field are required to obtain the same number of metastable atoms. However, as the pulse-width is decreased further, the rate at which the electric field must increased grows substantially.

Eventually, for short enough pulses, it is no longer possible to maintain the same metastable density, regardless of further increases in the electric field. This occurs for the same reason that the EEDF from the PIC simulations was depressed between 20 and 100 eV—eventually, the cross sections fall off with increasing electron energy. This places an upper limit on the rate coefficient as a function of electron temperature and a limit on the number of metastables which can be generated for a given period of time.

Figure 5.8 shows the ionization and metastable rate coefficients as functions of electron temperature. The ionization rate coefficient peaks at approximately 320 eV, while the metastable rate coefficient peaks much lower at around 23 eV. The disparity in the peaks is a result of the shape of the cross sections. The ionization cross section peaks just past 100 eV while the peak metastable cross section occurs at its threshold value, 19.8 eV. These rate coefficients suggest that there is an optimal field strength for ionization and excited state generation. Increases past this field strength would reduce the final density of these particles. However, there may be additional benefits in the use of a higher electric field. The runaway electrons which are generated at these field strengths, as described by Vasilyak et

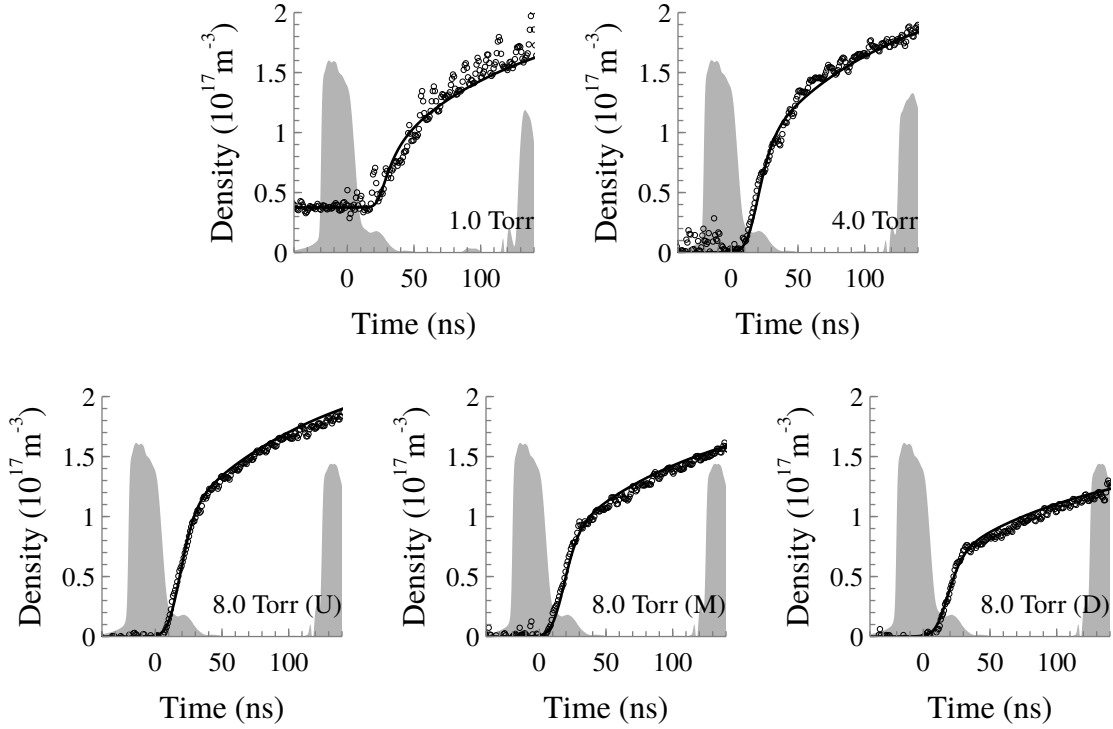


Figure 5.9: Comparison of the measured metastable densities (open circles) to the global model simulations. The shaded region illustrates the measured voltage pulse. The parentheses following the 8.0 Torr labels indicate the axial location of the measurement: U - upstream, M - midstream, and D - downstream.

al. [19], Starikovskaia and Starikovskii [61], and others, can deposit their energy far from the accelerating field. This could potentially result in an increased discharge volume which would be advantageous in processing applications.

Figure 5.9 shows the comparison of the measured metastable densities for 1.0, 4.0, and 8.0 Torr overlaid atop the applied voltage pulse². As seen in chapter 4, there was little axial variation in the metastable measurements at 1.0 and 4.0 Torr. For this reason, simulations were conducted only for the measurements at the midstream positions. In contrast, the axial distribution of metastables showed noticeable variation at 8.0 Torr. Therefore, each location was considered independently in the simulations.

Despite the assumptions involved in the development of the global model, the simulation

²The relative timing of the metastable measurements and the voltage pulse are approximate. Corrections were made in post-processing to account for different cable lengths in the system.

results show impressive agreement with the measurements. This includes the period of 0-40 ns when the metastable growth rate is the largest. The plasma behavior during this time is dominated by energetic electrons that have been accelerated by the large electric fields. Given the relatively short period, inter-atomic and radiative processes are relatively unimportant. However the radiative processes are an important source of metastable atoms in the post-pulse period as the electron population cools.

The most significant discrepancies appear in the 1.0 Torr simulations where the global appears to overestimate the metastable density during the pulse, followed by an underestimate after the pulse. While it is difficult to determine given the noise in the measurements, this condition appears to require a pulse-width *wider* than the 40 ns used in the other simulations. More evidence of this exceptionally broad excitation period is discussed in the following chapter.

Figure 5.10 shows the evolution of the estimated electron temperatures in the system, overlaid on the applied electric field. At 4.0 and 8.0 Torr, the electron temperatures show a relatively modest growth and fall that correspond with the electric field. The 4.0 Torr results peak at 16.3 eV and while each of the 8.0 Torr cases peak at above 11.4 eV. The cooling of the electrons through approximately 30 ns is dominated by inelastic losses to atomic states. As the electron temperatures fall so do the rate coefficients until most of the electron-related excitation processes stop. At this point, the electron cooling is dominated by elastic scattering.

Again, the results at 1.0 Torr are exceptional, in this case, for the exceptionally large values. A temperature of 80 eV is unreasonably large in the context of low temperature plasmas. This suggests that the assumptions used in the global model may be failing at this condition. This is somewhat reinforced by the electric fields were required to match the metastable measurements. As can be observed in table 5.2 where the electric field approaches 350 Td for the 1.0 Torr discharge. As observed earlier, this falls within the range of electric fields where the Maxwell-Boltzmann distribution shows a marked difference from

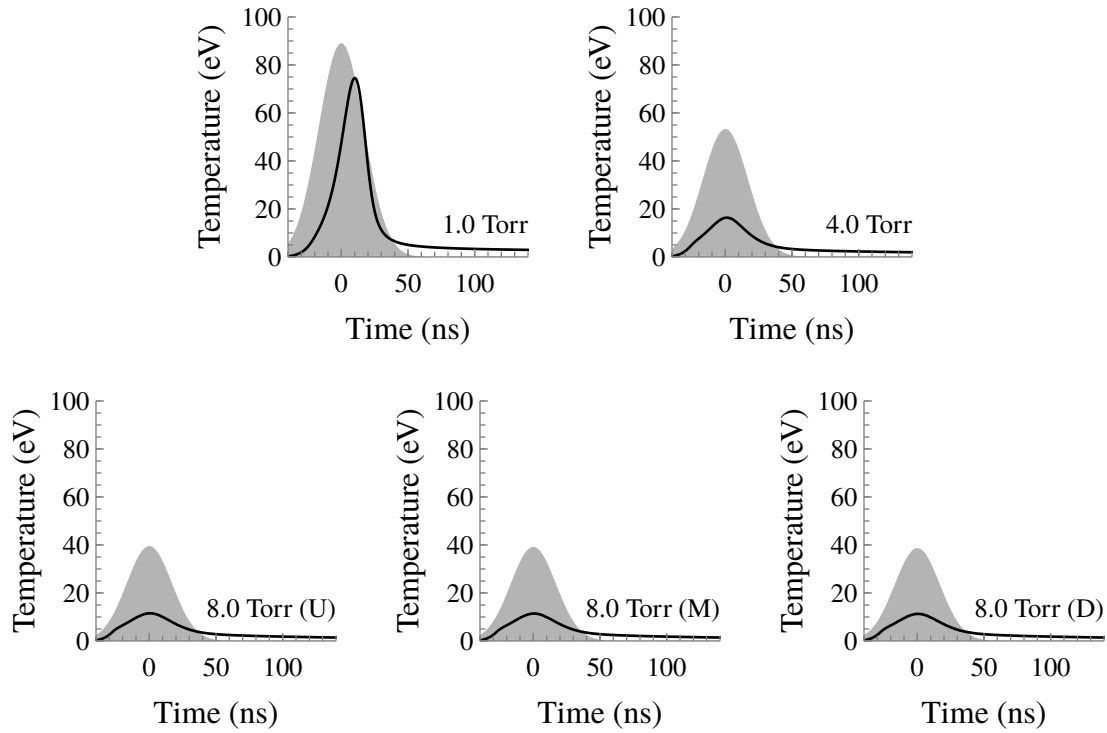


Figure 5.10: Global model predictions of the electron temperatures at the simulated conditions, overlaid on the corresponding electric field.

Table 5.2: Summary of the peak values for several plasma parameters from the global model simulations.

Pressure (Torr)	E/N (Td)	T_e (eV)	N_m (m^{-3})	n_e (m^{-3})
1.0	346	74.6	1.62×10^{17}	5.17×10^{17}
4.0	207	16.3	1.87×10^{17}	3.41×10^{17}
8.0 (Upstream)	154	11.5	1.88×10^{17}	2.60×10^{17}
8.0 (Midstream)	152	11.4	1.57×10^{17}	2.16×10^{17}
8.0 (Downstream)	150	11.3	1.21×10^{17}	1.67×10^{17}

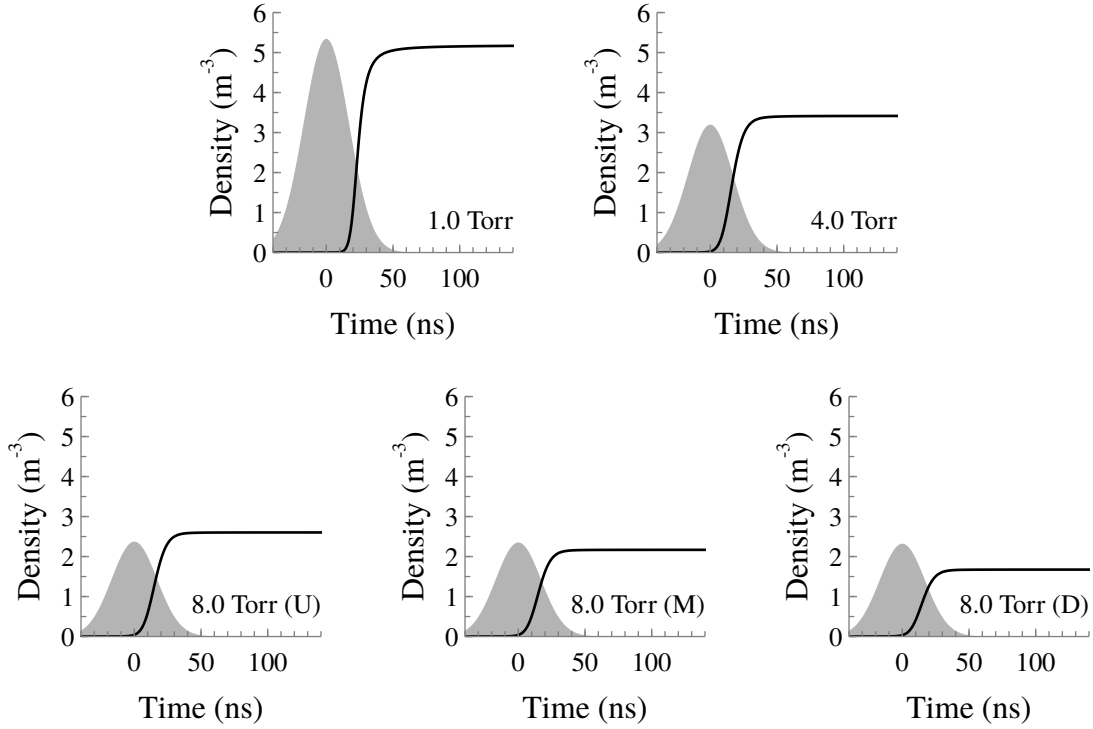


Figure 5.11: Global model predictions of the electrons densities at the simulated conditions overlaid on the reduced electric field.

the PIC predictions. As a result it is not clear that this electric field value or the electron temperature measurements can be trusted for the 1.0 Torr case.

To the extent that the results can be trusted, the table suggests that the reduced electric field falls with increasing pressure. Though this would be expected given the fixed amplitude of the applied voltage pulse, the change in the reduced field is less than what would be expected from changes in neutral density alone.

Notably, the metastable densities and electron densities peak for different conditions. The simulated electron density trends can be observed in figure 5.11 overlaid on the reduced electric fields. The electron density peaks at the lowest simulated pressure whereas the metastable density peaks at 4.0 Torr. Again, this can be seen as a result of the rate coefficients for the respective reactions. The ionization rate coefficient continues to increase well past 100 eV, whereas the metastable rate coefficient decreases after 23 eV. While the increase in

electron density competes with the decline in the metastable rate coefficient, ultimately the rate coefficient falls too quickly.

Also observable in the evolution of the electron densities is a time-delay between the peak electric field and peak electron production rate for all conditions. For the cases under consideration the peak ionization rate occurs at about 23.5 ns at 1.0 Torr, 16.4 ns at 4.0 Torr, and 15.5 ns at 8.0 Torr. In contrast, the electron temperatures in figure 5.10 show little to no such delay. In part, this behavior reflects the need for a finite amount of time before the electron population reaches temperatures for which there is an appreciable ionization rate. This delay is compounded by the relatively low seed electron densities and would likely be reduced with increased pre-ionization.

Finally, the behavior axial behavior in the 8.0 Torr condition exhibits several interesting characteristics. At the position closest to the anode, the peak metastable density exceeds that of operation at 4.0 Torr. This contrasts with the position furthest from the anode which features the lowest measured metastable density for this range of conditions. However, the electric field and electron temperatures across all three locations only vary by about one percent. This recalls the electric field sensitivity that was noted in the earlier perturbation study and suggests that even small variations in the electric field of the RPND can have large implications on its homogeneity.

5.4 Summary

The metastable density measurements provide limited insight on the development of the RPND. However, production of the metastable atoms is determined by a number of other plasma quantities such as electron temperature, density, and electric field strength. Following a series of assumptions, a global model simulation was developed in order to infer the dynamics of these other quantities. The development of the model made an attempt to evaluate the impact of the choice of distribution function. This was followed by an investigation

of the model's sensitivity to changes in various system parameters.

A comparison of several preliminary simulations to measured metastable data indicated the need for an electric field with a duration longer than applied voltage pulse. Examination of the plasma emissions showed that the extended excitation could be attributed to a return stroke in the system. Another possible explanation includes the generation and slowing of an electron beam by large electric fields. Use of this extended excitation time yielded excellent agreement for all but the 1.0 Torr condition. In this case, what appeared to be mild deviations appeared with the model overestimating metastable production rate during the pulse, and underestimating it afterward. Given the large electric fields in this condition, these discrepancies can most likely be attributed to differences between the assumed EEDF and those in the actual device.

It was found that breakdown of the RPND was accompanied by a finite delay between the peak electric field value and the peak ionization rate. As the generation of electrons is essentially exponential, this appeared to be the result of the low pre-pulse electron densities and the finite heating time. Interestingly, the peak electron and metastable densities did not coincide. Instead, highest predicted electron density occurred at the same condition as optimal energy coupling to the plasma, as seen in Chapter 3. Simultaneously, as will be seen in Chapter 6, the peak metastable density is associated with the peak brightness of the plasma, the largest number of excited states, and the highest wave velocity. These contrasting results demonstrate that the RPND can be optimized for one of two conditions: production of excited atomic states, or ionization.

CHAPTER 6

Population Kinetics

The global model was used to infer the electric field, electron densities, and electron temperatures in the RPND from the metastable measurements. However, as was described in the development of the model, it is also capable of predicting the densities of other excited states and the optical emissions of the RPND. This chapter describes the measurement of the optical emissions of the RPND and their analysis in the determination of wave velocities, electron temperatures, and the identification of other phenomena pertinent to the development of the RPND.

6.1 Emission Measurements

The emissions of the RPND were studied over the same operating conditions as the metastable measurements—for pressures from 0.3-16.0 Torr, and at three axial locations. The light from the system was collected by a optical fiber bundle, 1 cm in diameter. The bundle was positioned several millimeters from the glass envelope and no additional collection optics were used.

The other side of the bundle was aligned with the entrance slit of an ISA Jobin-Yvon SPEX HR460 monochromator. The monochromator had a focal length of 460 mm, and was fitted with a grating with 1200 grooves/mm. The entrance slit was set to $250 \mu\text{m}$, and the exit slit was set to $500 \mu\text{m}$. The specified dispersion of the monochromator was 1.76 nm/mm , therefore the approximate bandpass of the monochromator was 0.88 nm . This

Table 6.1: Table of the observed optical transitions and their transition rates.

Initial State	Final State	Wavelength (nm)	$A (s^{-1})$	$\sum A (s^{-1})$
3^3P^o	2^3S	388.97	9.46×10^6	1.06×10^7
4^1P^o	2^1S	396.59	6.95×10^6	2.52×10^8
4^3D	2^3P^o	447.28	2.46×10^7	3.12×10^7
4^3S	2^3P^o	471.45	9.52×10^6	1.60×10^7
4^1D	2^1P^o	492.33	1.99×10^7	2.70×10^7
3^1P^o	2^1S	501.71	1.34×10^7	5.80×10^8
3^3D	2^3P^o	587.73	7.07×10^7	7.07×10^7
3^1D	2^1P^o	668.00	6.37×10^7	6.37×10^7
3^3S	2^3P^o	706.72	2.79×10^7	2.79×10^7
3^1S	2^1P^o	728.34	1.83×10^7	1.83×10^7

was sufficiently large to collect the integrated emissions of a single transition, given proper positioning of the grating.

The detector was a photomultiplier tube (PMT) of model C31034. The tube voltage was set to 1900 V and was terminated into a $50\ \Omega$ resistor. Measurements demonstrated a rise time of, at most, 3.5 ns. The emissions of each line were measured from approximately $1\ \mu s$ prior to the pulse, to $4\ \mu s$ after the pulse. The time domain was chosen in order to capture all detectable emissions. The sampling rate was 1 GHz, and each emission curve was averaged over 1000 separate pulses.

The range of spectral sensitivity for the photocathode of the PMT limited measurements to transitions occurring between 350-750 nm. Table 6.1 lists the transitions which were recorded. The optical response of the system varied with respect to wavelength. This was a result of several factors, such as the fiber, the grating, and photocathode coating. An irradiance standard was used to correct for the varying spectral sensitivity of the system. The standard was an Optronic Laboratories M-1179 tungsten lamp, powered by an Optronic Laboratories OL 65 power supply. The fiber was repositioned to collect light from the lamp and the PMT signal was measured at each of the emission wavelengths listed in table 6.1.

The measured signals were then combined with the tabulated spectrum of the lamp to generate correction factors at each transition wavelength.

6.2 Wave Velocities

The breakdown of RPNDs and FIW is often described in terms of waves. This recalls the terminology used by Loeb [26] to describe the fundamental mechanisms involved. From a physical perspective, the wave is really a moving region of a large potential gradient, accompanied by significant amounts of ionization and excitation. The velocity of this wave can be measured with relative ease, using optical or physical probes, which has made it one of the most common diagnostics for these discharges [19]. A large number of factors can affect the wave velocity such as the gas, pressure, surrounding dielectric, pre-pulse electron density, and pulse shape.

The maximum detectable velocity was 5.0×10^7 m/s, and was primarily determined by the jitter in the timing of the pulser output. Additional uncertainty was introduced in the determination relative delay in emissions between the various axial locations. In order to minimize the uncertainty in the delay values, the timing was determined by the largest positive derivative of each emissions curve. However, even minor noise in the PMT signals made this approach unreliable. Subsequently, a smoothing spline was used to minimize the uncertainty introduced by the noise.

Wave velocities were calculated independently for each transition. This was necessary as some transitions exhibited much slower rise times than others. The upper states of these transitions are most likely populated by the decay of higher excited states (radiative cascade), rather than the energetic electrons associated with the wave. Despite this, the velocity estimates did not appear to possess any meaningful dependence on the transition used. As a result, the velocity estimates were averaged together in order to obtain a single estimate. The results are recorded in table 6.2.

Table 6.2: Wave velocities in the RPND.

Pressure (Torr)	Upstream Velocity (m/s)	Downstream Velocity (m/s)
8.0	$3.01 \pm 1.21 \times 10^7$	$1.73 \pm 0.26 \times 10^7$
16.0	$1.46 \pm 0.19 \times 10^7$	$6.80 \pm 1.75 \times 10^6$

Ultimately, only the 8.0 and 16.0 Torr conditions exhibited any statistically significant delay in the emission signals. For all other cases, the wave velocity exceeded the maximum detectable value. The results are comparable to other measurements made for similar discharges. The early work of Schonland and Collens [32] determined that the luminous front of lightning propagated with a velocity of 0.72 and 5.3×10^7 m/s for the forward and return stroke respectively. The studies reported by Vasilyak et al. [19] give a range of approximately $2 - 5 \times 10^7$ m/s for a 200 kV FIW in helium at pressures from 0.1-760 Torr. Propagation velocities for atmospheric plasma jets of helium have been measured at about 10^5 m/s [83] with simulations providing confirmation [85] of these values. Fast imaging by Ito et al. [79] determined a velocity of 10^6 m/s for a hydrogen RPND.

6.3 Electron Temperatures

Measurement of the electron temperature in RPNDs poses a large difficulty for several reasons. The most significant of which is the concept of temperature itself. As was noted in Chapter 5, the RPND is a highly dynamic system which does not necessarily result in a population of electrons with a Maxwell-Boltzmann distribution. In the absence of this property, the “temperature” quantity can have an ambiguous meaning. Often, reported temperatures will describe the Maxwell-Boltzmann distribution which best matches some specified plasma property (such as plasma emissions). In other cases, the temperature may describe the mean electron energy of the EEDF, such as in Chapter 5 or in the work of Starikovskaia

and Starikovskii [24].

The temperatures generated in these two cases will coincide only for a limited number of situations and certain diagnostics. Thus, it is of interest to search for useful electron temperature diagnostics which could be used for the RPND. The electron temperature of a plasma is most often determined by the use of electrostatic probes, such as Langmuir probes [90]. However, as was discussed at the beginning of Chapter 4, physical probes are not a reasonable option of the RPND. An active optical technique, such as Thomson scattering [103], would be an ideal solution if the electron densities in the RPND were not below its sensitivity threshold.

Without the option of physical probes or active spectroscopic techniques, several attempts were made to translate the measured plasma emission results to electron temperatures. Such techniques have been successful in the analysis of steady-state systems with relatively low electron densities [100], however they are subject to several limitations. The largest of these is the need for a measurable amount of emissions. However, the RPND emissions only last for a few hundred nanoseconds. The second limitation is the finite lifetime of the excited states. This places a physical limit on the time resolution of passive optical electron temperature measurements. Given these issues, the use of such techniques must be carefully considered and qualified.

6.3.1 Boltzmann Plots

The first attempt to determine the electron density of the RPND involved the use of a Boltzmann plot. When the EEDF is a Maxwell-Boltzmann distribution and the population of two excited states are in equilibrium with the electrons (partial local thermodynamic equilibrium, PLTE), the ratio of their densities and line intensities can be written as [96]

$$R = \frac{I_{i,j}N_j}{I_{i',j'}N_{j'}} \approx \frac{\lambda_{i,j}A_{i,j}g_j}{\lambda_{i',j'}A_{i',j'}g_{j'}} \exp\left(-\frac{\Delta\varepsilon_{i,j} - \Delta\varepsilon_{i',j'}}{k_B T_e}\right), \quad (6.1)$$

where I is the line intensity, N is the density, the subscripts represent different electronic states, λ is the transition wavelength, A is the spontaneous transition rate, g is statistical degeneracy, and $\Delta\epsilon$ is the energy separation between the identified states. As can be seen, this ratio only depends tabulated physical quantities for helium and the electron temperatures.

This ratio can be transformed to obtain the relation

$$\log \left(\frac{I_{ij}\lambda_{ij}}{g_j A_{ij}} \right) \propto -\frac{\Delta\epsilon_{ij}}{k_B T_e}. \quad (6.2)$$

Therefore a plot of the logarithmic quantity with respect to the transition energy would yield a line with a slope equal to the negative reciprocal of the electron temperature. The use of several lines for this Boltzmann plot obviates the need for absolute density measurements and makes for a more accurate determination of the slope of the line. However, it also extends the requirement for PLTE to additional combinations of excited states.

In order to evaluate this method, Boltzmann plots were generated for both the measured and simulated emissions data. Each set of states were assumed to be in PLTE. At each time step, a line was fitted to the data with a least-squares algorithm, and the electron temperature was calculated. This produced the temperature estimates seen in figure 6.1. The limited intensity of the plasma emissions prevented temperature estimates for the experimental data soon after the pulse. Even after the emission intensities rose to adequate values, the electron temperature estimates appeared to provide poor results for the duration of the measurement period. Peak temperatures, relative to the actual results from the global model simulations, were underestimated by at least a factor of ten, if not more.

This disagreement is not altogether unexpected. Even in the ideal case of electron with a fixed temperature, PLTE only occurs after each electron has undergone many collisions with atoms in the gas. The changes in electron temperatures of the RPND occur too rapidly for this kind of equilibrium to occur. This is true, not only for the actual RPND operation, but the simulation as well.

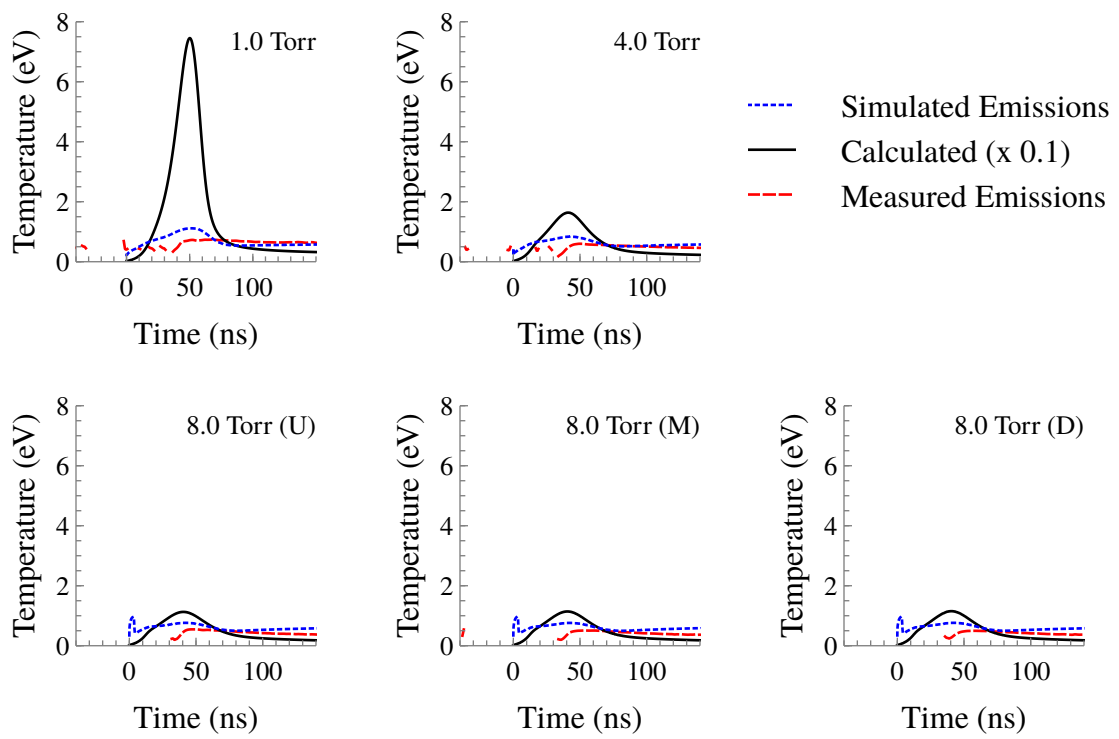


Figure 6.1: Temperatures estimated using Boltzmann plots of the measured emissions (dashed, red lines) and simulated emissions (dotted, blue lines) compared to the simulated temperatures (solid, black line).

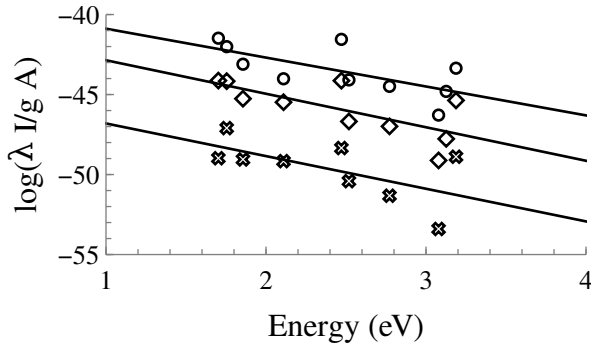


Figure 6.2: Boltzmann plot examples for the RPND. Open symbols represent the measured values and the solid lines are the corresponding best fits.

Based on this reasoning, it might be expected that the validity of the Boltzmann plot approach would improve as the time increased. While this is eventually true, it does not appear that the RPND afterglow ever reaches the point where all the states associated with the measured transitions reach PLTE. For the results shown, the Boltzmann plots for the measured and simulated emissions continue to under-predict the electron temperatures well into the afterglow. This reflects Kunze's statement that "one always has to check if indeed the assumption of a Boltzmann distribution is justified ..., equilibrium may not be reached even if the steady-state conditions seem to indicate that." [100]

Given this analysis, Boltzmann plots appear to be poor indicators of the electron temperatures within an RPND. Though the results may improve as the time after the pulse increases, it is possible that the emissions will fall below detectable limits well before PLTE applies. This is emphasized by an examination of the individual Boltzmann plots, figure 6.2, obtained from the measurements. The open symbols represent the measurements for three different times (circles - 50 ns after the pulse, diamonds - 1 μ s, crosses - 2 μ s), and the straight lines are the best fits to the measured data. While the trends are consistent between data sets, none appear to have the linear trend which would be expected for PLTE. Furthermore, while the electron temperatures should be different for the wide range of times presented, the estimates only range from 0.5-0.55 eV.

6.3.2 Coronal Model

The failure of the PLTE assumption indicates the need for a different model in the determination of the electron temperature. One such model is the coronal model. In this case, the excited states are all assumed to be generated by electron collisions with ground state atoms. However, these excited states decay by optical emission. This model excels at electron low densities where states are not subject to a great degree of mixing and inter-atomic collisions can be neglected [100]. As with PLTE, it is not immediately clear that these assumptions hold for the RPND.

Per Kunze [100], the line intensity ratio resulting from the coronal model may be expressed as

$$\frac{I_{i,j}}{I_{i',j'}} = \frac{\lambda_{i',j'} A_{i,j} \sum A_{i'} K_{0,i}(T_e)}{\lambda_{i,j} A_{i',j'} \sum A_i K_{0,i'}(T_e)} \quad (6.3)$$

where the sum is over all possible radiative decay pathways, the subscript ‘0’ is the ground state, and K is the rate coefficient. Note that the rate coefficients are explicitly functions of the electron temperature. As with the global model, the rate coefficients must be calculated from the interaction cross sections with an assumed EEDF. For consistency, we assume that this is a Maxwell-Boltzmann distribution. The upper states used for this line ratio must be carefully chosen so as to limit sensitivity to collisional mixing of excited states. Likewise, the rate coefficient ratio should exhibit a monotonic trend with electron temperature.

Kunze and others have suggested several line ratios for use with helium, including: $4^3S - 2^3P^o$ over $4^1S-2^1P^o$, $3^3S-2^3P^o$ over $3^1S-2^1P^o$, and $4^3S-2^3P^o$ over $4^1D-2^1P^o$. The ratios with the upper state in an S subshell are attractive as they are less have the lowest energy for a given n and thus are less susceptible to collisional mixing between states of equal n [100]. However, limited emission intensity prevented accurate measurements of the $4^1S-2^1P^o$ transition. As a result, only the former two ratios were considered for analysis.

Like the other mentioned ratios, $4^3S-2^3P^o$ over $4^1D-2^1P^o$ compares a transition from the triplet manifold to one from the singlet manifold. Triplet-singlet ratios have been found to

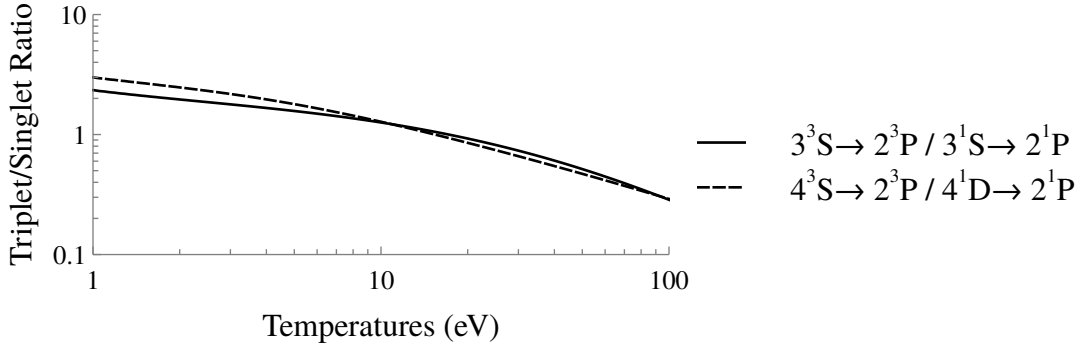


Figure 6.3: The emission ratios of $4^3S-2^3P^o$ over $4^1D-2^1P^o$ and $3^3S-2^3P^o$ over $3^1S-2^1P^o$, as functions of the electron temperature.

be mostly dependent to electron temperature which makes them ideal for this purpose [96]. Figure 6.3 shows the relation between the emission intensity of the two transitions and the electron temperature of the system. The rate coefficients were calculated with the assumption of a Maxwell-Boltzmann distribution, using the cross sections produced by Ralchenko et al. [125].

These calculations for the triplet-singlet ratios were used to estimate the electron temperature from the simulated emissions as well as the measured emissions. As with the Boltzmann plots, the temperatures calculated from the simulated emissions represent the best attainable result with this method. The results obtained with the $4^3S-2^3P^o$ to $4^1D-2^1P^o$ ratio, seen in figure 6.4, were not promising. As before, neither the simulated nor the measured ratios proved to provide good estimates of the electron temperatures. However, unlike the Boltzmann plots, this line ratio generally resulted in an overestimate of the temperatures. The signal prior to 30 ns is marked by a large amount of spurious results. This is attributable to the very small optical signals during this time period. After 30 ns, once the emission intensities have reached relatively large values, the large variations in the temperature estimates disappear.

Based on the curve for this ratio from figure 6.3, the high temperature estimates indicate a low value for the triplet-singlet ratio. This suggests either an excess in 4^1D states, or a

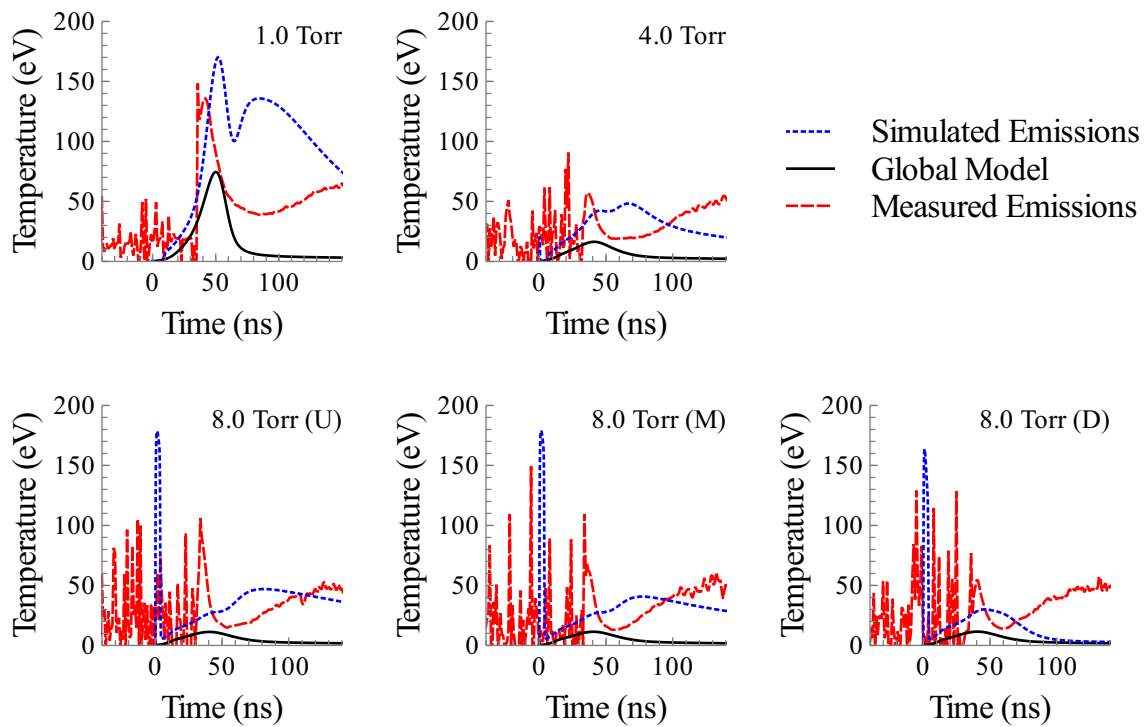


Figure 6.4: Estimates of the electron temperatures based on the ratio of the $4^3S-2^3P^o$ and $4^1D-2^1P^o$ transitions. The estimates were generated for the simulated emissions (dotted, blue lines) and measured emissions (dashed, red lines), and are compared to the actual temperature results from the global model simulation (solid, black lines).

deficit of 4^3S states. Additionally, both the measured and simulated ratios show growing or otherwise elevated temperature well after the pulse. This may be partially explained by the use of the 4^1D state for the singlet transition, an approach warned against by Kunze [100].

Also notable is the disagreement between the measured and simulated ratios. While the temperatures estimated from the measurements quickly decrease after the pulse, the temperatures from the simulations continue to rise. This situation reverses at about 75 ns when the temperature estimates from the measurements begin to rise while the simulated ones fall. The reason for this difference in behavior is not immediately clear, however Boivin et al. reported several problems with this line ratio which they attributed to the omission of $n = 5$ states from their simulations [135].

Unlike the prior line ratio, a comparison of 3^3S - 2^3P^o to 3^1S - 2^1P^o , removes the use of a D subshell for the upper level. Therefore this set of transitions should be less susceptible to collisional effects. Additionally, the lower n results in a greater energy spacing between the different subshells. For both of these reasons, this ratio should be less susceptible to collisional mixing. While the lower threshold energies make this ratio less desirable for very high electron temperatures, it was believed to be more than adequate for the RPND. This reasoning is somewhat borne out by the results in figure 6.5.

The temperature estimates based on the simulated emissions show excellent agreement with the temperatures from the global model. This does not confirm the temperature predictions made by the global model, however it does demonstrate the promise of this approach compared to the previous line ratio. The simulated emission results match both the magnitude of the values and the overall behavior of the trends. The initial increase in temperature is captured particularly well, with only moderate deviations in the afterglow. These differences are believed to be the result of the radiative cascade from higher excited states which contribute to the population of the upper excited states, mildly violating the coronal model.

Unfortunately, the experimental results do not appear to bear out the promise indicated by the simulated emissions. From a fundamental perspective, this temperature estimate

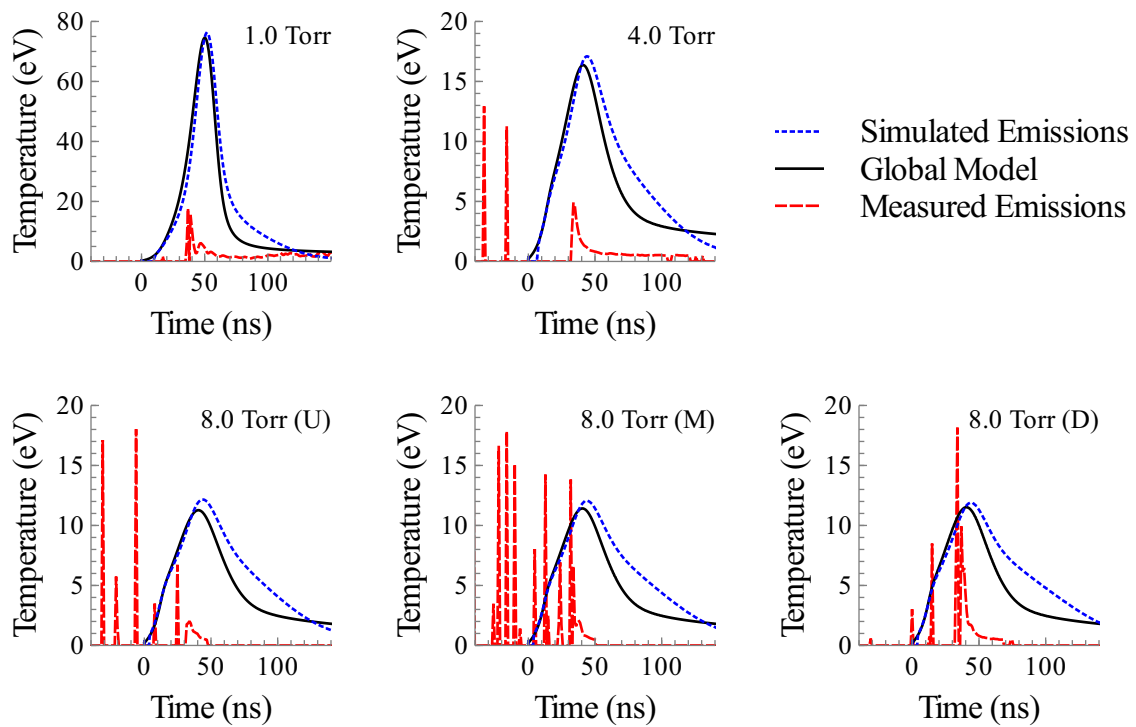


Figure 6.5: Estimates of the electron temperatures based on the ratio of the $3^3S-2^3P^o$ to $3^1S-2^1P^o$, transitions. The estimates were generated for the simulated emissions (dotted, blue lines) and measured emissions (dashed, red lines), and are compared to the actual temperature results from the global model simulation (solid, black lines).

is based on predictions which assume a Maxwell-Boltzmann distribution, an assumption which may not be valid for the RPND. That said, while the results from figure 6.5 may not correspond to an equilibrium EEDF, they can provide a relative comparison of mean electron energies.

Aside from the possible complications introduced by the distribution assumptions, estimates using this line ratio were also impacted by experimental difficulties. The two transitions occur at wavelengths to which the PMT is noticeably less sensitive. As a result, the absolute intensities of these lines were particularly low. This led to substantial uncertainties in the line ratios, particularly for times prior to 30 ns and, to some extent, afterward.

Of the available data, the two transitions were most intense at 4.0 Torr. As a result, this represents the most accurate measurements of the line ratio in described cases. In contrast to the temperatures produced by the global model, the 4.0 Torr emission measurements suggest that the temperature peaks at 4.9 eV followed by a rapid relaxation to about 0.5 eV. If accurate, the fast relaxation of the electrons suggests that additional inelastic processes should be considered by the global model. The most likely reservoir for this energy would be the excited states of molecular nitrogen which is believed to compose about 70% of the estimated 80 ppm of impurities in the system.

Given the low intensities, difficulty in obtaining accurate intensity measurements [96], and the sensitivity of the temperature estimate to the line ratio, these results should be considered quite preliminary. The use of these transitions is promising for measurements of the electron temperature in the RPND—the global model simulations show a good agreement between the estimates and the actual temperatures, and the ratio changes quickly enough to capture at least some of the RPND dynamics. That said, the use of a Maxwell-Boltzmann distribution in the line ratio calculations may need to be reconsidered. Additionally, improvements to the spectral sensitivity at these wavelengths are necessary in order to confirm the presented measurements and to better understand the discrepancies with the simulation.

6.4 Emission Comparisons

The emission curves of the simulated and experimental RPND contain a number of minor and significant differences. Likewise, some provide meaningful insight on the plasma characteristics, others are more ambiguous. For example, the greater than expected prominence of the $4^3D-2^3P^o$ transition at 447 nm may either indicate a more substantial high energy electron tail, or the need for the inclusion of $n = 5$ states. Two differences will be analyzed here, however the full set of emission measurements are presented in Appendix D.

6.4.1 Excitation Duration

As was noted in Chapter 5, several assumptions were needed to develop the global model used to simulate the RPND. Among these were the assumption that the EEDF was always a Maxwell-Boltzmann distribution, and that the applied electric field was a Gaussian function in time with a width of 40 ns. The PIC simulations as well as the results from Boltzmann plots and line ratios have already suggested that the former assumption is not rigorously true. While the electric field shape was originally inferred from the observation of a return stroke in the system, this assumption was considered in more detail via the $3^1D-2^1P^o$ transition at 668 nm.

Figure 6.6 features a comparison of the measured and simulated emissions for the $3^1D-2^1P^o$ transition over the range of simulated pressures. Both sets of results have been normalized to the maximum value of the 4.0 Torr transition so that the relative trends could be compared.

This transition was initially chosen for investigation because it was particularly prominent in both the measured and simulated emissions. Additionally, at $n = 3$, the upper state is below the maximum n considered in the global model. Therefore, the evolution of the upper state density and its emission curve reflects re-population effects as a result of radiative decay from $n = 4$. Finally, the comparative behavior of the emission curves is representative

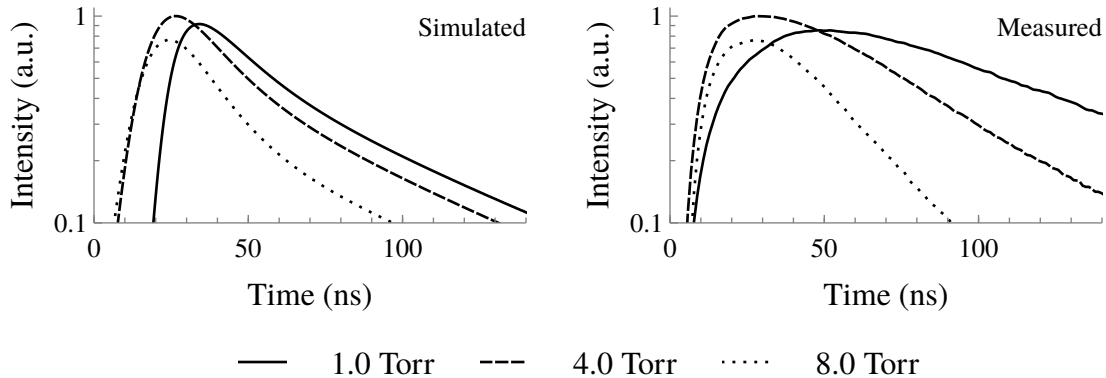


Figure 6.6: Comparison of the measured and simulated emissions from the 3^1D - 2^1P^{o} transition at pressures of 1.0, 4.0, and 8.0 Torr.

of most of the other transitions.

The simulations and the experimental measurements share a number general features. The optical intensity peaks at 4.0 Torr, followed by 1.0 Torr, and lastly, by 8.0 Torr. The relative magnitude of the optical intensities also agree for times greater than 50 ns after the pulse. Additionally, the timing of the peaks are also consistent between the two sets of data. It is interesting to note that this occurs in part because of the long delay before the onset of the emissions in the 1.0 Torr simulation.

Despite the similarities, there are several notable differences. As already mentioned, there is a significant delay prior to the appearance of emissions from the 1.0 Torr simulation. This is probably caused by the low pre-pulse electron density in the 1.0 Torr case—approximately two orders of magnitude less than the other cases. Though this value is believed to be accurate, this behavior must be reconciled with that of the observed emissions which all appear at approximately the same time.

Also observable is an apparent pressure dependence for the rate at which the measured emissions grew. At 1.0 Torr, the emissions took noticeably longer to reach their peak intensity as compared to the measurements at 8.0 Torr, or 4.0 Torr which was the fastest. This is similar to what appeared to be a relatively slow growth in the metastable density at 1.0 Torr,

as seen in figure 5.9. Again, this suggests that something unexpected is occurring at the 1.0 Torr condition. To some extent, the behavior of the emissions and the metastable densities almost appear to be the result of a broadening of the applied voltage pulse.

It may also be explained by a more beam-like EEDF with an elevated population of high-energy electrons. Interaction cross sections monotonically decline for electrons with energies greater than about 10 eV. This extends the time required for the high energy electrons to interact with the surrounding gas. Similarly broad emission curves were observed in the 0.5 and 0.3 Torr experiments as well.

Another important difference is the post-pulse shape of the curves. The simulated emissions, after reaching their peak, have decays which could be best described by a superposition of a fast and a slow component. This behavior—a fast decay following the pulse followed by a slow one, is similar to the behavior of the electron temperature from figure 5.10. It seems likely that the two are related as the fast fall in electron temperature would result in a fall of the excitation rate of the 3^1D state, reducing its emissions.

By comparison, each of the measured emission curves are best matched by a single exponential decay process. While the slow exponential decay rate of the simulated results is relatively constant across pressures, there is a distinct pressure dependence in the measured emissions. This tends to suggest some type of atomic collision process as the global model provides a relatively complete accounting for the electron collision processes. Likewise, excitation transfer processes were also considered. The next most likely candidate would be the impurities within the system which were not included in the model.

6.4.2 Radiation Trapping

Another phenomena which may alter the shape of the observed emissions is radiation trapping. The basis for this process is stimulated absorption, the same as laser-absorption spectroscopy, however radiation trapping occurs in the absence of any external photon field. Consider a photon emitted in a plasma by excited atomic state transitioning to one of lower

energy. If this photon encounters an atom in the same lower state, it stands some finite chance of re-absorption before exiting the plasma. Re-absorption would lead to the excitation of the atom and eventually the isotropic emission of a second photon [100].

This isotropic emission makes radiation trapping a random-walk process which can effectively increase the residence time of energy within a plasma. From an observers perspective, radiation trapping manifests as a longer than expected radiative lifetime. The probability of re-absorption per unit path-length is proportional to the density of the lower atomic state. Thus, as the ground state density is the highest in the RPND, radiation trapping will be most significant for transitions from an excited state to ground. This makes the ^1P states the most susceptible to trapping in a helium plasma.

As these transitions involve deep-UV emissions, they were not directly observable with the previously described setup. However, as radiation trapping results in an effective increase of the lifetime for the atomic states involved there should be a corresponding increase in the intensity and duration of other transitions involving the ^1P states. Therefore the simulated and experimental emissions for the 3^1P^o - 3^1S transition were compared. In addition, the 3^3P^o - 3^3S transition, whose upper state does not have a transition to ground, were plotted to provide a baseline for comparison.

Figure 6.7 shows the results of this comparison. As can be seen, the triplet transition shows relatively good agreement between the simulated and experimental emissions. The decay rates are comparable at 1.0 and 4.0 Torr, though there is some discrepancy at 8.0 Torr. However, a similar comparison of the results for the singlet transition reveals a very different case. The simulated emissions from the transition decay away almost immediately as a result of the large A coefficient for the 3^1P - 1^1S transition, $5.66 \times 10^8 \text{ s}^{-1}$. In contrast, the measured emissions for this state have decay rates which are generally similar to those for the triplet transition. This appears to confirm the possible effects of radiation trapping on the measured emissions.

The importance of radiation trapping has previously been considered by Compton [136]

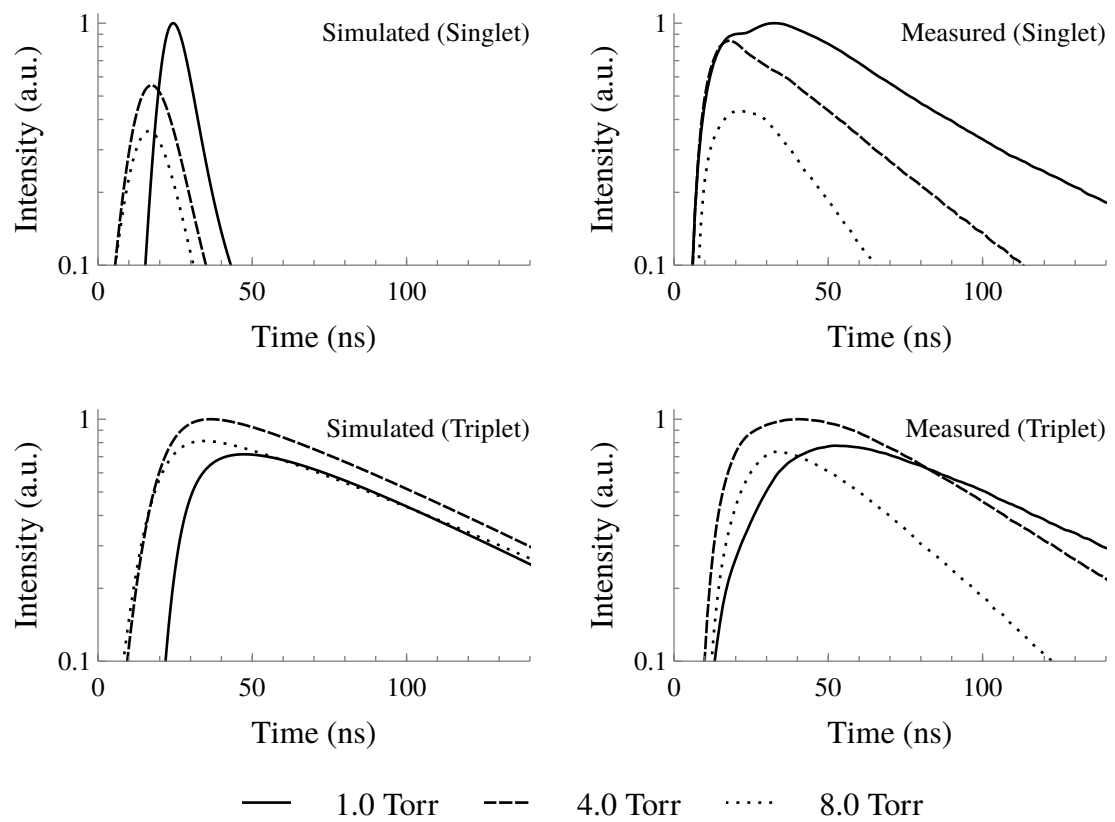


Figure 6.7: Comparison of the measured and simulated $3^1\text{P}^o - 2^1\text{S}$ and $3^3\text{P}^o - 2^3\text{S}$ emissions normalized to the most intense condition at 1.0, 4.0, and 8.0 Torr.

Table 6.3: The effective lifetimes of the $3^1\text{P}-1^1\text{S}$ transition resulting from radiation trapping.

Pressure (Torr)	Trapping Factor	Effective Lifetime (s)
1.0	8773	1.549×10^{-5}
4.0	38031	6.715×10^{-5}
8.0	78837	1.392×10^{-4}

and later by Holstein [137, 138]. Holstein's work allowed the calculation of an effective lifetime for trapped radiation in the form of the nominal radiative lifetime, multiplied by a trapping factor. The trapping factor is dependent on the geometry of the absorbing medium and the lineshape of the transition. For an infinite cylinder primarily subject to Doppler broadening, the trapping factor may be written as

$$T = \frac{k_0 R [\pi \log(k_0 R)]^{1/2}}{1.6}, \quad (6.4)$$

where R is the radius of the cylinder and k_0 is the absorption coefficient at the line center,

$$\frac{\lambda_0^3 N_1}{8\pi} \frac{g_2}{g_1} \frac{A_{21}}{\pi^{1/2} v_{\text{th}}}. \quad (6.5)$$

Here, λ_0 is the transition wavelength, N_1 is the density of lower resonant state, g is the statistical degeneracy of the upper and lower states, and A is the natural radiative lifetime. For a gas temperature of 300 K and a radius of 1.65 cm, the resulting trapping coefficients and effective lifetimes of the $3^1\text{P}-1^1\text{S}$ transition are listed in table 6.3. For comparison, the normal lifetime of this transition is about 1.77 ns. Therefore, even at these moderate pressures, energy entering the 3^1P state can remain in the system for an exceptionally long period of time. A similar conclusion may be made regarding the 2^1P and 4^1P states.

The conclusion that radiation trapping occurs within the RPND is not surprising given the relatively high pressure of operation. However, the magnitude of the phenomena is larger than expected with the effective lifetimes approaching the pulse period. The long

persistence of energy in the ^1P states at higher pressures may provide ample opportunity for collisional redistribution to one of the two metastable states. The importance of this effect will clearly grow as RPND operating pressures increase.

6.5 Summary

The active spectroscopy used to measure the metastable densities within the RPND and the subsequent modeling provided a number of insights on its development. Passive spectroscopy was then used to provide further information on the development of the discharge. Initial analysis of the emissions indicated that the wave developed with a velocity of $1.7\text{-}3.0 \times 10^7$ m/s at 8.0 Torr and $0.7\text{-}1.5 \times 10^7$ m/s at 16.0 Torr. All other operating conditions developed with velocities in excess of 5.0×10^7 m/s.

Estimates of the wave velocity were followed by several attempts to determine the evolution of the electron temperature in the RPND. This included the use of Boltzmann plots (with the corresponding assumption of PLTE), as well as line ratios based on the coronal excitation model. The Boltzmann plot method proved to be a poor and unreliable indicator of electron temperature in the system. Examination of the individual Boltzmann plots revealed that the excited states were far from PLTE. Attempts to use the ratio of the $4^3\text{S}-2^3\text{P}^\circ$ to the $4^1\text{D}-2^1\text{P}^\circ$ transition also proved to be fruitless as even the temperatures from the simulated emissions did not match the actual temperatures in the global model. Eventually the simulated emission ratio of $3^3\text{S}-2^3\text{P}^\circ$ over $3^1\text{S}-2^1\text{P}^\circ$, was shown to provide good agreement with the temperatures of the global model. However, use of this line ratio with the actual RPND was limited by experimental uncertainties.

The emissions of the RPND were further analyzed for three transitions. The measured and simulated $3^1\text{D}-2^1\text{P}^\circ$ emissions were considered because of their prominence and representative nature. General trends such as the relative emission intensities and timing of the peak intensities were consistent between the simulations and measurements. However,

several significant differences also appeared. The decay of the experimental emissions featured a notable pressure dependence which was not present in the simulated emissions. It was speculated that this resulted from collisional processes with impurities which were not accounted for in the global model. Additionally, the 1.0 Torr measurements showed an unusually extended excitation period. This trend continued to the lower pressures, and the metastable trends at 1.0 Torr appear to support the existence of an extended excitation period. The reason for this change in behavior at low pressures is not entirely clear though it was speculated to be the result of an excess in high energy electrons.

Finally, the emissions from the 3^1P^o - 3^1S transition were compared to those from the 3^3P^o - 3^3S transition in search of evidence for radiation trapping. A comparison of the measured and simulated emissions illustrated the prevalence of radiation trapping at 1.0, 4.0, and 8.0 Torr. This was confirmed by subsequent calculations of the effective radiative lifetime for the 3^1P state. Aside from the observable impact on the plasma emissions, the increased effective lifetimes of the 1^1P almost certainly contribute to additional metastable excitation as well as ionization. The importance of these effects should increase with the RPND operating pressure and may play an important role in maintaining the stability of the RPND between pulses.

CHAPTER 7

Conclusions

The repetitively-pulsed nanosecond discharge RPND is a low temperature plasma with several properties which make it amenable to novel applications. Some of these properties include its production of a large uniform discharge (on the order of liters), negligible gas heating, and operation over a wide range of pressures (from 10^{-3} –1 atmospheres) [24]. Though the RPND has only recently been enabled by recent advances in semiconductor technology, it shares a long history with other pulsed discharges. This includes the fast ionization wave (FIW), streamers, sparks, and lightning [26].

Despite this long history, in-depth study of these phenomena has been challenging. A review of the literature found that the important dynamics of the RPND, which can occur in a matter of nanoseconds, were not well-explored. Time-scales this short present a number of technical difficulties for plasma measurements. Separately, the high electric fields and the substantial collisionality within the RPND precludes the use of many traditional plasma diagnostic techniques. Thus, most studies have focused on measurements of the plasma properties after the pulse or averaged over the pulse.

However, as with most plasmas, the properties of the RPND are determined by the coupling between the applied electric field and the gas. As this coupling is a result of fundamental processes which occur during the nanosecond pulse, such as electron acceleration and collisional excitation, the RPND can not be understood without more detailed consideration of the dynamics which occur during its initial phases.

7.1 Overview of Results

The over-arching goal of the study, then, was to elucidate the flow of energy from the electric field, through the electrons, to the gas, during the formation of the RPND. This was subdivided into several complementary measurements and simulations. The energy input was characterized through current-voltage characteristics and energy coupling measurements. This was then followed by measurements of the excited atomic state dynamics with passive and active spectroscopic techniques. Finally, the results were compared to estimates produced by a global model of the RPND.

The process of accomplishing these goals, began with the development of the theories necessary to describe the RPND. Specifically, the Boltzmann equation and Maxwell's equations, were used as the starting point of the theoretical analysis. Several reductions of the Boltzmann equation were presented in the form of moments. These moments averaged over the velocity space of the probability distribution in order to simplify the solution of the equations.

Following this, the criteria for a plasma were presented. A plasma is distinct from an ionized gas in the sense that its behavior is dominated by its electromagnetic properties. Thereafter, the initiation of a plasma from one or a few seed electrons was explained for the two primary cases. The first, the Townsend mechanism, occurs for relatively small electric fields, long periods of time, and does not involve the formation of appreciable space charge. In contrast, the streamer mechanism, involves a high electric field, develops over a shorter period of time, and is influenced by the formation of large regions of space charge.

It is the properties of the streamer mechanism which bear the most resemblance to the RPND. However, the streamer model does not automatically account for the uniform nature of the RPND. Instead, this was described by the work of Levatter and Line [3]. They demonstrated that a streamer can develop in a uniform manner provided a sufficient density of pre-pulse electrons. Calculations for the subsequent experimental conditions found that the natural background electron density was sufficient to guarantee uniform breakdown at

all operating pressures.

As the plasma measurements were focused on spectroscopic quantities, this was followed by a explanation of atomic structure and notation. Afterward, several factors affecting the spectral lineshape of atomic transitions were discussed. The theory concluded with a brief description of stimulated absorption by atoms, the cross section for interaction, and the concept of saturation.

Subsequently, an experimental RPND was described. It was generated by repetitive positive voltage pulses in ultra-high purity helium at several different pressures. The discharge geometry was of a coaxial design similar to the FIW studies reviewed by Vasilyak et al. [19]. Visual observations and the ease with which breakdown was obtained suggested that the plasma was most stable at a pressure of 4.0 Torr. However, estimates of the energy coupling from the current-voltage measurements indicated that greatest energy coupling occurred at 1.0 Torr, with a peak value of 5.5 mJ. This was consistent with previous experimental measurements of the energy coupling in RPNDs and FIWs.

Laser-absorption spectroscopy (LAS) of the 2^3S , or triplet metastable, state of helium was the primary means by which the nanosecond discharge dynamics were measured. This technique produced measurements of the temperature and line-integrated density of the triplet metastable state over the duration of the pulse. The triplet metastable level was investigated because it can act as a large energy reservoir in helium discharges and can increase the charged particle population via associative ionization and Penning ionization. The use of an active optical diagnostic, meant that the time resolution of the measurements were only limited by the bandwidth of the detector, 5 ns.

The results of the LAS confirmed that no gas heating was occurring in the RPND. The accuracy of the temperature measurements varied with respect to the metastable density, but was generally about ± 50 K. The largest detected line-integrated densities, prior to the reflected pulse, occurred for the 4.0 Torr condition at a value of about $5.9 \times 10^{16} \text{ m}^{-2}$. Assuming a uniform density distribution across the discharge tube, this is equivalent to a den-

sity of $1.8 \times 10^{17} \text{ m}^{-3}$. A significant number of metastable atoms persisted between pulses for pressures of 1.0 Torr and lower.

There were no observable trends in the metastable densities with respect to axial location for pressures of 4.0 Torr and lower. This provides additional confirmation of the homogeneous and volume-filling nature of the RPND. In contrast, results at 8.0 and 16.0 Torr showed a clear decline in metastables densities as a function of distance from the anode. This is believed to be akin to the wave attenuation in FIWs, described by Vasilyak et al. [19].

Long duration measurements of the metastable densities revealed the primary decay processes in this discharge geometry. Metastable destruction at low pressures was dominated by associative ionization; indicated by deviations from a purely exponential decay. As the pressure of the system was increased, the three-body reaction (leading to the formation of helium dimers) became the dominant destruction process. Decay constants significantly larger than those reported by Deloche et al. [116] and Phelps and Molnar [104] suggest that gaseous impurities played a significant role in metastable destruction.

A global model was then developed in order to infer various other plasma parameters from the metastable measurements. The development of the model included an analysis of the likely electron energy distribution functions (EEDFs) in the RPND with a series of zero-dimensional particle-in-cell (PIC) simulations. For fields of 100 Td and less, the PIC simulations showed good agreement with Maxwell-Boltzmann distributions of the same mean electron energy. However, above 300 Td, the Maxwell-Boltzmann distributions exhibited significantly fewer high-energy (greater than 100 eV) electrons.

It was speculated that this disagreement stemmed from the behavior of the interaction cross sections. In general, these cross sections peak at several times the threshold value, after which they rapidly decline. At the high electric fields, the electrons can reach the energies associated with these reduced electric fields, resulting in a higher-than-expected population of high-energy electrons. Better agreement with the PIC simulations at these

field strengths were obtained with solutions of the two-term expansion of the Boltzmann equation which can account for the cross section variation with energy. However, as a result of significant disagreements at lower electric fields, the global model assumed a Maxwell-Boltzmann distribution for the entirety of the simulations.

The global model simulations which best matched the measured metastable density trends required the use of an exceptionally long electric field, 40 ns in length, compared to the 25 ns length of the applied pulse. Upon inspection of the optical emissions from the plasma, a return stroke was identified that appeared to explain this longer-than-expected excitation. Based on previous results in FIW research [21], an alternative explanation was also proposed in which a beam-like electron population formed in the RPND and its relaxation was responsible for the extended excitation.

Using the long excitation period with the global model produced an excellent match to the measured metastable densities, both during the pulse and afterward. Particularly good agreement was obtained at 4.0 and 8.0 Torr conditions. Small deviations were observed at 1.0 Torr—the metastable density appeared to rise too quickly during the pulse, and too slowly after the pulse. This provided a second hint that energetic electrons may be present in the system, specifically at the lower pressure conditions.

This was reinforced by the magnitude of the electric fields and inferred electron temperatures necessary to match the metastable densities. At 1.0 Torr, the peak electric field was 346 Td and the peak electron temperature was estimated at 74.6 eV. This suggests that the global model is likely inaccurate for this condition given the disagreement between the Maxwell-Boltzmann distribution and the PIC simulations at field values over 300 Td. Additionally, the electron temperature is far in excess of what can be considered reasonable for an equilibrium population of electrons in a low temperature plasma.

In contrast, the global model predictions at 4.0 and 8.0 Torr were better aligned with previously reported values. The electron temperatures are similar to those recently obtained for a FIW [87], as well as those predicted from rate coefficient calculations [112]. Likewise,

the electric fields are more reasonable than those predicted at 1.0 Torr, though they fall in the intermediate region between 100 and 300 Td.

Interesting to note was a delay between the peak electric field and the highest ionization rate in the plasma. This was interpreted as the time required for the seed electron population to reach ionization-relevant temperatures. In a simplified system, the ionization rate is an exponential function of time, thus the density grows quickly thereafter.

Emission measurements of ten separate transitions in the visible wavelengths were used to measure the wave velocities of the RPND. While the rate of rise of the emissions depended on the transition, the wave velocity estimates remained largely the same. In the RPND the measure velocities were: $1.7\text{-}3.0 \times 10^7$ m/s at 8.0 Torr, and $0.7\text{-}1.5 \times 10^7$ at 16.0 Torr. All other conditions had wave velocities that were greater than 5×10^7 m/s.

The global model was designed to consider a total of 32 different species and 535 different reaction processes, including optical transitions. This allowed the evaluation of several potential optical diagnostics for electron temperature and an opportunity for comparison with results from the measured emissions.

This began with an attempt to determine the evolution of the electron temperature from a series of Boltzmann plots. The Boltzmann plots from the simulated emissions and measured emissions both resulted in temperature estimates of about 0.5-0.6 eV. However, the temperatures estimated from the simulated emissions were not consistent with the temperatures produced by the global mode simulations. This indicated that there was likely a fundamental flaw in the assumptions used to determine electron temperatures from Boltzmann plots.

The reason for this lies in the assumption of partial local thermodynamic equilibrium in the plasma. This requires that the excited state populations used in the Boltzmann plot are in equilibrium with the electrons [100]. However, the RPND likely develops too rapidly for this equilibrium to take place. This conclusion was reinforced by an examination of the individual Boltzmann plots for a series of times after the pulse.

Subsequently, an attempt was made to determine the electron temperature via a coronal model and the use of line ratios [96]. As with the global model, this approach requires the assumption of an EEDF. Subsequently, the accuracy of the results will depend on how closely the EEDF in a RPND adheres to the assumed one.

For consistency with the global model, a Maxwell-Boltzmann distribution was used. The use of this assumption likely produced estimates of the electron temperature that were not accurate with respect to their absolute magnitude. However, as long as the shape of the EEDFs are consistent for the duration of the measurement period, the results will be proportional to the some mean energy. This allows an evaluation and comparison of the relative temperatures in the RPND.

Overall, three line ratios were considered however one was immediately rejected for lack of detectable emissions. The second, which compared the 4^3S - 2^3P^o transition to the 4^1D - 2^1P^o transition was used with little success. The estimates based on the measured emissions produced unrealistic temperatures. Additionally, the estimates from the simulated emissions were not consistent with the actual temperatures from the global model, suggesting that this particular ratio was not suitable for temperature estimates.

The second line ratio which compared the 3^3S - 2^3P^o transition to the 3^1S - 2^1P^o transition produced more promising results. The estimates from the simulated emissions were consistent with the global model temperatures, which demonstrated that the line could potentially work provided the global model results are applicable. However, the estimates from the measured emissions were less successful. For most points in time, the two transitions were too dim to obtain a reliable ratio. In the cases that a temperature could be estimated, the results indicated a peak electron temperature of about 5 eV, followed by a quick cooling to 0.5 eV. As the coronal model relies on the assumption of a Maxwell-Boltzmann distribution, this approach will almost certainly produce misleading and incorrect results at pressures of 1.0 Torr and below.

Additional comparisons were made between the simulated and measured emissions for

the 3^1D - 2^1P^o transition, at 1.0, 4.0, and 8.0 Torr. Some general features, such as the timing of the peak intensity, and the relative intensities between pressures were consistent between the two. However the simulated emissions generally decayed away faster after the peak intensity as compared to the measured emissions. This suggested a prolonged excitation period in the RPND, again hinting at the presence energetic electrons.

Furthermore, the decay rate of the measured emissions had a noticeable pressure dependence. This suggested an atomic process was responsible, one which was not accounted for in the global model. The metastable measurements suggested that Penning ionization of impurities was an important loss mechanism. As a result, it is believed likely that the 3^1D state was also affected by collisions with gaseous impurities. This would explain the pressure dependence observed in the measured emissions.

Finally, the effects of radiation trapping in the RPND were investigated as another possible source of extended excitation. Observable effects of radiation trapping were confirmed by a comparison of the simulated and measured emissions from the 3^1P^o - 2^1S transition. Subsequent calculations showed that the effective lifetime of the 3^1P^o - 1^1S transition could be extended by a factor of nearly 10^5 for the geometry in question. The increased residence time of this energy increases the chance that it may be transferred to another excited state or lead to ionization via collisions. This suggests that radiation trapping in the RPND may lead to an increase in the excited state and charged particle densities, similar to the metastable states.

In summary, this work identified several key characteristics of the RPND based on spectroscopic measurements and modeling. Several processes affecting the charged particle population and energy residence time in the RPND were identified. In addition, several anomalies were noted at the analysis of the data at 1.0 Torr and below, indicating a high degree of non-equilibrium and the potential presence of beam-like electrons. Finally several approaches to the measurement of electron temperature trends were evaluated for their application to similar experiments.

7.2 Future Work

There are several opportunities to improve on the work presented here. From an experimental perspective, the metastable density measurements could be improved by the use of a more sensitive detector. This would decrease the minimum detectable metastable density and potentially provide pre-pulse metastable densities for the other operating pressures. It would also be desirable to revisit the existing metastable density measurements along various chords of the discharge cylinder. This would provide radial density profiles via inversion techniques.

The emission measurements could also stand to be improved by the use of a more efficient grating, a more efficient photocathode, or both. These changes should be made with measurement of the 706 and 728 nm lines in mind, as these appear to be the most promising for transitions for use in optical electron temperature measurements. Further improvements to the optical temperature measurements could be made with the development of an appropriate collisional radiative model and perhaps the use of alternative EEDFs in the calculation of the rate coefficients.

The experiment could also be improved with the relatively simple addition of a capacitive probe for sensing of the electric field within the plasma, similar to that used by Takashima et al. [87]. The electric field measurements would allow for confirmation of the return stroke which was observed in the emissions data. The probe may also be used to determine if a persistent electric field exists after the pulse.

The electric field information could then be incorporated into the global model for more accurate predictions of the RPND properties. Other improvements to the global model would include the addition of gas impurities and reactions in response to the evidence that they contribute to the RPND dynamics. Furthermore, the global model should be modified to include radiation trapping effects for resonant transitions.

However, the global model is still fundamentally limited in how it handles the EEDF within the RPND. This may be improved, to some extent, by the inclusion of a Boltzmann

solver. That said, the investigation of the EEDFs suggests that the two-term expansion may not be sufficient for the fields in the RPND. Another possibility is the use of a Boltzmann-like distribution where $f(\varepsilon) \propto \exp(-\varepsilon/k_B T_e)$, where α can be varied to obtain a distribution with a suitable high-energy tail.

Alternatively, a zero-dimensional PIC model could be used, similar to the one which was employed in the EEDF calculations. It should be possible develop such a code with the inclusion of the improved cross sections of Ralchenko et al. [125] as well as the optical transitions from Kramida [102], with suitable alterations to account for trapping effects. This approach would neatly sidestep the EEDF issues, however there is the concern that this may lead to an excessively demanding computational problem. Some simplification could be accomplished using a hybrid method or by only using PIC calculations above certain field values.

7.3 Final Remarks

The experimental and simulation results presented represent one of the few comprehensive attempts to analyze the nanosecond timescale dynamics of a RPND. Several mechanisms, including the dynamics of the metastable population and radiation trapping, have been identified which may influence the evolution and stability of a helium RPND. In addition, evidence has been provided for beam-like electrons at low operating pressures, and the effects of impurities on the lifetimes of excited states.

Each of these phenomena represent an important component of how the nanosecond pulse couples energy into a gas. In turn, it is the energy in that gas—the electrons, ions, excited states, internal fields, and photons, which lends the RPND its ability to purify water [12], sterilize surfaces [13], alter air flow [14], and generate nanoparticles [15]. It is only through an improved understanding of how this energy is distributed in a plasma that applications, such as these, can be realized.

APPENDIX A

Measurements in an Air RPND

As early as 2001, researchers have proposed the use of a novel, hybrid engine design for use in supersonic and hypersonic flight [139]. In some ways similar to an earlier program [140], it suggested that magnetohydrodynamic (MHD) accelerators were an enabling technology for hypersonic transport. Briefly, a MHD accelerator could be used to simultaneously produce energy and slow the inlet airflow. This would allow the use of a conventional turbojet engine at speeds well above its normal operational range.

However, MHD accelerators require an ionized fluid flow. Even at the high altitudes associated with hypersonic flight, this is not easy to achieve. Originally, Macheret suggested the use of electron beams, carefully tuned to coincide with the peak in the ionization cross section in air. However, the use of electron beams in the ionization of high pressure gases is accompanied by a large number of technical issues, similar to those of some excimer lasers. Therefore, in 2002, Macheret et al. proposed the use of a RPND to produce an “electron beam” *in situ* [64] akin to the beams observed in certain FIW studies.

The use of a RPND is accompanied by a reduced ionization efficiency in comparison to an electron beam. However, it reduces the some of the implementation challenges and Macheret argued that it offered a more efficient and stable option than breakdown with DC electric fields. Though the densities of FIWs in several air-related chemistries have been measured on several occasions [63, 112, 132, 141], similar studies do not appear to exist for RPNDs in air. Therefore, there is a need for electron density measurements to confirm that

RPNDs are adequate for the MHD accelerator requirements and to quantify their ionization efficiency.

In addition, previous studies of FIWs in air have observed fast gas heating of molecular systems [109]. Up to 40% of the input energy can be converted into translational energy through dissociation of oxygen and quenching or electronically excited nitrogen states. As the RPND physics are very similar to that of the FIW, there is the possibility that it may also cause fast gas heating. In combustion, this can play an important role in the chemistry, flame holding, and ignition delay. More generally, gas heating can impact material processing and ionization efficiency. As such, it is important to develop reliable temperature diagnostics for RPNDs in molecular gases.

This appendix records the development of two diagnostics for an air RPND at NASA Glenn Research Center (GRC). Measurement of the electron density was accomplished using millimeter-wave interferometry. Plasma interferometry measures changes in the phase and amplitude of an electromagnetic wave which has passed through the plasma [90]. The phase shift is proportional to the density of electrons while the change in amplitude is related to the electron-neutral collision frequency. As with other wave-based techniques, the density resulting from this approach is line integrated. The translational temperature of the system was measured via

Translational temperatures were measured by analysis of the rotational spectra associate with the second positive system of nitrogen. Rotational spectra result from changes in the rotational quanta of a molecule. As the energy spacing of the rotational levels is generally quite small (often on the order of 10^{-4} eV), inter-molecular collisions can easily redistribute them [142]. Provided enough collisions, the distribution of rotational states should reflect the distribution of translational energy for the molecules.



Figure A.1: Vacuum chamber used in RPND experiments at the NASA GRC along with an intensified CCD used for fast imaging.

A.1 Discharge Apparatus

Experiments were conducted in a cylindrical vacuum chamber, reproduced in figure A.1, with a volume of approximately 30 L. The chamber was evacuated by a Varian TriScroll 300, scroll pump and the pressure was monitored by a capacitance manometer. Before each experiment the chamber pressure was reduced to below 100 mTorr, after which the chamber was sealed from the pump by a bellows valve. The chamber was then back-filled with ambient air until the pressure reached 20.0 Torr.

The discharge was sustained between two parallel cylindrical electrodes, 2.5 cm in diameter and 0.625 cm in length. In the interferometry experiment, the electrodes were mounted in a silicone-based dielectric epoxy, cast such that it was flush with the faces of the electrodes. Optical emission experiments eliminated the dielectric epoxy in favor of a machineable ceramic and slightly different geometry, seen in figure A.2. This choice was made as a result of damage observed to the epoxy molds. Plasma breakdown appeared to be occurring at the interface of the mold and the electrodes. The use of the Mykroy fitting allowed longer duration operation necessary for the optical emissions measurements.



Figure A.2: The electrodes used in the RPND at NASA GRC. The electrodes are made of copper with a ceramic sheath made of Mykroy.

The power supply was built by FID (model FPG 60-100-MC4-S5) and supplied voltage pulses of up to 60 kV at repetition rates from 6-100 kHz with pulsedwidths of 5 ns. Unless otherwise stated, all measurements were made with the power supply operating at 20 kHz using a Wavetek FG3C as the master clock.

Maintenance of the electrodes and other components of the discharge apparatus required that the chamber volume regularly be brought up to atmospheric pressure. When the discharge was initiated after the chamber was returned to the 20.0 Torr operating pressure, a pressure transient was observed. This transient caused the chamber pressure to rise by about 2.0 Torr after several minutes of operation, after which the pressure would remain relatively stable. This was believed to be caused by the outgassing of the discharge apparatus surfaces. Throughout operation, the pressure would continue to increase at a greatly reduced rate, on the order of several tenths of a Torr per minute.

A.2 Millimeter-Wave Interferometry

Traditionally, plasma interferometry has been conducted with microwaves, as the electron densities in processing plasmas cause readily observable phase shifts at these wavelengths. However, results from similar RPNDs [24] suggested that the electron densities could ap-

proach 10^{13} cm^{-3} . Such densities exceed the cutoff wavelength of microwave interferometers [90]. As a result, it was necessary to use millimeter-wave (mmW) interferometry which uses much higher frequencies in order to avoid this issue.

A.2.1 Theory

The theory underlying interferometry can be found in many plasma diagnostic textbooks, however the majority of the treatments only concern plasmas in which there are no neutral particles. In contrast, the work of Akhtar et al. [143] introduces a frictional force to the derivation which accounts for the effects of neutral particles. Following this approach, the theory below provides the necessary set of equations in order to determine the electron density and collision frequency provided measurements of the mmW phase shift and change in amplitude.

The derivation begins with the motion of electron in an oscillating electromagnetic field. The position of a charged particle in such a field can be found from the non-relativistic Lorentz equation,

$$F = q(E + v \times B), \quad (\text{A.1})$$

where F is the force on the particle, q is its charge, E is the electric field, v is the particle's velocity, and B is the magnetic field. In the case of a weak electromagnetic field (such as in interferometry) the magnetic field component can be assumed to be zero. Without loss of generality, the equation may be reduced to a single dimension. Afterward, the drag force which accounts for the neutral particle collisions can be introduced. The acceleration of the electron can then be written as

$$\ddot{r} = -\frac{eE}{m} - v_{\text{eff}} m_e \dot{r}, \quad (\text{A.2})$$

where r is the position of the electron, e is the elementary charge, v_{eff} is the effective rate of momentum transfer, and m_e is the mass of the electron.

The electric field of the incident mmW can be expressed as $E_0 e^{i\omega t}$ where E_0 represents the peak field strength and ω is the angular frequency. The form of E suggests a sinusoidal solution such that $r \propto e^{i\omega t}$. Solving the differential equation for \dot{r} yields

$$\dot{r} = -\frac{eE}{m_e} \frac{v_{\text{eff}} + i\omega}{v_{\text{eff}}^2 + \omega^2}. \quad (\text{A.3})$$

This is the drift velocity of the electron. It can be used to solve for the complex plasma conductivity and, subsequently, the dielectric constant. This allows one to write the complex propagation coefficient for the mmW,

$$\gamma = \alpha + i\beta, \quad (\text{A.4})$$

where the real component, α , results in a decay of the wave amplitude. β on the other hand, induces a phase shift in the wave. The full solution for the separate propagation components is given by Akhtar [143] as,

$$\beta = \frac{\omega}{c} \left\{ \frac{1}{2} \left(1 - \frac{\omega_p^2}{\omega^2 + v_{\text{eff}}^2} \right) + \frac{1}{2} \left[\left(1 - \frac{\omega_p^2}{\omega^2 + v_{\text{eff}}^2} \right)^2 + \left(\frac{\omega_p^2}{\omega^2 + v_{\text{eff}}^2} \frac{v_{\text{eff}}}{\omega} \right)^2 \right]^{1/2} \right\}^{1/2}, \quad (\text{A.5})$$

$$\alpha = \frac{\omega}{c} \left\{ -\frac{1}{2} \left(1 - \frac{\omega_p^2}{\omega^2 + v_{\text{eff}}^2} \right) + \frac{1}{2} \left[\left(1 - \frac{\omega_p^2}{\omega^2 + v_{\text{eff}}^2} \right)^2 + \left(\frac{\omega_p^2}{\omega^2 + v_{\text{eff}}^2} \frac{v_{\text{eff}}}{\omega} \right)^2 \right]^{1/2} \right\}^{1/2}. \quad (\text{A.6})$$

From these components, explicit solutions can be derived for the electron density and ef-

fective collision frequency,

$$\nu_{\text{eff}} = 2 \frac{c^2}{\omega} \frac{\alpha\beta}{\xi}, \quad (\text{A.7})$$

$$n_e = \frac{m_e \epsilon_0}{e^2} \xi (\omega^2 + \nu_{\text{eff}}^2), \quad (\text{A.8})$$

where $\xi = 1 - (\beta^2 - \alpha^2)c^2/\omega^2$. The values for α and β come from the experimental measures of the phase shift and change in amplitude,

$$\Delta\varphi = \int_0^d (\beta_0 - \beta) dr, \quad \text{and} \quad (\text{A.9})$$

$$\Delta A = \int_0^d (\alpha_0 - \alpha) dr, \quad (\text{A.10})$$

where $\Delta\varphi$ is the phase change, ΔA is the amplitude change, d is the pathlength through the plasma, and α_0 and β_0 are free space propagation values. As any measurements are integrated over the pathlength of the system, it is necessary to make some assumption about the variation of the density with respect to the path of the wave. In this case, the density will be assumed to be constant along the path of the wave.

A.2.2 Experiment

The mmW interferometry was conducted using an HP 8510C network analyzer operating at 75 GHz. The network analyzer was controlled by a LabView script and had a maximum sample rate of 5 Hz. Each sample required approximately 100 μ s to complete.

The mmW signal was transmitted between two test sets which produced a variable frequency signal covering all of the V band (50-75 GHz). The output of each test set was connected to a high gain horn. The horns were aligned perpendicular to the axis of the discharge and transmitted through quartz windows on either side of the vacuum chamber. The horns were aligned by a maximization of the transmission through the chamber. During data analysis, the pathlength of the signal through the plasma was assumed to be 2.5

cm, however diffusion results in the transport of electrons outside of the discharge region, making this value an underestimate.

During operation, the actual pressures within the vacuum chamber varied from 19.9 to 22.6 Torr. The power supply was operated in a bipolar mode with one electrode pulsed to +9 kV and the other pulsed to -9 kV. Previous interest in the use of a DC sustainer discharge [65] prompted an investigation of the effects of the sustainer on the time-averaged electron density. The sustainer consisted of a pair of floating electrodes, perpendicular to the RPND. The sustainer electrodes were held at a potential difference that was slightly less than the DC breakdown voltage. The intended effect of the sustainer was to increase the time-averaged plasma density through additional ionization.

A.2.3 Results

The original intent was to obtain a measurement of the electron density as it evolved during and after the pulse. However, the acquisition rate of 5 Hz prevented acquisition of the electron density evolution for a single pulse. Instead, it necessitated measurements spanning several minutes and many thousands of pulses. This made it necessary to determine the repeatability of the plasma produced by these pulses.

This is generally not an issue in systems which feature gas flows, such as those studied by Adamovich et al. [67]. However, in this case, the vacuum chamber was sealed. This mode of operation can cause a slow accumulation of chemical species, increases in gas temperature, deposits on electrode surfaces, and more. Each of these has the ability to slowly alter the nature of the discharge and can complicate analysis of data acquired after different pulses.

Measurements were made of the electron density for a period of 30 minutes at a rate of 5 Hz. A SRS DG535 was used to trigger the network analyzer at the same delay after each pulse. Acquisition for longer periods were prevented as a result of significant electromagnetic interference EMI. The master clock was particularly susceptible to this electrical noise. This would occasionally shut off the triggering signal or alter its frequency. Several

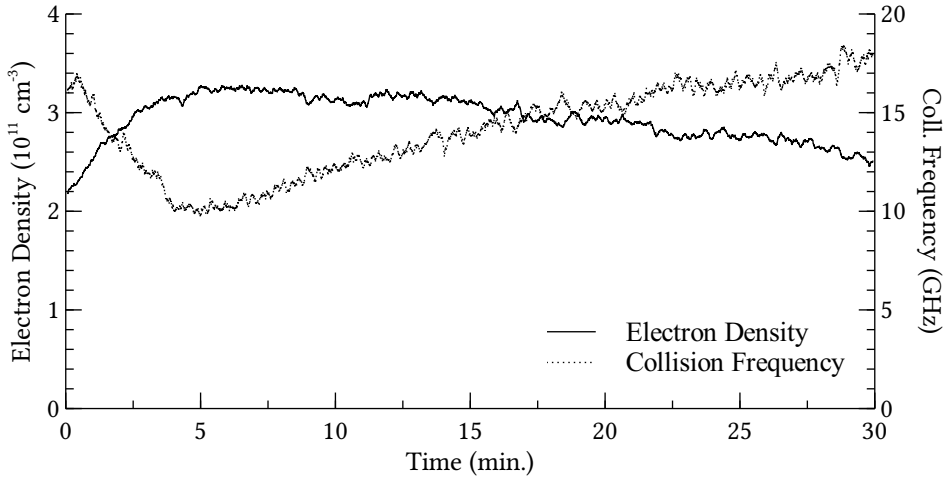


Figure A.3: The evolution of the density (—) and the collision frequency (··) in a RPND over a period of 30 minutes. These quantities reach their respective maximum and minimum after approximately five minutes, however these are not equilibrium values. The RPND continues to change over long durations.

attempts were made to limit the interference to the signal generator through shielding of the transmission cables and of the signal generator, however these attempts resulted in minimal benefit.

Figure A.3 shows the calculation of the electron densities and collision frequencies from the measured phase and amplitude changes. The data shown does not include the operation of the DC sustainer. The data appear to confirm the concern that the sealed vacuum chamber causes long-term variations in the plasma. The electron density changes by nearly 50% during the first five minutes of operation and is followed by a slow decline over the next 25 minutes. Overall, the electron density ranged from $2.25-3.25 \times 10^{11} \text{ cm}^{-3}$. This is somewhat less than the anticipated density. As previously noted, other studies in FIW discharges [81, 112, 144] measured densities well in excess of 10^{12} cm^{-3} . Separate experiments demonstrated similar electron densities. In each case, changes in the electron density occurred relatively slowly after the first ten minutes. The complex chemistry of air plasmas makes it difficult attribute the changes in electron density to a specific process. More likely is a number of subtle changes throughout the convoluted reaction chains that pertain to air

plasmas.

The collision frequency also exhibits changes on a time scale similar to that of the electron density. It begins quite high before quickly declining to a minimum, followed by a slow return to its original value. While the pressure changes by several percent over the course of operation, this is not large enough to explain the variation in collision frequency. Additionally, the trend in electron density is opposite of what would be necessary to explain the observed changes. The average electron temperature between pulses is almost certainly changing over time. The resulting changes in the interaction cross sections may be sufficient to explain the change in the collision frequency. The changes might also be explained by slow evolutions in the relative gas composition.

A.2.4 DC Sustainer

Six separate experiments were run with the DC sustainer discharge activated. In each case, the potential difference between the sustainer electrodes was fixed at 750 V. These experiments were to be compared to the result with the sustainer turned off. However, EMI caused the triggering signal generator to fail before any case could be run to completion. This makes it impossible to come to any firm conclusion on the impact of the sustainer. For the data that are available, the DC sustainer *reduced* the overall density of the RPND.

This reduction in electron density was not originally expected and should be more thoroughly investigated with a more robust apparatus. It is believed that the sustainer's predominant effect was an increased energy transfer to the excited rotational and vibrational states of the molecules.

It is believed that the sustainer may have caused increased energy transfer to the excited states of atoms and molecules, but was ineffective at increasing the electron density. Indeed, the sustainer voltage was insufficient to produce a glow discharge independent of the high voltage pulses. As such, one may conclude that it will tend to extract more electrons than it produces. This being the case, a DC sustainer may be useful in situations requiring fast

gas heating, but at the cost of a reduced ionization efficiency, followed by a slow decline over the next 25 minutes. Simultaneously, the effective collisions frequency of the electrons ranges from 10-18 GHz. Overall, the electron density ranged from $2.25\text{-}3.25 \times 10^{11} \text{ cm}^{-3}$. This is somewhat less than the anticipated density. As previously noted, other studies in FIW discharges [81, 112, 144] measured densities well in excess of 10^{12} cm^{-3} .

followed by a slow decline over the next 25 minutes. Simultaneously, the effective collisions frequency of the electrons ranges from 10-18 GHz. Overall, the electron density ranged from $2.25\text{-}3.25 \times 10^{11} \text{ cm}^{-3}$. This is somewhat less than the anticipated density. As previously noted, other studies in FIW discharges [81, 112, 144] measured densities well in excess of 10^{12} cm^{-3} .

$2.25 \times 10^{11} \text{ cm}^{-3}$ to $3.25 \times 10^{11} \text{ cm}^{-3}$. The magnitude of the electron density is somewhat less than anticipated; other papers such as [112], [144], and [81] state densities exceeding 10^{12} cm^{-3} . Separate experiments (not shown here) demonstrated similar electron densities and collision frequencies. However, the time for the system to reach its quasi-equilibrium varied and, in some cases, required 10 minutes.

The observed increase in collision frequency was, perhaps, a result of increasing pressure and gas temperature in the chamber. Meanwhile, the change in electron density may be a result of a changing chemical composition. It is not immediately clear what mechanism is responsible for this, but it is well-known that electrons will readily attach to water molecules. As they are destroyed through dissociation, the attachment rate would decline and it would be reasonable to expect an increase in electron density.

A.2.5 DC Sustainer

Six separate experiments were run with the DC sustainer discharge activated. The potential difference between the sustainer electrodes was approximately 750 V (current limited), and four experiments were run with the sustainer off (electrodes floating). Difficulties with EMI prevented a more complete evaluation of the sustainer's effect. Therefore, an abso-

lute statement on the influence of the DC sustainer is not possible. However, the available data suggest that the DC sustainer did not have an appreciable effect on the time-averaged electron density.

The use of electric potentials below the Townsend breakdown value may present a fundamental limit to the effectiveness of a DC sustainer. While the sustainer may induce additional electron avalanches in the afterglow of the RPND, the ions impacting the cathode will not produce enough secondary electrons to sustain the discharge. This will cause the discharge to eventually extinguish. Therefore, the sustainer will not increase the charged particle density, so much as extend its lifetime.

The sustainer may also be expected to increase the heating of the RPND for air plasmas. Fast gas heating has previously been observed for air RPNDs [145], and was found to primarily result from quenching of excited states and dissociation reactions. While the electric field of the sustainer is insufficient for a self-sustained discharge, the energy it deposits into the electrons generated by the RPND can still excite atoms and molecules, and also cause dissociation.

A.3 Rotational Spectroscopy

Given previous observations of gas heating in the air RPND, it was desirable to develop a diagnostic capable of detecting it for the system under consideration. The approach employed used measurements of the rotational spectra produced by nitrogen to infer the rotational temperature. The rotational temperature is generally accepted as a good measure of the translational temperature in a system, given the close spacing of the rotational energy levels [146].

This technique is subject to several limitations. Passive rotational temperature measurements can only be made when there is set of detectable rotational transitions. Additionally, temporal resolution of the technique is limited by the equilibration time between the rota-

tional states and the translation energy distribution. This is effectively the time required for several inter-molecular collisions to take place.

The measurement of rotational transitions is a common diagnostic for the measurement of gas temperatures, particularly in the field of combustion. Matching of the rotational spectra is typically accomplished with a computer program such as Specair [147] and LIF-BASE [148]. However, a survey of the available programs revealed little documentation about the calculation methods and none which provided the necessary flexibility how the spectra were generated. This necessitated the development of a program to automate the generation and matching of rotational spectra.

A.3.1 Emissions Model

The emissions model applied to the acquired emission spectra was based on previous work by Hartmann and Johnson [149] and Chelouah et al. [150]. The band examined was the (0, 0) vibrational transition of the nitrogen second positive system, $c^3\Pi_u - b^3\Pi_g$. This system features P, Q and R branches each with a number of sub-branches, determined by selection rules (Λ -doubling was assumed to be negligible). As the rotational quantum number, J , becomes large, the spin vector of the molecule is effectively uncoupled from the angular momenta, a situation known as Hund's case (b). However, for smaller J the spin vector couples with the angular momenta, forming a resultant total electronic angular momentum, a situation equivalent to Hund's case (a). In order to represent this varying degree of spin-coupling, a set of semi-empirical formulae for the rotational term values, initially suggested by Budó [151], was used. This set is represented in a simplified form by Herzberg [142] as

$$F_0(J) = B_v \left[J(J+1) - \sqrt{Z_1} - 2Z_2 \right] - D_v \left(J - \frac{1}{2} \right)^4 \quad (\text{A.11})$$

$$F_1(J) = B_v \left[J(J+1) + 4Z_2 \right] - D_v \left(J + \frac{1}{2} \right)^4 \quad (\text{A.12})$$

$$F_2(J) = B_v \left[J(J+1) + \sqrt{Z_1} - 2Z_2 \right] - D_v \left(J + \frac{3}{2} \right)^4 \quad (\text{A.13})$$

where

$$Z_1 = \Lambda^2 Y_v (Y_v - 4) + \frac{4}{3} + 4J(J+1) \quad (\text{A.14})$$

$$Z_2 = \frac{1}{3Z_1} \left[\Lambda^2 Y_v (Y_v - 1) - \frac{4}{9} - 2J(J+1) \right]. \quad (\text{A.15})$$

Here, F_Ω are the rotational term values for a given Ω while B_v and D_v are constants which depend on the vibrational state in question, and $Y_v = A/B_v$. The second positive system only concerns Π states, therefore, Λ is always equal to one. B_v and D_v were calculated using the expansions

$$B_v = B_e - \alpha_e \left(v + \frac{1}{2} \right) + \gamma_e \left(v + \frac{1}{2} \right)^2 + \dots \quad (\text{A.16})$$

$$D_v = D_e + \beta_e \left(v + \frac{1}{2} \right) + \dots \quad (\text{A.17})$$

where α_e and γ_e both represent fitting constants while the values for β_e and D_e can be calculated, per Herzberg,

$$D_e = \frac{4B_e^3}{\omega_e^2} \quad \text{and} \quad (\text{A.18})$$

$$\beta_e = D_e \left(\frac{8\omega_e x_e}{\omega_e} - \frac{5\alpha_e}{B_e} - \frac{\alpha_e^2 \omega_e}{24B_e^3} \right). \quad (\text{A.19})$$

Again, these representations require the use of measured constants such as ω_e and $\omega_e x_e$. The energy of each vibrational level was calculated using the expansion,

$$E_v = T_e + \omega_e \left(v + \frac{1}{2} \right) - \omega_e x_e \left(v + \frac{1}{2} \right)^2 + \dots, \quad (\text{A.20})$$

where

$$T_e = T_0 - \frac{\omega_e}{2} + \frac{\omega_e x_e}{4} - \dots. \quad (\text{A.21})$$

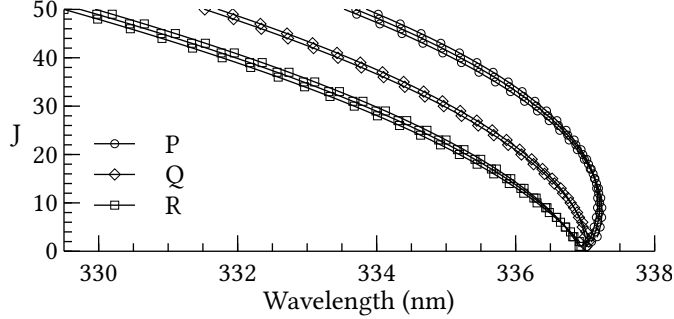


Figure A.4: A Fortrat diagram for the $(0, 0)$ transition of $c^3\Pi_u - b^3\Pi_g$. The P branch is identified by an open circle (\circ), the Q branch is identified by an open diamond (\diamond) and the R branch is identified by an open square (\square). Each branch features a number of sub-branches which can distinguished with an imaging system of sufficient resolution.

Many of the fitting constants were obtained from Laher and Gilmore [152] while the A terms for the $c^3\Pi_u$ and $b^3\Pi_g$ states were provided by Bullock and Hause [153] and Budó respectively. Figure A.4 shows the Fortrat diagram of the $(0, 0)$ transition for all final states of $J \leq 50$. The wavenumbers (in cm^{-1}) for each transition were calculated using the expressions

$$\nu_{\Omega}^P(J) = \nu_0 + F'_{\Omega}(J-1) - F''_{\Omega}(J) \quad \Omega = 0, 1, 2, \quad (\text{A.22})$$

$$\nu_{\Omega}^Q(J) = \nu_0 + F'_{\Omega}(J) - F''_{\Omega}(J) \quad \Omega = 1, 2, \quad (\text{A.23})$$

$$\nu_{\Omega}^R(J) = \nu_0 + F'_{\Omega}(J+1) - F''_{\Omega}(J) \quad \Omega = 0, 1, 2. \quad (\text{A.24})$$

Per conventions in the literature, a single prime notation indicates the initial state's rotational term value, and a double prime indicates the same value for the final state. The $\Delta J = 0, \pm 1$ selection rules are explicitly included for the rotational term values. ν_0 is the wavenumber of the head band origin, calculated from $E_v'' - E_v'$.

The individual line intensities were calculated with the assumption that excitation of the $c^3\Pi_u$ state was from $x^1\Sigma_{g;v=0}$. Furthermore, it was assumed that the rotational states were populated according to a Boltzmann distribution. Following Hartmann, the normalized line

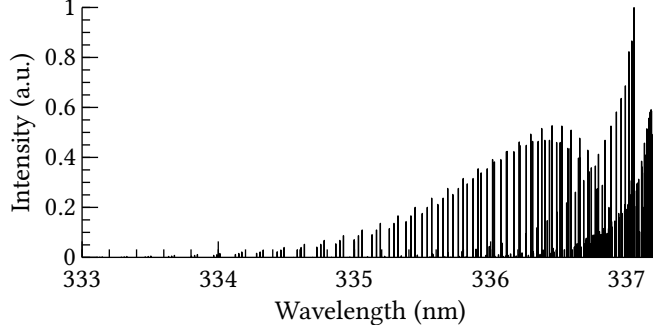


Figure A.5: A plot of the rotational lines generated by the Budó's expression for a varying degree of spin-coupling. All branches and their respective sub-branches are shown. The intensities were calculated by assuming a Boltzmann distribution and were normalized by the appropriate Honl-London factors.

intensities may be written as

$$\varphi_{\Omega}^{\alpha}(J') = \frac{S_{\Omega;J}^{\alpha}}{Q} \exp \left[-J'(J'+1) \frac{hcB_x}{kT_{\text{rot}}} \right]. \quad (\text{A.25})$$

Here, α represents the individual branches (P , Q or R), while B_x is the energy of the state $x^1\Sigma_{g;v=0}$ (1.9898 cm^{-1}) and T_{rot} is the rotational temperature of the system. Q is a normalizing factor that is equal to

$$Q = \sum_{J'} (2J'+1) \exp \left[-J'(J'+1) \frac{hcB_x}{kT_{\text{rot}}} \right]. \quad (\text{A.26})$$

$S_{\Omega}^{\alpha}(J')$ represents the Honl-London factors for each branch. They may be written as

$$S_{\Omega}^P(J') = \frac{(J'+1+\Omega)(J'+1-\Omega)}{(J'+1)}, \quad (\text{A.27})$$

$$S_{\Omega}^Q(J') = \frac{(2J'+1)\Omega^2}{J'(J'+1)}, \quad \text{and} \quad (\text{A.28})$$

$$S_{\Omega}^R(J') = \frac{(J'+\Omega)(J'-\Omega)}{J'}. \quad (\text{A.29})$$

The calculated intensities associated with $T_{\text{rot}} = 450 \text{ K}$ are shown in figure A.5. In a spectrum where the lines have been convolved with a Gaussian having a FWHM of 0.124

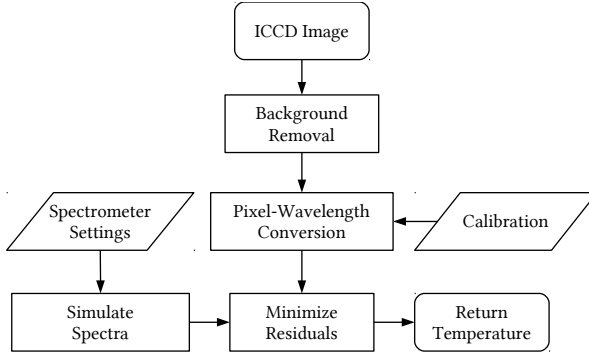


Figure A.6: Each spectrum was processed using a computer program, described by this flowchart. The only required inputs are the spectrometer settings, the CCD image and the wavelength calibrations. Each measured spectrum is compared to a number of simulated spectra in order to determine the appropriate match.

nm (not shown) a peak at 337.11 nm is observed which differs by 0.02 nm from the value cited in Lofthus and Krupenie's monograph on the nitrogen spectrum [154]. Each line was considered a δ -function, neglecting the natural linewidths.

A.3.2 Temperature Matching

The correct temperature was found by a comparison of many simulated spectra to the measured one via a computer program. An illustration of the procedure can be found in figure A.6.

The input to the program was an image from an intensified CCD. The background of the CCD was subtracted in pre-processing, however the intensifier introduced additional noise. In order to compensate for this, two areas of the image were identified as background. These regions were used to calculate the noise induced by the intensifier in the signal region. Calibrations using the mercury lamp provided a conversion from pixel position to wavelength (based on the grating orientation). All spectra were normalized to their peak intensities. The measured spectra, after post-processing, had resolutions of approximately 0.124 nm and wavelength accuracies of ± 0.02 nm.

The previously described emissions model was used to generate a series of lines and rel-

ative intensities for a range of temperatures. The intensities of each line were then linearly mapped to the wavelengths of the experimental spectrum. That is, the modeled line intensity was split between the two nearest experimental wavelengths, proportional to the proximity of the modeled wavelength. At this point, the simulated spectra were convolved with an instrument function, in this case a Gaussian with a FWHM of 0.124 nm. This width represents a best-fit Gaussian for several atomic transitions of mercury. The simulated spectra were then then normalized to their peak intensities.

Afterward, the residual sum of squares, defined as

$$S = \sum_i [I_{\text{exp}}(\lambda_i) - I_{\text{sim}}(\lambda_i)]^2, \quad (\text{A.30})$$

were calculated for each simulated spectra with a specific experimental one. A cubic spline interpolation was used to fit the residuals as a function of the temperature for each simulated spectrum. The program searched for a minimum of the interpolation, corresponding to a minimal residual. If it successfully identified a minimum, the associated temperature was considered to be the correct one. This approach was iterated over 110 images from a period just before breakdown to approximately 55 ns afterward.

A.3.3 Verification

Figure A.7 is a comparison of a measured spectrum with its match and the difference between the two. Overall, the two spectra show a high degree of similarity, however there are several places where they are significantly different. The largest discrepancy occurs around the peak of the spectra. The simulated spectrum appears to be shifted toward higher wavelengths relative to the measured spectrum. Furthermore, there are two distinct peaks at 331.00 and 333.85 nm which do not appear in the simulated spectrum. These peaks correspond to other vibrational transitions of the second positive system, (2, 2) and (1, 1) respectively. The error associated with disregarding these features during simulation is es-

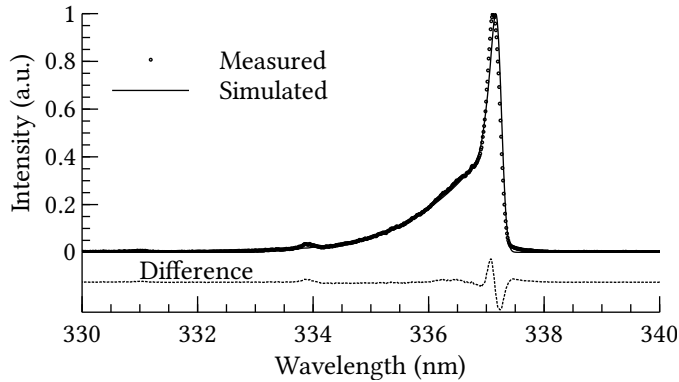


Figure A.7: A plot of a measured spectrum, the simulated match and the difference between the two. The measured spectrum is illustrated with solid circles while the simulation is represented by the solid black line and the differences are shown with a dashed red line. The peak of the simulated spectrum is shifted toward higher wavelengths when compared to the measured spectrum.

sentially fixed and should not affect the calculated temperature. It should be noted that these additional transitions could be used to determine a vibrational temperature. Finally, the measured spectrum has a distinct foot adjacent to the peak toward the higher wavelengths. This same feature is not found in the simulated spectrum and is likely the result of a non-Gaussian instrument function.

A.4 Experiment

The discharge apparatus is described in section A.1. Three operating conditions were examined, ± 4.3 , ± 6.1 and ± 7.3 kV. The optical emissions of the discharge were collected with a series of lenses, focused into a fiber and coupled to a Spex 500M monochromator by aperture matching optics. Light was collected from the entire discharge volume. The monochromator, with a 2400 g/mm grating, was used as an imaging spectrometer with the detection plane provided by a LaVision PicoStar HR intensifier connected to a LaVision ImagerQE CCD. The intensifier gate was 500 ps however the CCD integrated for a total of 2.560 ms. Therefore, as a result of operation at 20 kHz, each image was the sum of the emissions from 51 individual pulses. The wavelength response of the spectrometer was

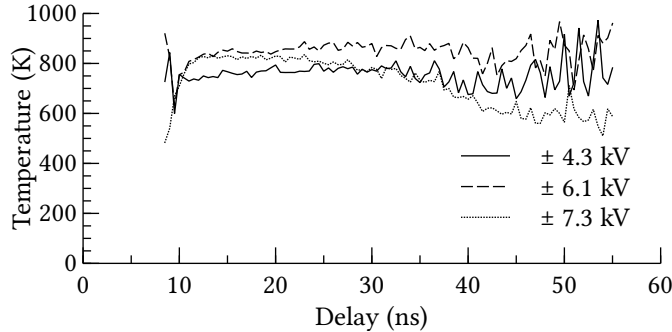


Figure A.8: Rotational temperature trends for three operating conditions: ± 4.3 (solid black), ± 6.1 (dashed red) and ± 7.3 kV (dotted blue). The first two cases exhibit significant variations near the end of the measurement period as a result of low signal-noise ratios. Only ± 7.3 kV case shows any clear trends over the duration of the measurement.

calibrated using the atomic transitions of a mercury lamp. The intensity response of the spectrometer was assumed to be flat over the range of wavelengths (approximately 16 nm) under consideration.

A.5 Results

The evolution of the rotational temperatures for varying time delays of all three operating conditions are shown in Figure A.8. Matching temperatures were not found for all time points as, in some cases, the signal was too weak to reliably measure the temperature.

The ± 7.3 kV case appears to show a consistent rise in temperature during the pulse. The signal-noise ratio is too low in the ± 4.3 and ± 6.1 kV cases to make a clear determination. Likewise, the ± 4.3 and ± 6.1 kV case show little or no decrease for the duration of observation, while the ± 7.3 kV case does appear to show a steady decrease during the observation period. The peak rotational temperatures ranged from 750 to 850 K.

One possibility for downward trend in the ± 7.3 kV case is the depletion of $c^3\Pi_u$ rotational states with higher J due to the dissociation of nitrogen molecules. The dissociation energy of molecular nitrogen is $113\,029\text{ cm}^{-1}$ and the energy of $c^3\Pi_{u;v=0}$ is $88\,977.9\text{ cm}^{-1}$. Therefore an additional $24\,051.1\text{ cm}^{-1}$, or approximately 2.98 eV, is required to dissociate

ate the molecule. The ± 7.3 kV case likely produced a more energetic electron population and, therefore, would have a greater depletion of the higher rotational states in the system. This would have prevented those states from transitioning to $\text{v}^3\Pi_g$ and thus resulted in an artificially low temperature. Measurements of the effective electron temperature in similar systems suggests a range of possibilities from 0.6–33 eV [110], [87], and [68].

Relation of the rotational temperatures to kinetic temperatures must be done carefully on these time scales. In most cases, the rotational temperature equilibrates with the kinetic temperature much faster than it can change. Assuming, however, that the kinetic temperature changes on a time scale on the order of the ionization wave, this is no longer the case. The ionization wave traverses the length of the discharge in several nanoseconds and may cause an abrupt increase in kinetic temperature. Equilibration with this change requires the excited nitrogen molecules undergo several collisions with the neutral gas. The time between collisions at a temperature of 750 K is approximately 1.5 ns [155]. The time resolution of the gas temperature is effectively several times this number, conservatively 10 ns. Therefore, the initial upward trend of the ± 7.3 case does not readily translate to an increase in gas temperature.

It is difficult to quantify the degree of uncertainty associated with these measurements. The uncertainty is minimal for the largest signals, from approximately 11 ns through 30 ns. Based on the oscillations of the final temperature measurements in this time period, the random error appears to be on the order of ± 50 K. As the signal strength decreases, this error increases significantly. In addition, systematic errors were present which may have affected the matching process. As mentioned, the (1, 1) and (2, 2) transitions were not included in the simulations. Additionally, the lack of an intensity calibration may have influenced the results; the efficiency of the grating may have changed over the range of wavelengths under investigation. Finally, the instrument function featured a slightly wider base than the Gaussian used to represent it.

A.6 Conclusions

The RPND is promising for use in air-breathing hypersonic propulsion as part of an energy bypass mechanism. However, the successful application of the RPND required that its electron density and gas heating be measured. Both of these help to describe its overall efficiency in the ionization of an inlet airflow.

The electron density and collision frequency were measured as functions of time using mmW interferometry. It was found that the two quantities underwent significant changes in the first five to ten minutes of operation, after which the values stayed approximately constant. It is hypothesized that these changes were a result of evolving chemical composition and temperature in the discharge chamber, resulting from the use of stagnant air. No evidence was found to support the claims that the DC sustainer improved the time-average particle density, however experimental difficulties require that this measurement be revisited.

Literature suggested that the sustainer and the RPND itself may be responsible for a significant degree of gas heating. This represents an important loss mechanism for the applied energy and can impact the downstream combustion chemistry. Heating in the RPND was analyzed via measurements of the rotational spectra in the system. A program was written to automatically generate synthetic spectra for a variety of conditions and then to pick the one most appropriate for a measured spectrum. It was found that the temperature of the RPND was reliably between 750-850 K. A decline in temperature was observed for the case with the highest bias. It is believed that this was caused by a depletion of the higher rotational states due to dissociation, resulting in an artificially lower temperature.

APPENDIX B

Laser-Absorption Analysis Code

The laser-absorption spectroscopy code was written in Python (version 2.7) using the standard libraries, NumPy (version 1.6), SciPy (version 0.11) [107], and Matplotlib 1.3 [156]. The code will be included here for reference, however the most up-to-date version will be maintained at <https://github.com/l3enny/lasana>. Below is a diagram of the directory structure used for the laser analysis code.

```
/  
|   analyze.py  
|   atoms  
|   |   __init__.py  
|   |   He.py  
|   gui.py  
|   lineshapes.py  
|   main.py  
|   models.py  
|   offset.py  
|   parse.py  
|   preprocess.py  
|   transition.py
```

The analysis package can be initialized by running the command `python main.py` from the root of the directory. This starts a script which handles all of the settings, sub-modules, and main processing loop. While much of the program logic is handled here, the actual calculations are handed off to separate modules. The code listing for `main.py` is as follows,

```
1  """  
  | Simple frontend to the Laser Absorption Spectroscopy ANalysis package.  
  |
```

```

    || Makes use of the modules 'parse.py', and 'analyze.py'.
    || Submodules notwithstanding.
    """
6
    # Standard
    from os import path, makedirs

    # Part of package
11   import analyze
    from atoms import He
    import gui
    import models
    import parse
16   import preprocess
    import transition

    # Third Party
    import numpy as N
21
    # Define transitions to simulate
    # TODO: Find better way to set up a database of transmission constants than
    # the one used by crammer. SQLite perhaps? Is there an API for the NIST ASD?
    A = 1.0216e7
26   D0 = transition.Transition(He.II3S1(), He.II3P0(), A)
    D1 = transition.Transition(He.II3S1(), He.II3P1(), A)
    D2 = transition.Transition(He.II3S1(), He.II3P2(), A)
    transitions = [D0, D1, D2]

31   # Pick directory of signal scan, then parse and load data
    target = gui.pickdir('Pick the data directory')
    print "\nProcessing", target
    settings = parse.config(target)
    print "Loading data..."
36   plasma, times, freq = parse.data(path.join(target, 'Plasma'), **settings)
    background = parse.data(path.join(target, 'Background'), **settings)[0]

    # Calculated transmission profiles with preprocessor
    print "Running preprocessor..."
41   transmitted = preprocess.transmission(plasma, background, **settings)

    # Define model and some sensible estimates of the parameters
    model = models.voigt(transitions, settings['pressure'] * He.torr2hz)
    guesses = [300, 1e16]
46
    # Pass transmission profiles to analysis routine
    params = [0] * settings['points'] # matching parameter list
    cov = [0] * settings['points'] # covariance estimate list
    print "Analyzing data..."
51   for i in range(settings['points']):
        try:
            (params[i], cov[i]) = analyze.match(model, freq, transmitted[:, i],
                                                 guesses)
        if cov[i] is N.inf:
            cov[i] = N.zeros((len(guesses), len(guesses)))
56   except RuntimeError:
        # Set values to zero in case of failure to find a match
        params[i] = N.zeros(len(guesses))
        cov[i] = N.zeros((len(guesses), len(guesses)))

61
    # Everything below this is just data processing -----
    temperatures = N.array([i[0] for i in params])
    temperatures_stdev = N.sqrt(N.array([i[0, 0] for i in cov]))
    metastables = N.array([i[1] for i in params])
    metastables_stdev = N.sqrt(N.array([i[1, 1] for i in cov]))

    adir = path.join(target, "Analysis")

```

```

71 | if not path.exists(adir):
    |     makedirs(adir)
    |
    | output = N.array([temperatures, temperatures_stdev, metastables,
    |                   metastables_stdev])
76 |     with open(path.join(adir, "fit_params.csv"), mode="wb") as f:
        |         f.write("Temperatures,+-,Metastables,+-\n")
        |         N.savetxt(f, output.T, delimiter=",")
    |
    | import matplotlib.pyplot as plt
81 |
    | time = N.array([0.35, 0.4, 0.5, 1.0, 1.5, 1.75])
    | check = N.round(1e-6 * time / settings['dt']).astype(int)
    | pos = 230
    | plt.hold(True)
86 | for i in check:
    |     pos = pos + 1
    |     plt.subplot(pos)
    |     plt.plot(1e-9 * freq, transmitted[:, i], '.r')
    |     plt.plot(1e-9 * freq, model(freq, *params[i]), '-k')
91 |     plt.hlines(1.0, 1e-9 * N.min(freq), 1e-9 * N.max(freq), colors='k',
    |                linestyles='dashed')
    |     t = i * 1e6 * settings['dt']
    |     plt.title('Time=%g\n%s' % t)
    |     plt.axis([1e-9 * N.min(freq), 1e-9 * N.max(freq), 0, 1.1])
96 | plt.hold(False)
    | plt.savefig(path.join(adir, r"samples.pdf"))
    | plt.savefig(path.join(adir, r"samples.png"))
    | plt.clf()
    |
101 prepulse = 100
    | baseline = N.mean(transmitted[:, :prepulse], axis=1)
    | param_base, cov_base = analyze.match(model, freq, baseline, guesses)
    | Tbase = param_base[0]
    |
106 plt.plot(1e6*times, temperatures, '-k')
    | plt.hold(True)
    | plt.plot([0, 200], [Tbase, Tbase], '--k')
    | plt.hold(False)
    | plt.xlabel('Time($\mu s$)')
111 plt.ylabel('Temperature(K)')
    | plt.axis([0, max(1e6*times), 0, 600])
    | plt.legend(['Temperatures', 'Pre-pulse, $T_0=%g$' % Tbase])
    | plt.savefig(path.join(adir, r"temperatures.pdf"))
    | plt.savefig(path.join(adir, r"temperatures.png"))
    | plt.clf()
    |
116 plt.plot(1e6*times, metastables, '-k')
    | plt.xlabel('Time($\mu s$)')
    | plt.ylabel('Line-Integrated-Metastable-Density($m^{-2}$)')
    | plt.axis([0, max(1e6*times), 0, 5e16])
    | plt.savefig(path.join(adir, r"metastables.pdf"))
    | plt.savefig(path.join(adir, r"metastables.png"))
    | plt.clf()

```

It begins by importing several packages from the Python standard library. These are used to manage directory names consistently across different operating systems. This is followed by the importation of the included submodules and NumPy.

Also imported at this time is the file defining the physical properties of helium, He.py.

```

1 | from scipy.constants import e, atomic_mass

```

```

    torr2hz = 25.6e6 # pressure broadening coefficient

6   class II3S1(object):
    M = 4.002602 * atomic_mass
    E = 19.81961363388 * e
    J = 1.
    g = 2 * J + 1

11  class II3P2(object):
    M = 4.002602 * atomic_mass
    E = 20.96408592885 * e
    J = 2.
    g = 2 * J + 1

16  class II3P1(object):
    M = 4.002602 * atomic_mass
    E = 20.96409540439 * e
    J = 1.
    g = 2 * J + 1

21  class II3P0(object):
    M = 4.002602 * atomic_mass
    E = 20.96421789026 * e
    J = 0.
    g = 2 * J + 1

```

Includes in this file are the excited atomic states that were considered for the laser-absorption measurements, their energies, levels, and statistical degeneracies.

Afterward, the transition class is used to define the helium transitions of interest to the absorption analysis. The transitions can be held by any iterator object, in this case a list. The transition class is defined in the file `transition.py`.

```

from scipy.constants import c, h

3  def vac2air(w):
    """ Converts wavelengths from vacuum to air.
    Input wavelength should be in meters.
    """
    w = w * 1e10
8   return (w / (1.0 + 2.735182e-4 + 131.4182/w**2 +
               2.76249e8/w**4)) * 1e-10

13  class Transition(object):
14      def __init__(self, state_i, state_f, A):
15          self.A = A
16          self.M = state_i.M

17          self.Ei = state_i.E
18          self.Ej = state_f.E
19          self.dE = self.Ej - self.Ei

20          self.f = self.dE/h
21          self.l = vac2air(c/self.f)

22          if self.dE <= 0:
23              raise ValueError("Transition is not spontaneous.")

24          self.gi = state_i.g
25          self.gj = state_f.g

```

The class has no built in methods to speak of, instead it merely acts as a simple container for the transition information. When defining a transition, it does make a simple check to ensure that the transition is downward. Of some note is the fact that it takes the vacuum wavelength and converts it to the air value.

After the main script defines the transitions, it initializes a graphical user interface (GUI) in order to select the directory containing the data to be analyzed. This functionality is provided by the GUI submodule contained in `gui.py`,

```

# Standard packages
import sys
import Tkinter, tkFileDialog

# Third party packages
import matplotlib.pyplot as plt
import numpy as np

def pickdir(text, dir='..'):
    """GUI directory picker.

    Uses the Tk module to provide the user with a simple way of selecting
    a directory for processing. Quits if no directory is chosen. Takes no
    inputs and returns a unicode string with the selected directory.
    """
    root = Tkinter.Tk()
    root.withdraw()
    top_dir = tkFileDialog.askdirectory(parent=root, initialdir=dir,
                                         title=text)
    if top_dir is '':
        print 'No directory provided, quitting...'
        sys.exit(0)
    return top_dir

def contour(data):
    levels = np.linspace(np.min(data), np.max(data), 100)
    plt.contourf(data, levels=levels)
    plt.colorbar()
    plt.show()

def slice(**sets):
    """Plots a variable number of dataset slices.

    Takes an unrolled dictionary of datasets (keywords are the legend
    titles) and plots them all on a single axis. Useful for comparing
    different slices or processing methods.
    """
    plt.hold(True)
    for k in sets.keys():
        plt.plot(sets[k])
    plt.legend(sets.keys(), loc=4)
    plt.show()
    plt.hold(False)

```

The GUI uses the Tcl/Tk toolkit for interoperability between systems. The graphical directory picker is contained in the `pickdir` function which accepts a string (used to title

the window), and a default directory value. Several other functions are available in the `gui` submodule which can be used in analysis, but are not currently employed.

Following the identification of a valid directory, the processing of the data is handed off to the `parse.py` submodule.

```

    """
2  Processes the data from whatever format it was captured in and renders
    it in a usable form to whoever's knocking.
    """

7  # Standard modules
import ConfigParser
import os
from os import path
import sys

12 # Third party
import numpy as N

def config(top_dir='.', debug=False):
    # Parse the settings file, check for proper formatting
    config = ConfigParser.RawConfigParser()
    read_return = config.read(path.join(top_dir, 'settings.cfg'))
    if read_return == []:
        raise ConfigParser.Error('No settings file detected.')

22 samples = config.getint('Settings', 'WavelengthSamples')
points = config.getint('Settings', 'DataPoints')
mod_initial = config.getfloat('Settings', 'InitialModulation')
mod_final = config.getfloat('Settings', 'FinalModulation')
averages = config.getint('Settings', 'Averages')
time_domain = config.getfloat('Settings', 'TimeDomain')
pressure = config.getfloat('Settings', 'Pressure')
offset = config.getfloat('Settings', 'Offset')
voffset = config.getfloat('Settings', 'VerticalOffset')
return {'samples':samples,
32     'points':points,
        'mod_initial':mod_initial,
        'mod_final':mod_final,
        'averages':averages,
        'dt':time_domain/points,
        'pressure':pressure,
        'offset':offset,
        'voffset':voffset}

42 def _load(dir, samples, points, obsolete, debug=False):
    """Generate data arrays and load data from file.

    Private method for reading in data in the format determined by my experiment.
    Modify as necessary.
    """
47     # Initialize storage arrays
pd_r = N.zeros((samples, points))
ref_r = N.zeros((samples, points))
v_r = N.zeros((samples, points))
i_r = N.zeros((samples, points))
52     pd_s = N.zeros((samples, points))
ref_s = N.zeros((samples, points))
v_s = N.zeros((samples, points))
i_s = N.zeros((samples, points))

57     # Loop over all acquired files
for i in range(samples):

```

```

    if obsolete:
        reference = N.loadtxt(path.join(dir, 'Reference%g.dat' % i),
                               delimiter='\t', skiprows=2)
    signal = N.loadtxt(path.join(dir, 'Signal%g.dat' % i),
                       delimiter='\t', skiprows=2)
else:
    reference = N.loadtxt(path.join(dir, 'Reference%g.dat' % i),
                           delimiter='\t', usecols=(1,2,3,4))
signal = N.loadtxt(path.join(dir, 'Signal%g.dat' % i),
                   delimiter='\t', usecols=(1,2,3,4))

pd_r[i,:] = reference[:,0]
ref_r[i,:] = reference[:,1]
v_r[i,:] = reference[:,2]
i_r[i,:] = reference[:,3]

pd_s[i,:] = signal[:,0]
ref_s[i,:] = signal[:,1]
v_s[i,:] = signal[:,2]
i_s[i,:] = signal[:,3]

return (pd_s, pd_r), (ref_s, ref_r)

def data(dir='.', obsolete=False, debug=False, **settings):
    """Custom parser for measurement files.

    Reads in the data related to a particular set of measurements. Assumes
    that the tuning of the diode has a 0.8 GHz/mA relation. Reads in
    voltage and current signals, but does not return them. Only returns
    the wavelength *range* and signals. The wavelength range is a 1D numpy
    array. The signals are a 2D numpy array where the first index is the
    sample index (essentially wavelength) and the second index is the time
    index.

    Keyword arguments:
    top_dir -- the reference directory for measurement files (default '.')
    """

ma2hz = 0.6067e9 # diode-specific tuning values

if obsolete:
    print "*WARNING* You're running with the obsolete parser."
trace_dir = path.join(dir)
signal, reference = _load(trace_dir, settings['samples'],
                           settings['points'], obsolete)
times = settings['dt'] * N.arange(settings['points'])
freq = N.linspace(settings['mod_initial'], settings['mod_final'],
                  settings['samples']) * ma2hz + settings['offset']
return signal, times, freq

```

It contains all of the situation-specific details of where the data are stored, how to read them in. This submodule can be rewritten to reflect the user's own particular directory structure, configuration files, file format, etc. In this case when the `config` function is called, the standard module, `ConfigParser`, is used to read in processing information from a configuration file generated by the LabView data acquisition software. This is returns a dictionary with all of the configuration settings to the main script.

Subsequently, the main script calls the `data` function from the `parse` submodule in

order to load the actual experimental data sets. This function takes a directory as its input as well as the settings. Also included in the function is the laser-specific conversion value from current to frequency. The function returns the data set, the acquisition time array, and the frequency values for which the data were obtained. These are returned to the main script which then loads the data from the background.

These two data sets are then passed to the preprocessor which is defined in `preprocess.py`.

```

    """
    Pre-process information which is usually experiment-specific. Customize
3   to your liking (just make sure it jives with parse.py if you're using
    it).
    """

# Third party
8 import numpy as np

def transmission(signal, background, debug=False, **settings):
    """Generates a proper transmission curve from input data.

13   Method subtracts out the plasma-induced emissions (unrelated to the
    laser) and corrects for the baseline shift resulting from increased
    diode power.
    """

# Determine 100% transmission signal and average over acquisition time
18 unabsorbed = np.mean(background[0] - background[1], axis=1)

# Correct transmission signal for normal plasma emissions
signal_total = signal[0]
signal_plasma = signal[1]
23 transmitted = signal_total - signal_plasma + settings['voffset']

# Normalize transmission signal to full transmission value
baseline_adjusted = transmitted/unabsorbed[:, np.newaxis]

28 return baseline_adjusted

def transmission2(signal, background, debug=False, **settings):
    signal_total = signal[0]
    signal_plasma = signal[1]
    transmitted = signal_total - signal_plasma + settings['voffset']

    low = np.mean(signal_total[0, :])
    high = np.mean(signal_total[-1, :])
    q = (high - low)/settings['samples'] * np.arange(0, settings['samples']) + \
        + (low + high)/2

    #import matplotlib.pyplot as plt
    #plt.plot(transmitted[:, 0])
    #plt.hold(True)
    #plt.plot(q)
    #plt.legend(('Measured', 'Fit'))
    #plt.show()

43 return transmitted/q[:, np.newaxis]
```

The preprocessor makes the necessary adjustments, noise subtractions, and laser power

corrections, in order to obtain the transmission spectra for each time step. The transmission spectra are then passed back to the main script for analysis.

At this point, the main script defines the model to which the transmission spectra will be matched. This is defined in the models submodule, `model.py`.

```

import math as m
import numpy as N
from scipy.constants import k, c
import lineshapes

def bimodal_voigt(transitions, fwhm_p):
    def func(x, T, amp, drift):
        # Pressure broadening/lorentzian part of profile
        f = 0
        V = lineshapes.voigt
        # Assumes origin is located at the center of the first listed transition
        origin = transitions[0].f
        for t in transitions:
            fwhm_a = t.A + fwhm_p
            gamma = fwhm_a/2
            # Doppler broadening/gaussian part of the profile
            fwhm_d = N.sqrt((8*m.log(2)) * k*T / (t.M*c**2)) * t.f
            sigma = fwhm_d/(2*m.sqrt(2*m.log(2)))
            temp = 0.5 * (V(x + t.f - origin + drift, sigma, gamma)
                           + V(x + t.f - origin + drift, sigma, gamma))
            temp = temp * t.l**2 * t.A * (t.gj/t.gi) / (8 * N.pi)
            f += temp
        return N.exp(- amp * f)
    return func

def voigt(transitions, fwhm_p):
    def func(x, T, amp):
        # Pressure broadening/lorentzian part of profile
        f = 0
        V = lineshapes.voigt
        # Assumes origin is located at the center of the first listed transition
        origin = transitions[0].f
        for t in transitions:
            fwhm_a = t.A + fwhm_p
            gamma = fwhm_a/2
            # Doppler broadening/gaussian part of the profile
            fwhm_d = N.sqrt((8*m.log(2)) * k*T / (t.M*c**2)) * t.f
            sigma = fwhm_d/(2*m.sqrt(2*m.log(2)))
            temp = V(x + t.f - origin, sigma, gamma)
            temp = temp * t.l**2 * t.A * (t.gj/t.gi) / (8 * N.pi)
            f += temp
        return N.exp(- amp * f)
    return func

def gaussian(transitions):
    def func(x, T, amp):
        f = 0
        G = lineshapes.gaussian
        # Assumes origin is located at the center of the first listed transition
        origin = transitions[0].f
        for t in transitions:
            # Doppler broadening/gaussian part of the profile
            fwhm_d = N.sqrt((8*m.log(2)) * k*T / (t.M*c**2)) * t.f
            sigma = fwhm_d/(2*m.sqrt(2*m.log(2)))
            temp = G(x + t.f - origin, sigma)
            temp = temp * t.A * t.l**2 * (t.gj/t.gi) / (8*N.pi)
            f += temp
        return N.exp(- amp * f)
    return func

```

```
||     return func
```

Several models are available in this submodule including a Gaussian model and a bi-modal Voigt. None of these functions are the actual lineshape, but rather the lineshape multiplied by the necessary constants to obtain the cross sections, followed by exponentiation for the actual transmission curve. The definition of the Voigt, Lorentzian, Gaussian, and pseudo-Voigt profiles is done in `lineshapes.py`.

```
1  """ Convenient lineshape definitions.
2
3  Several different lineshapes which are frequently found in spectroscopy.
4  These can be used to build more complex models.
5  """
6
7  from math import sqrt, log
8  import numpy as np
9  from scipy.special import wofz
10
11 def lorentzian(x, gamma):
12     """Evaluation of a lorentzian or cauchy distribution
13     """
14     return 1/(np.pi * gamma * (1 + np.power(x/gamma, 2)))
15
16 def gaussian(x, sigma):
17     """ Evaluation of a gaussian distribution.
18     """
19     return 1/(sigma*sqrt(2*np.pi)) * np.exp(-0.5 * np.power((x+x0)/sigma, 2))
20
21 def voigt(x, sigma, gamma):
22     """Evaluation of a Voigt profile using the complex error function.
23
24     This function evaluates a Voigt function and returns it to the user.
25     It is an "exact" calculation of the complex error function making it
26     more expensive than the pseudo-Voigt.
27
28     Keyword arguments:
29     sigma -- Standard deviation of the Gaussian portion
30     gamma -- Standard deviation of the Lorentzian portion
31     """
32     z = (x + 1j*gamma)/(sigma*sqrt(2))
33     return wofz(z).real/(sigma*sqrt(2*np.pi))
34
35 def pseudo_voigt(gamma, eta):
36     """Generates a pseudo-Voigt function.
37
38     The pseudo-Voigt is a less expensive way of calculating the Voigt
39     lineshape. It uses a weighted sum of the individual Gaussian and
40     Lorentzian distributions.
41     """
42     sigma = 2*gamma*sqrt(2*log(2))
43     G = gaussian(sigma)
44     L = lorentzian(gamma)
45     return (1 - eta) * G(x) + eta * L(x)
```

After the main script has defined the model, it generates reasonable starting guesses to seed the solver. This is followed by the allocation of data arrays for the converged solutions

and the covariance matrices. Finally, the script hands off the model and the transmission spectra to the analysis submodule, `analyze.py`.

```

5      """
6      The mematical component. Generates synthetic spectra. Runs comparison
7      algorithm. Tells you what you want to know. At present only considers
8      Doppler broadening and pressure broadening. User must provide pressure
9      broadening FWHM in angular frequency.
10     """
11
12     # Third Party
13     from scipy.optimize import curve_fit
14
15     def match(sigma, freq, measured, guesses, debug=False):
16         """Fits the sigma model to the transmission data.
17
18         Uses an input model of the absorption cross section to do a least-
19         squares fit to the transmission signal. Returns the fitting param-
20         eters and covariances for user processing. Thin wrapper over the SciPy
21         curve_fit routine
22
23         Keyword arguments:
24         """
25
26     return curve_fit(sigma, freq, measured, guesses)

```

At one point, this submodule contained its own matching algorithm. However, this was eventually replaced with SciPy's `curve_fit` function which utilizes the Levenberg-Marquardt algorithm.

Once the main script has successfully looped over all the transmission spectra, it has finished. A fair amount of post-processing is included in the present version however no further data analysis is done. One additional file is included in the laser-absorption analysis package. This is the `offset.py` script.

```

4      """
5      Simple frontend to the Laser Absorption Spectroscopy ANalysis package.
6      Makes use of the modules 'parse.py', and 'analyze.py'.
7      Submodules notwithstanding.
8      """
9
10
11     # Standard
12     from os import path, makedirs
13     import math as m
14
15     # Part of package
16     from atoms import He
17
18     import gui
19     import lineshapes
20     import parse
21     import preprocess
22     import transition
23
24     # Third Party
25     import numpy as N
26     from scipy.optimize import curve_fit

```

```

24    from scipy.constants import k, c
25
26    torr2hz = 25.6e6 # pressure broadening coefficient
27
28    # Define transitions to simulate
29    # TODO: Find better way to set up a database of transmission constants than
30    # the one used by crammer. SQLite perhaps? Is there an API for the NIST ASD?
31    A = 1.0216e7
32    D0 = transition.Transition(He.II3S1(), He.II3P0(), A)
33    D1 = transition.Transition(He.II3S1(), He.II3P1(), A)
34    D2 = transition.Transition(He.II3S1(), He.II3P2(), A)
35    transitions = [D0, D1, D2]
36
37    # Pick directory of signal scan, then parse and load data
38    target = gui.pickdir('Pick the data directory')
39    print "\nProcessing", target
40    settings = parse.config(target)
41    print "Loading data..."
42    plasma, times, freq = parse.data(path.join(target, 'Plasma'), obsolete=False, **settings)
43    background = parse.data(path.join(target, 'Background'), obsolete=False, **settings)[0]
44
45    # Calculated transmission profiles with preprocessor
46    print "Running preprocessor..."
47    transmitted = preprocess.transmission(plasma, background, **settings)
48
49    # Define model and some sensible estimates of the parameters
50    def model(x, T, amp, offset):
51        # Pressure broadening/lorentzian part of profile
52        f = 0
53        V = lineshapes.voigt
54
55        # Assumes origin is located at the center of the first listed transition
56        origin = transitions[0].f
57        for t in transitions:
58            fwhm_a = t.A + settings['pressure'] * torr2hz
59            gamma = fwhm_a/2
60            # Doppler broadening/gaussian part of the profile
61            fwhm_d = N.sqrt((8*m.log(2)) * k*T / (t.M*c**2)) * t.f
62            sigma = fwhm_d/(2*m.sqrt(2*m.log(2)))
63            temp = V(x + t.f - origin + offset, sigma, gamma)
64            temp = temp * t.l**2 * t.A * (t.gj/t.gi) / (8 * N.pi)
65            f += temp
66        return N.exp(-amp * f)
67    guesses = [300, 5e15, -10e6]
68
69    # Find the offset for the "largest signal"
70    mn = N.std(transmitted, axis=0)
71    largest = N.where(max(mn) == mn)[0]
72    (p, co) = curve_fit(model, freq, transmitted[:, largest][:, 0], guesses)
73
74    print "Largest:", largest
75    print "Offset is:", p[2], "Hz"

```

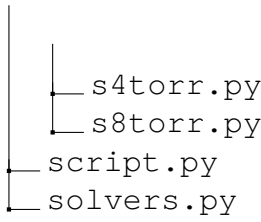
This script is functionally the same as the main.py script, with the exception that its sole purpose is to determine the frequency offset which is used in the configuration file. This script was written when it became clear that the diode laser frequency drifted by tens of MHz during the course of regular operation. Briefly, the script determines the transmission spectra with the largest signal and then uses a modified modeling function to calculate its offset from zero.

APPENDIX C

Global Model Code

The global model code was written in Python (version 2.7) using the standard libraries, NumPy (version 1.6), SciPy (version 0.11) [107], and Matplotlib 1.3 [156]. The code will be included here for reference, however the most up-to-date version will be maintained at <https://github.com/13enny/crammer>. Presently, the `conserve` branch is the one that is in regular use, however its changes will eventually be merged into the main branch. Below is a diagram of the directory structure used for the global model code. Some additional files are present in the repository, but were not used in producing the analysis presented here.

```
/  
|   distributions.py  
|   equilibrium  
|   gases  
|       __init__.py  
|       helium  
|           __init__.py  
|           atomic.py  
|           constants.py  
|           optical.py  
|           states.py  
|   handler.py  
|   initcond.py  
|   matrixgen.py  
|   rates.py  
|   ratio.py  
|   script.py  
|   settings  
|       sltorr.py
```



The global model is initialized by running the `script.py` file.

```

1  """
2      Main script for running CRM simulation. The code is written in a frame-
3      work manner allowing the user some flexibility in how the problem is
4      solved. I don't have a lot of time for comprehensive documentation so
5      this script will be heavily commented to compensate.
6
7      Requirements: Numpy 1.6+, Scipy 0.10+
8      """
9
10
11     # Standard Modules
12     from datetime import datetime
13     import csv
14
15     # Third Party Modules
16     import numpy as np
17     from scipy.constants import k, e, m_e
18
19     # Included Modules
20     import handler          # Input/output handling
21     import matrixgen         # Generates the rate matrices
22     import rates             # Handles general state calculations
23     import solvers           # Handles general state calculations
24
25     # User-specified options
26     from settings.s4torr import *      # load user settings file
27
28     # Convenient localization of state information, and ordering in
29     # ascending energy.
30     # TODO: This is a bit inelegant; there should be a better way to do this
31     states = gas.states.states
32     order = sorted(states.keys(), key=lambda state:states[state]['E'])
33
34     # Generate initial transition matrices and constants
35     Ao = matrixgen.optical(gas)
36     Alin = matrixgen.linopt(gas)
37     Ae = matrixgen.electronic2(gas, coeffs, Te)
38     Aa = matrixgen.atomic(gas)
39     dE = solvers.dE(states, order)
40     E = np.array([states[i]['E'] for i in order])
41
42     def dNdt(t, N):
43         term = np.dot(Ae*ne + Ao + Aa * Ng, N)
44         return term
45
46     def dTedt(t, Te):
47         source = e**2 * ne * Ef(t)**2 / (m_e * km(Te) * Ng)
48         elastic = - 3 * ne * km(Te) * Ng * (m_e / M) * 1.5 * k * (Te - Tg)
49         inelastic = - np.sum(np.dot(ne * Ae * dE, N))
50         return (source + elastic + inelastic) * (2./3) / (k * ne)
51
52     N = Ni
53     N[0] = Ng - ne # correct for fractional ionization
54     N[1] = Nm0 # override with measured metastables
55     N[-1] = ne # override with measured electrons
56
57     # Initialize solution arrays
58     errors = [0.0]
59     populations = [N]

```

```

emissions = [np.zeros(Alin.shape)]
temperatures = [Te]
field = [0.0]
times = [0.0]
energies = [np.sum(N * E + 1.5 * k * Te * ne)]
coupled = [0.0]

# Solution loop
start = datetime.now()
#solver = solvers.rkf45(dNdt, times[-1], N, dt * 1e6, dt * 1e-6, 1e-1)
steps = 0
while times[-1] < T:
    # Integrate population (and energy) equations.
    # N, dt, error = solver.next()
    N = solvers.rk4(dNdt, times[-1], N, dt)
    N = N.clip(min=0)
    times.append(times[-1] + dt)
    if energy:
        Te = solvers.rk4(dTeDt, times[-1], Te, dt)
        # Regenerate temperature-dependent quantities
        Ae = matrixgen.electronic2(gas, coeffs, Te)
    ne = N[-1]           # enforce quasi-neutrality

    # There must be a more elegant way of accomplishing this ...
    Nalign = []
    for i in range(1, len(N)):
        Nalign.extend([N[i]] * i)

    # Python lists are much faster than appending to ndarrays
    emissions.append(Alin * Nalign * dt)
    populations.append(N)
    temperatures.append(Te)
    field.append(Ef(times[-1]))
    energies.append(np.sum(N*E) + 1.5 * k * Te * ne)
    coupled.append(dt * e**2 * ne * Ef(times[-1])**2 /
                  (m_e * km(Te) * Ng) + coupled[-1])
    steps += 1

    # Output some useful information every 1000 steps
    if steps%100 == 0:
        end = datetime.now()
        print "Te=%eV" % (Te * k / e)
        print "Simulation_time=%gs of %gs" % (times[-1], T)
        print "Elapsed_Time:", (end - start), "\n"

print "Final_triplet metastable density:", N[1]

# Generate all emission wavelengths in the proper order
wavelengths = solvers.wavelengths(states, order)
order = np.array(order)
names = ['times', 'populations', 'wavelengths', 'temperatures', 'emissions',
        'energies', 'field', 'coupled']
data = [times, populations, wavelengths, temperatures, emissions, energies,
        field, coupled]
# Replace the order dump with something a tad more elegant
with open(prefix + '_order.csv', 'wb') as csvfile:
    writer = csv.writer(csvfile, delimiter=',')
    writer.writerow(order)
    handler.save(data, names, prefix)

```

As with the laser-absorption analysis code, this script mostly handles the logic of the solutions and hands off the actual calculations to other libraries or submodules. Aside from

the importation of several submodules, the script critically imports a settings file which determines much of how the solver behaves. The settings file is intended to be much more straightforward to edit in comparison to the solution script. An example of this is the settings file for the 4.0 Torr conditions, `s4torr.py`.

```

1  ||| from scipy.constants import e, k
2  ||| import numpy as np
3  ||| from numpy import exp, sqrt, log, maximum, minimum
4  ||| from gases import helium as gas      # choose gas to simulate
5  ||| import cPickle
6
7  with open('./gases/helium/pack_1p0.pickle', mode='r') as f:
8      pack = cPickle.load(f)
9
10 km = pack.km
11
12 with open('./gases/helium/combined.pickle', mode='r') as f:
13     coeffs = cPickle.load(f)
14
15 T = 1.9e-7           # duration to simulate, s
16 dt = 5e-12          # target step time
17
18     # Output options (user-defined)
19 prefix = '4torr'      # file prefix for data files
20 energy = True         # track electron energy changes
21
22     # Physical system options (user-defined)
23 Tg = 300              # neutral gas temperature, K
24 Te = 0.2 * e / k       # initial electron temperature, K
25 P = 4.0 * 133.322      # neutral gas pressure, Pa
26 M = gas.constants.M
27 Ng = P/(k*Tg)          # gas density, 1/m^3
28 ne = 5.363255e13        # initial electron density, 1/m^3
29 Nm0 = 1.99e14
30 Ni = np.load("equilibrium.npy")
31
32     # Applied electric field function
33 E0 = 2.66440e2 / 1e-2   # amplitude
34 tau = 4.0e-8             # width
35 tail = 0.125            # tail fraction
36 t0 = 4.0e-8              # center
37
38 def E_gaussian(t):
39     a = E0
40     b = t0
41     c = tau / (2 * sqrt(2 * log(2)))
42     return a * exp(-(t - b)**2 / (2 * c**2))
43
44 Ef = E_gaussian

```

Because the main script imports all of the settings into its namespace, it is important that the settings file define all of the variables listed in this example. The settings file is generally well-commented, therefore little will be said about the variables contained therein. The one notable exception is at the beginning where two serialized objects (“pickles”) are loaded in to the variables `km` and `coeffs`. As recorded in the comments, `km` contains the function

which generates the momentum transfer rate coefficient. Similarly, `coeffs` contains the functions which generate the electron-induced transition rate coefficients.

Both of these coefficient files are generated by a separate script, called `rategen`. The function of this script will be described at the end of this appendix. From an application standpoint, the `coeffs` function accepts a float, and two integers as its inputs. The float is the electron temperature in K, and the integers are unique identifiers of the excited atomic state (in the form of nSL).

Finally, it should be noted that the settings file also imports a file called `equilibrium.npy`. This file is generated by the settings file `equilibrium.py` and contains the equilibrium values for the various excited atomic states.

After the importation of the settings, the script also imports the states information from the gas defined in the settings. It should be noted that the `__init__.py` file in the `gases` directory contains a single line: `__all__ = ['helium']`. This provides a hint to the Python runtime about what submodules are included in the `gases` module. In this case, the gas is helium, and the `states.py` file is recorded below.

```

1 | from scipy.constants import e
2 |
3 | states = {
4 |     100:{'g':1., 'E':0.0},
5 |     210:{'g':3., 'E':19.81961358228*e},
6 |     200:{'g':1., 'E':20.6157738231*e},
7 |     211:{'g':9., 'E':20.96410374974*e},
8 |     211:{'g':9., 'E':20.96410369516*e},
9 |     201:{'g':3., 'E':21.2180216732*e},
10 |    310:{'g':3., 'E':22.718465298*e},
11 |    300:{'g':1., 'E':22.920316225*e},
12 |    311:{'g':9., 'E':23.0070769442*e},
13 |    312:{'g':15., 'E':23.07365082550*e},
14 |    302:{'g':5., 'E':23.07407365281*e},
15 |    301:{'g':3., 'E':23.0870173854*e},
16 |    410:{'g':3., 'E':23.5939575362*e},
17 |    400:{'g':1., 'E':23.6735694086*e},
18 |    411:{'g':9., 'E':23.7078920598*e},
19 |    412:{'g':15., 'E':23.73608960429*e},
20 |    412:{'g':15., 'E':23.73608954249*e},
21 |    402:{'g':5., 'E':23.73633384917*e},
22 |    413:{'g':21., 'E':23.737006465895*e},
23 |    403:{'g':7., 'E':23.737008536459*e},
24 |    401:{'g':3., 'E':23.7420688828*e},
25 |    #510:{'g':3., 'E':23.9719702176*e},
26 |    #500:{'g':1., 'E':24.0112137867*e},
#511:{'g':9., 'E':24.0282248728*e},
#512:{'g':15., 'E':24.042661313590*e},
#502:{'g':5., 'E':24.042802206755*e},
#513:{'g':21., 'E':24.043153263722*e},

```

```

31     #503:{'g':7.,  'E':24.043154443358*e},
#514:{'g':27.,  'E':24.0432147700577*e},
#504:{'g':9.,   'E':24.0432153260405*e},
#501:{'g':3.,   'E':24.0457992013*e},
'ion':{'g':2.,  'E':24.587387777*e}
36 }

```

The states are contained in a single dictionary and referenced by their unique integer identifier. The energy of each state as well as its degeneracy is also recorded here. Any commented state is automatically excluded from the simulation.

After the states are imported by the script, a list is generated with their identifiers in order of energy. This is done because Python does not guarantee the order of dictionaries. This order listing is later used for consistent generation of the transition matrices. The transition matrices are produced by the `matrixgen.py` submodule.

```

"""
4 Generates the electronic, optical and atomic transition matrices
for a specified gas module. A functional EEDF, f, must be supplied
which takes the energy as its only argument. The matrices are
populated in an "intelligent" order such that the total population
is preserved and de-excitation rates are calculated via the
principle of detailed balance.
"""

9
14 import numpy as N
import rate

def km(gas, Te):
    return gas.km.K(Te)

19 def electronic2(gas, coeffs, Te):
    states = gas.states.states
    order = sorted(states.keys(), key=lambda state:states[state]['E'])
    dim = len(states)
    mat = N.zeros((dim, dim))
    # Move down the rows, equivalent to rate equation for each final state
    for f in range(dim):
        # Move across the columns: access each upper initial state
        for i in range(dim):
            mat[f,i] = coeffs.rate(Te, order[i], order[f])
    for i in range(dim):
        mat[i, i] = -N.sum(mat[:, i])
    return mat

29 def atomic(gas):
    states = gas.states.states
    order = sorted(states.keys(), key=lambda state:states[state]['E'])
    dim = len(states)
    mat = N.zeros((dim, dim))
    # Move down the rows, equivalent to rate equation for each final state
    for f in range(dim):
        # Move across the columns: access each upper initial state
        for i in range(dim):
            mat[f,i] = gas.atomic.K(order[i], order[j])
    for i in range(dim):
        mat[i, i] = -N.sum(mat[:, i])
    return mat

```

```

44 def electronic(gas, Te):
45     states = gas.states.states
46     order = sorted(states.keys(), key=lambda state:states[state]['E'])
47     dim = len(states)
48     mat = N.zeros((dim, dim))
49     # Move down the rows, equivalent to rate equation for each final state
50     for f in range(dim):
51         # Move across the columns: access each upper initial state
52         for i in range(dim):
53             mat[f, i] = gas.electronic.rates(Te, order[i], order[f])
54     for i in range(dim):
55         mat[i, i] = -N.sum(mat[:, i])
56     return mat
57
58 def optical(gas):
59     states = gas.states.states
60     order = sorted(states.keys(), key=lambda state:states[state]['E'])
61     dim = len(states)
62     mat = N.zeros((dim, dim))
63     for i in range(1, dim):
64         for j in range(i):
65             mat[j, i] = gas.optical.A(order[i], order[j])
66         mat[i, i] = -sum(mat[:, i])
67     return mat
68
69 def linopt(gas):
70     states = gas.states.states
71     order = sorted(states.keys(), key=lambda state:states[state]['E'])
72     dim = len(states)
73     lin = []
74     for f in range(dim):
75         for i in range(f):
76             lin.append(gas.optical.A(order[f], order[i]))
77     return N.array(lin)
78
79 def atomic(gas):
80     states = gas.states.states
81     order = sorted(states.keys(), key=lambda state:states[state]['E'])
82     dim = len(states)
83     mat = N.zeros((dim, dim))
84     for i in range(dim):
85         for j in range(dim):
86             mat[j, i] = gas.atomic.K(order[i], order[j])
87         mat[i, i] = -sum(mat[:, i])
88     return mat

```

This submodule contains all the function definitions necessary to generate the various transition matrices. Conceptually, the row index is the same index as the final state identifier in the `order` list. Likewise, the column indicates the initial state index. The matrix generation functions automatically track the losses and gains for each state and ensure conservation of particles.

After the transition matrices are generated, the `solvers.py` submodule is used to generate the transition energies.

² """
Sets up the matrix and calculates the solutions.

```

    """
from scipy.constants import h, c, m_e

7 import numpy as np

def svd(matrix):
    """
Determines the solution for a homogeneous system of equations in
the form  $Ax = 0$ . The user supplies a matrix,  $A$ , as the input and
the solution is found using the singular value decomposition
method.
"""
12 u, s, v = np.linalg.svd(matrix)
#TODO: Is the last row of v always associated with the lowest s?
17 null = np.abs(v[0,:]).T
return null

22 def dE(states, order):
dim = len(states)
mat = np.zeros((dim, dim))
for i in range(dim):
    Ei = states[order[i]]['E']
    for f in range(dim):
        Ef = states[order[f]]['E']
        mat[i, f] = (Ei - Ef)
27 return mat

32 def wavelengths(states, order):
w = []
dim = len(order)
for f in range(dim):
    Ef = states[order[f]]['E']
    for i in range(f):
        Ei = states[order[i]]['E']
        w.append((h * c) / (Ef - Ei))
37 return np.array(w)

# ODE Solvers
# These are a selection of different solvers.
#
42 def rk4(f, x, y, h):
    # Simple fourth-order Runge-Kutta solver.
k1 = h * f(x, y)
k2 = h * f(x + 0.5*h, y + 0.5*k1)
k3 = h * f(x + 0.5*h, y + 0.5*k2)
k4 = h * f(x + h, y + k3)
47 return y + k1/6 + k2/3 + k3/3 + k4/6

52 def rkf45(f, t0, y0, hmax, hmin, TOL):
    """
Runge-Kutta-Fehlberg generator implemented per B. Bradie's "A
Friendly Introduction to Numerical Analysis," incorporating
57 automatic step control. Initialized by assigning the function to a
variable which outputs the next step every time the .next() method
is called.
"""

62 A = [0.25,      0.25]
B = [3./8,       3./32,       9./32]
C = [12./13,     1932./2197, -7200./2197,   7296./2197]
D = [11.0,       439./216,    -8.0,        3680./513,   -845./4104]
E = [0.5,        -8./27,      2.0,         -3544./2565, 1859./4104, -11./40]
67 F = [1./360,    -128./4275, -2197./75240, 1./50,      2./55]

def k(f, t, y, h):
    k1 = h * f(t, y)

```

```

72     k2 = h * f(t + A[0]*h, y + A[1]*k1)
    k3 = h * f(t + B[0]*h, y + B[1]*k1 + B[2]*k2)
    k4 = h * f(t + C[0]*h, y + C[1]*k1 + C[2]*k2 + C[3]*k3)
    k5 = h * f(t + D[0]*h, y + D[1]*k1 + D[2]*k2 + D[3]*k3 + D[4]*k4)
    k6 = h * f(t + E[0]*h, y + E[1]*k1 + E[2]*k2 + E[3]*k3 + E[4]*k4
                + E[5]*k5)
77   errors = (F[0]*k1 + F[1]*k3 + F[2]*k4 + F[3]*k5 + F[4]*k6) / h
   return k1, k2, k3, k4, k5, k6, errors

82   h = hmax
   y = y0
   t = t0

87   while True:
     k1, k2, k3, k4, k5, k6, errors = k(f, t, y, h)
     rerrors = errors/y
     eps = np.max(abs(rerrors))

92   if eps < TOL:
     y = y + (16./135)*k1 + (6656./12825)*k3 + (28561./56430)*k4 \
           - (9./50)*k5 + (2./55)*k6
     t += h
     yield y, h, eps

97   q = 0.84 * (TOL/eps)**0.25
   q = min(4.0, max(q, 0.1))
   h = min(q * h, hmax)

   if h < hmin:
     print "Warning, required step size is below minimum (h=%e)." % h
     raw_input('')

```

This submodule does most of the calculations, though some of the functions (such as the singular value decomposition) are wrappers for the SciPy equivalent. Also in this submodule is a function which returns all the possible optical transition wavelengths. Furthermore, two types of Runge-Kutta integrators are in this submodule. The first is a simple fourth order method. The second implements a fourth order method with a fifth order adaptive step size adjustment. The latter of the two implements a generator pattern so that it could conceivably be used without looping.

Returning to the main script, the differential equation describing the evolution of the state density is set up, followed by the energy equation. Then, the initial values are set up (based on the settings file), and the solution arrays are initialized. This is followed by the solution loop which steps through the evolution of the system and adjusts the rate coefficients as necessary. After the end of the simulation period has been reached, the output files are opened for writing, a process taken care of by `handler.py`.

```

"""
Basic load and save functions.

```

```

4     """
5     import os
6     import re
7
8     import numpy as N
9
10    def save(data, names, prefix='dump'):
11        print "Saving data to disk...\n"
12        # responsible for saving all the passed variables
13        if len(names) != len(data):
14            raise ValueError('Insufficient output data')
15        for i in range(len(names)):
16            with open(prefix + '_' + names[i] + '.csv', 'w') as fid:
17                N.savetxt(fid, data[i], delimiter=',')
18
19    return None

```

As was mentioned earlier, the rate coefficients which are important to the use of the global model are generated by a separate program and compiled into serialized objects. The objects implement a `Rates` class which is contained in `rates.py`.

```

1  from scipy.interpolate import UnivariateSpline
2  from scipy.interpolate import interp1d
3
4  class Rates(object):
5
6      def __init__(self, temperatures, rates, comments=None):
7          if len(rates) != len(temperatures):
8              raise ValueError('There must be an equal number of rate tables and',
9                               'temperatures.')
10             self.rates = rates
11             self.temperatures = temperatures
12             self.comments = comments
13
14      def rate(self, Te, i, f):
15          select = []
16          for table in self.rates:
17              select.append(table[i][f])
18          func = UnivariateSpline(self.temperatures, select, s=0, k=2)
19          #func = interp1d(self.temperatures, select)
20          return func(Te)
21
22      def km(self, Te):
23          func = UnivariateSpline(self.temperatures, self.rates, s=0, k=2)
24          #func = interp1d(self.temperatures, self.rates)
25          return func(Te)

```

The class acts as a data container for rate coefficients calculated at fixed temperatures. It then implements a simple interpolating spline in order to return appropriate rate coefficients as requested by the main script.

The `rategen` program can be accessed at the online repository, <https://github.com/l3enny/rategen>. For the most part, it implements a simple convolution routine around the transcribed cross sections and parses the results into the above class. The contents of the `rategen` directory include the listing below as well as several other files which

are not necessary for the analysis presented here.

```
/  
|   settings  
|   |   combined.py  
|   |   pack1p0.py  
|   xsections  
|   |   __init__.py  
|   |   helium  
|   constants.py  
|   convolve.py  
|   distributions.py  
|   main.py  
|       rates.py
```

The program begins with a call to `main.py`.

```
# Standard library modules  
import cPickle  
  
# Third party packages  
5  from scipy.constants import *  
  
# Included packages  
import convolve  
import rates  
  
10 from settings import combined as settings  
  
output = []  
for temperature in settings.temperatures:  
    eedf = settings.distribution(temperature, **settings.kargs)  
    print "Calculating at temperature:", temperature  
    if settings.elastic:  
        K = convolve.rate2(settings.sigma, eedf)  
        output.append(K)  
    else:  
        output.append({})  
        for i in settings.states:  
            output[-1][i] = {}  
            for f in settings.states:  
                25             if i == 'ion':  
                    K = settings.nahar_rrc(f, temperature)  
                else:  
                    transition = settings.xsections.Transition(i, f)  
                    K = convolve.rate(transition, eedf)  
                output[-1][i][f] = K  
  
    container = rates.Rates(settings.temperatures/k, output, settings.comments)  
  
    with open(settings.dump + '.pickle', mode='w') as f:  
        35         p = cPickle.Pickler(f, protocol=2)  
         p.dump(container)
```

This script begins with the necessary imports as well as the necessary imports, most notably, the importation of the `settings` file. The `settings` file contains the necessary information for the generation of the rate constants: temperatures to use, type of distribution,

comments, output name. Two examples follow, the first, `combined.py`, was used to generate the electron-related rate coefficients.

```

1 import xsections.helium.ralchenko as xsections
2 import xsections.helium.nahar as nahar
3 from xsections.helium.states import states
4
5 import distributions
6 import numpy as np
7 from scipy.constants import e
8
9 temperatures = np.logspace(-1, np.log10(300), 1e2) * e
10
11 # Define the distribution to use and any inputs besides the temperature
12 distribution = distributions.drumax
13 kargs = {'x':1.0}
14
15 dump = 'combined'
16 comments = {'Cross-Sections':'(Ralchenko\u20142008), (Nahar\u20142010)', 
17             'Distribution':'Generalized\u2014Maxwellian',
18             'x':kargs['x'],
19             'Temperatures':'0.1\u2014300\u00b5eV, \u2014log\u2014spacing, \u2014100\u00b7points',
20             'Compiler':'Ben\u2014Yee'}
21
22 elastic = False

```

In this case the cross sections and rates are imported from separate files contained in the `xsections` directory. However, given the copyright on these cross sections, this information is not reproduced here. The settings file also imports the same `states.py` submodule as the `crammer` script. Additionally, the settings import the distribution submodule, `distributions.py`.

```

"""
File containing various distribution functions for testing. These can
be imported and passed to the rate solver as desired. It should be
easy to add to this file. NOTE: All distribution functions must be
continuous! Yes, this is inconvenient, but (at the moment) the rate
calculations do not evaluate at predictable or specified values of E.
"""

from numpy import array, log, exp
from scipy.special import gamma
from scipy.constants import *

def drumax(T, x):
    def dist(E):
        # Maxwellian for x = 1, Druyvesteyn for x = 2
        c1 = x * (2.0/3.0)**1.5 * (gamma(2.5/x))**1.5 / (gamma(1.5/x))**2.5
        c2 = ((2.0/3.0) * gamma(2.5/x) / gamma(1.5/x))**x
        return c1 * T**-1.5 * E**0.5 * exp(-c2 * (E/T)**x)
    return dist

def maxwellian(T):
    def dist(E):
        return 2/pi**0.5 * T**-1.5 * E**0.5 * exp(-E/T)
    return dist

```

This submodule includes a Maxwell-Boltzmann distribution, as well as a two-factor distribution which is continuously variable between a Druyvesteyn distribution and a Maxwell-Boltzmann.

After the settings are imported by the main script, it proceeds to assemble the rate coefficients by convolving the selected distribution function with the appropriate cross section. This is done via the `convolve.py` submodule.

```

1 | from numpy import array, log, exp, isnan, logspace, log10
2 | from scipy.integrate import quad, trapz
3 | from scipy.special import gamma
4 |
5 | from scipy.constants import e, m_e
6 |
7 | def rate(transition, f):
8 |     if transition.undefined:
9 |         return 0.0
10 |     sigma = transition.sigma
11 |     dE = transition.dE
12 |     def integrand(E):
13 |         # set up integrand for quadpack
14 |         return sigma(E) * f(E) * (2*E/m_e)**0.5
15 |     # Calculate the rate coefficient provided a list of electron temperatures
16 |     # and the expected distribution
17 |     if transition.inverse:
18 |         Emin = -2
19 |     else:
20 |         Emin = log10(dE/e)
21 |     Emax = log10((dE*1e3)/e)
22 |     energies = logspace(Emin, Emax, num=1e4) * e
23 |     values = integrand(energies)
24 |     integral = trapz(values, energies)
25 |     return integral
26 |
27 | def rate2(sigma, f):
28 |     def integrand(E):
29 |         # set up integrand for quadpack
30 |         return sigma(E) * f(E) * (2*E/m_e)**0.5
31 |     # Calculate the rate coefficient provided a list of electron temperatures
32 |     # and the expected distribution
33 |     Emin = -2
34 |     Emax = log10((1e3)/e)
35 |     energies = logspace(Emin, Emax, num=1e4) * e
36 |     values = integrand(energies)
37 |     integral = trapz(values, energies)
38 |     return integral

```

The convolve routine is a relatively simple numerical integration of the cross section with That said, the maximum integration energy is hard-coded, therefore the user should make the appropriate adjustments for reaction cross sections and distribution functions with significant values past 100 eV. the distribution function. That said, the maximum integration energy is hard-coded, therefore the user should make the appropriate adjustments for

reaction cross sections and distribution functions with significant values past 100 eV.

APPENDIX D

Additional Emission Measurements

D.1 0.3 Torr Emissions

D.2 0.5 Torr Emissions

D.3 1.0 Torr Emissions

D.4 2.0 Torr Emissions

D.5 3.0 Torr Emissions

D.6 4.0 Torr Emissions

D.7 8.0 Torr Emissions

D.8 16.0 Torr Emissions

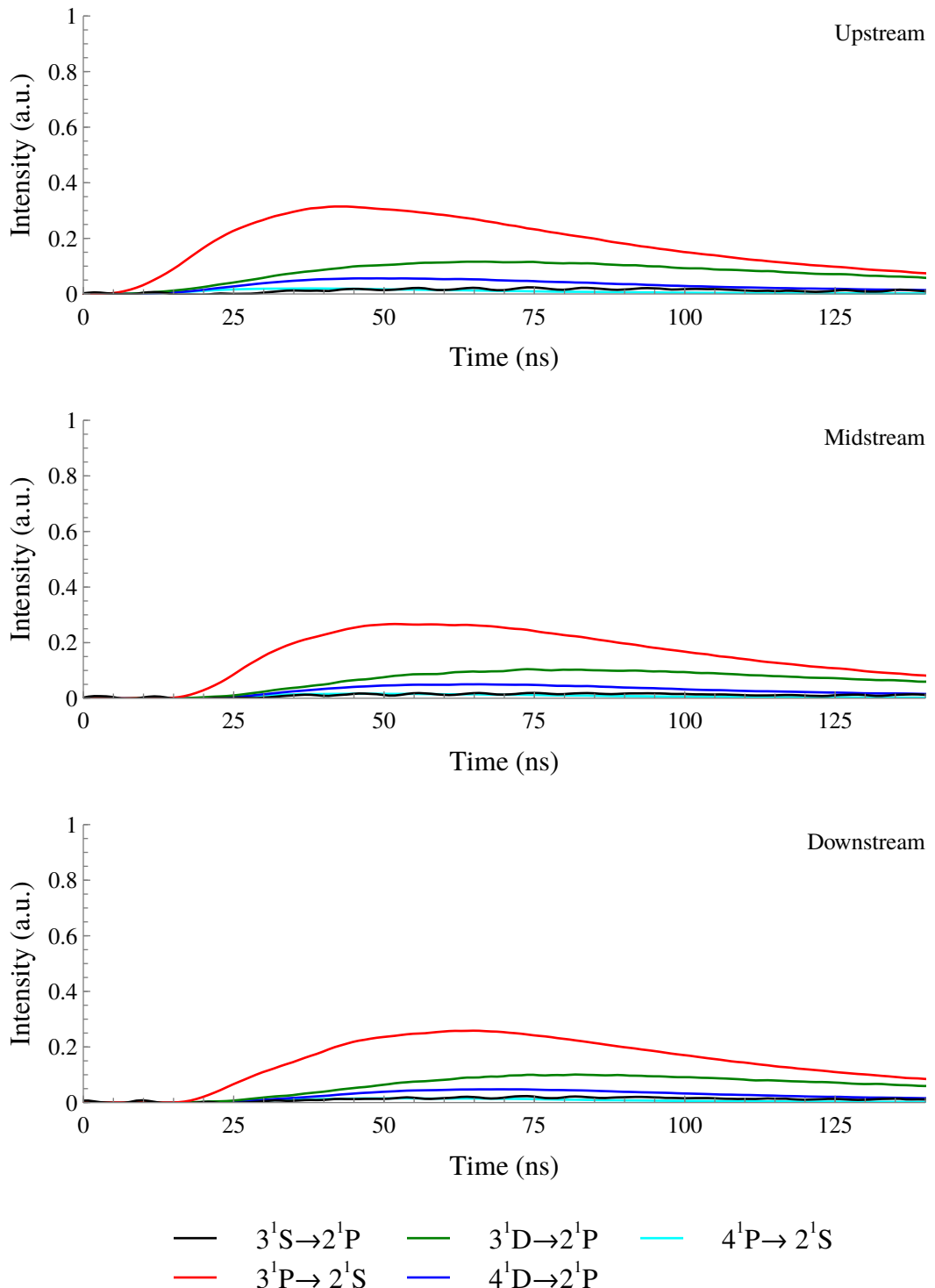


Figure D.1: Singlet emissions at 0.3 Torr.

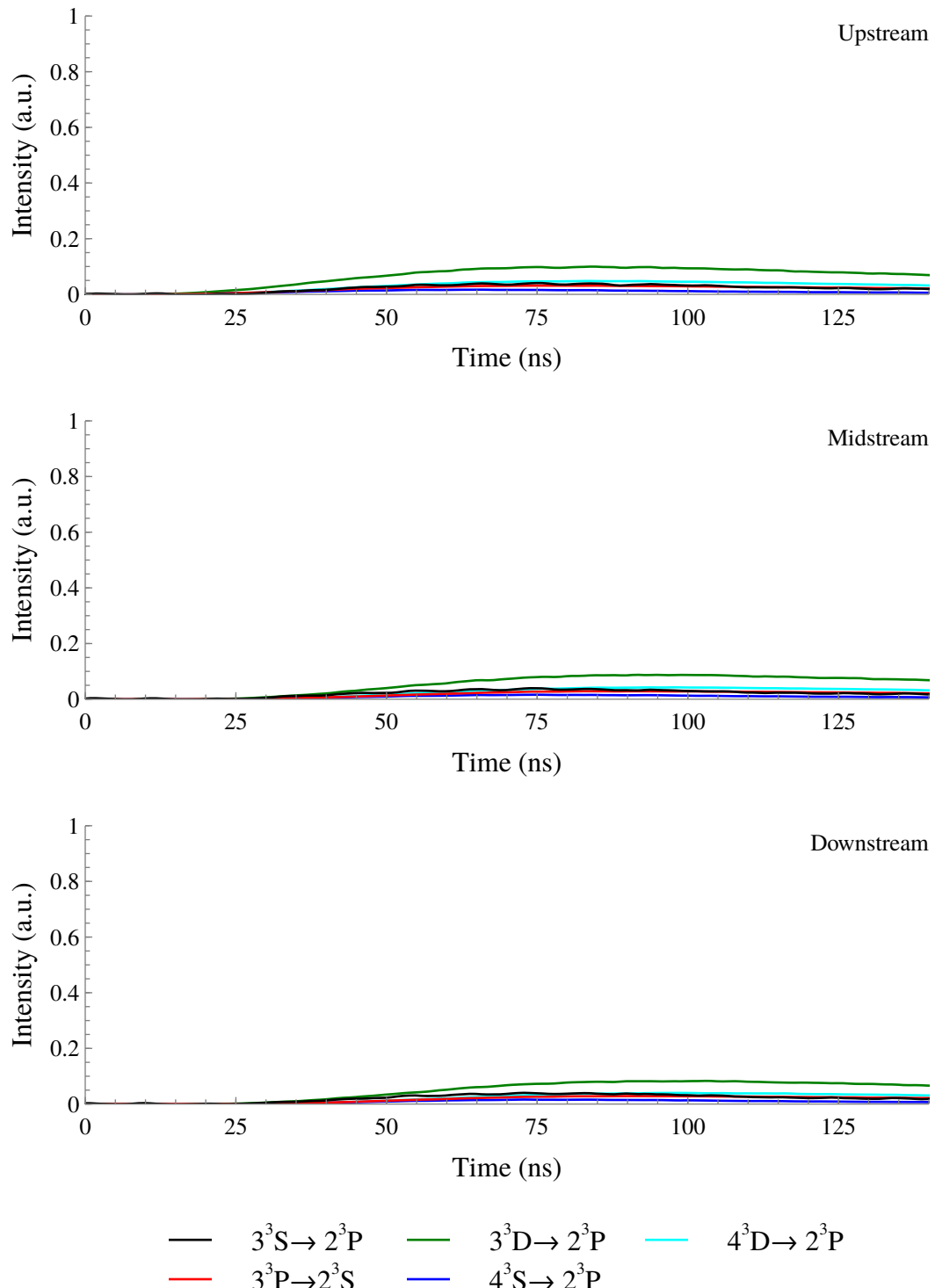


Figure D.2: Triple emissions at 0.3 Torr.

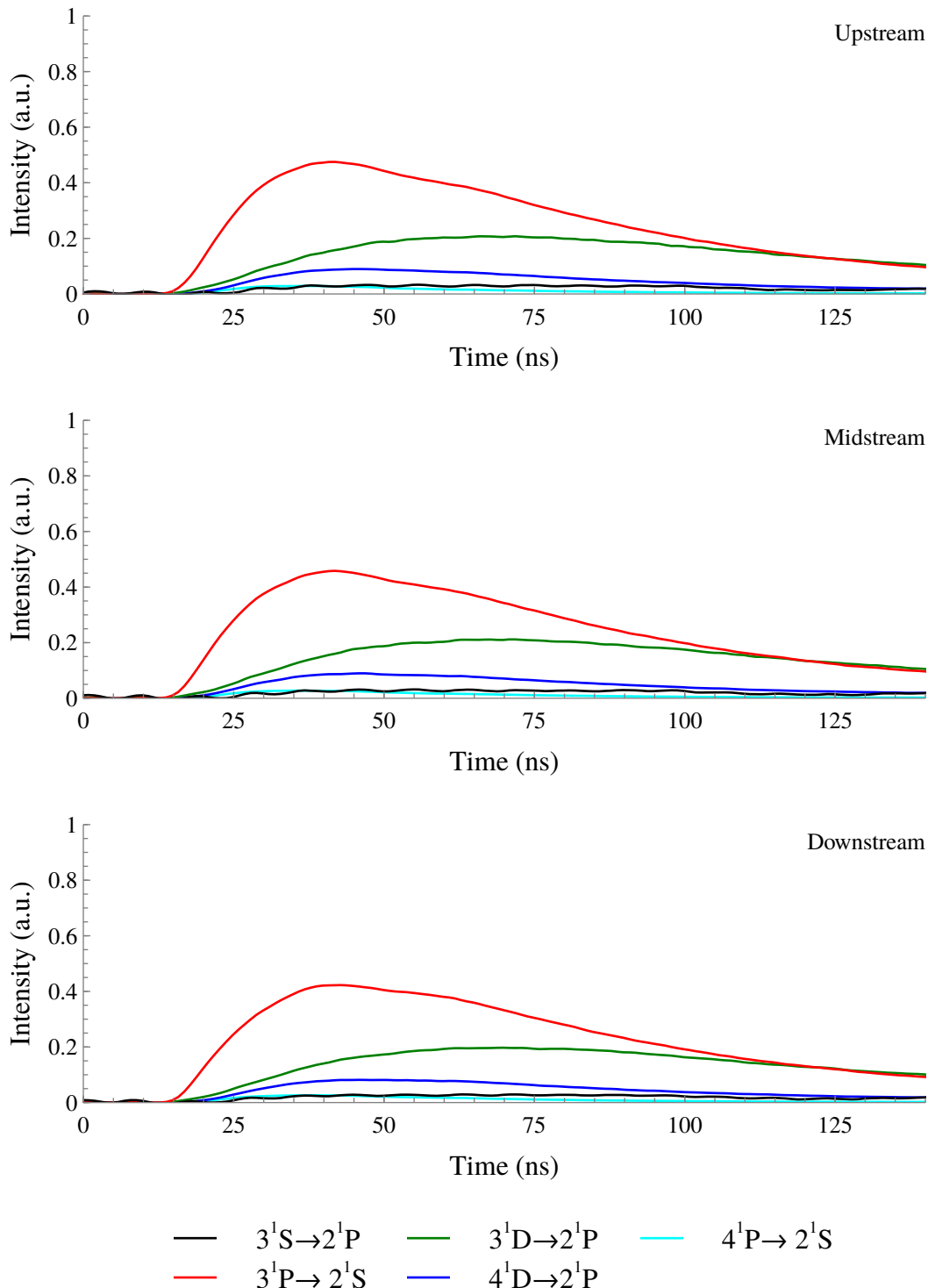


Figure D.3: Singlet emissions at 0.5 Torr.

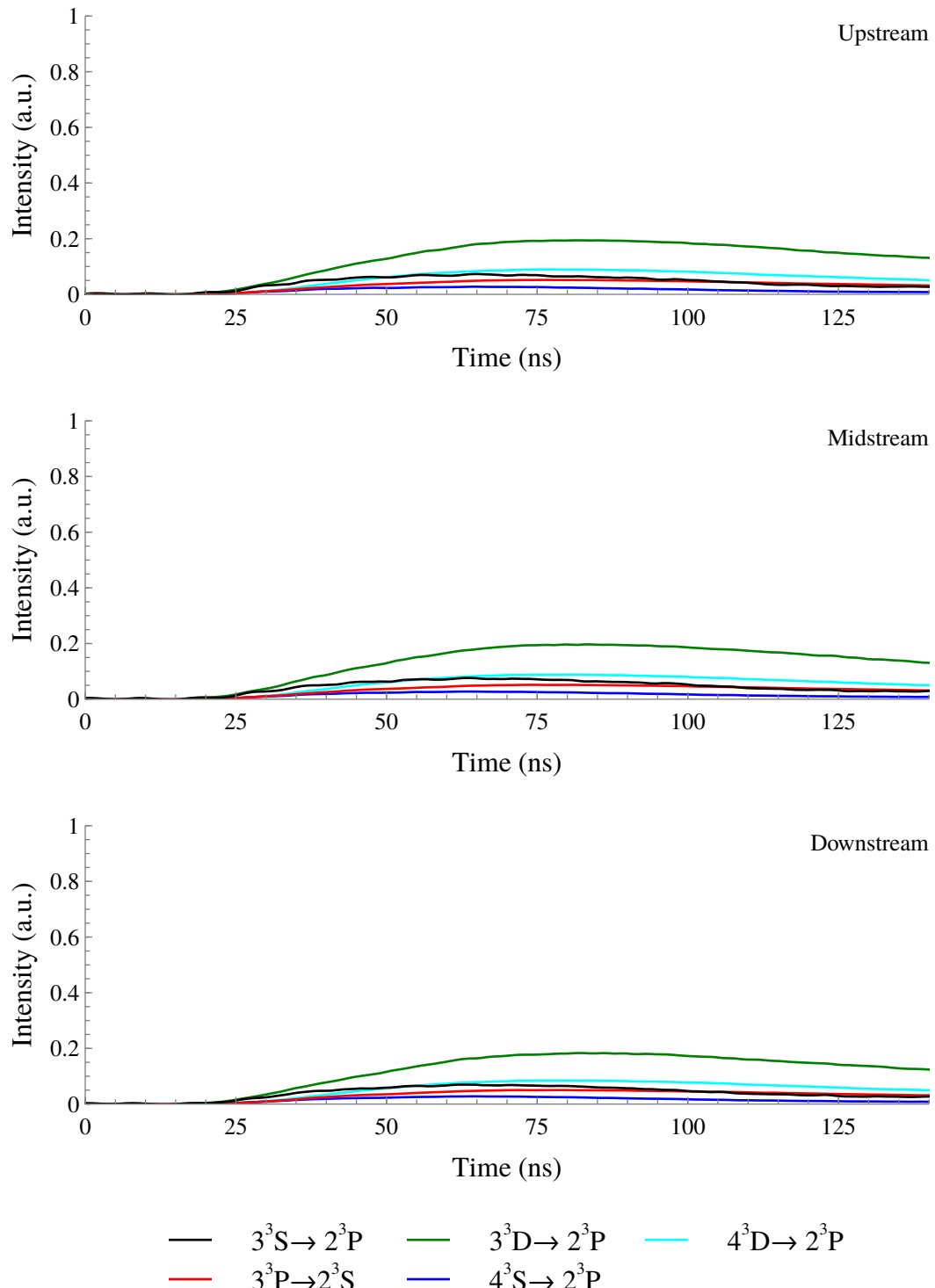


Figure D.4: Triple emissions at 0.5 Torr.

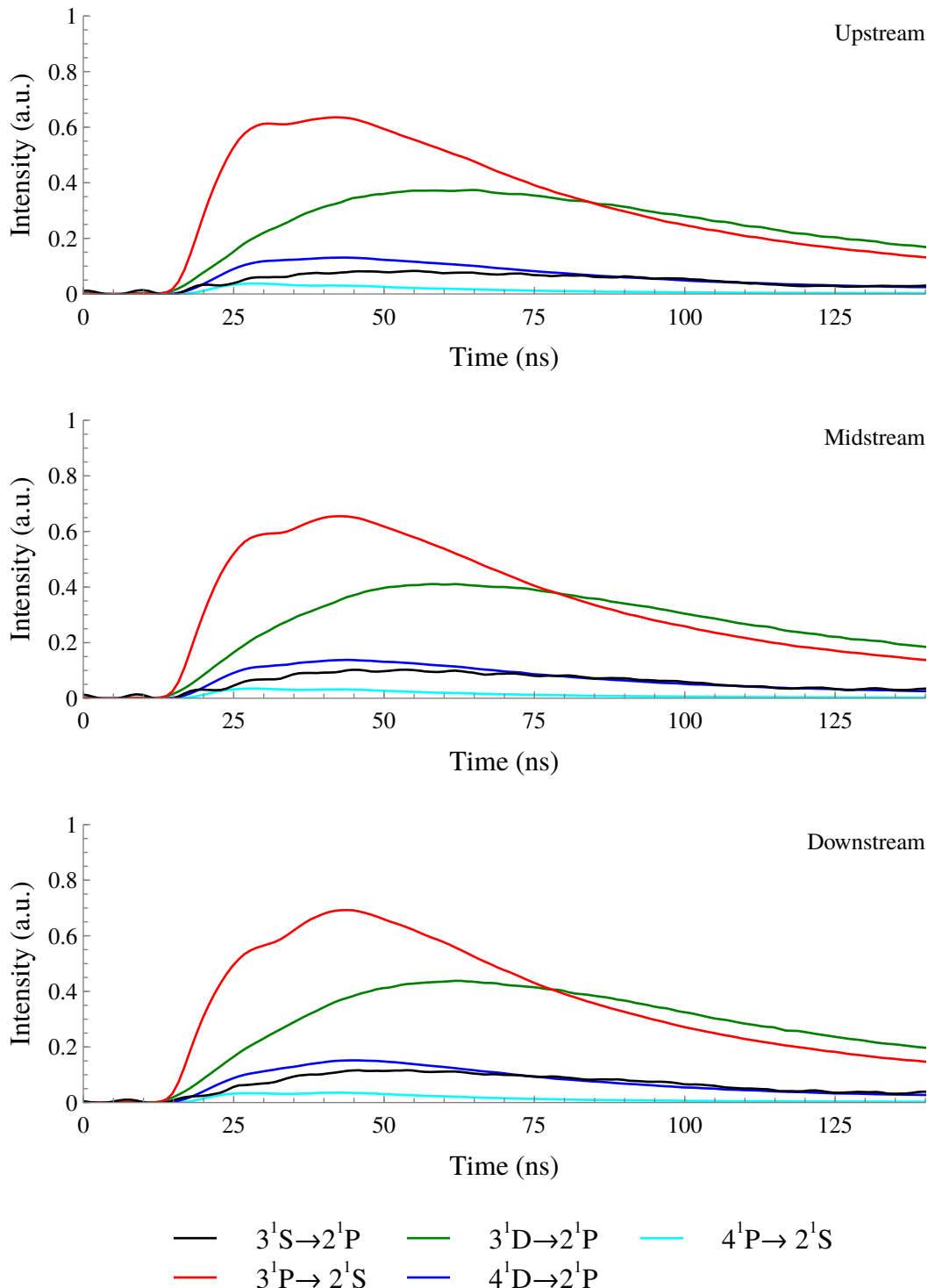


Figure D.5: Singlet emissions at 1.0 Torr.

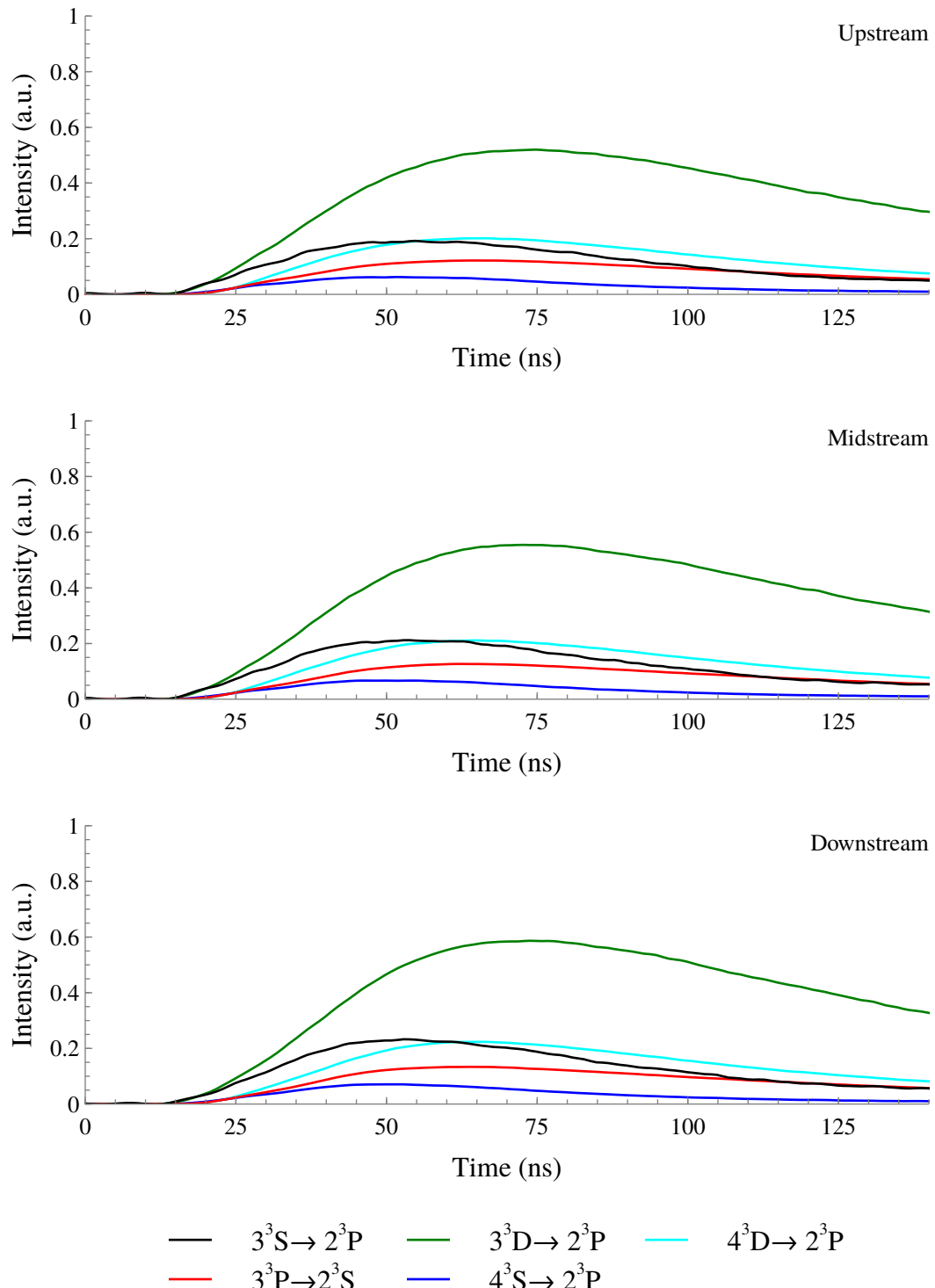


Figure D.6: Triple emissions at 1.0 Torr.

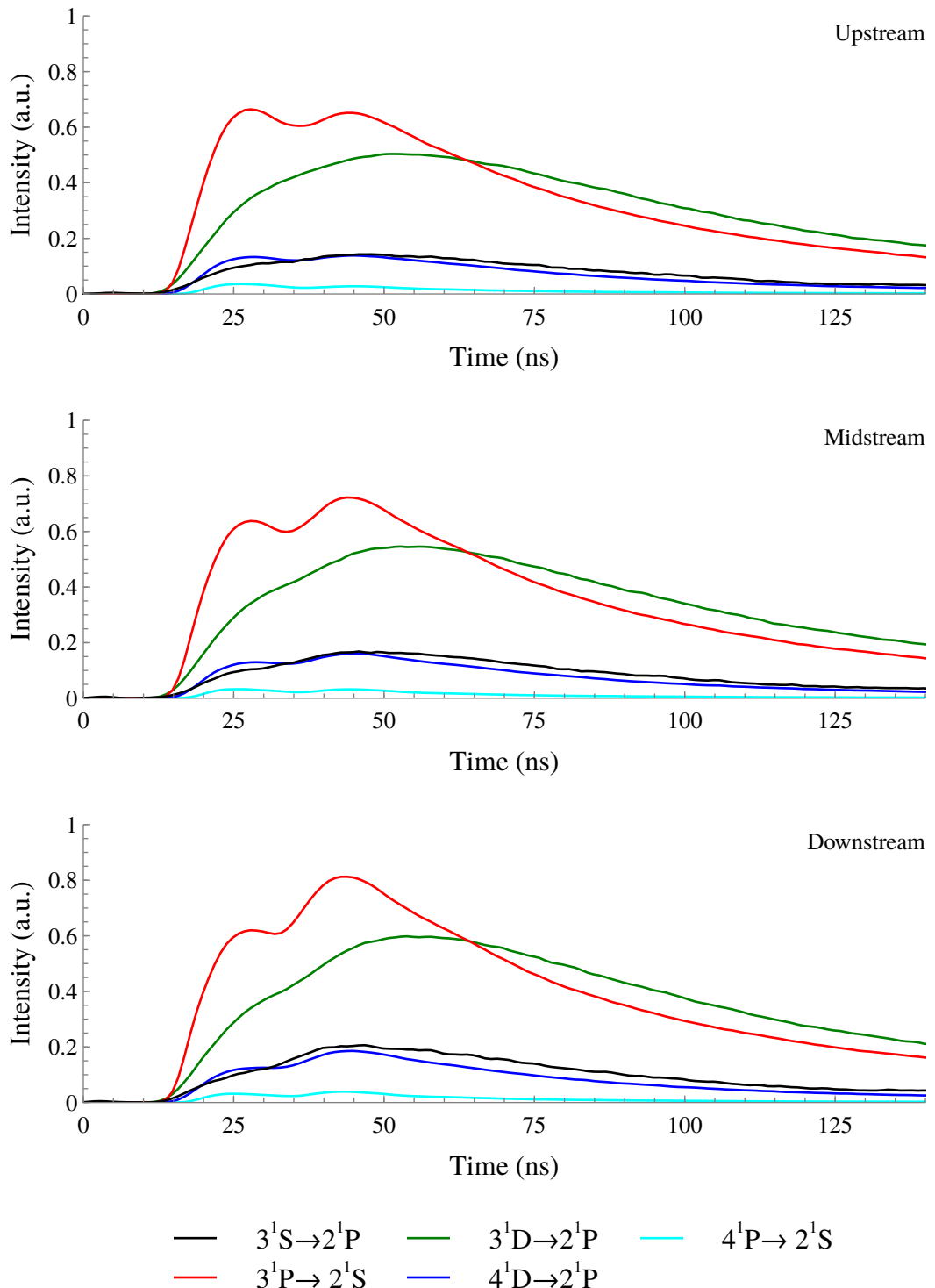


Figure D.7: Singlet emissions at 2.0 Torr.

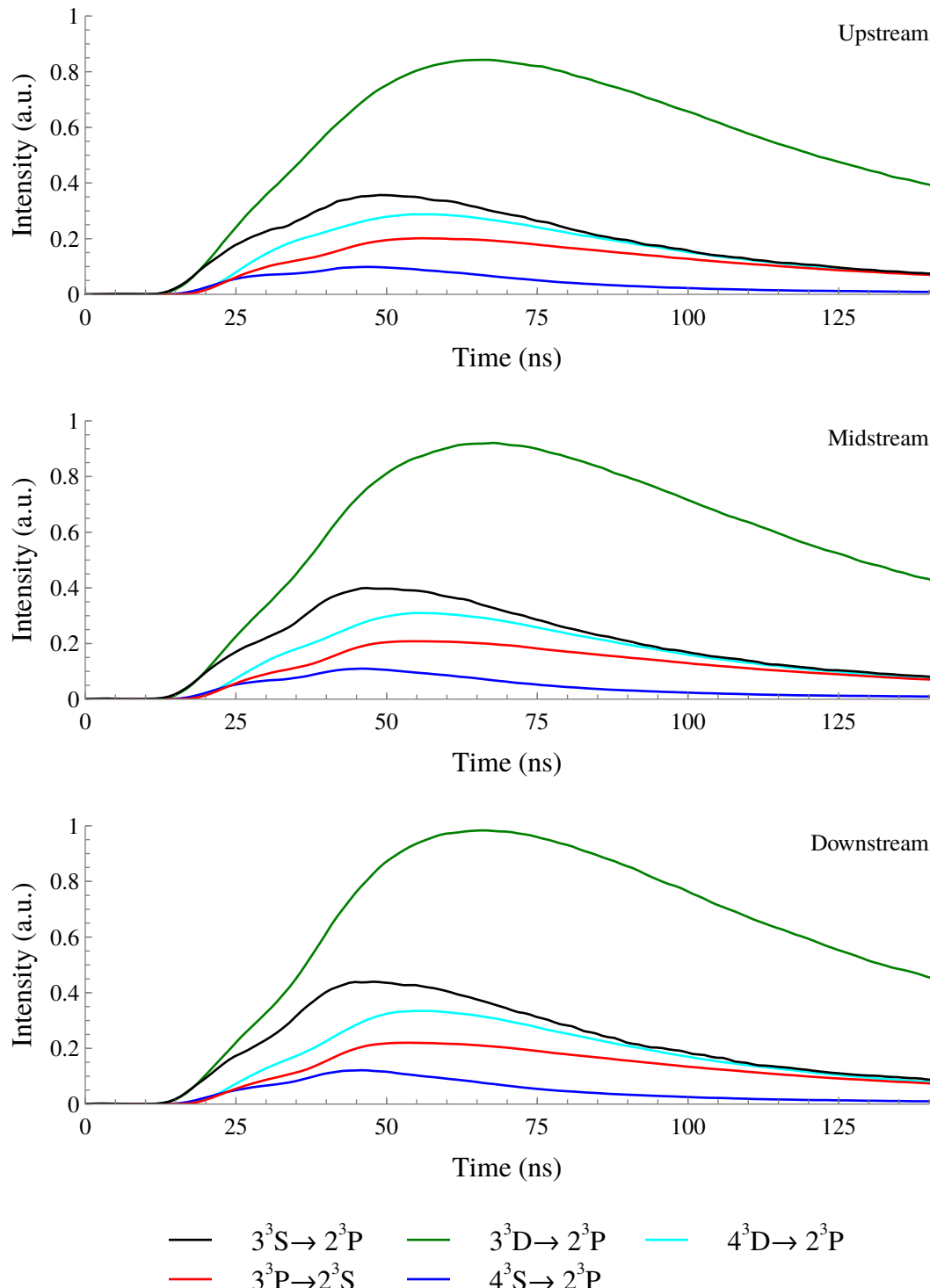


Figure D.8: Triple emissions at 2.0 Torr.

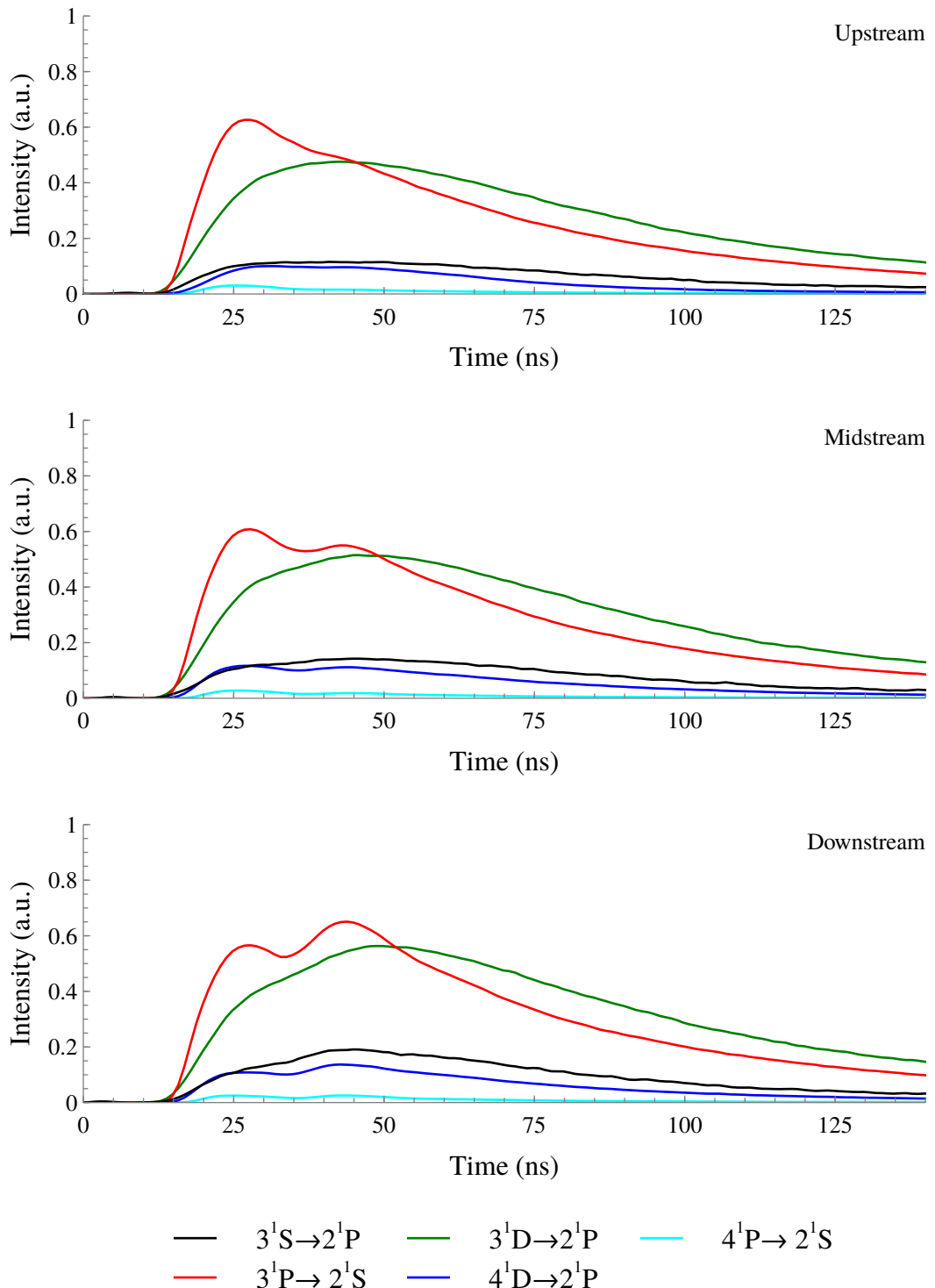


Figure D.9: Singlet emissions at 3.0 Torr.

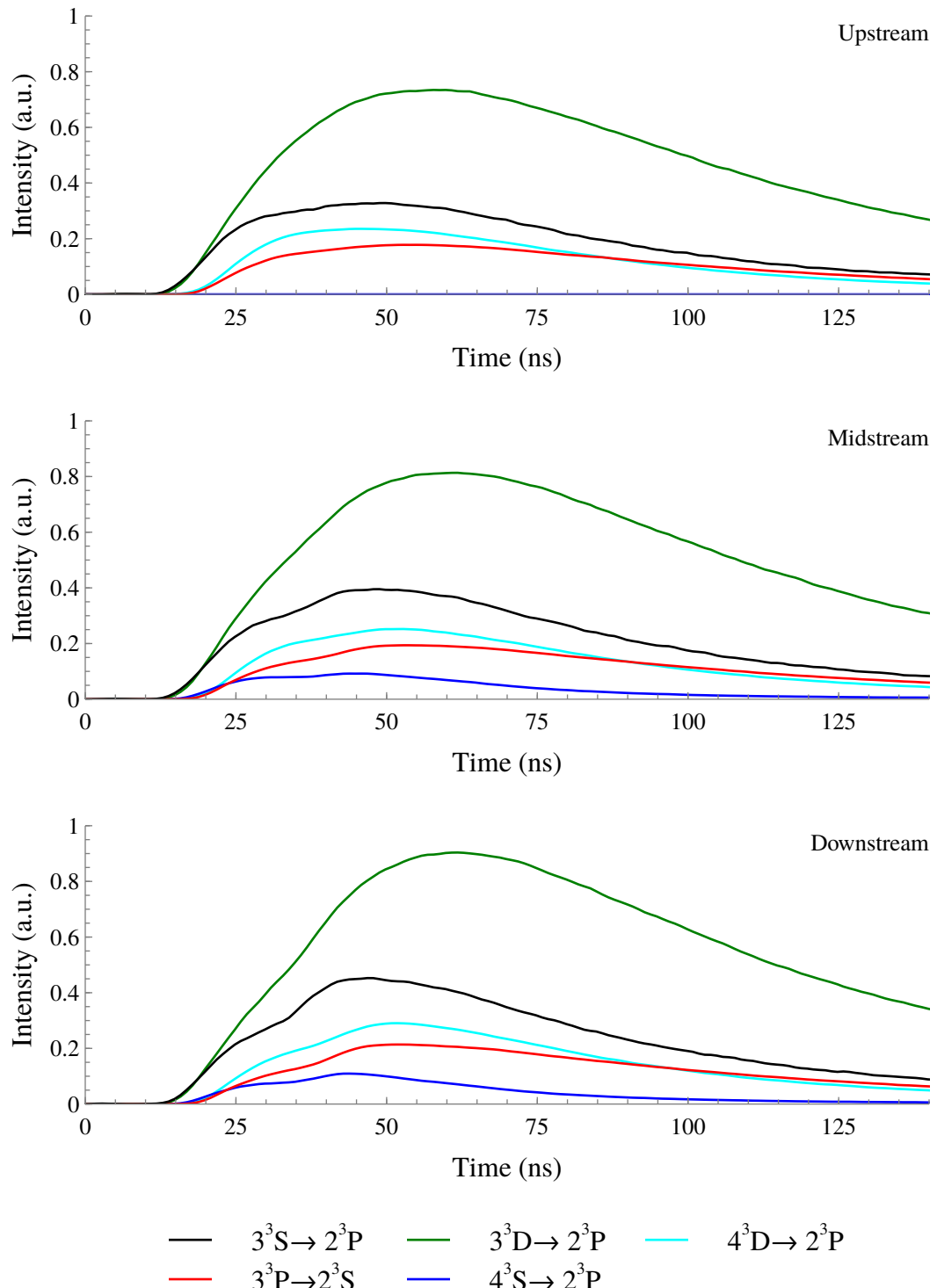


Figure D.10: Triple emissions at 3.0 Torr.

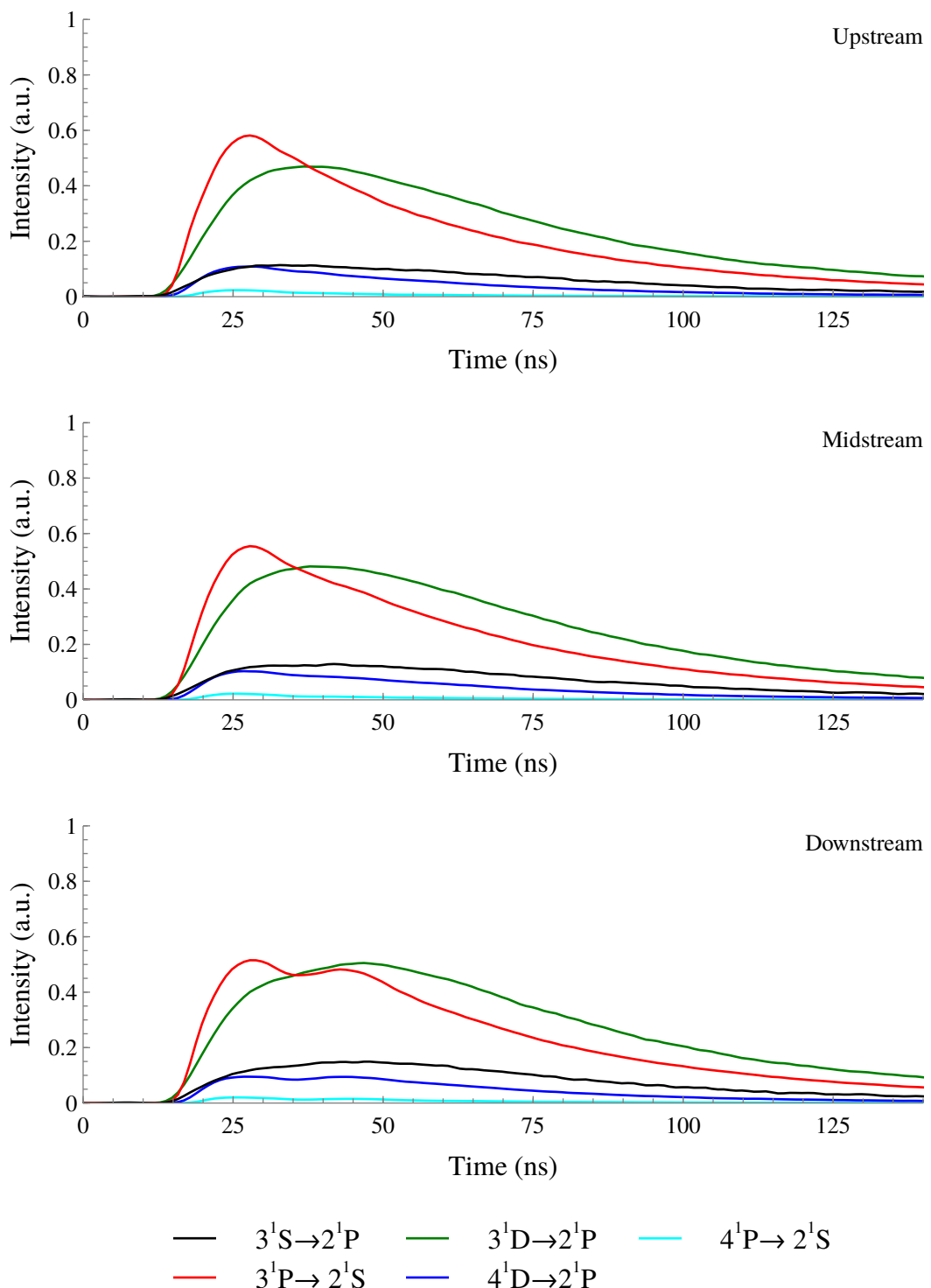


Figure D.11: Singlet emissions at 4.0 Torr.

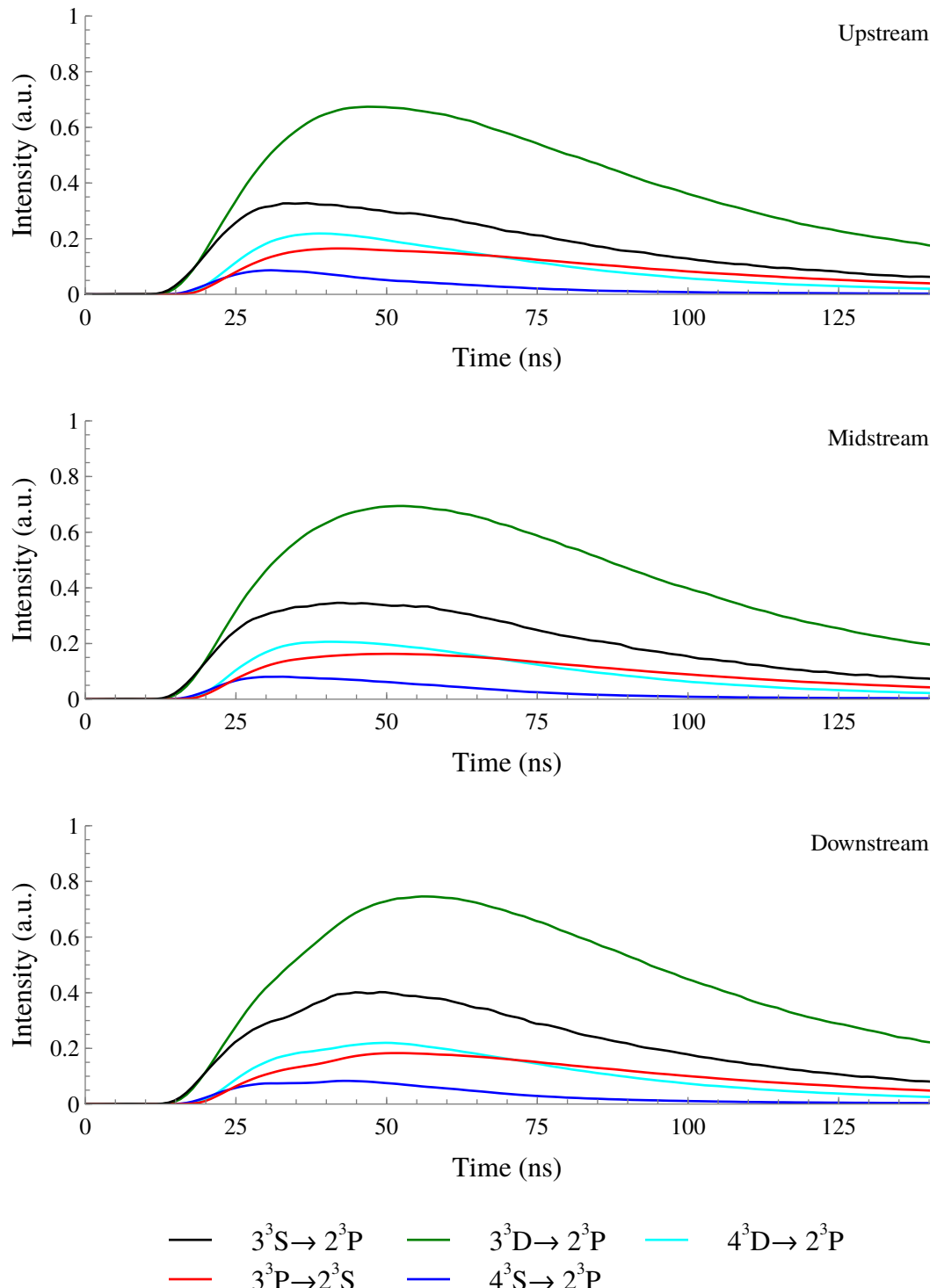


Figure D.12: Triple emissions at 4.0 Torr.

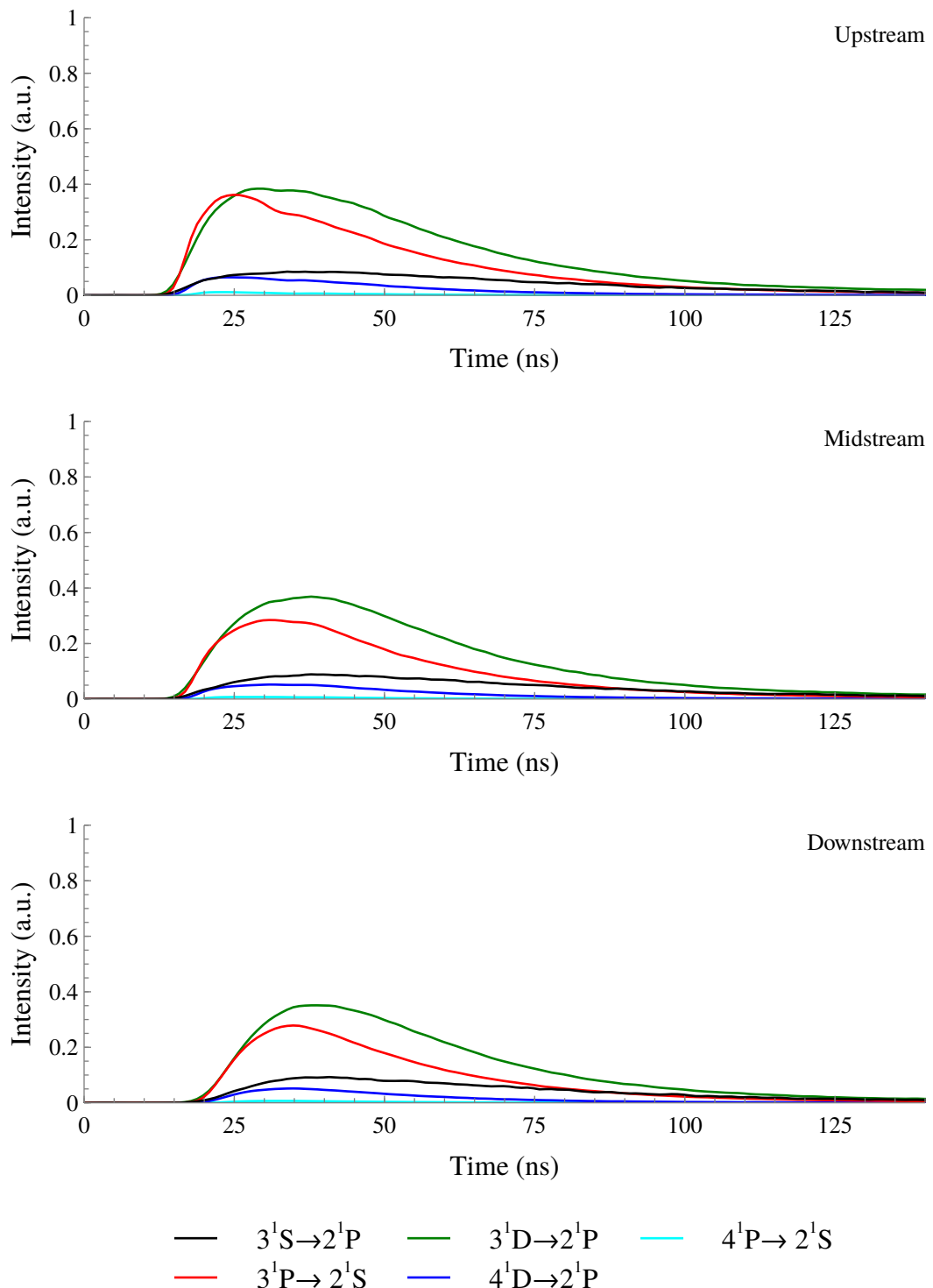


Figure D.13: Singlet emissions at 8.0 Torr.

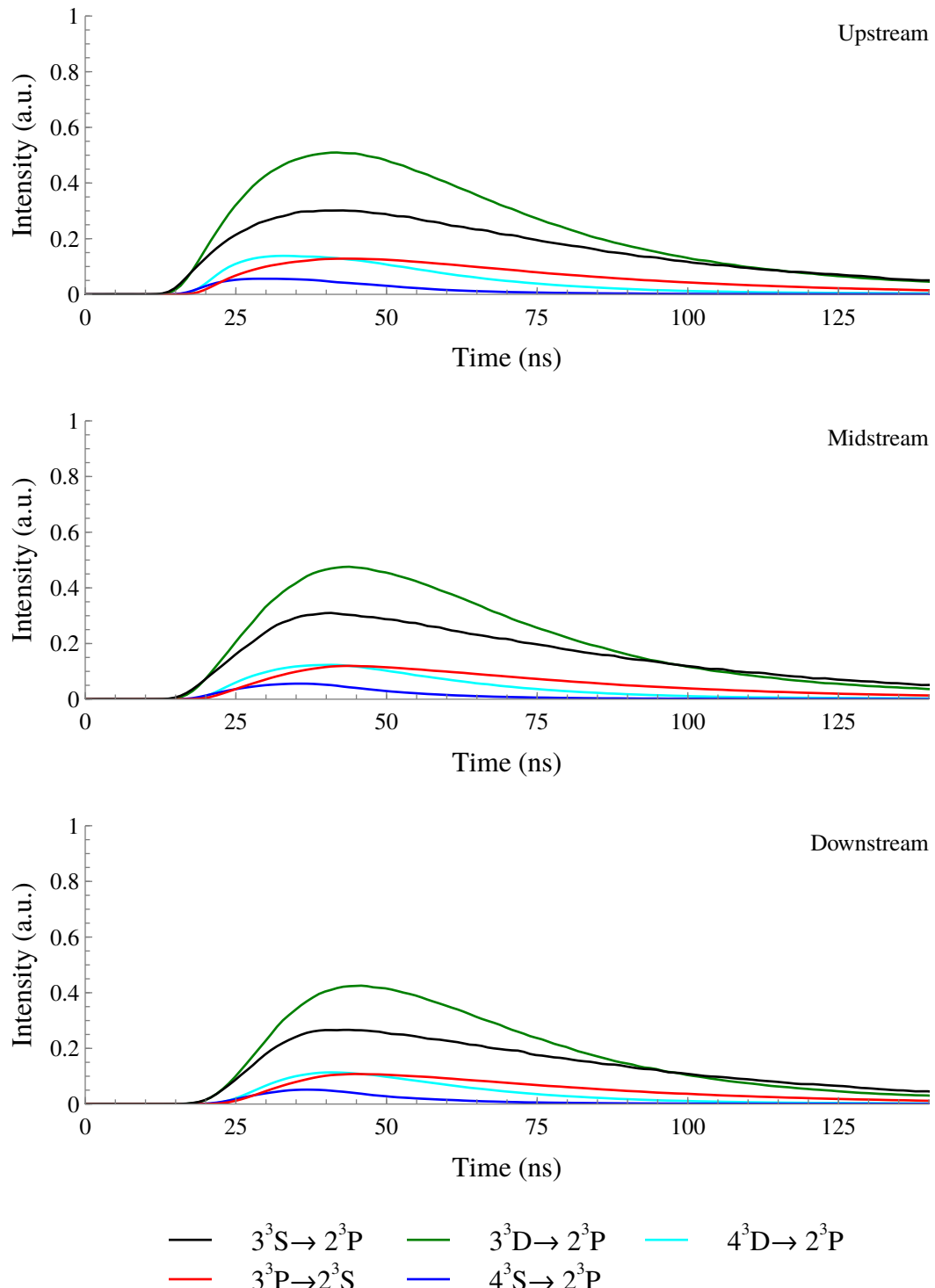


Figure D.14: Triple emissions at 8.0 Torr.

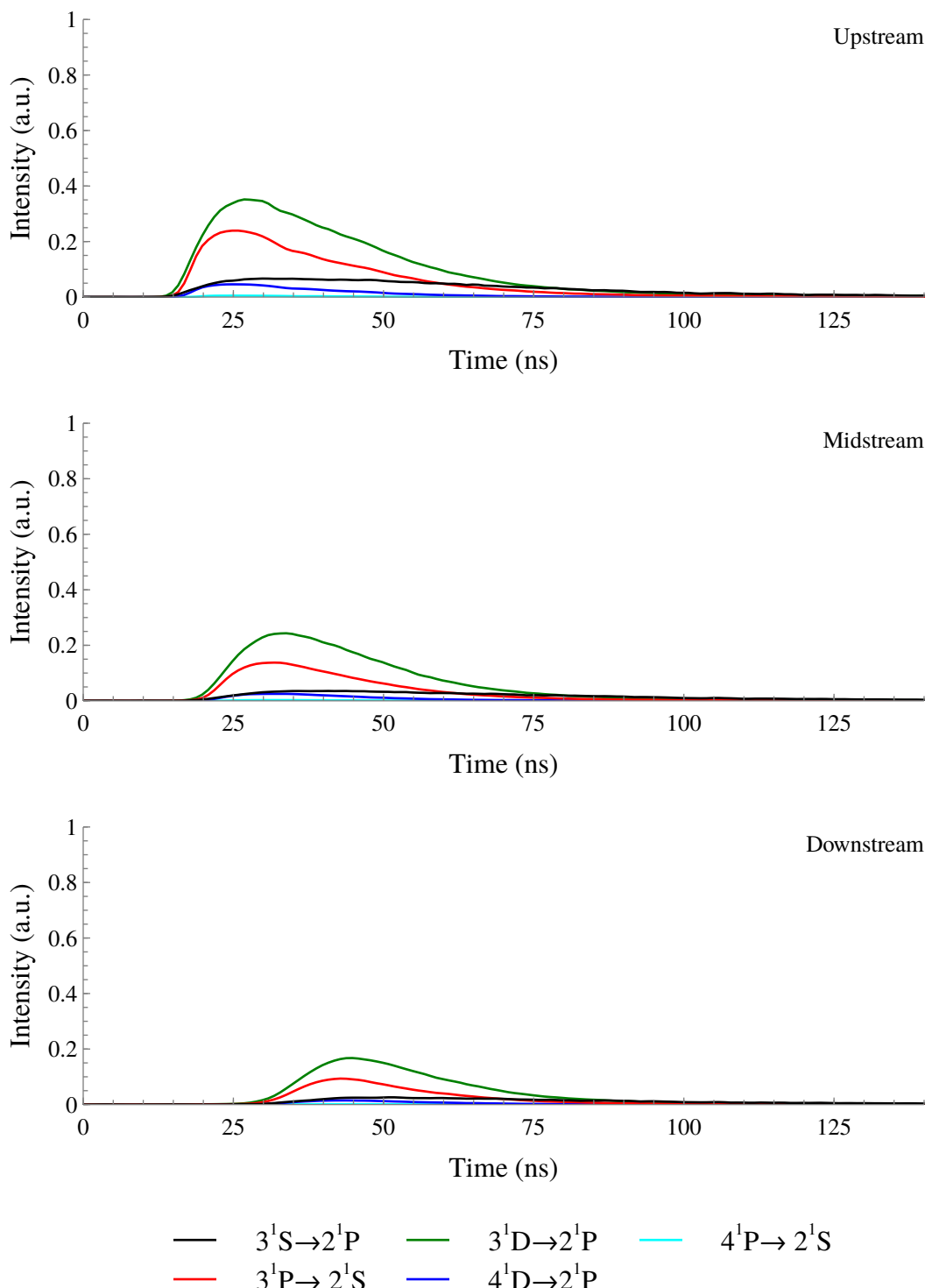


Figure D.15: Singlet emissions at 16.0 Torr.

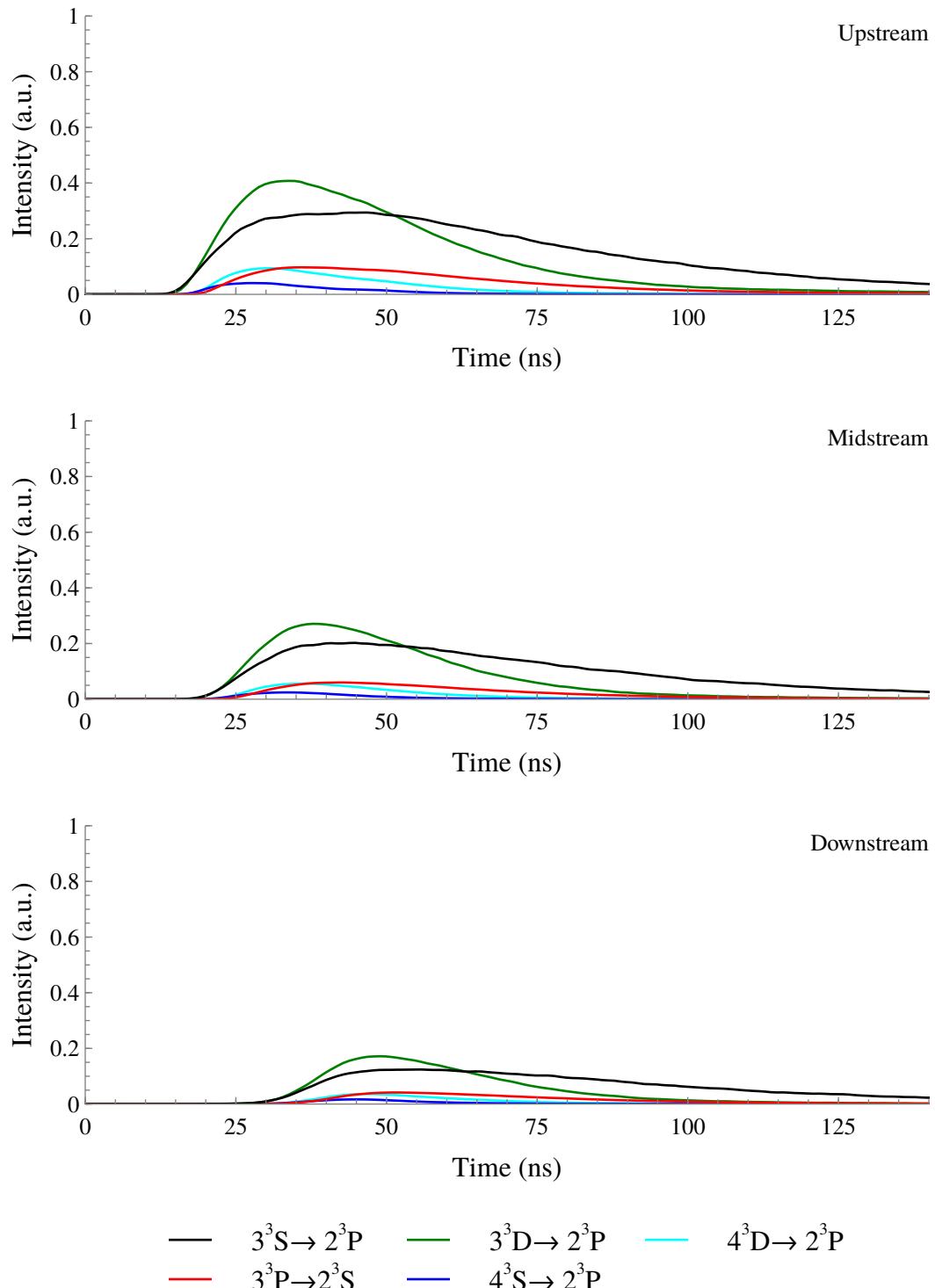


Figure D.16: Triple emissions at 16.0 Torr.

BIBLIOGRAPHY

- [1] J. J. Thomson. *Notes on Recent Researches in Electricity and Magnetism*. Clarendon Press, Oxford, UK, 1893.
- [2] J. D. Huba. *NRL Plasma Formulary*. Naval Research Laboratory, Washington, D.C., 2011.
- [3] J. I. Levatter and S. C. Lin. Necessary conditions for the homogeneous formation of pulsed avalanche discharges at high gas pressures. *Journal of Applied Physics*, 51(1):210, 1980.
- [4] E. E. Kunhardt and W. Byszewski. Development of overvoltage breakdown at high gas pressure. *Physical Review A*, 21(6):2069–2077, June 1980.
- [5] C. E. Moore and P. W. Merrill. Partial Grotrian Diagrams of Astrophysical Interest. Technical report, National Bureau of Standards, Washington, D.C., 1968.
- [6] C. K. Birdsall. Particle-in-cell charged-particle simulations, plus Monte Carlo collisions with neutral atoms, PIC-MCC. *IEEE Transactions on Plasma Science*, 19(2):65–85, April 1991.
- [7] Plasma 2010 Committee. *Plasma Science: Advancing Knowledge in the National Interest*. Number 2007. The National Academies Press, Washington, D.C., 2007.
- [8] K. E. Greenberg and G. A. Hebner. Electric-field measurements in 13.56 MHz helium discharges. *Applied Physics Letters*, 63(24):3282, 1993.
- [9] E. E. Kunhardt. Generation of large-volume, atmospheric-pressure, nonequilibrium plasmas. *IEEE Transactions on Plasma Science*, 28(1):189–200, 2000.
- [10] K. H. Becker, U. Kogelschatz, K. H. Schoenbach, and R. J. Barker. *Non-Equilibrium Air Plasmas at Atmospheric Pressure*. Institute of Physics Publishing, Bristol, UK, 2005.
- [11] S. Rauf and M. J. Kushner. Dynamics of a coplanar-electrode plasma display panel. II. Cell optimization. *Journal of Applied Physics*, 85(7):3470, 1999.
- [12] M. A. Malik, A. Ghaffar, and S. A. Malik. Water purification by electrical discharges. *Plasma Sources Science and Technology*, 10(1):82–91, February 2001.

- [13] H. Ayan, D. Staack, G. Fridman, A. Gutsol, Y. Mukhin, A. Yu. Starikovskii, A. Fridman, and G. Friedman. Application of nanosecond-pulsed dielectric barrier discharge for biomedical treatment of topographically non-uniform surfaces. *Journal of Physics D: Applied Physics*, 42(12):125202, June 2009.
- [14] M. Nishihara and I. V. Adamovich. Numerical Simulation of a Crossed Pulser-Sustainer Discharge in Transverse Magnetic Field. *IEEE Transactions on Plasma Science*, 35(5):1312–1324, October 2007.
- [15] K. Ostrikov, U. Cvelbar, and A. B. Murphy. Plasma nanoscience: setting directions, tackling grand challenges. *Journal of Physics D: Applied Physics*, 44(17):174001, May 2011.
- [16] U. Kogelschatz. Dielectric-Barrier Discharges: Their History, Discharge Physics, and Industrial Applications. *Plasma Chemistry and Plasma Processing*, 23(1):1–46, 2003.
- [17] F. Iza and J. Hopwood. Split-ring resonator microplasma: microwave model, plasma impedance and power efficiency. *Plasma Sources Science and Technology*, 14(2):397–406, May 2005.
- [18] I. V. Adamovich, W. R. Lempert, M. Nishihara, J. W. Rich, and Yu. G. Utkin. Repetitively Pulsed Nonequilibrium Plasmas for Magnetohydrodynamic Flow Control and Plasma-Assisted Combustion. *Journal of Propulsion and Power*, 24(6):1198–1215, November 2008.
- [19] L. M. Vasiliyak, S. V. Kostyuchenko, N. N. Kudryavtsev, and I. V. Filyugin. Fast ionisation waves under electrical breakdown conditions. *Physics-Uspekhi*, 37(3):247–268, March 1994.
- [20] J. L. Walsh, J. J. Shi, and M. G. Kong. Submicrosecond pulsed atmospheric glow discharges sustained without dielectric barriers at kilohertz frequencies. *Applied Physics Letters*, 89(16):161505, 2006.
- [21] S. M. Starikovskaia, A. Yu. Starikovskii, and D. V. Zatsepин. The development of a spatially uniform fast ionization wave in a large discharge volume. *Journal of Physics D: Applied Physics*, 31(9):1118–1125, May 1998.
- [22] L. Tonks and I. Langmuir. A General Theory of the Plasma of an Arc. *Physical Review*, 34(6):876–922, September 1929.
- [23] A. Anders. Tracking down the origin of arc plasma science-II. early continuous discharges. *IEEE Transactions on Plasma Science*, 31(5):1060–1069, October 2003.
- [24] S. M. Starikovskaia, N. B. Anikin, S. V. Pancheshnyi, D. V. Zatsepин, and A. Yu. Starikovskii. Pulsed breakdown at high overvoltage: development, propagation and energy branching. *Plasma Sources Science and Technology*, 10(2):344–355, May 2001.

- [25] V. M. Efanov, V. V. Karavaev, A. F. Kardo-Sysoev, and I. G. Tchashnikov. Fast ionization dynistor (FID)-a new semiconductor superpower closing switch. In *Digest of Technical Papers. 11th IEEE International Pulsed Power Conference (Cat. No.97CH36127)*, volume 2, pages 988–991. IEEE, 1997.
- [26] L. B. Loeb. Ionizing Waves of Potential Gradient: Luminous pulses in electrical breakdown, with velocities a third that of light, have a common basis. *Science (New York, N.Y.)*, 148(3676):1417–26, June 1965.
- [27] C. Wheatstone. Versuche, die Geschwindigkeit der Elektricität und die Dauer des elektrischen Lichts zu messen. *Annalen der Physik und Chemie*, 110(3):464–480, 1835.
- [28] W. v. Zahn. Spectralröhren mit longitudinaler Durchsicht. *Annalen der Physik und Chemie*, 244(12):675–675, 1879.
- [29] J. James. Die Abraham-Lemoinesche Methode zur Messung sehr kleiner Zeitintervalle und ihre Anwendung zur Bestimmung der Richtung und Geschwindigkeit der Entladung in Entladungsrohren. *Annalen der Physik*, 320(15):954–987, 1904.
- [30] R. Whiddington. The Discharge of Electricity through Vacuum Tubes. *Nature*, 116(2918):506–509, October 1925.
- [31] J. Beams. The Time Interval Between the Appearance of Spectrum Lines in Spark and in Condensed Discharges. *Physical Review*, 28(3):475–480, September 1926.
- [32] B. F. J. Schonland and H. Collens. Development of the Lightning Discharge. *Nature*, 132(3332):407–408, September 1933.
- [33] A. M. Cravath and L. B. Loeb. The Mechanism of the High Velocity of Propagation of Lightning Discharges. *Physics*, 6(4):125, 1935.
- [34] L. Snoddy, J. Beams, and J. Dietrich. The Propagation of Potential in Discharge Tubes. *Physical Review*, 50(5):469–471, September 1936.
- [35] E. Flegler and H. Raether. Der elektrische Durchschlag in Gasen nach Untersuchungen mit der Nebelkammer. *Zeitschrift f r Physik*, 99(9-10):635–642, September 1936.
- [36] L. B. Loeb and J. M. Meek. The Mechanism of Spark Discharge in Air at Atmospheric Pressure. I. *Journal of Applied Physics*, 11(6):438, June 1940.
- [37] L. B. Loeb and J. M. Meek. The Mechanism of Spark Discharge in Air at Atmospheric Pressure. II. *Journal of Applied Physics*, 11(7):459, 1940.
- [38] J. Meek. A Theory of Spark Discharge. *Physical Review*, 57(8):722–728, April 1940.
- [39] L. Fisher and B. Bedderson. Formative Time Lags of Spark Breakdown in Air in Uniform Fields at Low Overvoltages. *Physical Review*, 81(1):109–114, January 1951.

- [40] G. Kachickas and L. Fisher. Formative Time Lags of Uniform Field Breakdown in N₂. *Physical Review*, 88(4):878–883, November 1952.
- [41] G. Kachickas and L. Fisher. Formative Time Lags of Uniform Field Breakdown in Argon. *Physical Review*, 91(4):775–779, August 1953.
- [42] E. E. Kunhardt and Y. Tzeng. Development of an electron avalanche and its transition into streamers. *Physical review. A*, 38(3):1410–1421, August 1988.
- [43] I. D. Chalmers. The transient glow discharge in nitrogen and dry air. *Journal of Physics D: Applied Physics*, 4(8):1147–1151, August 1971.
- [44] W. Rogowski, E. Flegler, and R. Tamm. Über Wanderwelle und Durchschlag. *Archiv für Elektrotechnik*, 18(5):479–512, September 1927.
- [45] K. Buss. Der Stufendurchschlag. *Archiv für Elektrotechnik*, 26(4):266–272, April 1932.
- [46] T. E. Allibone and J. M. Meek. The Development of the Spark Discharge. II. *Proceedings of the Royal Society A: Mathematical, Physical and Engineering Sciences*, 169(937):246–268, December 1938.
- [47] T. E. Allibone and J. M. Meek. The Development of the Spark Discharge. *Proceedings of the Royal Society A: Mathematical, Physical and Engineering Sciences*, 166(924):97–126, May 1938.
- [48] T. E. Allibone. The Mechanism of a Long Spark. *Journal of the Institute of Electrical Engineers*, 82(497):513–521, 1938.
- [49] C. V. Boys. Progressive Lightning. *Nature*, 118(2977):749–750, November 1926.
- [50] T. E. Allibone. Development of the Spark Discharge. *Nature*, 161(4103):970–971, June 1948.
- [51] R. F. Saxe and J. M. Meek. Development of Spark Discharges. *Nature*, 162(4111):263–264, August 1948.
- [52] Yu. L. Stankevich and V. G. Kalinin. Fast Electrons and X-Ray Radiation during the Initial Stage of Growth of a Pulsed Spark Discharge in Air. *Soviet Physics Doklady*, 12, 1968.
- [53] G. A. Mesyats, Yu. I. Bychkov, and V. V. Kremnev. Pulsed nanosecond electric discharges in gases. *Soviet Physics Uspekhi*, 15(3):282–297, March 1972.
- [54] L. P. Babich, T. V. Loiko, and L. V. Tarasova. The physics of high-voltage nanosecond discharges in dense gases. *Radiophysics and Quantum Electronics*, 20(4):436–442, April 1977.

- [55] L. P. Babich, T. V. Loško, and V. A. Tsukerman. High-voltage nanosecond discharge in a dense gas at a high overvoltage with runaway electrons. *Soviet Physics Uspekhi*, 33(7):521–540, July 1990.
- [56] C. A. Fenstermacher. Electron-Beam-Controlled Electrical Discharge as a Method of Pumping Large Volumes of CO₂ Laser Media at High Pressure. *Applied Physics Letters*, 20(2):56, 1972.
- [57] A. J. Palmer. A physical model on the initiation of atmospheric-pressure glow discharges. *Applied Physics Letters*, 25(3):138, 1974.
- [58] R. O. Hunter. Electron beam controlled switching. In *International Pulsed Power Conference*, pages IC8–1 –IC8–6, New York, NY, 1976. Institute of Electrical Engineers, Inc.
- [59] B. M. Koval’chuk and G. A. Mesyats. Rapid cutoff of a high current in an electron-beam-excited discharge. *Soviet Technical Physics Letters*, 2(252), 1976.
- [60] B. B. Slavin and P. I. Sopin. Breakdown of a neutral gas by ionizing waves of the gradient of a negative potential. *High Temperature*, 30(1):1–9, 1992.
- [61] S. M. Starikovskaya and A. Yu. Starikovskii. Numerical modelling of the electron energy distribution function in the electric field of a nanosecond pulsed discharge. *Journal of Physics D: Applied Physics*, 34(23):3391–3399, December 2001.
- [62] S. V. Pancheshnyi, D. A. Lacoste, A. Bourdon, and C. O. Laux. Ignition of Propane-Air Mixtures by a Repetitively Pulsed Nanosecond Discharge. *IEEE Transactions on Plasma Science*, 34(6):2478–2487, December 2006.
- [63] S. M. Starikovskaya. Plasma assisted ignition and combustion. *Journal of Physics D: Applied Physics*, 39(16):R265–R299, August 2006.
- [64] S. O. Macheret, M. N. Schneider, and R. B. Miles. Modeling of air plasma generation by repetitive high-voltage nanosecond pulses. *IEEE Transactions on Plasma Science*, 30(3):1301–1314, June 2002.
- [65] S. J. Schneider, H. Kamhawi, and I. M. Blankson. Efficient Ionization Investigation for Flow Control and Energy Extraction. *AIAA 47th Aerospace Sciences Meeting*, 2009.
- [66] A. Yu. Starikovskii, A. A. Nikipelov, M. M. Nudnova, and D. V. Roupasov. SDBD plasma actuator with nanosecond pulse-periodic discharge. *Plasma Sources Science and Technology*, 18(3):034015, August 2009.
- [67] I. V. Adamovich, M. Nishihara, I. Choi, M. Uddi, and W. R. Lempert. Energy coupling to the plasma in repetitive nanosecond pulse discharges. *Physics of Plasmas*, 16(11):113505, 2009.

- [68] D. S. Nikandrov, L. D. Tsendar, V. I. Kolobov, and R. R. Arslanbekov. Theory of Pulsed Breakdown of Dense Gases and Optimization of the Voltage Waveform. *IEEE Transactions on Plasma Science*, 36(1):131–139, 2008.
- [69] J. L. Zimmermann, T. Shimizu, H. U. Schmidt, Y. F. Li, G. E. Morfill, and G Isbary. Test for bacterial resistance build-up against plasma treatment. *New Journal of Physics*, 14(7):073037, July 2012.
- [70] J. E. Foster, G. Adamovsky, S. N. Gucker, and I. M. Blankson. A Comparative Study of the Time-Resolved Decomposition of Methylene Blue Dye Under the Action of a Nanosecond Repetitively Pulsed DBD Plasma Jet Using Liquid Chromatography and Spectrophotometry. *IEEE Transactions on Plasma Science*, 41(3):503–512, March 2013.
- [71] G. Pilla, D. Galley, D. A. Lacoste, F. Lacas, D. Veynante, and C. O. Laux. Stabilization of a Turbulent Premixed Flame Using a Nanosecond Repetitively Pulsed Plasma. *IEEE Transactions on Plasma Science*, 34(6):2471–2477, December 2006.
- [72] M. Nishihara, J. W. Rich, W. R. Lempert, I. V. Adamovich, and S. Gogineni. Low-temperature $M=3$ flow deceleration by Lorentz force. *Physics of Fluids*, 18(8):086101, 2006.
- [73] A. Bao, Yu. G. Utkin, S. Keshav, G. Lou, and I. V. Adamovich. Ignition of Ethylene–Air and Methane–Air Flows by Low-Temperature Repetitively Pulsed Nanosecond Discharge Plasma. *IEEE Transactions on Plasma Science*, 35(6):1628–1638, December 2007.
- [74] G. Lou, A. Bao, M. Nishihara, S. Keshav, Yu. G. Utkin, J. W. Rich, W. R. Lempert, and I. V. Adamovich. Ignition of premixed hydrocarbon–air flows by repetitively pulsed, nanosecond pulse duration plasma. *Proceedings of the Combustion Institute*, 31(2):3327–3334, January 2007.
- [75] D. Z. Pai, G. D. Stancu, D. A. Lacoste, and C. O. Laux. Nanosecond repetitively pulsed discharges in air at atmospheric pressure—the glow regime. *Plasma Sources Science and Technology*, 18(4):045030, November 2009.
- [76] Y. Zuzeek, I. Choi, M. Uddi, I. V. Adamovich, and W. R. Lempert. Pure rotational CARS thermometry studies of low-temperature oxidation kinetics in air and ethene–air nanosecond pulse discharge plasmas. *Journal of Physics D: Applied Physics*, 43(12):124001, March 2010.
- [77] M. Nishihara, K. U. Takashima, J. R. Bruzzese, I. V. Adamovich, and D. Gaitonde. Experimental and Computational Studies of Low-Temperature Mach 4 Flow Control by Lorentz Force. *Journal of Propulsion and Power*, 27(2):467–476, March 2011.
- [78] T. Ito, D. Luggenhölscher, K. Kobayashi, S. Müller, U. Czarnetzki, and S. Hamaguchi. Electric field measurement in an atmospheric or higher pressure gas by coherent Raman scattering of nitrogen. *Journal of Physics D: Applied Physics*, 42(9):092003, May 2009.

- [79] T. Ito, K. Kobayashi, U. Czarnetzki, and S. Hamaguchi. Rapid formation of electric field profiles in repetitively pulsed high-voltage high-pressure nanosecond discharges. *Journal of Physics D: Applied Physics*, 43(6):062001, February 2010.
- [80] S. Müller, D. Luggenhölscher, and U. Czarnetzki. Ignition of a nanosecond-pulsed near atmospheric pressure discharge in a narrow gap. *Journal of Physics D: Applied Physics*, 44(16):165202, April 2011.
- [81] S. O. Macheret, M. N. Shneider, and R. C. Murray. Ionization in strong electric fields and dynamics of nanosecond-pulse plasmas. *Physics of Plasmas*, 13(2):023502, 2006.
- [82] M. Laroussi and X. Lu. Room-temperature atmospheric pressure plasma plume for biomedical applications. *Applied Physics Letters*, 87(11):113902, 2005.
- [83] X. Lu and M. Laroussi. Dynamics of an atmospheric pressure plasma plume generated by submicrosecond voltage pulses. *Journal of Applied Physics*, 100(6):063302, 2006.
- [84] J. L. Walsh, D. X. Liu, F. Iza, M. Z. Rong, and M. G. Kong. Contrasting characteristics of sub-microsecond pulsed atmospheric air and atmospheric pressure helium–oxygen glow discharges. *Journal of Physics D: Applied Physics*, 43(3):032001, January 2010.
- [85] G. V. Naidis. Modelling of streamer propagation in atmospheric-pressure helium plasma jets. *Journal of Physics D: Applied Physics*, 43(40):402001, October 2010.
- [86] D. Breden, K. Miki, and L. L. Raja. Computational study of cold atmospheric nanosecond pulsed helium plasma jet in air. *Applied Physics Letters*, 99(11):111501, 2011.
- [87] K. U. Takashima, I. V. Adamovich, Z. Xiong, M. J. Kushner, S. M. Starikovskaia, U. Czarnetzki, and D. Luggenhölscher. Experimental and modeling analysis of fast ionization wave discharge propagation in a rectangular geometry. *Physics of Plasmas*, 18(8):083505, 2011.
- [88] P. M. Bellan. *Fundamentals of Plasma Physics*. Cambridge University Press, 2008.
- [89] M. J. Druyvesteyn and F. M. Penning. The Mechanism of Electrical Discharges in Gases of Low Pressure. *Reviews of Modern Physics*, 12(2):87–174, April 1940.
- [90] M. A. Lieberman and A. J. Lichtenberg. *Principles of Plasma Discharges and Materials Processing*. John Wiley & Sons, Inc., Hoboken, NJ, USA, 2nd edition, April 2005.
- [91] F. F. Chen. *Introduction to plasma physics and controller fusion*. Springer, New York, NY, 2nd edition, 1984.

- [92] L. G. H. Huxley, R. W. Crompton, and M. T. Elford. Use of the parameter E/N. *British Journal of Applied Physics*, 17(9):1237–1238, September 1966.
- [93] J. Hornbeck. The Drift Velocities of Molecular and Atomic Ions in Helium, Neon, and Argon. *Physical Review*, 84(4):615–620, November 1951.
- [94] A. V. Phelps. Compilation of Electron Cross Sections, 2002.
- [95] T. W. Johns. Ionization Instability in Atmospheric-Pressure Gas Discharges. *Applied Physics Letters*, 20(12):495, June 1972.
- [96] H. R. Griem. *Principles of Plasma Spectroscopy*. Cambridge University Press, Cambridge, UK, 2005.
- [97] G. W. F. Drake. *Springer Handbook of Atomic, Molecular, and, Optical Physics: High Precision Calculations for Helium*. Springer New York, New York, NY, January 2006.
- [98] G. Herzberg. *Atomic Spectra and Atomic Structure*. Dover Publications, New York, NY, 2nd edition, 1944.
- [99] A. E. Siegman. *Lasers*. University Science Books, Sausalito, CA, 1986.
- [100] H. J. Kunze. *Introduction to Plasma Spectroscopy*, volume 56 of *Springer Series on Atomic, Optical, and Plasma Physics*. Springer Berlin Heidelberg, Berlin, Heidelberg, 2009.
- [101] W. Demtröder. *Laser Spectroscopy, Vol. 1*. Springer Berlin Heidelberg, Berlin, Heidelberg, 2008.
- [102] A. Kramida, Yu. Ralchenko, J. Reader, and NIST ASD Team. NIST Atomic Spectra Database (version 5.0), 2012.
- [103] A. F. H. van Gessel, E. A. D. Carbone, P. J. Bruggeman, and J. J. A. M. van der Mullen. Laser scattering on an atmospheric pressure plasma jet: disentangling Rayleigh, Raman and Thomson scattering. *Plasma Sources Science and Technology*, 21(1):015003, February 2012.
- [104] A. V. Phelps and J. Molnar. Lifetimes of Metastable States of Noble Gases. *Physical Review*, 89(6):1202–1208, March 1953.
- [105] M. W. Millard, P. P. Yaney, B. N. Ganguly, and C. A. DeJoseph. Diode laser absorption measurements of metastable helium in glow discharges. *Plasma Sources Science and Technology*, 7(3):389–394, August 1998.
- [106] D. W. Marquardt. An Algorithm for Least-Squares Estimation of Nonlinear Parameters. *Journal of the Society for Industrial and Applied Mathematics*, 11(2):431–441, June 1963.

- [107] E. Jones, T. Oliphant, and P. Peterson. SciPy: Open Source Scientific Tools for Python, 2001.
- [108] M. W. Kiehlbauch and D. B. Graves. Inductively coupled plasmas in oxygen: Modeling and experiment. *Journal of Vacuum Science & Technology A: Vacuum, Surfaces, and Films*, 21(3):660, 2003.
- [109] N. A. Popov. Fast gas heating in a nitrogen–oxygen discharge plasma: I. Kinetic mechanism. *Journal of Physics D: Applied Physics*, 44(28):285201, July 2011.
- [110] N. L. Aleksandrov, S. V. Kindysheva, M. M. Nudnova, and A. Yu. Starikovskii. Mechanism of ultra-fast heating in a non-equilibrium weakly ionized air discharge plasma in high electric fields. *Journal of Physics D: Applied Physics*, 43(25):255201, June 2010.
- [111] S. V. Pancheshnyi. Collisional deactivation of N₂(C3Πu, v=0, 1, 2, 3) states by N₂, O₂, H₂ and H₂O molecules. *Chemical Physics*, 262(2-3):349–357, December 2000.
- [112] N. L. Aleksandrov, S. V. Kindysheva, A. A. Kirpichnikov, I. N. Kosarev, S. M. Starikovskaia, and A. Yu. Starikovskii. Plasma decay in N₂, CO₂ and H₂O excited by high-voltage nanosecond discharge. *Journal of Physics D: Applied Physics*, 40(15):4493–4502, August 2007.
- [113] J. M. Pouvesle, a. Khacef, J. Stevefelt, H. Jahani, V. T. Gylys, and C. B. Collins. Study of two-body and three-body channels for the reaction of metastable helium atoms with selected atomic and molecular species. *The Journal of Chemical Physics*, 88(5):3061, 1988.
- [114] K. Urabe, T. Morita, K. Tachibana, and B. N. Ganguly. Investigation of discharge mechanisms in helium plasma jet at atmospheric pressure by laser spectroscopic measurements. *Journal of Physics D: Applied Physics*, 43(9):095201, March 2010.
- [115] G. Nersisyan, T. Morrow, and W. G. Graham. Measurements of helium metastable density in an atmospheric pressure glow discharge. *Applied Physics Letters*, 85(9):1487, August 2004.
- [116] R. Deloche, P. Monchicourt, M. Cheret, and F. Lambert. High-pressure helium afterglow at room temperature. *Physical Review A*, 13(3):1140–1176, March 1976.
- [117] S. Rauf and M. J. Kushner. Dynamics of a coplanar-electrode plasma display panel cell. I. Basic operation. *Journal of Applied Physics*, 85(7):3460, 1999.
- [118] T. J. Linde, T. I. Gombosi, P. L. Roe, K. G. Powell, and D. L. DeZeeuw. Heliosphere in the magnetized local interstellar medium: Results of a three-dimensional MHD simulation. *Journal of Geophysical Research*, 103(A2):1889, 1998.
- [119] G. J. M. Hagelaar and L. C. Pitchford. Solving the Boltzmann equation to obtain electron transport coefficients and rate coefficients for fluid models. *Plasma Sources Science and Technology*, 14(4):722–733, November 2005.

- [120] B. R. Weatherford, E. V. Barnat, Z. Xiong, and M. J. Kushner. Two-Dimensional Electron and Metastable Density Profiles Produced in Helium Fast Ionization Wave Discharges. *Bulletin of the American Physical Society*, Volume 57,, October 2012.
- [121] B. R. Weatherford. (personal communication), 2012.
- [122] S. N. Nahar. Photoionization and electron–ion recombination of He I. *New Astronomy*, 15(5):417–426, July 2010.
- [123] A. Catherinot and B. Dubreuil. Quenching and excitation-transfer processes in the n=4 helium sublevels in a low-pressure glow discharge. *Physical Review A*, 23(2):763–774, February 1981.
- [124] B. Dubreuil and A. Catherinot. Quenching and excitation transfer in the n=3 helium sublevels in a low-pressure glow discharge. *Physical Review A*, 21(1):188–199, January 1980.
- [125] Yu. Ralchenko, R. K. Janev, T. Kato, D. V. Fursa, I. Bray, and F. J. de Heer. Electron-impact excitation and ionization cross sections for ground state and excited helium atoms. *Atomic Data and Nuclear Data Tables*, 94(4):603–622, July 2008.
- [126] P. L. Pritchett, D. Cai, Y. Li, K.-I. Nishikawa, C. Xiao, B. Lembege, Y. Omura, T. Umeda, H. Matsumoto, D. Schriver, R. D. Sydora, G. Joyce, M. Lampe, G. Ganguli, Winskem D., L. Yin, N. Omidi, H. Karimabadi, K. Quest, J. D. Huba, A. Otto, H. Zhu, J. Raeder, T. I. Gombosi, D. L. De Zeeuw, K. G. Powell, T. Tanaka, T. Ogino, and T. D. de Wit. *Space Plasma Simulation*. Springer, 2003.
- [127] J. P. Verboncoeur, M. V. Alves, V. Vahedi, and C. K. Birdsall. Simultaneous Potential and Circuit Solution for 1D Bounded Plasma Particle Simulation Codes. *Journal of Computational Physics*, 104(2):321–328, February 1993.
- [128] T. Holstein. Energy Distribution of Electrons in High Frequency Gas Discharges. *Physical Review*, 70(5-6):367–384, September 1946.
- [129] William Allis. Semidivergence of the Legendre expansion of the Boltzmann equation. *Physical Review A*, 26(3):1704–1712, September 1982.
- [130] L. L. Alves and C. M. Ferreira. IST-Lisbon Helium Cross Sections. Technical report, Instituto Superior Técnico, Lisbon, PT, 2013.
- [131] J. L. Pack, R. E. Voshall, A. V. Phelps, and L. E. Kline. Longitudinal electron diffusion coefficients in gases: Noble gases. *Journal of Applied Physics*, 71(11):5363, 1992.
- [132] N. B. Anikin, S. V. Pancheshnyi, S. M. Starikovskaia, and A. Yu. Starikovskii. Breakdown development at high overvoltage: electric field, electronic level excitation and electron density. *Journal of Physics D: Applied Physics*, 31(7):826–833, April 1998.

- [133] F. Mitchell and L. Snoddy. Ionization Processes in a Long Discharge Tube with Application to Lightning Mechanism. *Physical Review*, 72(12):1202–1208, December 1947.
- [134] A. Yu. Starikovskii and N. L. Aleksandrov. Plasma-assisted ignition and combustion. *Progress in Energy and Combustion Science*, 39(1):61–110, February 2013.
- [135] R. F. Boivin, S. D. Loch, C. P. Ballance, D. Branscomb, and M. S. Pindzola. Line ratio diagnostics in helium and helium seeded argon plasmas. *Plasma Sources Science and Technology*, 16(3):470–479, August 2007.
- [136] K. Compton. Theory of Ionization by Cumulative Action and the Low Voltage Arc. *Physical Review*, 20(4):283–299, October 1922.
- [137] T. Holstein. Imprisonment of Resonance Radiation in Gases. *Physical Review*, 72(12):1212–1233, December 1947.
- [138] T. Holstein. Imprisonment of Resonance Radiation in Gases. II. *Physical Review*, 83(6):1159–1168, September 1951.
- [139] S. O. Macheret, R. J. Lipinski, R. B. Miles, and M. N. Shneider. Electron-Beam-Generated Plasmas in Hypersonic Magnetohydrodynamic Channels. *AIAA Journal*, 39(6):1127–1138, June 2001.
- [140] E. P. Gurijanov and P. T. Harsha. AJAX: New Directions in Hypersonic Technology. In *International Space Planes and Hypersonic Systems and Technologies*, pages 1–9, Seal Beach, CA, 1996. AIAA.
- [141] N. L. Aleksandrov, S. V. Kindysheva, I. N. Kosarev, and A. Yu. Starikovskii. Plasma decay in air and N₂ : O₂ : CO₂ mixtures at elevated gas temperatures. *Journal of Physics D: Applied Physics*, 41(21):215207, November 2008.
- [142] G. Herzberg and J. W. T. Spinks. *Molecular Spectra and Molecular Structure: Spectra of Diatomic Molecules*. Krieger Publishing Company, Malabar, FL, 2nd edition, 1950.
- [143] K. Akhtar, J. E. Scharer, S. M. Tysk, and E. Kho. Plasma interferometry at high pressures. *Review of Scientific Instruments*, 74(2):996, January 2003.
- [144] S. V. Pancheshnyi, S. M. Starikovskaia, and A. Yu. Starikovskii. Population of nitrogen molecule electron states and structure of the fast ionization wave. *Journal of Physics D: Applied Physics*, 32(17):2219–2227, September 1999.
- [145] E. I. Mintoussov, S. J. Pendleton, F. G. Gerbault, N. A. Popov, and S. M. Starikovskaia. Fast gas heating in nitrogen–oxygen discharge plasma: II. Energy exchange in the afterglow of a volume nanosecond discharge at moderate pressures. *Journal of Physics D: Applied Physics*, 44(28):285202, July 2011.

- [146] C. O. Laux. *Optical Diagnositcs and Radiative Emission of Air Plasmas*. PhD thesis, Stanford University, 1993.
- [147] C. O. Laux. Radiation and Nonequilibrium Collisional-Radiative Models. In D. Fletcher, J.-M. Charbonnier, G. S. R. Sarma, and T. Magin, editors, *von Karman Institute Lecture Series 2002-07*, Rhode-Saint-Genese, Belgium, 2002.
- [148] J. Luque and D. R Crosley. LIFBASE: Database and spectral simulation program, 1999.
- [149] G. Hartmann and P. C. Johnson. Measurements of relative transition probabilities and the variation of the electronic transition moment for N 2 C 3 Π u -B 3 Π g second positive system. *Journal of Physics B: Atomic and Molecular Physics*, 11(9):1597–1612, May 1978.
- [150] A Chelouah, E Marode, G Hartmann, and S Achat. A new method for temperature evaluation in a nitrogen discharge. *Journal of Physics D: Applied Physics*, 27(5):940–945, May 1994.
- [151] A. Budó. Über dieTriplet-Bandentermformel für den allgemeinen intermediären Fall und Anwendung derselben auf dieB3 Π -,C3 Π -Terme des N2-Moleküls. *Zeitschrift für Physik*, 96(3-4):219–229, March 1935.
- [152] R. R. Laher and F. R. Gilmore. Improved Fits for the Vibrational and Rotational Constants of Many States of Nitrogen and Oxygen. Technical report, Defense Nuclear Agency, Alexandria, VA, December 1990.
- [153] L. Bullock and C. Hause. Molecular constants of the B3 Π and A3 Σ states of N2. *Journal of Molecular Spectroscopy*, 39(3):519–520, September 1971.
- [154] A. Lofthus and P. H. Krupenie. The spectrum of molecular nitrogen. *Journal of Physical and Chemical Reference Data*, 6(1):113, 1977.
- [155] T Hasegawa and J. D. Winefordner. Spatially resolved rotational and vibrational temperatures of a neutral nitrogen molecule in the ICP. *Spectrochimica Acta Part B: Atomic Spectroscopy*, 42(5):651–663, January 1987.
- [156] J. D. Hunter. Matplotlib: A 2D graphics environment. *Computing in Science \& Engineering*, 9(3):90–95, 2007.